



HAL
open science

Modelling growing epithelium

Qiuyang Qu

► **To cite this version:**

Qiuyang Qu. Modelling growing epithelium. Physics [physics]. Université Paris sciences et lettres, 2021. English. NNT : 2021UPSLE042 . tel-03956847

HAL Id: tel-03956847

<https://theses.hal.science/tel-03956847v1>

Submitted on 25 Jan 2023

HAL is a multi-disciplinary open access archive for the deposit and dissemination of scientific research documents, whether they are published or not. The documents may come from teaching and research institutions in France or abroad, or from public or private research centers.

L'archive ouverte pluridisciplinaire **HAL**, est destinée au dépôt et à la diffusion de documents scientifiques de niveau recherche, publiés ou non, émanant des établissements d'enseignement et de recherche français ou étrangers, des laboratoires publics ou privés.



THÈSE DE DOCTORAT

DE L'UNIVERSITÉ PSL

Préparée à l'École Normale Supérieure

Modélisation de l'épithélium en croissance

Soutenue par

Qiuyang QU

Le 07 Juillet 2021

École doctorale n°564

Physique en Île-de-France

Spécialité

Physique

Composition du jury :

Francois GRANER Université de Paris	<i>Président</i>
Martin MÜLLER Université de Lorraine	<i>Rapporteur</i>
Jean Marc ALLAIN École Polytechnique	<i>Rapporteur</i>
Benoit ROMAN Université PSL	<i>Examineur</i>
Loïc LE GOFF Université de Aix-Marseille	<i>Examineur</i>
Martine BEN AMAR École Normale Supérieure	<i>Directrice de thèse</i>

Contents

Introduction	v
0.1 Motivation	v
0.2 Approach of the present work	ix
1 Basic theories	1
1.1 Finite strain theory	1
1.1.1 Strain-displacement relation	2
1.1.2 Stress	2
a) Hyper-elasticity	3
b) Equilibrium equation	4
1.1.3 Variational method for fiber anisotropy	4
1.2 Overview of plate and shell theories	6
1.2.1 Föppl-Von Kármán (FvK) model	7
a) Strain-displacement assumption	7
b) Hooke’s law for the stress-strain relation	8
c) Lagrange-Euler equations by variational method	8
1.2.2 Classical shell theory	9
1.2.3 Strain-displacement assumption	10
a) Variational method with the linear stress-strain relation	10
b) Shallow shell approximation	11
1.2.4 Mindlin–Reissner model	11
1.2.5 Difficulties in numerical implementation	12
I Crack opening on epithelium of <i>C. elegans</i>	15
2 Stress assessment in <i>C. elegans</i> elongation	17
2.1 Simplified cylindrical geometry	17
2.2 Calculation of the elastic stress	21
2.3 Planar active stress by actin-myosin networks	23
2.4 Active strain/stress with simulations	25
2.5 Conclusion	30

3	Solutions for crack opening by laser ablation	31
3.1	Linear elastic fracture mechanics (LEFM) for a planar crack	31
3.1.1	Review of LEFM	31
3.1.2	Analytical solution by Theocaris	36
3.1.3	Modified formula for finite strain	38
3.2	Numerical simulations with XFEM in MATLAB	43
3.2.1	Basic algorithm	43
3.3	Results and discussion	47
3.3.1	Geometry effects	47
3.3.2	Tilting angle in biaxial loading	50
3.4	Conclusion	61
II	Buckling of Drosophila wing disc	63
4	Bilayer Fvk model with growth	65
4.1	Governing equations with growth	65
4.1.1	Active momentum by ECM and initial curvatures	67
4.1.2	Reduced 1D case with clamped boundary	68
4.1.3	Solution with nonlinear effects	70
4.1.4	Solution with ECM defect	71
4.1.5	Quadratic effect calculated in MANLAB	72
4.2	Numerical implementation in COMSOL	76
4.2.1	Active bending with growth	76
4.2.2	Equivalent monolayer shell with in-plane growth	79
4.2.3	Additional bending	84
4.2.4	ECM stiffness contribution	86
4.2.5	Nonlinear effects	89
4.2.6	Conclusion	91
4.3	Conclusion	92
5	Finite element simulations with beams and solids	93
5.1	Algorithm of geometrical nonlinearity	93
5.2	Finite element simulations in MATLAB	96
5.2.1	Nonlinear Euler-Bernouli beam	97
5.2.2	3D Solids with beams	98
5.2.3	2D wrinkling and folding simulations	106
	a) Geometry effects	109
	b) Material properties	113
	c) Clamped boundary	116
5.3	Conclusion	119
6	Conclusion	121
6.1	Crack opening on epithelium of C.elegans	121
6.2	Buckling of Drosophila wing disc	122
	Publication	123

<i>CONTENTS</i>	iii
List of figures	151
List of tables	161
Bibliography	163

Introduction

0.1 Motivation

Shapes in nature, from cauliflower to brain, arise from growth of tissues. Growth intrinsically generates strains and stresses. Conversely, through mechano-transduction mechanisms, stresses regulate growth as growing plants [1, 2]. Understanding ultimately the emergence of shapes, in particular in biological tissues, requires to capture the mechanical features that are inherent to the living material [3].

Our human body consists of four types of tissues: epithelial, connective, muscular, and nervous. The aim of this thesis is to investigate growing epithelial tissues with an extracellular matrix (ECM). The epithelium is a composite of specialized cellular organizations arranged into sheets without significant intercellular substance. It covers the body, lines all cavities, and composes the glands. It may be simple, consisting of a single layer in Fig.(0.1), or stratified, consisting of several layers in Fig.(0.2).

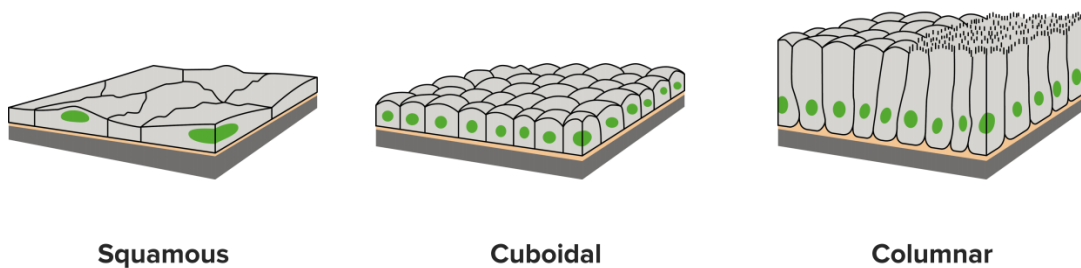


Fig. 0.1 *Simple classification of epithelium tissue*

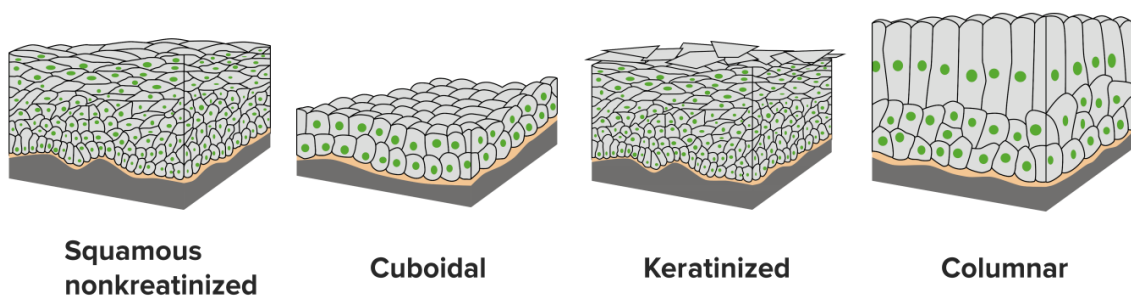


Fig. 0.2 *Stratified classification of epithelium tissue*

There are two biological systems for basic research in our interest: epithelium in *C.elegans* [4] and *Drosophila* wing disc [5, 6, 7].

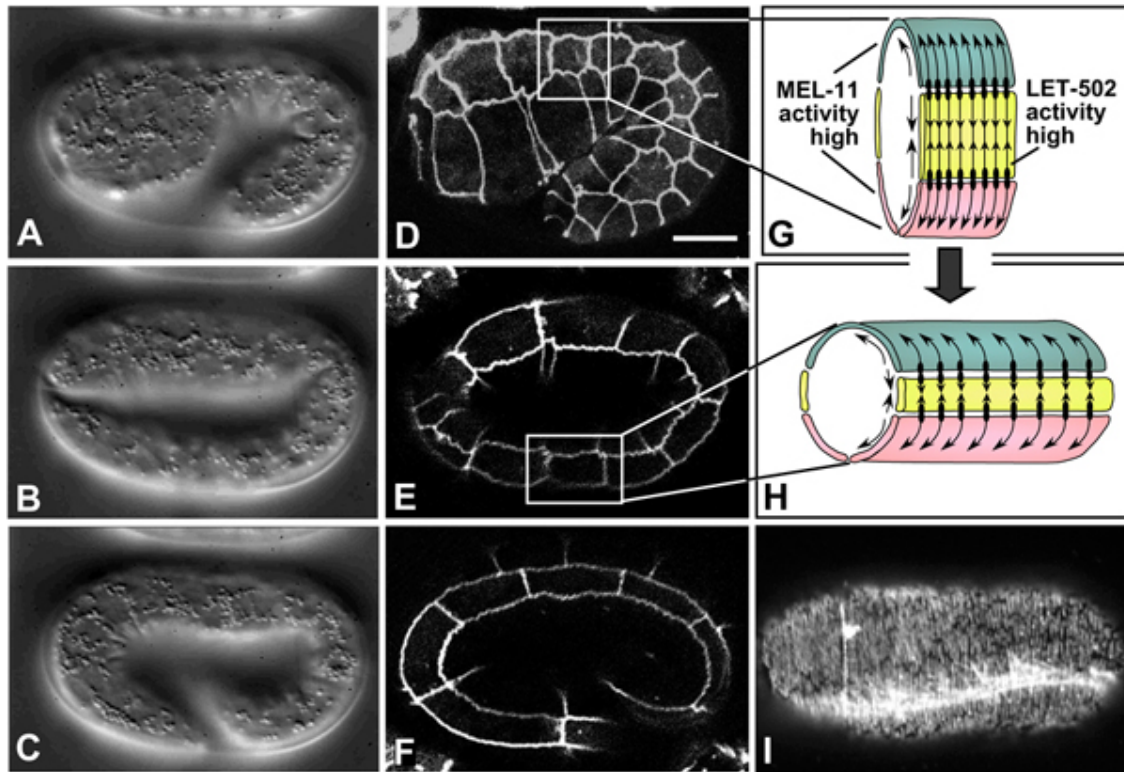


Fig. 0.3 *C. elegans* embryonic elongation: ventral cells are shown in pink, seam cells in yellow, and dorsal cells in teal. Contractile forces are produced predominantly by seam epidermal cells (arrows pointing toward one another), and transmitted to dorsal and ventral cells via adherens junctions (black ovals), which anchor circumferential actin filament bundles (CFBs) in dorsal and ventral cells (black lines and arrows within dorsal and ventral cells). CFBs are thought to transmit and distribute the forces of contraction evenly throughout the epidermis. Scale bar = $5\mu m$ (from [4]).

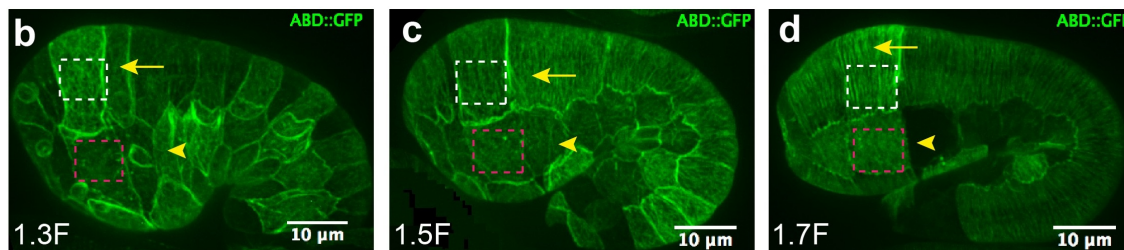


Fig. 0.4 Actin filament organization during *C. elegans* embryonic elongation when $\Delta L/L_0 = 30\%, 50\%, 70\%$ (from [8]).

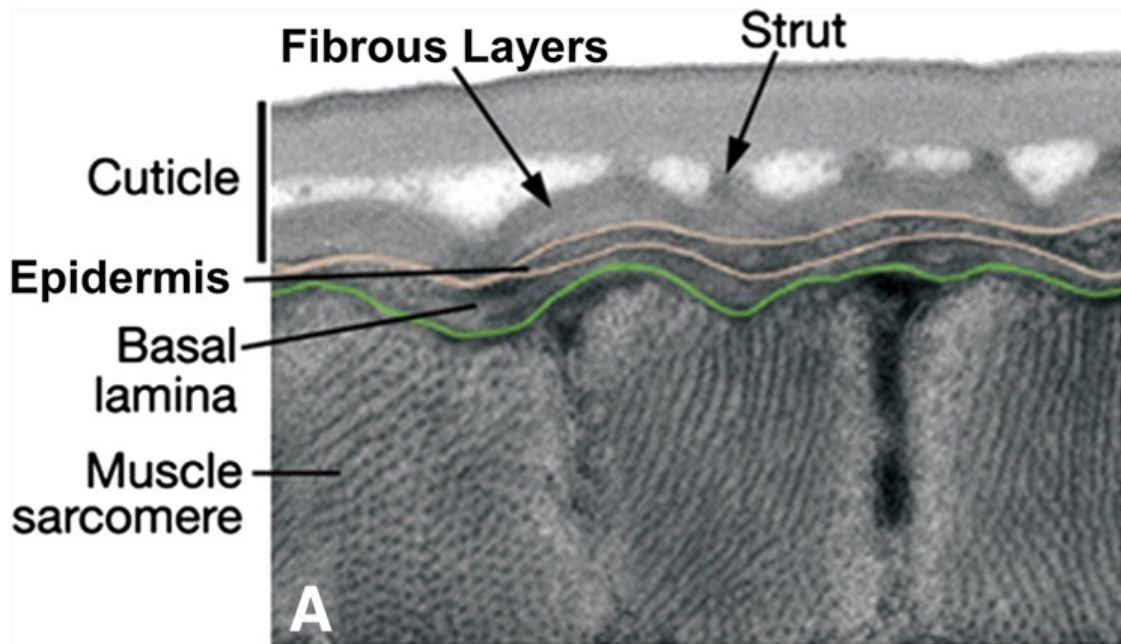


Fig. 0.5 Cross-section of the outer layers of the *C. elegans* tissue showing muscle cells below the epidermis and cuticle viewed by transmission electron microscopy (from [9]).

Fig.(0.3) and Fig.(0.4) show a *C. elegans* embryo during morphogenesis. We give attention to the role of monolayer epidermis with an extracellular matrix (ECM) in elongation. In this course of the development, an actin-myosin network is found active [8] which acts as a pivotal part in chemical-mechanical transmission. It will exert inner stress along the circumferential direction (see arrows) in Fig.(0.3). In Fig.(0.4) we can see clearly the fiber distribution indicated by yellow arrows. Filaments (fibers) are more ordered in the white box (dorsal cells) than in the red one (seam cells) after extension. And they align circumferentially as elongation passes from 30% to 70%. This implies that the network with filaments is coupled with the mechanical deformation which might generate the active force for the development. Fig.(0.5) demonstrates the final multilayer structure of the animal surface. Each layer has its own structure and there are wrinkles in the epidermis and basal lamina. Although it is not easy to quantify the stresses in vivo, there are some methods to measure the force more or less at the cell scale [10, 11, 12, 13, 14]. In this thesis, we exploit results from the laser ablation technique [8] for our case study. We attempt to use an analytical method to understand the mechanism of *C. elegans* elongation. We shall focus on stresses in each part tagged by different colors (see Fig.0.3) with finite strain and use laser cuts to give an estimate for the stress distribution in the experiment.

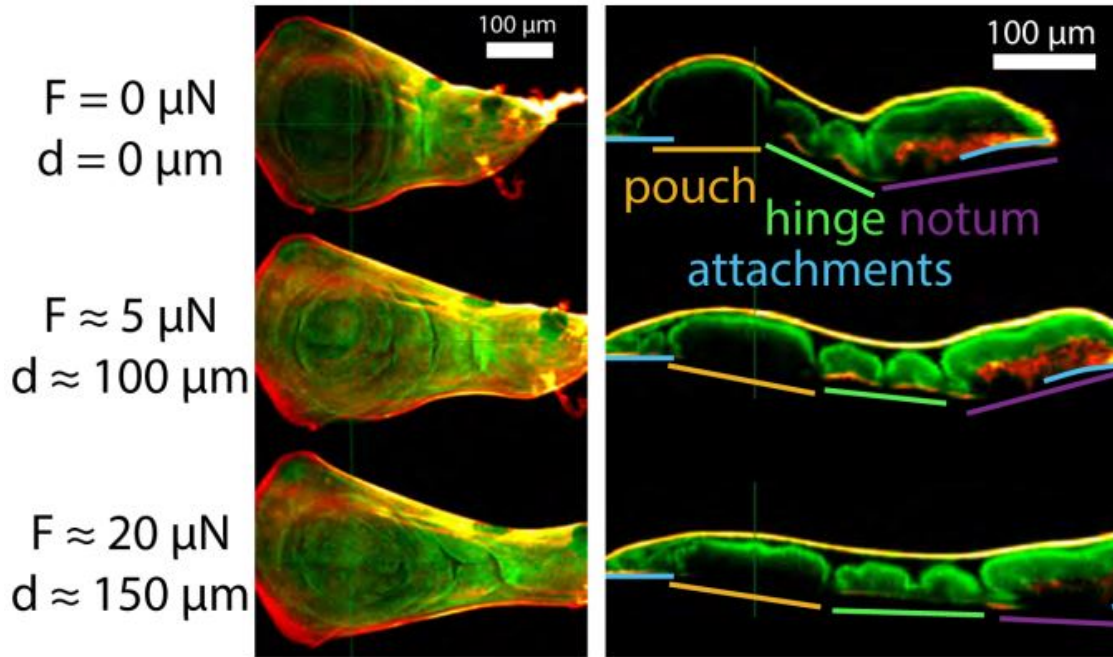


Fig. 0.6 Images of a stretched disc for increasing force-displacement (F - d) values (from [7]).

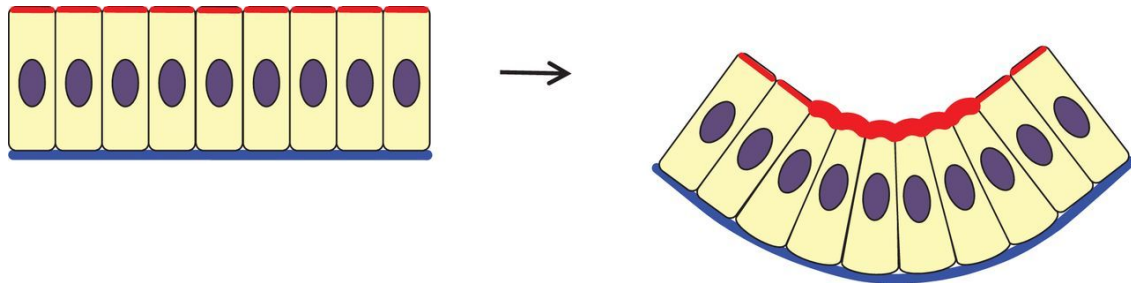


Fig. 0.7 Classical apical constriction. In a monolayer where cells keep constant volumes, accumulated actomyosin meshwork at the apical end of the cells constricts, giving rise to wedge-shaped cells. This forces the epithelium into a concave apical surface with an enlarged basal area. Red, actomyosin (note enrichment on the apical side of the cells); blue, basal lamina; purple, nucleus (from [15]).

The second biological system of our work is the *Drosophila* wing disc in Fig.(0.6). We find two scales of deformation on the right picture: global bending curve shown in yellow and local folding deformation in green. As far as we know, growth with constraints will induce buckling [16, 17] resulting in large geometry change. Moreover, there is always differential growth rate in various kinds of cells during morphogenesis. In-plane cell-cell compression induced by growth as well as boundary squeezes naturally generate out-of-plane bending. In addition, active networks can also play an important role in tissue deformation. In Fig.(0.7), there is a schematic diagram explaining such a mechanism: a contractile network and stress gradient give rise to the bending

of a multilayer structure. These two mechanisms often appear simultaneously in the experimental observation. With genetic control, we can regulate the final shape and size of the epithelium tissue [18] on the basis of a full understanding of the development of multicellular organisms. It is possible to use structure design with growth for shape programming. In this thesis, we try to explain the buckling phenomena and provide some ideas for tissue scale deformation with geometrical nonlinearity.

0.2 Approach of the present work

There are some successful models at micro and meso scale [19, 20, 21]. We shall use classical continuum mechanics as the main tool with the traditional finite element method [22, 23, 24, 25] in numerical simulations. At the macroscopic tissue scale, the theory of nonlinear elasticity is shown to be most often appropriate for large deformation. This thesis will deal with two scientific problems about *C. elegans* and *Drosophila*.

We introduce the basic knowledge on finite elasticity in chapter 1 and briefly review the theory of plates and shells. We employ a general variational method to get the governing equations of a type of fiber-reinforced materials in our concern. Then we introduce the Föppl-Von Kármán (FvK) model for a thin plate. Finally we mention the shallow shell theory and difficulties in numerical implementation.

For the first part (*C. elegans*), we want to study the results of the laser ablation technique to obtain the stress distribution estimate [8]. Tiny laser cuts with several micrometers are made in the external epithelium. The crack will open in a stretched state and the ratio of opening size over equilibrium length can reflect the value of stress vertical to the cut. But we need to consider the effect of finite strain in practice. Besides, an analytical formula as simple as possible is favored by biologists for a quick evaluation. So we modify the linear formula in our problem.

In chapter 2, a simplification of the geometry assuming cylindrical configuration with an opening angle provides the possibility for theoretical analysis, which perfectly matches the experimental data [26]. Fiber anisotropy is judged in calculations with finite elasticity. Active stress induced by molecular motors is important in the elongation of *C. elegans* which explains the crack opening in both orthogonal directions in seam (S) cells.

In chapter 3, linear elastic fracture mechanics (LEFM) is surveyed for mode I crack opening. The analytical solution in the isotropic case is given for the plane problem under biaxial loading. In order to extend the simple theory for finite strain, a modified formula with the fracture factor is proposed by replacing the original Young's modulus with an equivalent one from the tangent stiffness matrix. Results demonstrate the validity of the method in the real application for stress assessment. On the other hand, XFEM is utilized for the real size simulation. A basic algorithm is introduced and we apply the open source code in MATLAB in our situation. A tilting angle of the initial crack in biaxial loading is then discussed.

For the second part (*Drosophila*), we want to employ the theory of plates and shells on a thin cell lamina with an extracellular matrix (ECM) for tissue scale buckling. As we know, many thin living objects are composed of several layers which might have varying elastic properties and also follow different rules of growth. So it is necessary to extend the traditional monolayer model to multilayer slender structures with geometrical nonlinearity. We hope the theory with simulations can more or less offer some valuable opinions.

In chapter 4, an equivalent monolayer model is obtained through a homogenization method

by integral over the thickness. A bilayer Föppl-Von Kármán (FvK) representation is acquired in consideration of growth, active bending and initial curvatures. Governing equations are deduced with different boundary conditions. An extra nonlinear term appears and one analytical solution is derived in 1D. More complicated situations involving ECM defects are examined through the numerical calculation in MATLAB. Afterwards, COMSOL is used to calculate a 3D growing shell with nonlinear effects. We emphasize on the localized growth. Various cases are tackled and implemented in the module of solid mechanics.

Eventually in chapter 5, a finite element simulation is carried out in a MATLAB platform. Geometrical nonlinearity is implemented in the toolbox with beam and solid elements. The Riks solver is employed for the buckling solution. A 3D strip case is discussed considering nonuniform growth and the stiffer ECM. Then 2D wrinkling and folding simulations are analyzed with viscoelasticity for pattern formation. We find geometry as well as material properties like modulus and viscosity will affect the final solutions obviously.

Chapter 1

Basic theories

In this chapter, we shall first review the theory of finite elasticity with fiber anisotropy by introducing the deformation gradient tensor and the special direction vector for fibers. The main idea of finite strain theory is to distinguish the initial and current configuration for the description of the geometry. Different strain measurements are set up in both configurations with the relative transform rule. Hereafter, stresses can be calculated once the strain energy density function is known. A variational method unifies the governing equations in different configurations with the corresponding stress definition. One class of nonlinear visco-elastic models is derived and the energy decomposition is employed for further simplification.

Then it comes to an overview of plate and shell theories. A Classical model, Föppl-Von Kármán (FvK) limit, is favored for the thin plate and the initial curvature is considered by shallow shell theories. In order to obtain the governing equations in 2D, a variational method is used again with perturbation of the thickness. Difficulties in numerical implementation are also mentioned briefly in this section.

1.1 Finite strain theory

We begin with a brief review of the finite deformation theory. We assume the initial configuration \mathbf{X} and the current one $\mathbf{x}(\mathbf{X}, t)$. The deformation gradient tensor is defined as

$$F_{iJ} = \frac{\partial x_i}{\partial X_J} = \delta_{iJ} + \frac{\partial u_i}{\partial X_J} \quad (1.1)$$

where $\mathbf{u}(\mathbf{X}, t)$ is the displacement vector and we have $\mathbf{u}(\mathbf{X}, t) = \mathbf{x}(\mathbf{X}, t) - \mathbf{X}$. We can see from Fig.(1.1) that the deformation gradient tensor (Matrix) contains all the kinematic information. Here the alphabet i, j, k, l takes the value from 1 to 3. The uppercase and the lowercase represent the initial point (undeformed) and the current one (after deformation) respectively. In some references [27, 28, 29] \mathbf{F} is called a two-point tensor because it connects two configurations and contains geometric information. Obviously the gradient tensor ought to satisfy the compatibility condition

$$\mathbf{F} \times \nabla_{\mathbf{X}} = \mathbf{0} \Rightarrow \frac{\partial F_{iJ}}{\partial X_K} E_{JKL} = 0_{iL} \quad (1.2)$$

where $E_{JKL} = (E_J \times E_K) \cdot E_L$.

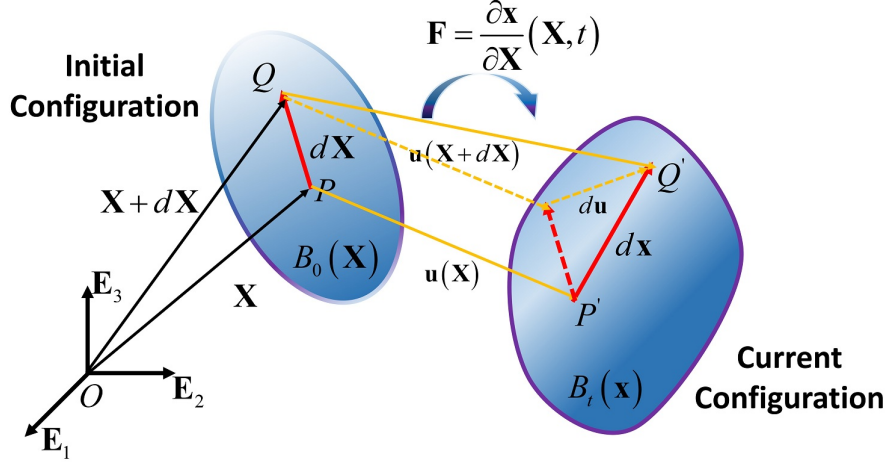


Fig. 1.1 Illustration of the deformation map

1.1.1 Strain-displacement relation

According to Eq.(1.1), we know $dx = F \cdot dX$ and then $dx \cdot dx - dX \cdot dX = dX^T (F^T F - I) dX$. Henceforward we define the Green-Lagrange strain tensor [27, 28, 29]

$$\mathbf{E} = \frac{1}{2}(\mathbf{F}^T \mathbf{F} - \mathbf{I}) = \frac{1}{2}(\nabla_X \mathbf{u} + \mathbf{u} \nabla_X + \nabla_X \mathbf{u} \cdot \mathbf{u} \nabla_X) \quad (1.3)$$

where $\mathbf{u} \nabla_X = (\partial_J u_i) e_i \otimes E_J$ and $\nabla_X \mathbf{u} = (\mathbf{u} \nabla_X)^T$. We could decompose the strain tensor into a linear and a nonlinear part [30, 31]

$$E_{IJ} = e_{IJ} + \eta_{IJ} \\ e_{IJ} = \frac{1}{2}(\partial_J u_i + \partial_I u_j); \eta_{IJ} = \frac{1}{2} \partial_I u_k \partial_J u_k \quad (1.4)$$

In comparison, we define the Euler-Almansi strain [27, 28, 29] in the current configuration as

$$\boldsymbol{\varepsilon} = \frac{1}{2}(\mathbf{I} - \mathbf{F}^{-T} \mathbf{F}^{-1}) \approx \frac{1}{2}(\nabla_x \mathbf{u} + \mathbf{u} \nabla_x) \quad (1.5)$$

and there is a relation between the two strains as

$$\mathbf{E} = \mathbf{F}^T \cdot \boldsymbol{\varepsilon} \cdot \mathbf{F} \quad (1.6)$$

In 1D, for example, we have $\frac{dx^2 - dX^2}{dX^2} = [(1 + \frac{\partial u}{\partial X})^2 - 1]$ and the right hand side equals $2E_{11}$ with Eq.(1.3). In linear theory, $\boldsymbol{\varepsilon} \approx \frac{1}{2}(\nabla_x \mathbf{u} + \mathbf{u} \nabla_x)$ with compatibility condition: $-\nabla \times \boldsymbol{\varepsilon} \times \nabla = \mathbf{0}$.

Surely, we could offer a more general definition of the strain measurement via the Seth-Hill family [27, 28, 29]. Nevertheless, we henceforth limit our discussion in the dissertation using Eq.(1.3) to Eq.(1.6).

1.1.2 Stress

There are many text books presenting a full discussion of stress with finite strain [27, 28, 29]. The main idea is that we should be very careful of the area or volume change due to large deformation. In infinitesimal theory, there is no difference between the current and initial configuration.

The Cauchy stress is thus enough with the linear part of the strain in Eq.(1.4) and Eq.(1.5). In nonlinear analysis, however, the Green-Lagrange strain is of practical usage even though the equilibrium equation is expressed in the current body after deformation. Here we want to summarize the comprehension by work duality [27, 28, 29]. The virtual work principle on the total elastic energy density function \mathcal{E} reads

$$\delta\mathcal{E} = \int_{{}^tV} \sigma_{ij} \delta\varepsilon_{ij} d{}^tV = \int_{{}^0V} S^I_{iJ} \delta F_{iJ} d{}^0V = \int_{{}^0V} S^{II}_{IJ} \delta E_{IJ} d{}^0V \quad (1.7)$$

where ε and \mathbf{E} are described by Eq.(1.3) and Eq.(1.5). σ_{ij} is the Cauchy stress tensor, S^I_{iJ} is the first Piola-Kirchhoff (PK-I) stress tensor and S^{II}_{IJ} is the second Piola-Kirchhoff (PK-II) stress tensor. 0V is the domain in the reference configuration and tV in the current one. In order to change the integral domain, we need to use the volume transform

$$d{}^tV = \det(\mathbf{F}) d{}^0V = J d{}^0V \quad (1.8)$$

After we employ Eq.(1.3) and

$$\delta\varepsilon \approx \frac{1}{2} \mathbf{F}^{-T} (\delta \nabla_X \mathbf{u}) + \frac{1}{2} (\delta \mathbf{u} \nabla_X) \cdot \mathbf{F}^{-1} \quad (1.9)$$

then we arrive at the clarification of Cauchy $\boldsymbol{\sigma}$, PK-I \mathbf{S}^I and PK-II \mathbf{S}^{II} stresses as

$$\boldsymbol{\sigma} = J^{-1} \mathbf{S}^I \cdot \mathbf{F}^T = J^{-1} \mathbf{F} \cdot \mathbf{S}^{II} \cdot \mathbf{F}^T \quad (1.10)$$

where we assume $\boldsymbol{\sigma}$ and \mathbf{S}^{II} are symmetric in the proof of the relationship above. In other words, we do not consider the micro-polar effect [32, 33, 34]

a) Hyper-elasticity

A material is called hyper-elastic if it satisfies the integrability condition [27, 28, 29]

$$S^I_{iJ} \delta F_{iJ} = \delta \mathcal{W}(\mathbf{F}) \Rightarrow S^I_{iJ} = \frac{\partial \mathcal{W}}{\partial F_{iJ}} \quad (1.11)$$

Thanks to Eq.(1.10), we can obtain the Cauchy stress from the elastic energy density function $\mathcal{W}(\mathbf{F})$

$$\boldsymbol{\sigma} = J^{-1} \frac{\partial \mathcal{W}(\mathbf{F})}{\partial \mathbf{F}} \cdot \mathbf{F}^T \quad (1.12)$$

But the function $\mathcal{W}(\mathbf{F})$ can not be chosen arbitrarily and there are the limitations called objectivity and symmetry

$$\mathcal{W}(\mathbf{F}) = \mathcal{W}({}^t\mathbf{Q} \cdot \mathbf{F}) \quad (1.13a)$$

$$\mathcal{W}(\mathbf{F}) = \mathcal{W}(\mathbf{F} \cdot {}^0\mathbf{H}) \quad (1.13b)$$

where ${}^t\mathbf{Q}$ is the orthogonal matrix for rigid rotations and ${}^0\mathbf{H}$ is the transform operator for the symmetry of matter. Obviously, with principle of objectivity [27, 28, 29], we obtain

$$\mathcal{W}(\mathbf{F}) = \mathcal{W}(\mathbf{C}) = \mathcal{W}(\mathbf{F}^T \mathbf{F}) \quad (1.14)$$

where \mathbf{C} is called the right Cauchy-Green tensor. We introduce the polar decomposition for a better understanding. We know that an arbitrary non-singular matrix is a map which consists of a rotation \mathbf{R} and a distortion \mathbf{U} as

$$\mathbf{F} = \mathbf{R}\mathbf{U} \Rightarrow \mathbf{F}^T\mathbf{F} = \mathbf{U}^2 > 0 \quad (1.15)$$

where $\mathbf{R}^{-1} = \mathbf{R}^T$ is a two-point tensor and $\mathbf{U} = \mathbf{U}^T$ is defined in the reference configuration. So we find $\mathcal{W}(\mathbf{C}) = \mathcal{W}(\mathbf{U}^2)$. Furthermore, if the material is isotropic then we have ${}^0\mathbf{H}$ is in the orthogonal group too. Then we can get

$$\mathcal{W}(\mathbf{U}^2) = \mathcal{W}({}^0\mathbf{H}^T\mathbf{U}^2{}^0\mathbf{H}) = \mathcal{W}(\lambda_1, \lambda_2, \lambda_3) \quad (1.16)$$

where $\lambda_i > 0$ are the eigenvalues of \mathbf{U} . In physics, they represent the average deformation field of a representative volume element in the local eigen-space. In practice we can use an invariant form for the isotropic hyper-elastic constitutive relation [28, 29, 35, 36]

$$\begin{aligned} \mathcal{W}(\mathbf{C}) &= \mathcal{W}(I_1, I_2, I_3) \\ I_1 &= \text{tr}(\mathbf{C}), \quad I_2 = \frac{1}{2}(\text{tr}(\mathbf{C})^2 - \text{tr}(\mathbf{C}^2)), \quad I_3 = \det(\mathbf{C}) \end{aligned} \quad (1.17)$$

b) Equilibrium equation

In classical continuum mechanics, momentum conservation reads the same for both the linear and nonlinear problem [37] as

$$\rho\ddot{x}_i = \frac{\partial}{\partial x_j}\sigma_{ij} + b_i \quad (1.18)$$

where ρ is the density of matter, \mathbf{b} is the body force and $\boldsymbol{\sigma}$ is the Cauchy stress tensor with $\boldsymbol{\sigma} = \boldsymbol{\sigma}^T$ due to the equilibrium of angular momentum. Furthermore, if we neglect the inertial term and the body force, the equation becomes

$$\frac{\partial}{\partial x_j}\sigma_{ij} = \partial_j\sigma_{ij} = 0 \quad (1.19)$$

We can also obtain the equilibrium equation in the initial configuration by the variation Eq.(1.7)

$$\partial_J(S_{i,J}^I) = 0 \quad (1.20)$$

In a numerical implementation like the finite element method (FEM), we also employ the virtual work of the PK-II stress [27, 28, 29] as Eq.(1.7) and Eq.(1.4) by an incremental-iterative solver from the point view of the total and updated Lagrangian form [30, 31, 38, 39, 40]. The total Lagrangian formulation refers the stress and the strain variables at time $t + \Delta t$ to the original configuration at time zero. In comparison, the updated Lagrangian method is that the geometry (initial configuration) is updated after calculation of each time step.

1.1.3 Variational method for fiber anisotropy

In this section, we want to use the principle of virtual work to get the governing equations for elasticity with fiber anisotropy. We employ the method [41] taking dissipation into account. It

is a general approach for a material with a special direction \mathbf{n} . We start with the power balance equation

$$\delta \dot{\mathcal{E}}_{elas} + \delta \dot{\mathcal{R}} + \delta \dot{\mathcal{E}}_{kine} - \delta \dot{W}_{ext} = 0 \quad (1.21)$$

where \mathcal{E}_{elas} is the total free energy, $\dot{\mathcal{R}}$ is the dissipative part of the system, \mathcal{E}_{kine} is the kinetic energy (inertial term in Eq.(1.18)) and W_{ext} is the external work. Generally, we can define

$$\mathcal{E}_{elas} = \int {}^t\mathcal{W}(\mathbf{F}, \mathbf{n}, \mathbf{n}_0, \mathbf{n}\nabla, \eta, \eta_0) d {}^t\mathcal{V} \quad (1.22a)$$

$$\dot{\mathcal{R}} = \int \dot{R}(\mathbf{D}, \mathbf{n}^J, \dot{\eta}) d {}^t\mathcal{V} \quad (1.22b)$$

$$\mathcal{E}_{kine} = \int \rho \frac{1}{2} \mathbf{v}^2 d {}^t\mathcal{V} \Rightarrow \delta \dot{\mathcal{E}}_{kine} = \int \rho \dot{\mathbf{v}} \delta \mathbf{v} d {}^t\mathcal{V} \quad (1.22c)$$

$$\delta \dot{W}_{ext} = \int (\mathbf{b} \cdot \delta \mathbf{v} + \mathbf{b}_n \cdot \delta \dot{\mathbf{n}} + b_\eta \delta \dot{\eta}) d {}^t\mathcal{V} + \int \gamma \mathbf{n} \cdot \delta \dot{\mathbf{n}} d {}^t\mathcal{V} \quad (1.22d)$$

where \mathbf{n} is a unit vector field with a Lagrange multiplier γ representing the specific direction of the material, \mathbf{n}_0 is the initial vector and η is an inner parameter (could be the dispersion angle of the fibers) which reflects the degree of anisotropy. ${}^t\mathcal{W}$ is the elastic energy density function at time t and \dot{R} is the dissipation density function. The variables like \mathbf{D}, \mathbf{n}^J will be explained in Eq.(1.23). Body forces $\mathbf{b}, \mathbf{b}_n, b_\eta$ and the Lagrange constraint γ appear in the variation of the external work.

In order to obtain the variation of the energy in a rate form, also for the dissipative function $\dot{\mathcal{R}}$, we need to define several kinds of velocity quantities here.

$$\dot{\mathbf{F}} = \frac{d}{dt} \frac{\partial \mathbf{x}}{\partial \mathbf{X}} = \frac{\partial \mathbf{v}}{\partial \mathbf{X}} = \frac{\partial \mathbf{v}}{\partial \mathbf{x}} \cdot \frac{\partial \mathbf{x}}{\partial \mathbf{X}} = \mathbf{L} \cdot \mathbf{F} \quad (1.23a)$$

$$\mathbf{L} = \mathbf{D} + \mathbf{W} = \frac{1}{2}(\mathbf{L} + \mathbf{L}^T) + \frac{1}{2}(\mathbf{L} - \mathbf{L}^T) \quad (1.23a)$$

$$\mathbf{n}^J = \dot{\mathbf{n}} - \mathbf{W} \cdot \mathbf{n} \quad (1.23b)$$

where $\mathbf{L} = \mathbf{v} \nabla_{\mathbf{x}} = \mathbf{grad}(\mathbf{v})$ is the gradient of the velocity of a material point after deformation with $\dot{\mathbf{F}} = \mathbf{v} \nabla_{\mathbf{X}} = \mathbf{Grad}(\mathbf{v})$ in the initial configuration. Here we can divide \mathbf{L} in two matrices: the symmetric part \mathbf{D} for deformation and the anti-symmetric one \mathbf{W} for rigid rotations. For objectivity, we employ the Jaumann derivative \mathbf{n}^J to eliminate rotation effects while it is not the unique choice [41]. Then we can calculate $\delta \dot{\mathcal{E}}$ with generalized velocities

$$\delta \dot{q} = \delta(\mathbf{v}, \dot{\mathbf{n}}, \dot{\eta}) \quad (1.24)$$

In addition, we shall use the integral transform $\int d {}^t\mathcal{V} = \int J d {}^0\mathcal{V}$ to change the domain for time derivative calculations since \mathbf{X} is independent of t . For the variation of the gradient operator, we take $\nabla_{\mathbf{X}} = \nabla_{\mathbf{x}} \cdot \mathbf{F}$ for the transform. Finally, it is not difficult to get governing equations back in the current configuration as

$$\rho \dot{\mathbf{v}} = \boldsymbol{\sigma} \cdot \nabla + \mathbf{b} \quad (1.25a)$$

$$\frac{\partial \dot{R}}{\partial \mathbf{n}^J} = \mathbf{b}_n + \gamma \mathbf{n} - \frac{\partial {}^t\mathcal{W}}{\partial \mathbf{n}} + \frac{\partial {}^t\mathcal{W}}{\partial \mathbf{n} \nabla} \cdot \nabla \quad (1.25b)$$

$$\frac{\partial \dot{R}}{\partial \dot{\eta}} = b_\eta - \frac{\partial {}^t\mathcal{W}}{\partial \eta} \quad (1.25c)$$

In this dissertation, we just take the symmetric part of the Cauchy stress tensor as

$$\boldsymbol{\sigma} = \frac{\partial {}^t\mathcal{W}}{\partial \mathbf{F}} \mathbf{F}^T + \frac{\partial \dot{R}}{\partial \mathbf{D}} - \nabla \mathbf{n} \cdot \frac{\partial {}^t\mathcal{W}}{\partial \mathbf{n} \nabla} \quad (1.26)$$

If we take ${}^t\mathcal{W} = {}^t\mathcal{W}_{elas}(\mathbf{F}, \mathbf{n}, \mathbf{n}_0) + \frac{K_n}{2} \text{Tr}(\mathbf{n} \nabla \cdot \nabla \mathbf{n})$ and $\dot{R} = \frac{\mu_D}{2} \text{Tr}(\mathbf{D}^2)$, omitting inertia terms and body forces, governing equations and the constitutive relation reduce to

$$\boldsymbol{\sigma} \cdot \nabla = 0 \quad (1.27a)$$

$$K_n \Delta \mathbf{n} - \frac{\partial {}^t\mathcal{W}}{\partial \mathbf{n}} + \gamma \mathbf{n} = 0 \quad (1.27b)$$

$$\boldsymbol{\sigma} = \frac{\partial {}^t\mathcal{W}}{\partial \mathbf{F}} \mathbf{F}^T + \mu_D \mathbf{D} - K_n (\mathbf{n} \nabla)^T \cdot \mathbf{n} \nabla \quad (1.28)$$

Considering the decomposition of the elastic energy in the reference configuration as following

$$\mathcal{W} = \mathcal{W}_{Mat}(\mathbf{C}) + \mathcal{W}_{fib}(\mathbf{F}, \mathbf{n}_0, \eta_0) \quad (1.29)$$

where \mathbf{C} is the right Cauchy-Green tensor, One can study the statistics for a hyper-elastic material with fiber reinforcement in the known direction \mathbf{n}_0 . For example, Holzapfel and Ogden [42] take

$$\begin{aligned} \mathcal{W} &= \mathcal{W}_{Mat}(\mathbf{C}) + \mathcal{W}_{fib}(\mathbf{C}, \mathbf{H}(\mathbf{n}_0, \eta_0)) \\ \mathbf{H} &= \eta_0 \mathbf{I} + (1 - 3\eta_0) \mathbf{n}_0 \otimes \mathbf{n}_0 \end{aligned} \quad (1.30)$$

Then one can get the stress via a superposition form

$$\boldsymbol{\sigma} = J^{-1} \mathbf{F} \cdot \frac{\partial \mathcal{W}}{\partial \mathbf{C}} \cdot \mathbf{F}^T = \boldsymbol{\sigma}_{Mat} + \boldsymbol{\sigma}_{fib} \quad (1.31)$$

$$\boldsymbol{\sigma}_{fib} = J^{-1} \mu_{fib}(I_4, \eta_0) \mathbf{F} \cdot \mathbf{n}_0 \otimes \mathbf{n}_0 \cdot \mathbf{F}^T = J^{-1} \mu_{fib}(I_4, \eta_0) (\mathbf{F} \cdot \mathbf{n}_0) \otimes (\mathbf{F} \cdot \mathbf{n}_0)$$

where $I_4 = I_4(\eta_0, \text{tr}(\mathbf{C}), \mathbf{n}_0 \cdot \mathbf{C} \cdot \mathbf{n}_0)$.

1.2 Overview of plate and shell theories

Slender structures are quite common in biology from membranes at cell scale to the skin at tissue scale, which always result in the large displacement and finite deformation induced by morphology. When continuum mechanics is favored to study strain and stress in biological problems, theory of plates and shells [43, 44, 45, 46, 47, 48, 49] is frequently employed to deal with surface systems. In this section, we will present a brief review of the basic knowledge.

Following the method of the previous section, a variational principle is taken to help us obtain governing equations in elasticity. The only extra assumption is the strain-displacement relationship. We shall write down the physical conservation law on the 2D curved surface with the integral over the thickness, namely reducing the original 3D problem into 2D mathematical PDEs. From the point view of physics, bending together with in-plane stretching dominate the total elastic energy, which makes it possible to reduce the dimension.

We will first introduce the Föppl-Von Kármán (FvK) plate theory, which is the primary model for analytical work in this thesis, and then we review concisely the general shell formula for an implementation of the initial curvature. Mindlin–Reissner theory will also be mentioned for plates with moderate thickness.

1.2.1 Föppl-Von Kármán (FvK) model

The FvK model is the simplest one for a plate undergoing large deflections. More precisely, it holds the effect of geometrical nonlinearity induced by bending. This model is popular among physicists and engineers because it not only keeps nearly all the pictures of nonlinear phenomena such as buckling but also it is still valid not far beyond the limit of the small-strain constraint.

a) Strain-displacement assumption

We start by providing the displacement relation between the initial configuration $R(x, y, Z)$ and the current shape $r(x, y, Z)$ with a first order expansion.

$$\begin{aligned} r &= \mathbf{R} + \mathbf{u}^0(x, y) + Z\mathbf{u}^1(x, y) \\ &\approx \mathbf{R} + (U^0(x, y) + ZU^1(x, y))\mathbf{e}_1 + (V^0(x, y) + ZV^1(x, y))\mathbf{e}_2 + \zeta(x, y)\mathbf{e}_3 \end{aligned} \quad (1.32)$$

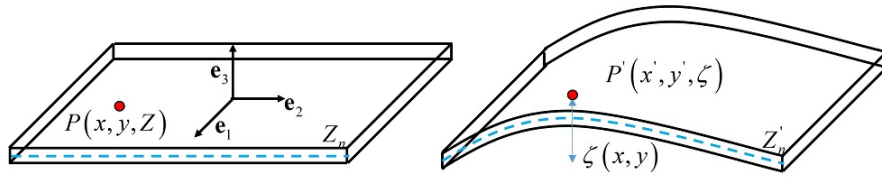


Fig. 1.2 Illustration of geometry

Each e_i represents the Cartesian unit vector and the superscripts “0” and “1” denote the perturbation order. Indeed, the ratio between the thickness and the horizontal scale L is a small parameter as $\epsilon_1 = h/L$. And the magnitude of the displacement in the Z direction ζ compared to L is another small quantity as $\epsilon_2 = \zeta/L$. In the classical FvK approach, $\epsilon_2 \sim \sqrt{\epsilon_1}$.

We introduce later the position of the neutral surface Z_n , a constant of order h , whose role is to minimize the free energy. For a homogeneous monolayer material, Z_n corresponds to the middle plane. We also take into account later in the shallow shell approximation that the sample is slightly curved before buckling with a tiny deviation w^0 in the simulation. After we can calculate the deformation gradient tensor \mathbf{F} as

$$F_{iJ} = \delta_{iJ} + \frac{\partial}{\partial X_J} u_i \approx \delta_{ij} + \frac{\partial u_i^0}{\partial x_j} + u_i^1 \delta_{3j} + (Z - Z_n) \frac{\partial u_i^1}{\partial x_j} \quad (1.33)$$

So the elastic strain tensor becomes

$$\begin{aligned} \mathbf{E} &= \frac{1}{2}(\mathbf{F}^T \mathbf{F} - \mathbf{I}) \Rightarrow \\ E_{ij} &\approx \frac{1}{2} \left(\frac{\partial u_i^0}{\partial x_j} + \frac{\partial u_j^0}{\partial x_i} + \frac{\partial u_k^0}{\partial x_i} \frac{\partial u_k^0}{\partial x_j} + u_k^1 u_k^1 \delta_{3i} \delta_{3j} \right) + \frac{1}{2} (u_j^1 \delta_{3i} + u_i^1 \delta_{3j}) + \frac{1}{2} \left(\frac{\partial u_k^0}{\partial x_i} u_k^1 \delta_{3j} + \frac{\partial u_k^0}{\partial x_j} u_k^1 \delta_{3i} \right) \\ &\quad + \frac{Z - Z_n}{2} \left(\frac{\partial u_i^1}{\partial x_j} + \frac{\partial u_j^1}{\partial x_i} \right) \end{aligned} \quad (1.34)$$

If we just take the in-plane components and neglect higher order terms of $u^0(x, y)$

$$\varepsilon_{\alpha\beta} \approx \frac{1}{2} \left(\frac{\partial u_\alpha^0}{\partial x_\beta} + \frac{\partial u_\beta^0}{\partial x_\alpha} + \frac{\partial \zeta}{\partial x_\alpha} \frac{\partial \zeta}{\partial x_\beta} \right) + \frac{Z - Z_n}{2} \left(\frac{\partial u_\alpha^1}{\partial x_\beta} + \frac{\partial u_\beta^1}{\partial x_\alpha} \right) \quad (1.35)$$

The Greek alphabet like α, β, γ is limited from 1 to 2.

b) Hooke's law for the stress-strain relation

We apply Hooke's law with the plane stress assumption: $\sigma_{i3} = 0$. Then it reads for the Cauchy stress components with Young's modulus E and Poisson coefficient ν for an isotropic material

$$\sigma_{\alpha\beta} = \frac{E}{1 - \nu^2} \left((1 - \nu)\varepsilon_{\alpha\beta} + \nu\varepsilon_{\gamma\gamma}\delta_{\alpha\beta} \right) \quad (1.36)$$

where $\varepsilon_{\alpha\beta} = \varepsilon_{\alpha\beta}^0 + (Z - Z_n)\varepsilon_{\alpha\beta}^1$ with $\nu = 1/2$ for the incompressible case, an assumption commonly used for living tissues. Taking into account the plane stress assumption again for thin samples, $\sigma_{13} = \sigma_{23} = 0$, we take $E_{13}^0 = E_{23}^0 = 0$ which leads to the first order for U and V from Eq. (1.32) and Eq.(1.34)

$$U^1(x, y) \approx -\frac{\partial \zeta}{\partial x}; \quad V^1(x, y) \approx -\frac{\partial \zeta}{\partial y} \quad (1.37)$$

So the zero and first order strain tensor read

$$\varepsilon_{\alpha\beta}^0 = \frac{1}{2} \left(\frac{\partial u_\alpha}{\partial x_\beta} + \frac{\partial u_\beta}{\partial x_\alpha} + \frac{\partial \zeta}{\partial x_\alpha} \frac{\partial \zeta}{\partial x_\beta} \right); \quad \varepsilon_{\alpha\beta}^1 = -\partial_{\alpha\beta}\zeta \quad (1.38)$$

where $u_\alpha(x, y)$ is the first order displacement $\{U^0, V^0\}$. With Eq.(1.36), we can also obtain the perturbation of stress as $\sigma_{\alpha\beta} = \sigma_{\alpha\beta}^0 + (Z - Z_n)\sigma_{\alpha\beta}^1$.

c) Lagrange-Euler equations by variational method

The elastic energy reads

$$\mathcal{E} = \int_{\Omega} \frac{1}{2} \sigma_{\alpha\beta} \varepsilon_{\alpha\beta} dV = \frac{1}{2} \frac{E}{1 - \nu^2} \int_{\Omega} (\varepsilon_{11})^2 + (\varepsilon_{22})^2 + 2\nu\varepsilon_{11}\varepsilon_{22} + 2(1 - \nu)(\varepsilon_{12})^2 dV \quad (1.39)$$

The linearity between the stress and strain leads to $\delta\mathcal{E} \sim \sigma_{\alpha\beta} \delta\varepsilon_{\alpha\beta}$ and then the Euler-Lagrange equations result from the variation of \mathcal{E} with respect to ζ and u_α

$$\begin{aligned} \Delta(D\Delta\zeta) - \partial_\alpha(N_{\alpha\beta}\partial_\beta\zeta) + \partial_{\alpha\beta}M_{\alpha\beta}^g &= 0 \\ \frac{\partial}{\partial x_\beta} \left(\int \sigma_{\alpha\beta} dZ \right) &= \frac{\partial}{\partial x_\beta} (N_{\alpha\beta}) = 0 \end{aligned} \quad (1.40)$$

The first equation represents the out-of-plane bending equilibrium and the second one stands for the in-plane stress equilibrium with definitions as following

$$\begin{aligned}
D &= \int \frac{E}{1-\nu^2} (Z - Z_n)^2 dZ \\
M_{\alpha\beta}^g &= - \int (Z - Z_n) \sigma_{\alpha\beta}^0 dZ
\end{aligned} \tag{1.41}$$

For a monolayer [50], $M_{\alpha\beta}^g = 0$ automatically due to $\int (Z - Z_n) dZ = 0$ with $Z_n = h/2$.

1.2.2 Classical shell theory

The FvK model can be extended to a slightly curved sheet. We use the method by Sanders [51] to get the governing equations for a curved plate or shell. But we change some notations to keep consistency with the thesis. We suppose the initial curved middle surface in 3D physical space is given by a 2D parametric form as

$${}^0x^i = {}^0x^i(\xi_1, \xi_2) \tag{1.42}$$

According to differential geometry [52, 53], we can create a group of local basis on the surface as

$$Span\left\{ \frac{\partial {}^0\mathbf{x}}{\partial \xi_1}, \frac{\partial {}^0\mathbf{x}}{\partial \xi_2}, {}^0\mathbf{n} = \frac{\frac{\partial {}^0\mathbf{x}}{\partial \xi_1} \times \frac{\partial {}^0\mathbf{x}}{\partial \xi_2}}{\left\| \frac{\partial {}^0\mathbf{x}}{\partial \xi_1} \times \frac{\partial {}^0\mathbf{x}}{\partial \xi_2} \right\|} \right\} \tag{1.43}$$

where $\mathbf{n}(\boldsymbol{\xi})$ is the normal vector and the left superscript “0” represents the initial undeformed configuration. And we shall use “ t ” for the current deformed one with the kinematic relation by displacement ${}^0u^i$ as

$$\begin{aligned}
{}^t x^i &= {}^0 x^i + {}^0 u^i \\
{}^0 u^i &= \bar{u}^\alpha(\boldsymbol{\xi}) \partial_\alpha {}^0 x^i + w(\boldsymbol{\xi}) {}^0 \mathbf{n}^i(\boldsymbol{\xi})
\end{aligned} \tag{1.44}$$

where \bar{u}^α is the in-plane part on the middle surface. Then the metric referred to the tangent space ${}^0G_{\alpha\beta}$ could be calculated

$$d^0s^2 = \partial_\alpha {}^0x^i \partial_\beta {}^0x^i d\xi^\alpha d\xi^\beta = {}^0G_{\alpha\beta} d\xi^\alpha d\xi^\beta \tag{1.45}$$

with the element of area as $d^0a = \sqrt{\det({}^0G)} d\xi^\alpha d\xi^\beta$.

Gauss, Weingarten and Codazzi equations are concluded as

$$\begin{aligned}
\partial_{\alpha\beta} {}^0x^i &= - {}^0B_{\alpha\beta} {}^0n^i \\
\partial_\alpha {}^0n^i &= {}^0B_\alpha^\beta \partial_\beta {}^0x^i \\
\partial_\gamma {}^0B_{\alpha\beta} &= \partial_\beta {}^0B_{\alpha\gamma}
\end{aligned} \tag{1.46}$$

where $B_{\alpha\beta} = \partial_\alpha \mathbf{n} \cdot \partial_\beta \mathbf{x}$ denotes the second fundamental form and $B_\alpha^\beta = B_{\alpha\gamma} G^{\gamma\beta}$. The first two equations enable us to calculate the derivatives of the basis vectors and the last one is an extra constraint for surface geometry.

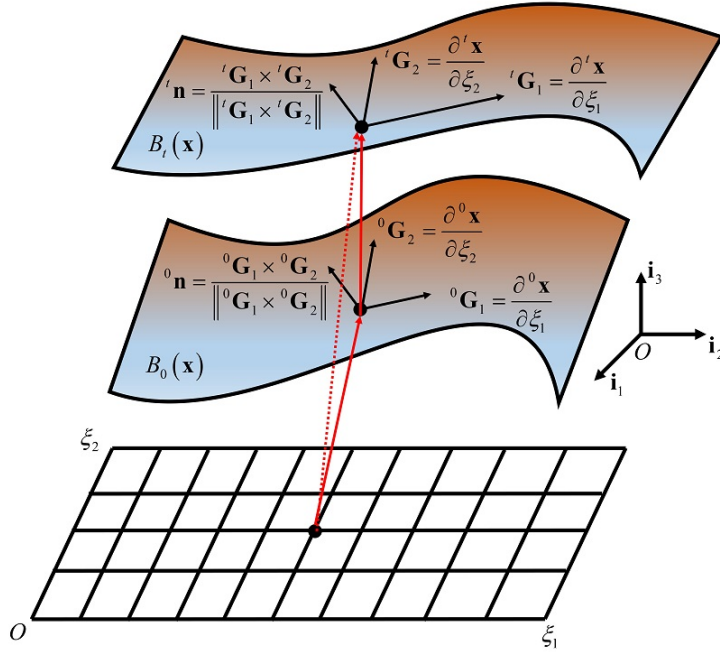


Fig. 1.3 Illustration of the surface coordinates

1.2.3 Strain-displacement assumption

We directly write down the in-plane strain defined by a difference of the metric between the current and the initial tangent space

$$E_{\alpha\beta} = \frac{1}{2}({}^tG_{\alpha\beta} - {}^0G_{\alpha\beta}) \quad (1.47)$$

and the out-of plane bending part by normal vector change as

$$K_{\alpha\beta} = {}^tB_{\alpha\beta} - {}^0B_{\alpha\beta} \quad (1.48)$$

Then we shall calculate the metric tensor after deformation ${}^tG_{\alpha\beta}$, ${}^tB_{\alpha\beta}$ with the kinematic relation Eq.(1.44). Here we do not expand all terms one by one with the surface basis Eq.(1.43). Given that $\mathbf{n} \cdot \partial_\alpha \mathbf{n} = 0$ as well as Eq.(1.46), it is not difficult to get a similar result as work by Sanders, Koiter and Buidiansky [48, 51, 54, 55, 56].

a) Variational method with the linear stress-strain relation

The variation of the elastic energy is

$$\delta \mathcal{E} = \int_{t_a} (N^{\alpha\beta} \delta E_{\alpha\beta} + M^{\alpha\beta} \delta K_{\alpha\beta}) d^t a \quad (1.49)$$

where the in-plane force $N_{\alpha\beta}$ and the out-of-plane bending $M_{\alpha\beta}$ satisfy the tensor transform rule

$$N_{\alpha\beta} = G_{\alpha\gamma} G_{\beta\delta} N^{\gamma\delta}; \quad M_{\alpha\beta} = G_{\alpha\gamma} G_{\beta\delta} M^{\gamma\delta} \quad (1.50)$$

with the linear constitutive relation for an isotropic material as an example

$$\begin{aligned} N_{\alpha\beta} &= \int dz \frac{E}{1-\nu^2} ((1-\nu)E_{\alpha\beta} + \nu E_{\gamma\gamma}\delta_{\alpha\beta}) \\ M_{\alpha\beta} &= \int Z^2 dz \frac{E}{1-\nu^2} ((1-\nu)K_{\alpha\beta} + \nu K_{\gamma\gamma}\delta_{\alpha\beta}) \end{aligned} \quad (1.51)$$

With this we can calculate the free elastic energy as

$$\mathcal{E} = \int_{t_a} \frac{1}{2} (N^{\alpha\beta} E_{\alpha\beta} + M^{\alpha\beta} K_{\alpha\beta}) d^t a \quad (1.52)$$

The Euler-Lagrange equation can be deduced by taking the variation of general field variables $\{u^\alpha, w\}$. The exact expression with boundary conditions in the part of small-strain approximations is fully discussed in the work by Sanders [51]. In this dissertation we focus on the shallow shell theory aiming at the initial curvature in the Fvk model.

b) Shallow shell approximation

We more or less simplify the general shell theory by the famous Donnell-Mushtari-Vlasov (DMV) approximation [44, 57]

$$\begin{aligned} E_{\alpha\beta} &= \frac{1}{2}(\partial_\beta \bar{u}_\alpha + \partial_\alpha \bar{u}_\beta) + {}^0 B_{\alpha\beta} w + \frac{1}{2} \partial_\alpha w \partial_\beta w \\ K_{\alpha\beta} &= -\partial_{\alpha\beta} w \end{aligned} \quad (1.53)$$

For a slightly curved plate, we could suppose the middle surface before deformation as ${}^0 \mathbf{x} = [x, y, w^0(x, y)]$ with ${}^0 G_{\alpha\beta} \approx \delta_{\alpha\beta}$ and ${}^0 \mathbf{n} \approx [-\partial_x w^0, -\partial_y w^0, 1]^T$. Then we can get the shallow shell assumption as

$$\begin{aligned} {}^0 B_{\alpha\beta} &\approx -\partial_{\alpha\beta} w^0(x, y) \\ w &\approx \zeta(x, y) \\ \bar{u}_\alpha &\approx u_\alpha(x, y) + \zeta \partial_\alpha w^0 \end{aligned} \quad (1.54)$$

Neglecting the higher order terms of small quantity $w^0(x, y)$, we finally obtain the so-called Marguerre model [51, 58] as

$$\begin{aligned} E_{\alpha\beta} &= \frac{1}{2}(\partial_\beta u_\alpha + \partial_\alpha u_\beta + \partial_\alpha w^0 \partial_\beta \zeta + \partial_\beta w^0 \partial_\alpha \zeta + \partial_\alpha \zeta \partial_\beta \zeta) \\ K_{\alpha\beta} &= -\partial_{\alpha\beta} \zeta \end{aligned} \quad (1.55)$$

Compared with the Fvk model, we find there is a new bending momentum induced by the initial curvature as

$$\delta \mathcal{E} \sim \delta \mathcal{E}^{Fvk} + N_{\alpha\beta} {}^0 B_{\alpha\beta} \delta \zeta \quad (1.56)$$

Although we have made a lot of simplifications for the shell in the shallow case, the theory can be extended to small but finite deformation in many situations [59].

1.2.4 Mindlin–Reissner model

If we review the process of the derivation for the Fvk equations, we encounter the following hypotheses

1) Scaling of thickness h , deflection ζ and horizontal length L :

$$\frac{h}{L} \sim \left(\frac{\zeta}{L}\right)^2 \ll 1 \quad (1.57)$$

In practice, it still works as a conservative estimate with $\frac{\zeta}{h} \sim O(10)$ and $\frac{h}{L} < \frac{1}{10}$;

2) Love-Kirchhoff hypothesis: no transverse shear

$$u_\alpha(x, y, Z) = u_\alpha^0(x, y) - (Z - Z_n)\theta(x, y) ; \theta = \partial_\alpha u_3^0 = \partial_\alpha \zeta(x, y) \quad (1.58)$$

where u_α^0 is the first-order in-plane displacement on the neutral surface and θ is the rotation of the normal vector which approximately equals $\partial_\alpha \zeta$ within the shallow shell limit. For the notation consistency with the discussion before in FvK, we just simplify $u_\alpha^0(x, y)$ as u_α later;

3) $(u_\alpha^0)^2$ are higher order terms compared to ζ^2 for strain contribution (related with the first hypothesis here)

For a thick plate as $h/L > 1/10$, we should consider the rotation contribution by transverse strain

$$\theta_x = \frac{\partial \zeta}{\partial x} + \phi_x ; \theta_y = \frac{\partial \zeta}{\partial y} + \phi_y \quad (1.59)$$

Then we can get the Mindlin-Reissner modification for the Fvk model [45, 58, 60, 61]

$$\begin{aligned} \varepsilon_{\alpha\beta} &= \varepsilon_{\alpha\beta}^{FvK} - \frac{Z - Z_n}{2} \left(\frac{\partial \phi_\alpha}{\partial x_\beta} + \frac{\partial \phi_\beta}{\partial x_\alpha} \right) \\ \gamma_{13} &= 2\varepsilon_{13} = -\phi_x ; \gamma_{23} = 2\varepsilon_{23} = -\phi_y \end{aligned} \quad (1.60)$$

We can apply the linear stress-strain relation with 2 more shear moduli for the elastic energy. Surely, we should add 2 new degrees of freedom (DOFs) for the numerical implementation. In the commercial software COMSOL, the plate model for large deflections is based on the Mindlin-Reissner hypothesis. It can be used for thin panels. The standard FvK model can be recovered by substituting in the Love-Kirchhoff constraint Eq.(1.58).

1.2.5 Difficulties in numerical implementation

There is always a gap between the classical theory and the robust computational algorithm for practical applications. We shall use the scaling of the elastic energy to explain the main problem here. With the given thickness h and the length L of a plate or shell, it is obvious for a thin slender structure that $h/L \ll 1$. The elastic energy can be expanded as [38]

$$\mathcal{E} = h^3 \mathcal{E}_{bend} + h^2 \mathcal{E}_{bend-memb} + h \mathcal{E}_{memb} \quad (1.61)$$

For a couple of physical problems like crumpling a piece of paper [62], deformation ought to be mainly described by the bending equation referred to \mathcal{E}_{bend} . However, according to Eq.(1.61), we can see that the membrane deformation contributes a lot to the elastic energy especially when $h \rightarrow 0$ which may result in an ill-conditioned system during numerical simulations as well as transverse shear locking [38, 63]. Assuming the variable space $\{\mathbf{q}\}$, the elastic equilibrium state results from the minimization of the given potential function $\Pi(\mathbf{q})$ with the stability condition

$[K_{mn}] = [\frac{\partial^2 \Pi}{\partial q_m \partial q_n}] > 0$ [54, 64]. We will frequently need to solve the linearized incremental solution by $\{\Delta \mathbf{q}\} = [K_{mn}]^{-1} \{\Delta \mathbf{f}\}$ where $\{\Delta \mathbf{f}\}$ is the generalized incremental force and $[K_{mn}]$ is the Hessian matrix or stiffness matrix of the potential function. In finite element solvers, there is a catastrophic locking problem of ill-conditioned $[K_{mn}]$ due to Eq.(1.61) when h is small. This is the reason why many scientists try to develop new elements [46, 65, 66] and even new methods [64, 67, 68] to reduce or conquer the numerical difficulty. In addition, we have a strong prior hypothesis on the smoothness of the surface which also limits the test space of the solver. It seems we need to come back to the original physics with a discrete form of the energy in place of a differential operator and employ a more robust algorithm [69, 70, 71, 72] for the large deformation problem.

Part I

Crack opening on epithelium of *C. elegans*

We will discuss the experiment of [8] in this part. *C. elegans* embryos are observed in a particular stage of their development with an evaluation of the stress distribution by laser cuts in the epithelium. Method and analysis could be extended to other similar systems. We divide the calculation into two steps: first we simplify the geometry in chapter 2 and give the stress expression with the assumed deformation gradient matrix. Then we use the crack formula by Theocaris [73, 74] and revise it for finite strain in chapter 3. We suggest a cylindrical tube with an opening angle as the zero-stress configuration for the composite epithelium. Different areas on the animal surface are handled separately. The total stress is calculated in consideration of anisotropy and active motors. For fracture mechanics, we give a short review at the very beginning. We then introduce the linear theory for the crack shape and modify it for our case using the tangent stiffness matrix.

Chapter 2

Stress assessment in *C. elegans* elongation

It seems growth of a living system is quite natural but more complicated and subtle than a handmade clock. Perhaps one argument is that morphogenesis is always accompanied by large and soft deformation in order to adapt to the external environment. In addition, many scientists recognize [75] that stresses play a vital role during the development of an embryo. At the macroscopic level, differential growth generates residual stress creating the circumvolutions of the intestine [76, 77, 78], the brain cortex [79, 80, 81], and the fingerprints of skin [82, 83]. The folding of tissues is then directly linked to the coupling between volumetric growth, tissue properties and geometry. At the cellular level, the high mobility of cells is counterbalanced by the cellular filament networks, especially by the actomyosin cortex. It comprises a network of cross-linked actin filaments located below the plasma membrane, so that the local cell contractility results from the myosin molecular motors which transform the chemical energy of ATP hydrolysis into inner stresses.

Here we investigate the early stage of *C. elegans* elongation up to 70% when the embryo contains 65 epidermal cells in the cortical position in an ovoid shell. We try to use finite elasticity to get the stress distribution on the surface of *C. elegans*. Given the assumption of deformation gradient matrix and energy density function, we calculate the stress components with the constitutive relation as Eq.(1.31). However, in elasticity, we need to know the stress-free conformation. So we first characterize the geometry in section 2.1 which matches well with the experiment. Then we calculate stress components in section 2.2 with incompressibility after growth. Afterwards we introduce the active stress by a planar active network in section 2.3 with further explanations and simulations in section 2.4.

We consider a cylindrical tube with an opening angle as the starting point. Then we define different configurations for the corresponding stages of loading history. Anisotropy and active stress induced by the actin-myosin network and microtubules are covered in this part. It will be used in the next chapter to explain the ablation experiment.

2.1 Simplified cylindrical geometry

For theoretical analysis, we simplify the elongated *C. elegans* as a composite cylinder made of a row of epithelial cells and nascent intestine. Since the scientific concern is on the thin exterior

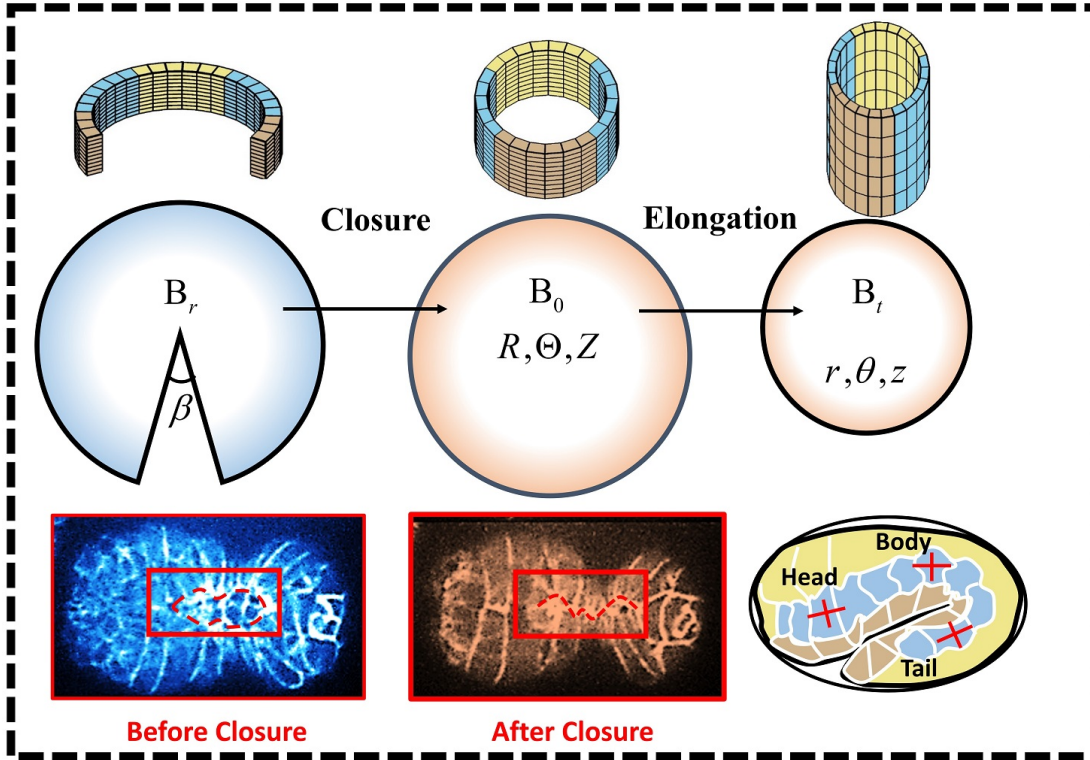


Fig. 2.1 Deformation map from left to right columns are: Before closure (B_r) and also the reference stress-free configuration B_r , initial state B_0 with cylindrical coordinates R, Θ, Z and the current elongated configuration B_t with coordinates r, θ, z . The pictures of the third row are taken from the experiments: we observe an opening angle (red dotted line) in the left slice. The opening angle is closed in the region of cells (brown area of the first row) with residual circumferential tensile stress (see middle slice). The picture on the right shows the position of the laser cuts during elongation.

surface of approximately $10\mu\text{m}$ thick, we use the inverse method by assuming the deformation gradient tensor Eq.(1.1) to calculate the stress components in 3D for the outer tube.

We introduce three configurations for our calculation: the initial state B_0 for zero elongation as the start of the experimental observation, the reference configuration B_r which is stress-free with an opening angle and finally the current one B_t with the laser cuts after deformation.

We label different cells with dissimilar colors in Fig(2.1): Brown area indicates the ventral cells which constitutes the abdominal part of the embryo. Hence yellow area is the dorsal part, and blue is used for the seam cells which corresponds to the waist of the worm. During the experiment [8, 84], there is a pre-stress or pre-strain [26] due to the closure of the ventral cells. When it comes to the elongation process, molecular motors are very active leading to the shrinking of the seam cells. Special concern is paid on the inner stress with the actin-myosin network where molecular motors are located. In order to offer the stress estimate, laser cuts are made after elongation in Fig.(2.1) in different parts of the embryo: Head, Body and Tail. We now attempt to calculate the elastic strain for our simplified composite cylindrical tube with three different cell types. The

deformation gradient matrix in cylindrical coordinates reads

$$\mathbf{F} = \begin{bmatrix} \frac{\partial r}{\partial R} & 0 & 0 \\ 0 & \frac{\partial \theta_i}{\partial \Theta_i} \frac{r}{R} & 0 \\ 0 & 0 & \frac{\partial z}{\partial Z} \end{bmatrix} = \begin{bmatrix} \frac{dr}{dR} & 0 & 0 \\ 0 & G_i \frac{r}{R} & 0 \\ 0 & 0 & \lambda_Z \end{bmatrix} = \begin{bmatrix} \lambda_R(R) & 0 & 0 \\ 0 & G_i \lambda(R) & 0 \\ 0 & 0 & \lambda_Z \end{bmatrix} \quad (2.1)$$

where we assume constant angle change G_i for different cells and homogeneous extension λ_Z . Specially, because of the diagonal form of the gradient tensor, strain compatibility is satisfied automatically for $\mathbf{F} \times \nabla = 0$ as Eq.(1.2). And thus there is only one variable R , the radius of the tube varied between value R_i and R_e . The rotation and axial extension G_i and λ_Z are regarded as measurable quantities, i.e., known data from the experiments. In addition, the elastic stress should also be diagonal. Furthermore, we build the observable deformation gradient after elongation as

$$\mathbf{F}_{Ob} = \begin{bmatrix} \Lambda_R & 0 & 0 \\ 0 & \Lambda & 0 \\ 0 & 0 & \Lambda_Z \end{bmatrix} = \Lambda_R \mathbf{e}_r \otimes \mathbf{E}_R + \Lambda \mathbf{e}_\theta \otimes \mathbf{E}_\Theta + \Lambda_Z \mathbf{e}_z \otimes \mathbf{E}_Z \quad (2.2)$$

with the incompressibility hypothesis as $\det(\mathbf{F}_{Ob}) = 1$. This is a strong condition based on the fact of nearly no growth during the extension and the assumption of incompressible deformation of every cell. We can solve the function $r(R)$ with $\Lambda_R \Lambda \Lambda_Z = 1$. To avoid solving the ordinary differential equation, we directly use the volume conservation of a cylindrical tube

$$r^2 - r_i^2 = \frac{1}{G_i \Lambda_Z} (R^2 - R_i^2) \quad (2.3)$$

where $r_i = r(R_i)$ and the governing equation is valid for all cells of the system.

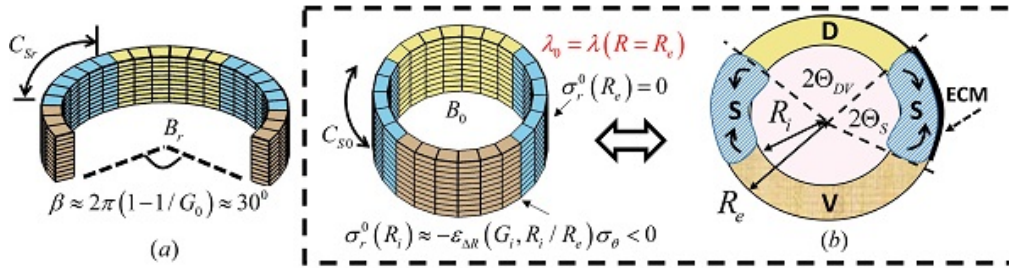


Fig. 2.2 Geometry of a simplified cylindrical tube for the strain calculation: The first picture (a) is the reference configuration B_r with an opening angle for pre-stress and C_r represents the arc-length of the outer surface for each part respectively. The second and the third sketch (b) show the initial complete tube B_0 after closure which is the domain for the following stress computation. D means dorsal section, V is the ventral part and S denotes the seam cell. Here we assume stress-free condition on the exterior boundary for the thin membrane tube. R is the radius varying from R_i to R_e and G_i is the angular change which shall be defined later. Θ_i is the absolute angle for each part $\{D, V, S\}$ and we take the double value because of the symmetry of the geometry. The exterior surface is covered by the extracellular matrix (ECM), a thin layer of secreted proteins.

Let us come back to the original geometry for a clear discussion. In Fig.(2.2a), we observe that there is an opening angle β . In this stress-free configuration, we define half of the system: D

cells are located in the interval $[-\phi_{DV}, \phi_{DV}]$, S cells occupy the sector $[\phi_{DV}, \pi - \beta/2 - \phi_{DV}]$ and V cells fill the remaining part up to $\pi - \beta/2$. From mechanics, we do not distinguish D and V cells so we call them DV cells. After the closure, the complete domain is demonstrated by Fig.(2.2b) with new angle Θ . Now we can write the geometric constraint with the missing angle β

$$\begin{aligned}\phi_{DV} + \phi_S &= \pi/2 - \beta/4 \\ \Theta_{DV} + \Theta_S &= \pi/2 \\ \Theta_{DV} &= G_{0,DV}\phi_{DV} ; \Theta_S = G_{0,S}\phi_S\end{aligned}\tag{2.4}$$

where $G_{0,i} > 1$ is the initial pre-stretch of each part. We can now calculate the initial deformation gradient \mathbf{F}_0 with the help of Eq.(2.2) and the volume conservation Eq.(2.3) assuming incompressibility

$$\begin{aligned}\mathbf{F} &= \mathbf{F}_{Ob} \cdot \mathbf{F}_0 \Rightarrow \\ \mathbf{F} &= \begin{bmatrix} (\Lambda\Lambda_Z)^{-1} & 0 & 0 \\ 0 & \Lambda(R) & 0 \\ 0 & 0 & \Lambda_Z \end{bmatrix} \begin{bmatrix} (\lambda_0\lambda_{0Z})^{-1} & 0 & 0 \\ 0 & \lambda_0 & 0 \\ 0 & 0 & \lambda_{0Z} \end{bmatrix}\end{aligned}\tag{2.5}$$

and

$$\begin{aligned}\Lambda(R) &= \frac{G_i}{\sqrt{\Lambda_Z}} \sqrt{1 + (G_i^{-1} - 1)\eta(R)} \\ \eta(R) &= 1 - \frac{R_i^2}{R^2} \\ \Rightarrow G_i &= \frac{-\eta(R_e) + \sqrt{\eta(R_e)^2 + 4(1 - \eta(R_e))\Lambda^2\Lambda_Z}}{2(1 - \eta(R_e))}\end{aligned}\tag{2.6}$$

Thus at $(R = R_e)$ we can calculate the superficial circumferential deformation with $\eta(R_e) = 1 - R_i^2/R_e^2$. In practice, we can use data of arc-length C_i in Fig.(2.2) as well as the length change $\Lambda_Z = L/L_0$, $\Lambda(R_e) = C/C_0$ to give an estimate for G_i and accordingly obtain the deformation information for the stress calculation. Besides, once we get the deformation of seam cells, the geometric constraint Eq.(2.4) allows us to calculate the quantity for DV cells as

$$C_{0,DV}\Lambda_{DV}(R_e) + C_{0,S}\Lambda_S(R_e) = \frac{C_{0,DV} + C_{0,S}}{\sqrt{\Lambda_Z}}\tag{2.7}$$

where $C_{0,i}$ is the arc-length of each part at $\Lambda_Z = 1$.

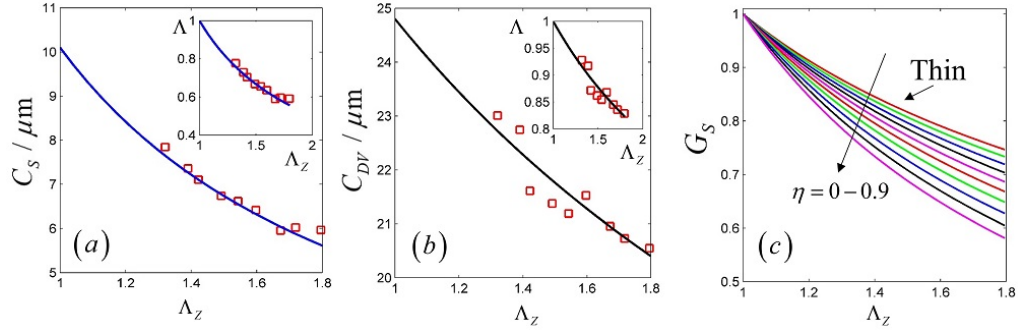


Fig. 2.3 (a) Experimental circumferential length of the seam cellular domain. In blue the best fitting curve corresponding to $C = C_0\Lambda$ and the ortho-radial stretch in the top inset. Red squares are experimental data [8]. (b) Analytical Results for the DV cells using Eq.(2.6) and Eq.(2.7). Experimental points [8] are included for comparison. (c) Theoretical G_S value as a function of Λ_Z according to Eq.(2.7) when the epithelium thickness is varied.

In Fig.(2.3), we use the limited data in an attempt to extrapolate the full information during elongation as Λ_Z increases from 1 to 1.7 (ΔL from 0 to 70% L_0). Here the only fitting is the blue curve for the circumferential length of seam cells. After we make a convention that $\Lambda = \Lambda(R = R_e)$ since we just make the laser cut on the surface of the skin. So far we have introduced the geometry of our system, but we need to get the expression of the stress by defining the energy density function in the next section.

2.2 Calculation of the elastic stress

Due to the diagonal form of the simplified \mathbf{F} in the above analysis, we prefer to employ the constitutive relation in the eigenspace [28]. We adopt the energy density function \mathcal{W} like Eq.(1.29) considering hyper-elasticity with fiber anisotropy. We introduce as few material parameters as possible.

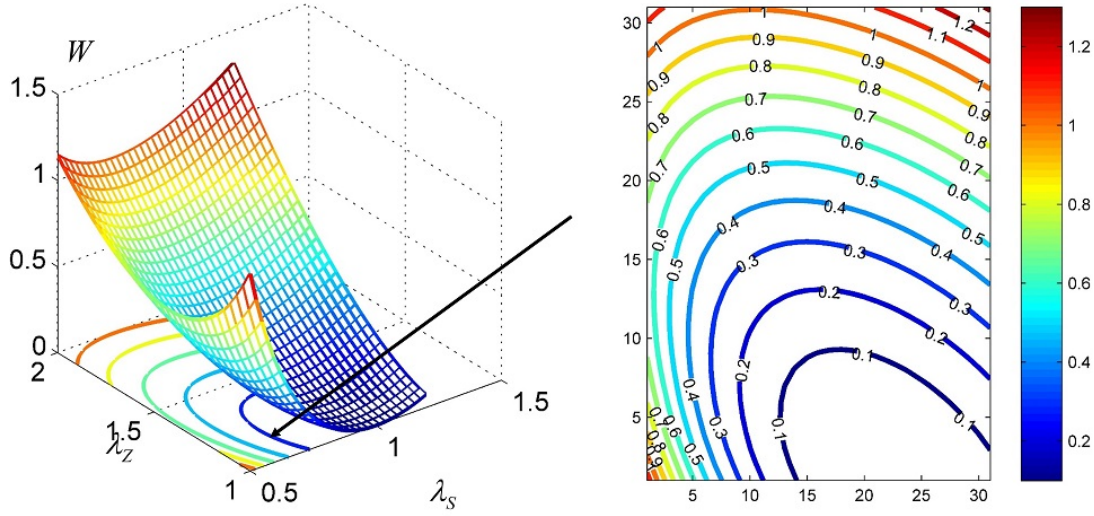
$$\begin{aligned} \mathcal{W} &= \mathcal{W}_{Mat}(\mathbf{F}^T \mathbf{F}) + \mathcal{W}_{fib}(\mathbf{F}, \mathbf{n}_0) \\ &= \mathcal{W}_{Mat}(\lambda_1, \lambda_2, \lambda_3) + \mathcal{W}_{fib}(\mathbf{n}_0^T \text{diag}(\lambda_1^2, \lambda_2^2, \lambda_3^2) \mathbf{n}_0) \end{aligned} \quad (2.8)$$

In our case, we suppose that the mean direction of the fiber is parallel to the eigenvector of the right Cauchy-Green tensor and consequently

$$\mathcal{W} \rightarrow \mathcal{W}(\lambda_R, \lambda, \lambda_Z) = \sum_{i=1}^3 \frac{2\mu}{\alpha_p^2} (\lambda_i)^{\alpha_p} + \sum_{i=1}^3 \frac{\tau_i}{4} (\lambda_i^2 - 1)^2 + \mathcal{W}(J) \quad (2.9)$$

where $\mu > 0$ is the mean average shear modulus of the continuum, $\tau > 0$ includes the contribution of fiber elasticity and α_p is a positive parameter for different material with $J = \prod_{i=1}^3 \lambda_i$ representing the volume change. In our system, we take $\alpha_p = 2$ for a Neo-Hookean solid and we

Convex energy density function



$$\hat{W}_s(\lambda, \lambda_z) = \frac{\mu_s}{2}(\lambda^{-2}\lambda_z^{-2} + \lambda^2 + \lambda_z^2 - 3) + \frac{\tau_s}{4}(\lambda^2 - 1)^2 \quad \mu_s = 1 \quad \tau_s = 0.15$$

Fig. 2.4 Depiction of \tilde{W} in Eq.(2.11) with dimensionless parameter $\tau/\mu = 0.15$.

assume the fiber effect only in the circumferential direction. Finally we employ the incompressibility condition $J = 1$ leading to

$$\mathcal{W}(\lambda_R, \lambda, \lambda_z) \rightarrow \frac{\mu}{2} \sum_{i=1}^3 \lambda_i^2 + \frac{\tau}{4}(\lambda^2 - 1)^2 - p(J - 1) = \mathcal{W}_m - p(J - 1) \quad (2.10)$$

where p is a Lagrange parameter for the constraint $J = 1$. If we do not want to keep it, we can define

$$\tilde{\mathcal{W}}(\lambda_R, \lambda, \lambda_z) = \frac{\mu}{2}[(\lambda\lambda_z)^{-2} + \lambda^2 + \lambda_z^2 - 3] + \frac{\tau}{4}(\lambda^2 - 1)^2 \quad (2.11)$$

It is a convex function as shown in Fig.(2.4).

Eventually, we can calculate the Cauchy stress as

$$\begin{aligned} \boldsymbol{\sigma} &= J^{-1} \frac{\partial \mathcal{W}}{\partial \mathbf{F}} \mathbf{F}^T = \frac{\partial \mathcal{W}_m}{\partial \mathbf{F}} \mathbf{F}^T - p \mathbf{I} \\ &\Rightarrow \sigma_i = \frac{\partial \mathcal{W}_m}{\partial \lambda_i} \lambda_i - p \end{aligned} \quad (2.12)$$

as well as the PK stress defined by Eq.(1.10). Furthermore, if we suppose $\sigma_r = 0$, we obtain $p = \frac{\partial \mathcal{W}_m}{\partial \lambda_R} \lambda_R$ and

$$\sigma_\theta = \frac{\partial \tilde{\mathcal{W}}}{\partial \lambda} \lambda; \quad \sigma_z = \frac{\partial \tilde{\mathcal{W}}}{\partial \lambda_z} \lambda_z \quad (2.13)$$

If we want to consider the stress distribution along the radial direction, we need to settle the ODE as following

$$\frac{\partial \sigma_r}{\partial r} + \frac{1}{r}(\sigma_r - \sigma_\theta) = 0 \quad \text{or} \quad \frac{\partial S_R}{\partial R} + \frac{1}{R}(S_R - S_\Theta) = 0 \quad (2.14)$$

We take S_I as the PK-I stress. Boundary conditions read

$$\begin{aligned} \sigma_r(r = r_e) &= -\frac{\kappa_{ECM}}{r_e} \approx 0 ; \sigma_r(r = r_i) = -p_i \\ \Leftrightarrow S_R(R_e) &= J\sigma_r(r_e)\Lambda_R^{-1} = \sigma_r(r_e)\Lambda_R^{-1} \approx 0 ; S_R(R_i) = -p_i\Lambda_R^{-1} = -p_I \end{aligned} \quad (2.15)$$

where $J = 1$ and we assume the surface tension effect κ_{ECM} is weak compared with the elastic stress, that's to say $\kappa_{ECM}/E \ll 1$ and p_i is the inner pressure which might be a function of the deformation change. In the thin membrane case, σ_r is a higher order term which can be neglected in the calculation of σ_θ and σ_z . In the following we need to introduce the inner force contribution by active networks in S cells.

2.3 Planar active stress by actin-myosin networks

Myosin II, the actin molecular motors, have been observed [84, 85] in the seam (S) domain. They can induce contractile deformation of the network and simultaneously generate inner-stress. Similarly, we could imagine heating a rubber-like material under stretch. High temperature (in a range) will make the rubber stiffer which generates a positive inner stress. And if we stretch it, temperature will increase. In other words, we could pump in energy for a contractile shape change. Here we suppose that the active stress [86] in S cells is induced by such a mechanism (see Fig.(2.5)). We also consider the fiber/filament anisotropy in the elastic energy. Fig.(2.6) demonstrates the dispersion angle of the fiber/filament. In the figure data are limited just to seam cells of the body part (see Fig.(2.1)) due to experimental difficulties. Because of symmetry, the planar angle distribution is a function of $\varphi = [0, \pi/2]$. Before elongation, the filaments lie in the circumferential direction in both S and DV cells. After, motors in S cells become active with an increase of the dispersion value κ generating contractile deformation with $G_S < 1$ and $G_{DV} > 1$ in Fig.(2.2).

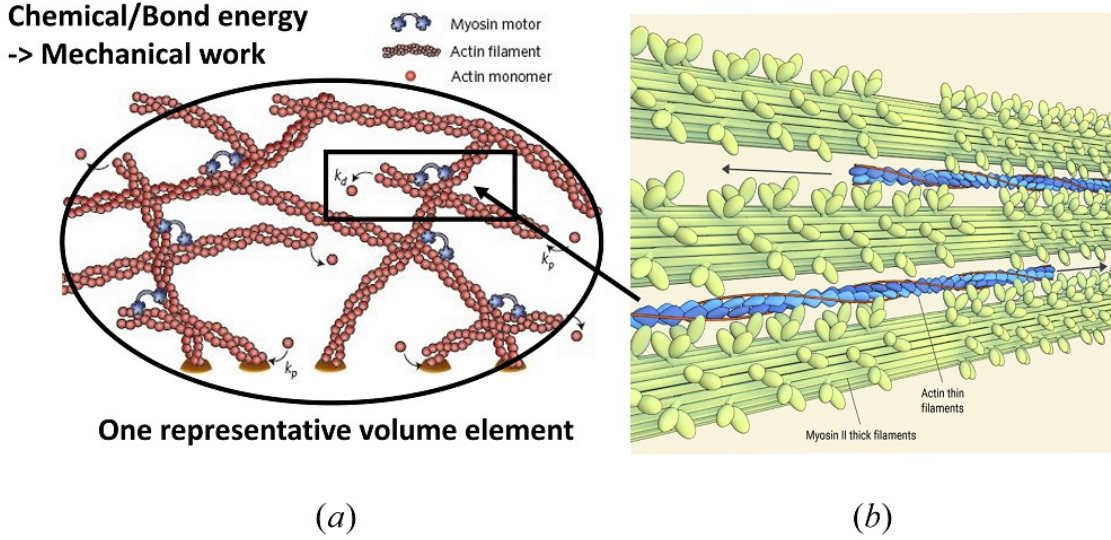
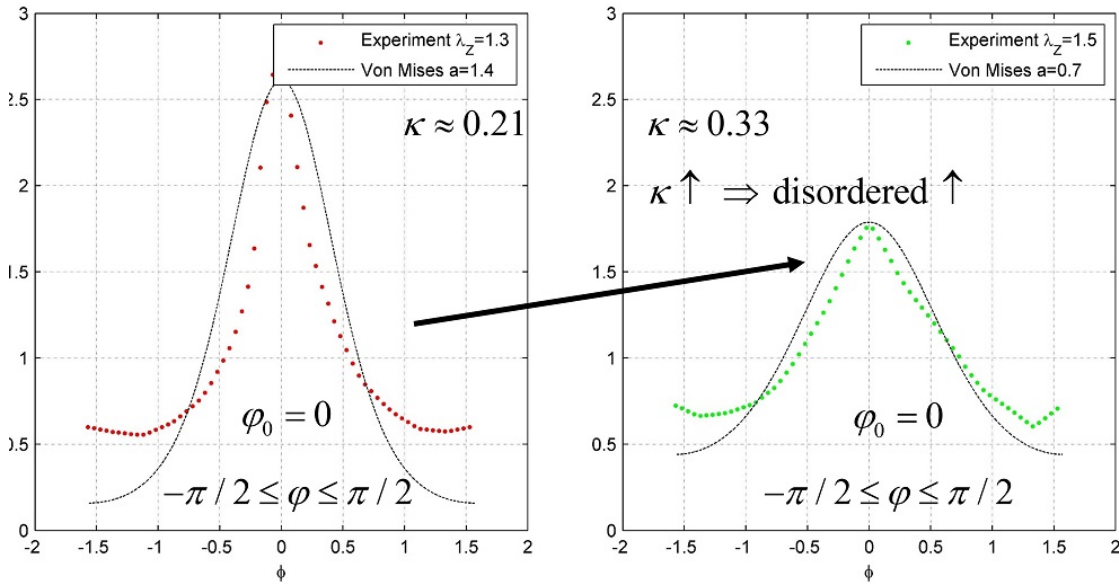


Fig. 2.5 Mechanism of the actin-myosin network with motors: (a) (From [87]) One representative volume element where there are numerous actin filaments with motors. Energy transmission happens through actin monomers resulting in polymer (filament) reorganization. (b) Visualization of the interaction between filaments. Contractility is produced through the concerted movement of myosin heads (green) along actin thin filaments, which are made up of f-actin (blue) and tropomyosin (red)

$$\rho(\varphi, \varphi_0) = \exp(a \cos 2(\varphi - \varphi_0)) / I_0(a)$$



$$\kappa = \frac{1}{\pi} \int_{-\pi/2}^{\pi/2} \rho(\varphi) \sin^2 \varphi d\varphi \quad I_0(a) = \frac{1}{\pi} \int_0^{\pi} \exp(a \cos \beta) d\beta$$

Fig. 2.6 Distribution of the planar fiber/filament direction in seam cells: Points in red are experimental data [8] when elongation Λ_Z equals 1.3 in comparison of points in green as Λ_Z equals 1.5. The curves in black are fitting results of the Von Mises distribution function [42]. φ is the angle along the average alignment and $\varphi = 0$ means that fibers align completely along the circumferential direction e_θ in our case and $\varphi = \pm\pi/2$ is the vertical direction e_z . The dispersion value κ characterizes the disorder of fiber anisotropy. Because of symmetry, we can calculate all the quantities as a function of $\varphi = [0, \pi/2]$ in practice.

If the active stress/strain merely depends on the distribution of the network, we have

$$\boldsymbol{\sigma} = \boldsymbol{\sigma}^p(\mathbf{F}) + \boldsymbol{\sigma}^a(\mathbf{n}) \quad (2.16)$$

where $\boldsymbol{\sigma}^p$ is the classical stress tensor induced by the elastic strain and $\boldsymbol{\sigma}^a$ is the active part [86] which is related to the fiber/filament direction. In a thin membrane system, the planar active stress [42] reads

$$\begin{aligned} \boldsymbol{\sigma}^a &= -p_a \mathbf{I} + \mathbf{H}^d \\ \mathbf{H}^d &= \mathbf{H} - \frac{1}{3} \text{tr}(\mathbf{H}) \mathbf{I} ; \mathbf{H} = -\tilde{\zeta}_1 \kappa \mathbf{I} + \tilde{\zeta}_2 (1 - 2\kappa) \mathbf{n} \otimes \mathbf{n} \\ \kappa &= \frac{1}{\pi} \int_{-\pi/2}^{\pi/2} \rho(\varphi) \sin^2 \varphi \, d\varphi ; \mathbf{n} \parallel \mathbf{F} \cdot \mathbf{n}_0 \end{aligned} \quad (2.17)$$

If we take $\rho(\varphi) = \delta(0)$, then $\mathbf{H} \sim -\tilde{\zeta}_1 \mathbf{I} + \tilde{\zeta}_2 \text{diag}[1, 0, 0]$ with $\mathbf{n} = [1, 0, 0]^T$. Surely we can use the similar formula for the multi-axis case as

$$\begin{aligned} \mathbf{H} &= \sum \mathbf{H}_i \\ \mathbf{H}_i &= -\tilde{\zeta}_{1(i)} \kappa_i \mathbf{I} + \tilde{\zeta}_{2(i)} (1 - 2\kappa_i) \mathbf{n}_i \otimes \mathbf{n}_i ; \kappa_i = \kappa_i(p_i^\varphi) \end{aligned} \quad (2.18)$$

Correspondingly we can employ $\rho_1(\varphi) = \delta(0)$, $\rho_2(\varphi) = \delta(\pi/2)$ and thus $\mathbf{H} \sim -\tilde{\zeta}_1 \mathbf{I} + \tilde{\zeta}_2 \text{diag}[1, -1, 0]$ with $\mathbf{n}_1 = [1, 0, 0]^T$, $\kappa_1 = 0$ and $\mathbf{n}_2 = [0, 1, 0]^T$, $\kappa_2 = 1$. We can use the superposition Eq.(2.18) to realize an inner stress in any direction.

2.4 Active strain/stress with simulations

We first take the general multiplicative decomposition for finite strain

$$\mathbf{F} = \mathbf{F}_e \mathbf{F}_a \mathbf{G} \quad (2.19)$$

which means the total deformation is decomposed by elastic part, inelastic self-strain [88] and growth. In our case, the diagonal form reads

$$\mathbf{F} = \begin{bmatrix} \lambda_R & 0 & 0 \\ 0 & \lambda & 0 \\ 0 & 0 & \lambda_Z \end{bmatrix} \begin{bmatrix} \lambda_R^a & 0 & 0 \\ 0 & \lambda^a & 0 \\ 0 & 0 & \lambda_Z^a \end{bmatrix} \begin{bmatrix} g_R & 0 & 0 \\ 0 & g_\Theta & 0 \\ 0 & 0 & g_Z \end{bmatrix} \quad (2.20)$$

where $J_e = J_a = 1$ for incompressibility and $J_g > 1$ for positive growth. Therefore the elastic energy function should be modified as

$$\mathcal{W} = \frac{\mu}{2} \text{tr}(\mathbf{F}_e^T \mathbf{F}_e) + \mathcal{W}_{fib}(\mathbf{F}_e, \mathbf{n}_0) - p(J/J_g - 1) \quad (2.21)$$

For example, we take $\mathbf{G} = \mathbf{I}$, $\mathbf{F}_a = \text{diag}[0, \lambda_a, \lambda_a^{-1}]$ which leads to, in the linear approximation, an active stress $\boldsymbol{\sigma}^a = \text{diag}[0, \sigma_\theta, -\sigma_\theta]$ with $\sigma_\theta > 0$ if $\lambda_a < 1$. On the other hand, if we take $\mathbf{F}_e = \mathbf{I}$ and $\mathbf{G} = (1 + g^2)^{1/3} \mathbf{I}$, it creates a hydrostatic pressure which might cause instability or buckling of solid [89].

Let us consider some simulations to show the mechanics of the deformation coupled with the network during elongation. In Fig.(2.2) and Fig.(0.3,0.4), there are at least two processes happening in the epithelium of different parts: Filaments in the DV area align along the peripheral

direction due to the external stretch of the S domain. And the driving force comes from the inner stress of active networks in S cells. We use the general theoretical framework introduced in Chapter 1 to simulate the two mechanisms. We suggest the elastic energy density and dissipative function for Eq.(1.25) in plane strain as

$$\begin{aligned}\mathcal{W} &= \mu \varepsilon_{\alpha\beta}^e \varepsilon_{\alpha\beta}^e + \frac{K}{2} (\varepsilon_{\gamma\gamma}^e)^2 + \frac{K_n}{2} \partial_\alpha n_\beta \partial_\alpha n_\beta \\ \dot{R} &= \frac{b_n}{2} (\mathbf{n} - \mathbf{W} \cdot \mathbf{n})^2\end{aligned}\quad (2.22)$$

where we suggest a linear isotropic stress-strain (constitutive) relation for simplification, with shear modulus μ and bulk modulus K , which results in a linear decomposition of the elastic strain $\varepsilon_{\alpha\beta}^e$ by

$$\varepsilon_{\alpha\beta}^e = \varepsilon_{\alpha\beta} - \varepsilon_{\alpha\beta}^f - \varepsilon_{\alpha\beta}^g \quad (2.23)$$

where $\varepsilon_{\alpha\beta}$ is the total strain, $\varepsilon_{\alpha\beta}^f$ is the inner strain by the fiber rotation and network reordering and $\varepsilon_{\alpha\beta}^g$ is the strain by growth. While we neglect the growth in the simulation with

$$\begin{aligned}\varepsilon_{\alpha\beta} &= \begin{bmatrix} \frac{\partial u}{\partial x} & \frac{1}{2} \left(\frac{\partial u}{\partial y} + \frac{\partial v}{\partial x} \right) \\ \frac{1}{2} \left(\frac{\partial u}{\partial y} + \frac{\partial v}{\partial x} \right) & \frac{\partial v}{\partial y} \end{bmatrix} \\ \varepsilon_{\alpha\beta}^f &= \gamma_n \text{diag}(\mathbf{n} \otimes \mathbf{n} - \mathbf{n}_0 \otimes \mathbf{n}_0) = \gamma_n \begin{bmatrix} \cos^2 \varphi - \cos^2 \varphi_0 & 0 \\ 0 & \sin^2 \varphi - \sin^2 \varphi_0 \end{bmatrix}\end{aligned}\quad (2.24)$$

In addition, we suppose b_n and K_n is fairly small compared to μ and K so that we could neglect the higher order terms related to b_n and K_n in the constitutive relation. Then we get the coupled time-dependent governing equations

$$\begin{aligned}\partial_\beta \sigma_{\alpha\beta} &= 0, \quad \sigma_{\alpha\beta} \approx \frac{\partial \mathcal{W}}{\partial \varepsilon_{\alpha\beta}} = 2\mu(\varepsilon_{\alpha\beta} - \varepsilon_{\alpha\beta}^f) + K \varepsilon_{\gamma\gamma} \delta_{\alpha\beta} \\ b_n \dot{\varphi} &= -\frac{\partial \mathcal{W}}{\partial \varphi} + K_n \Delta \varphi \Rightarrow \\ b_n \dot{\varphi} &= 2\mu \gamma_n \sin(2\varphi) (-\cos^2 \varphi + \sin^2 \varphi + \cos^2 \varphi_0 - \sin^2 \varphi_0 - \frac{\partial u}{\partial x} + \frac{\partial v}{\partial y}) + K_n \Delta \varphi\end{aligned}\quad (2.25)$$

where $\varphi(t=0) = \varphi_0(x, y)$ is the average dispersion angle and can be explained by discussion about Eq.(2.18). And we choose the Young's modulus $E = 10^5 \text{Pa}$ and the Poisson coefficient $\nu = 0.499$ which leads to $\mu = 33356 \text{Pa}$ and $K = 1.67 \times 10^7 \text{Pa}$.

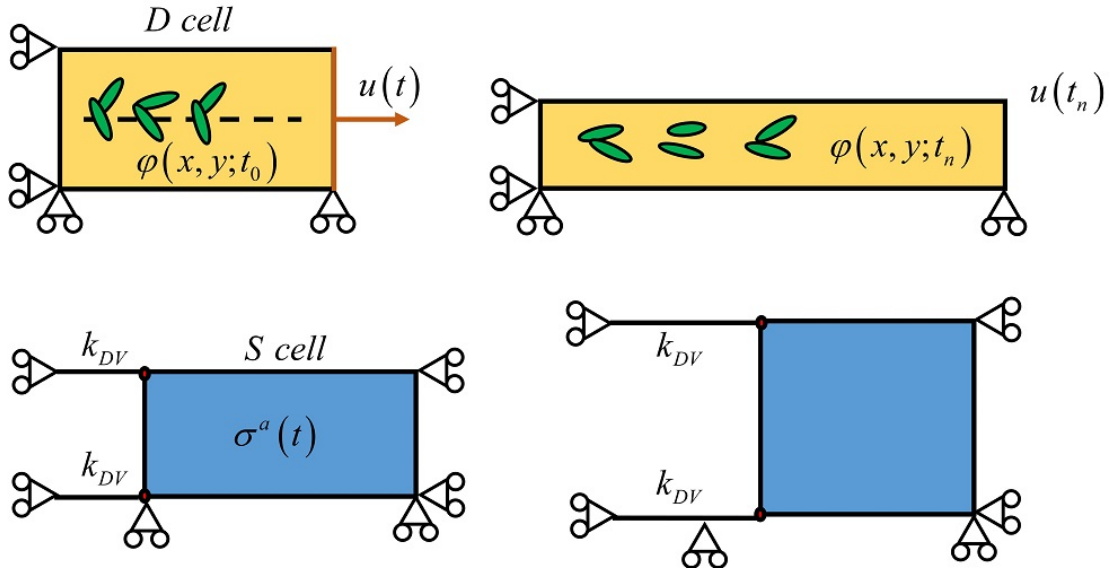


Fig. 2.7 Sketch of the two mechanisms in the epithelium during elongation. In D cells (yellow area), the arrangement of the filaments will change with external loading. In S cells (blue rectangular), positive active stress from the active network shortens the material with an contribution to the stretch of the D cell as $u(t)$. Here k_{DV} represents the stiffness of the D cell. Both cells are in a tension state.

We give an elementary illustration in Fig.(2.7) for the orientation-mechanical coupling in D and S cells. We then solve the governing equations Eq.(2.25) with appropriate boundary conditions $\varphi(x=0) = \varphi_0(x=0)$, $\varphi(x=1) = \varphi_0(x=1)$, $\frac{\partial \varphi}{\partial y}(y=0) = \frac{\partial \varphi}{\partial y}(y=1) = 0$, $u(x=0) = 0$, $v(y=0) = 0$, $u(x=1) = u(t)$ and initial conditions $\varphi(x, y, t=0) = \varphi_0(x, y)$. The initial stress-free configuration is a square with length $L = 1$. We first consider a uniform situation with $\varphi_0 = 45^\circ$.

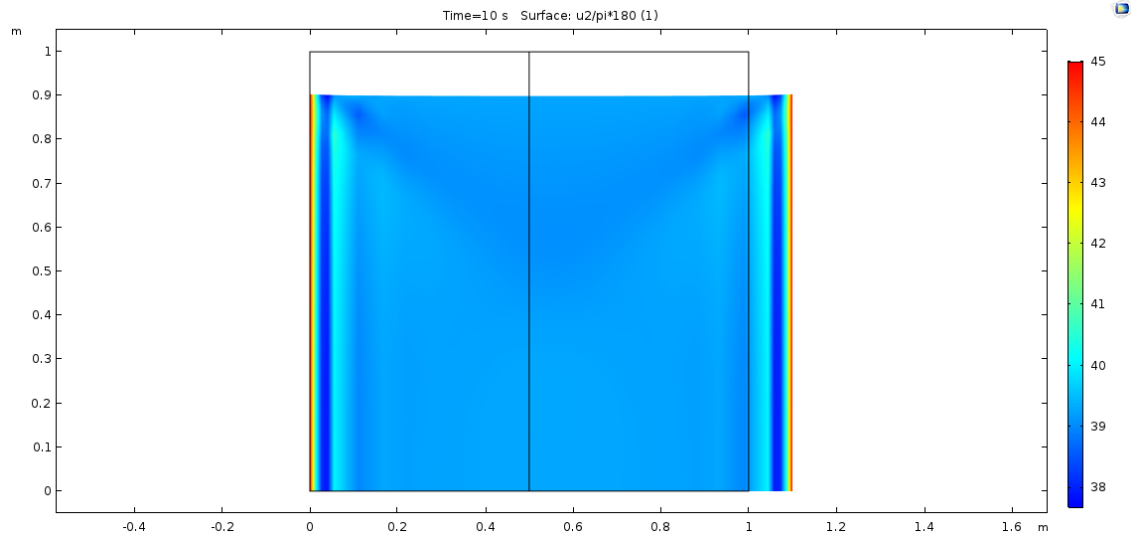


Fig. 2.8 Angle distribution $\varphi(x, y)$ with color bar after deformation: $\mu = 33356\text{Pa}$, $K = 1.67 \times 10^7\text{Pa}$, $b_n = 1\text{Pa} \cdot \text{s}$, $K_n = 10^{-4}\text{Pa} \cdot \text{m}^2$, $\gamma_n = 0.8$, $u(t) = 0.01 * t$

The total strain in Fig(2.8) equals 10% when $t = 10\text{s}$. We find that the filaments have an average rotation of about 7° . There is a large gradient on the left and right side since we assume a constant value on the boundary.

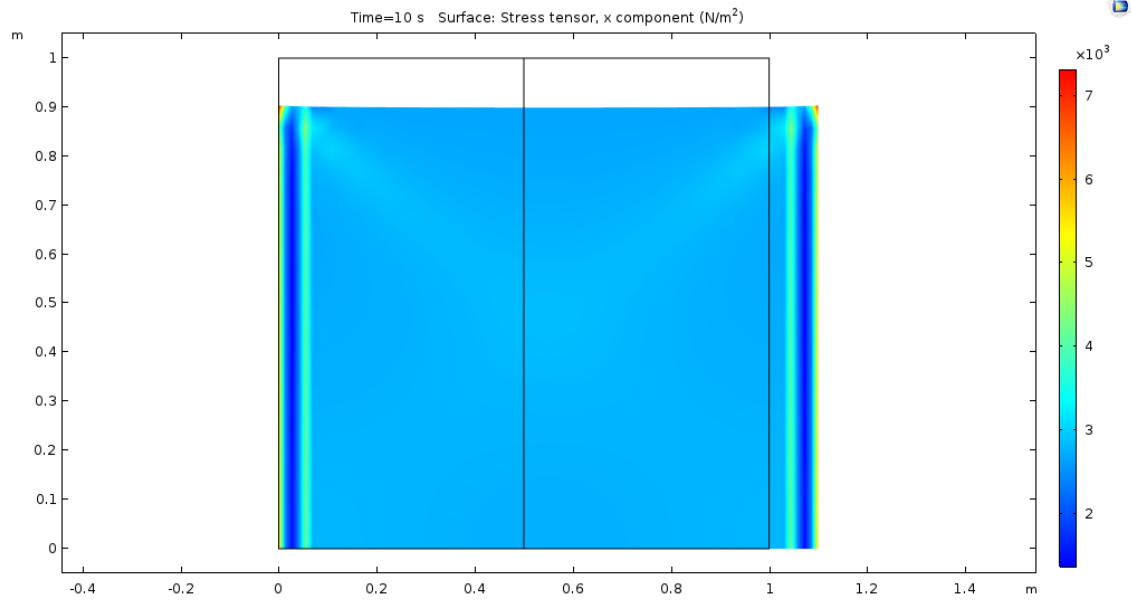


Fig. 2.9 Contour of $\sigma_x[\text{Pa}]$ with given material parameters in Fig.(2.8)

We find that the average stress in the middle plane $x = 0.5$ equals approximately $2.8 \times 10^3\text{Pa}$ which is smaller than the normal value due to $\varepsilon_{11}^f \approx 0.08$. Then we consider $\varphi_0(x, y) = 45^\circ |\sin(2\pi x)|$ leading to the following results

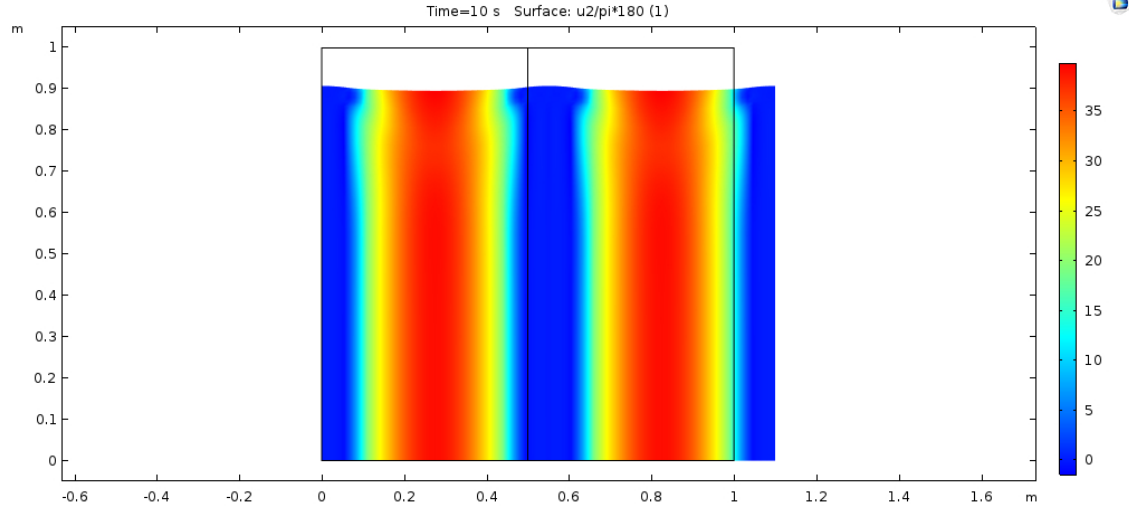


Fig. 2.10 Angle distribution $\varphi(x, y)$ with color bar after deformation: $\mu = 33356\text{Pa}$, $K = 1.67 \times 10^7\text{Pa}$, $b_n = 1\text{Pa} \cdot \text{s}$, $K_n = 10^{-4}\text{Pa} \cdot \text{m}^2$, $\gamma_n = 0.8$, $u(t) = 0.01 * t$

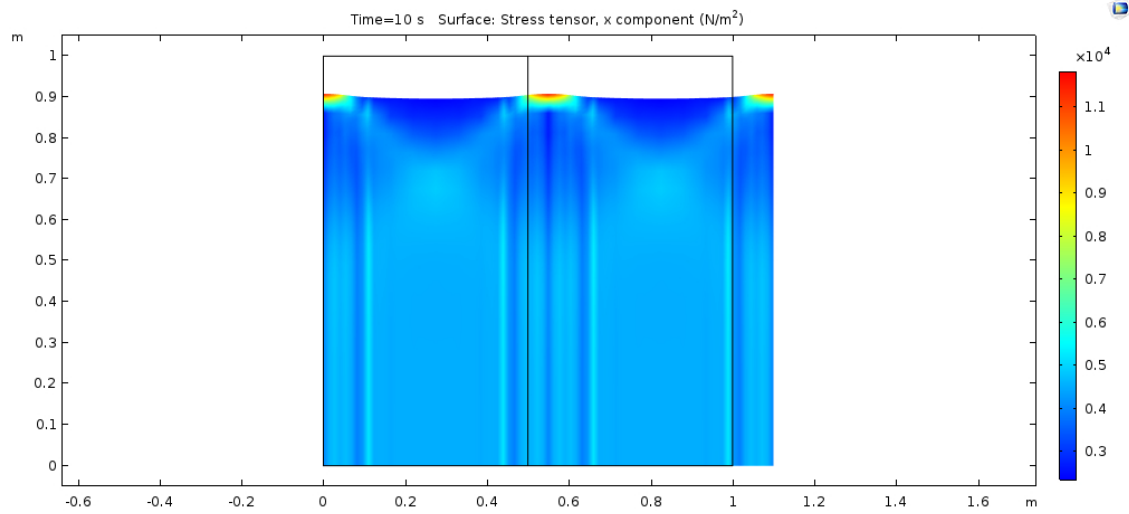


Fig. 2.11 Contour of $\sigma_x[\text{Pa}]$ with given material parameters in Fig.(2.10)

Fig(2.10) shows the corresponding angle distribution. There are two regions of dispersion in red as expected. As the elongation, the region $\varphi = 0$ grows and filaments rotate along the stretch direction. In addition, we find the upper free edge also has an interesting deformation compared with the straight line in the uniform case (see Fig.(2.8)). Fig(2.11) reflects the relative stress contour and we see the abnormal value on the upper border because of the boundary effect.

Admittedly deformation can give rise to the reordering of the network with filaments. Correspondingly, the self change of the network would generate the inner force of the elastic substrate. In Eq.(2.25), if we know $\varphi = \varphi(t)$, we can get the inner stress as $\sigma_{\alpha\beta}^f(t) = -2\mu\varepsilon_{\alpha\beta}^f(t)$. Fig.(2.6) shows the dispersion change in S cells during elongation which is an evidence for an active net-

work. Besides, it is proved that microtubules in the network will also generate an active force. So we combine the two terms in one expression like Eq.(2.17). After we suppose the active contribution in S cells as $\sigma^a(t) = \text{diag}[\sigma(t), -\sigma(t)]$.

2.5 Conclusion

To evaluate the stresses during *C. elegans* elongation, we start from a simplification of the geometry. Residual stress caused by the initial opening angle is introduced by adding an extra deformation gradient matrix before elongation. Different regions of the epithelium are distinguished in the theoretical analysis and interface continuity is considered. The geometric assumption based on finite elasticity is verified by experimental data in Fig.(2.3). The elastic stress is calculated by a constitutive relation. Hyper-elasticity with fiber reinforcement is suggested for the assessment. The equilibrium equations are solved with appropriate boundary conditions. Besides, active stress induced by the actomyosin network is considered by a deviatoric decomposition with fiber dispersion. Results from Simulations are given briefly for understanding the picture. In our system, we have to consider three effects of the network with filaments and microtubules. First, we need to consider the material strength of stretching the filaments. Second we should notice the self shortening and rotation of these filaments in the network. Finally, we ought to analyze the extra force contribution of the microtubules. In mechanics, we just adjust the force-displacement (constitutive) relation and combine the self-strain and inner stress as the force contribution. This chapter provides the stress calculation for the next section.

Chapter 3

Solutions for crack opening by laser ablation

In the experiment [8, 84], laser cuts are made on the surface of *C. elegans* after elongation. The crack length in equilibrium is l and the cut will open with size of b . The shape factor is defined by $\mathcal{F} = b/l$ which is related to the displacement field near the crack tip. In linear fracture mechanics, this ratio can be solved analytically by the far field stress distribution. Whereas, we will consider finite elasticity because the deformation of the epithelium is about 70%. So we employ the calculation of the previous chapter in our case. In addition, according to [8], cuts are made in two orthogonal directions on the epithelium during elongation and cracks open in both directions. This is strange since the tissue is in the compression state in one direction. So it visualizes the existence of the active network which was also discussed before.

In this chapter we shall first introduce the fundamental idea of linear elastic fracture mechanics (LEFM) and focus on a planar open crack. The analytical solution by Theocaris [73, 74] is applied to finite strain with our modified formula [26] in consideration of the fiber anisotropy and active stress. But the solution is for an infinite plane. So we employ the extended finite element method (XFEM) for finite size. The basic algorithm is reviewed in outline and then the complex scenario is studied in comparison with the analytical prediction.

3.1 Linear elastic fracture mechanics (LEFM) for a planar crack

In this section, we review the basic knowledge of linear elastic fracture mechanics following the idea of Inglis, Westergaard and Muschelisvili [90, 91, 92]. We try to use the complex method as well as the Airy stress function to obtain the asymptotic approximation near the crack tip due to strain compatibility and symmetry.

3.1.1 Review of LEFM

Fracture theory is relatively young compared with other branches in solid mechanics not only because it requires complicated mathematics but also the physical explanation is limited to the observation scale before we know better about the matter structure. Here we want to use classical mechanics to deal with the crack singularity within the linear assumption. Even with such simplifications, further analysis seemed impossible until some outstanding work made progress

[91, 93, 94, 95, 96, 97, 98, 99, 100]

Problem	Coordinate System	Analytical Method	Contributor	Year
Circular Hole	Polar	Real	Kirsch	1898
Elliptical Hole	Curvilinear	Complex	Kolosoff/Inglis	1913
Crack	Cartesian	Complex	Westergaard	1939
V Notch	Polar	Complex	Williams	1952
Dissimilar Materials	Polar	Complex	Williams	1959
Anisotropic Materials	Cartesian	Complex	Sih/Paris/Irwin	1965

Table 3.1: Summary of analytical solutions using the linear hypothesis (from lecture notes by Prof. VE Saouma)

To make a brief review of linear fracture mechanics (LFM), we adopt complex method to generalize the calculation. We begin with the homogeneous anisotropic constitutive relation in 2D defined by the flexible/compliance matrix a_{ij} [37] as

$$\begin{Bmatrix} \varepsilon_x \\ \varepsilon_y \\ \gamma_{xy} (2\varepsilon_{xy}) \end{Bmatrix} = \begin{bmatrix} a_{11} & a_{12} & a_{13} \\ a_{12} & a_{22} & a_{23} \\ a_{13} & a_{23} & a_{33} \end{bmatrix} \begin{Bmatrix} \sigma_x \\ \sigma_y \\ \tau_{xy} (\sigma_{xy}) \end{Bmatrix} \quad (3.1)$$

We can simplify this relation with symmetry of the material e.g. $a_{13} = a_{23} = 0$ for the orthotropic case. The strain compatibility in 2D reads

$$\frac{\partial^2 \varepsilon_x}{\partial y^2} + \frac{\partial^2 \varepsilon_y}{\partial x^2} = \frac{\partial \gamma_{xy}}{\partial x \partial y} \quad (3.2)$$

If we neglect the body force, the equilibrium equation in 2D becomes

$$\begin{aligned} \frac{\partial \sigma_x}{\partial x} + \frac{\partial \tau_{xy}}{\partial y} &= 0 \\ \frac{\partial \sigma_y}{\partial y} + \frac{\partial \tau_{xy}}{\partial x} &= 0 \end{aligned} \quad (3.3)$$

One can also introduce the Airy function to satisfy the governing equation Eq.(3.3) by

$$\sigma_x = \frac{\partial^2 \Phi}{\partial y^2} ; \sigma_y = \frac{\partial^2 \Phi}{\partial x^2} ; \tau_{xy} (\sigma_{xy}) = -\frac{\partial^2 \Phi}{\partial x \partial y} \quad (3.4)$$

The definition with a body force potential can be found in [37]. Substituting Eq.(3.1) and Eq.(3.4) into Eq.(3.2), we obtain

$$a_{11} \frac{\partial^4 \Phi}{\partial y^4} - 2a_{13} \frac{\partial^4 \Phi}{\partial x \partial y^3} + (2a_{12} + a_{33}) \frac{\partial^4 \Phi}{\partial x^2 \partial y^2} - 2a_{23} \frac{\partial^4 \Phi}{\partial x^3 \partial y} + a_{22} \frac{\partial^4 \Phi}{\partial x^4} = 0 \quad (3.5)$$

Specially in an isotropic situation, the constraint for the Airy function Eq.(3.5) reduces to

$$\Delta^2 \Phi = \left(\frac{1}{\alpha} - 2 \right) \Delta V = 0 \quad (3.6)$$

where $\alpha = 1 - \nu$ for plane strain and $\alpha = 1/(1 + \nu)$ for plane stress. $\mathbf{f} = -\nabla V$ is the body force which is neglected in the thesis. One key point for understanding the crack is that the singularity

of stress near the tip is $\sigma_{tip} \propto 1/\sqrt{r}$ [94] where r is the distance from a given point to the tip in the polar coordinate system. This is quite important for supposing a corresponding Airy function Φ in the actual problem.

The stress function can be written in complex form as

$$\Phi(x, y) = 2\text{Re}[\Phi_1(z_1) + \Phi_2(z_2)] \quad (3.7)$$

and there are different choices for Φ_1 and Φ_2 . For the isotropic case, we can use harmonic potential functions to represent the biharmonic operator [101, 102] such as the famous Goursat form [92]: $\Phi = \text{Re}[\bar{z}\psi(z) + \chi(z)]$. More generally, Φ can be expressed in either of the three equivalent forms as: $\Phi = y\Theta + \Theta_0 = x\Theta_2 + \Theta_1 = (x^2 + y^2)\Theta_4 + \Theta_3$ where Θ_i are various logarithmic potential functions [101, 102]. Here we shall focus on the isotropic case with the method by Westergaard [91, 103] for a physical picture about the crack tip asymptotic solution. Westergaard defines potential function for Mode I as

$$\begin{aligned} \Phi(x, y) &= \text{Re}(\phi_2 - iy\phi_1) = \text{Re}\phi_2(z) + y\text{Im}\phi_1(z) \\ \phi_1 &= \int \phi(z)dz ; \phi_2 = \int \phi_1 dz \end{aligned} \quad (3.8)$$

with the first and second derivative of $\phi(z)$ by ϕ' and ϕ'' . Thanks to the Cauchy-Riemann condition of analytical complex potential functions, we have obviously $\Delta\phi_i = 0$ and the stress components

$$\begin{aligned} \sigma_y &= \frac{\partial^2 \Phi}{\partial x^2} = \text{Re}\phi(z) + y\text{Im}\phi'(z) \\ \sigma_x &= \frac{\partial^2 \Phi}{\partial y^2} = \text{Re}\phi(z) - y\text{Im}\phi'(z) \\ \tau_{xy} &= -\frac{\partial^2 \Phi}{\partial x \partial y} = -y\text{Re}\phi'(z) \end{aligned} \quad (3.9)$$

which satisfy the 2D equilibrium equation without the body force Eq.(3.3). For an isotropic material under plane stress conditions we have

$$\begin{Bmatrix} \varepsilon_x \\ \varepsilon_y \\ \gamma_{xy} \end{Bmatrix} = \begin{bmatrix} \frac{\partial}{\partial x} & 0 \\ 0 & \frac{\partial}{\partial y} \\ \frac{\partial}{\partial y} & \frac{\partial}{\partial x} \end{bmatrix} \begin{Bmatrix} u \\ v \end{Bmatrix} = \frac{1}{E} \begin{bmatrix} 1 & -\nu & 0 \\ -\nu & 1 & 0 \\ 0 & 0 & 2(1+\nu) \end{bmatrix} \begin{Bmatrix} \sigma_x \\ \sigma_y \\ \tau_{xy} \end{Bmatrix} \quad (3.10)$$

and then the displacement via the integral of the strain with boundary conditions.

We rewrite Eq.(3.4) as [104]

$$\begin{aligned} \sigma_x + \sigma_y &= 4 \frac{\partial^2 \Phi}{\partial z \partial \bar{z}} = (\partial_x - i\partial_y)(\partial_x + i\partial_y)\Phi = \Delta\Phi(x, y) \\ \sigma_y - \sigma_x + 2i\tau_{xy} &= 4 \frac{\partial^2 \Phi}{\partial z^2} \\ \partial_z &= \frac{1}{2}(\partial_x - i\partial_y) ; \partial_{\bar{z}} = \frac{1}{2}(\partial_x + i\partial_y) \end{aligned} \quad (3.11)$$

where Φ is a real function and $\frac{\partial}{\partial z}$ and $\frac{\partial}{\partial \bar{z}}$ are formal operators defined by Eq.(3.11). In the next step we employ Eq.(3.10) as

$$\varepsilon_x + \varepsilon_y = \partial_z(u + iv) + \partial_{\bar{z}}(u - iv) = \frac{1-\nu}{E}(\sigma_x + \sigma_y) \quad (3.12a)$$

$$\varepsilon_y - \varepsilon_x + 2i\varepsilon_{xy} = -2\partial_z(u - iv) = \frac{1 + \nu}{E}(\sigma_y - \sigma_x + 2i\tau_{xy}) \quad (3.12b)$$

Substituting Eq.(3.11) into Eq.(3.12b) with the conjugate on both sides, we derive

$$\begin{aligned} -2\partial_{\bar{z}}(u + iv) &= 4\frac{1 + \nu}{E}\frac{\partial^2\Phi}{\partial\bar{z}^2} \Rightarrow \\ u + iv &= -\frac{1}{\mu}\frac{\partial\Phi}{\partial\bar{z}} + F(z); \quad \mu = \frac{E}{2(1 + \nu)} \end{aligned} \quad (3.13)$$

Since $\partial_{\bar{z}}(u - iv) = \overline{\partial_z(u + iv)}$, we can obtain a constraint for $F(z)$ by Eq.(3.12a)

$$F'(z) + \overline{F'(z)} = \left[\frac{2}{\mu} + \frac{4(1 - \nu)}{E} \right] \frac{\partial^2\Phi}{\partial z \partial \bar{z}} = \frac{4}{E} \text{Re}\phi(z) \quad (3.14)$$

which leads to

$$F(z) = \frac{2}{E}\phi_1(z) + (ic_1z + c_2) \quad (3.15)$$

where the last two terms represent the rigid rotation and movement. Finally we arrive at the displacement expression in complex form for plane stress as

$$u + iv = -\frac{1}{\mu}\frac{\partial\Phi}{\partial\bar{z}} + \frac{2}{E}\phi_1 = -\frac{1}{2\mu}(\partial_x + i\partial_y)\Phi(x, y) + \frac{2}{E}\phi_1(z) \quad (3.16)$$

Sih and Paris [97, 103, 104, 105] take the analytical method for a general anisotropic situation with a more complicated form. Here we want to continue the analysis of Westergaard for the crack tip singularity.

Considering the symmetry, we have reason to guess $\sigma_y \sim \sigma_y^\infty / (1 - a^2/x^2)$ where a is the semi-length of the center crack and σ_y^∞ is the boundary stress for $y \rightarrow \infty$. Here we use the notation σ_0 to follow the lecture notes by Saouma. However, in order to recover $\sigma_y = 0$ for $-a < x < a$, we need to modify the formula as $\sigma_y(y = 0) \sim \text{Re}(\sigma_0 / \sqrt{1 - a^2/x^2}) \rightarrow 0$. So Westergaard has the reason to suppose

$$\phi^I(z) = \frac{\sigma_0}{\sqrt{1 - \frac{a^2}{z^2}}} \Rightarrow \Phi_I(x, y) \quad (3.17)$$

We can get the stress components using Eq.(3.9). Let us do the Talyor expansion near the crack tip by $\epsilon = z - a = re^{i\theta}$ with $r/a \ll 1$ and thus

$$\begin{aligned} \sigma_y^I(\epsilon) &= \sigma_0 \sqrt{\frac{a}{2r}} \cos \frac{\theta}{2} \left(1 + \sin \frac{\theta}{2} \sin \frac{3\theta}{2} \right) + h.o.t \\ \sigma_x^I(\epsilon) &= \sigma_0 \sqrt{\frac{a}{2r}} \cos \frac{\theta}{2} \left(1 - \sin \frac{\theta}{2} \sin \frac{3\theta}{2} \right) + h.o.t \\ \tau_{xy}^I(\epsilon) &= \sigma_0 \sqrt{\frac{a}{2r}} \sin \frac{\theta}{2} \cos \frac{\theta}{2} \cos \frac{3\theta}{2} + h.o.t \end{aligned} \quad (3.18)$$

where σ_x could be reproduced by superposing a linear solution with $\tilde{\sigma}_x = -\sigma_0$. It is natural for Irwin [106, 107] to introduce the stress intensity factor (SIF) as

$$K_I = \lim_{r \rightarrow 0, \theta \rightarrow 0} \sqrt{2\pi r} \sigma_y \sim \sigma_0 \sqrt{\pi a} \quad (3.19)$$

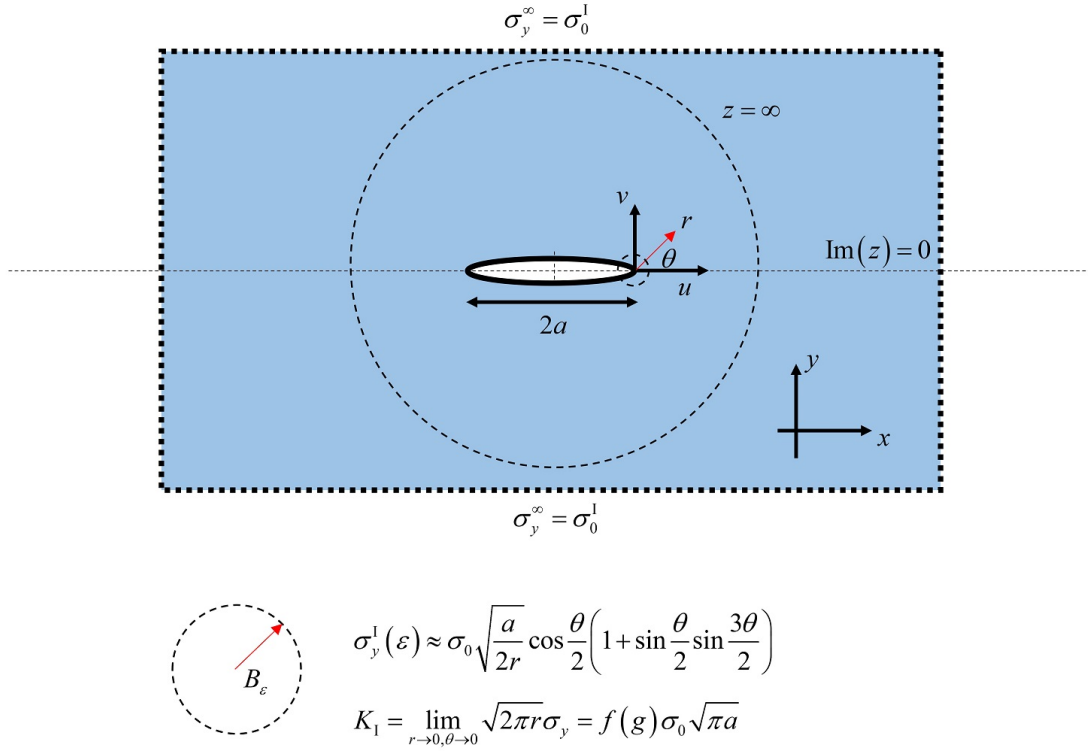


Fig. 3.1 Geometry of the Mode I open crack: $2a$ is the initial crack length and σ_0 is boundary stress in the y direction.

where 2π is merely a normalization factor. The work of Sih, Paris and Irwin [97] for Mode I crack opening in the plane anisotropic case finds [104, 106, 108]

$$\begin{aligned} u &= K_I \sqrt{\frac{2r}{\pi}} \text{Re} \left\{ \frac{1}{s_1 - s_2} \left[s_1 p_2 (\cos \theta + s_2 \sin \theta)^{1/2} - s_2 p_1 (\cos \theta + s_1 \sin \theta)^{1/2} \right] \right\} \\ v &= K_I \sqrt{\frac{2r}{\pi}} \text{Re} \left\{ \frac{1}{s_1 - s_2} \left[s_1 q_2 (\cos \theta + s_2 \sin \theta)^{1/2} - s_2 q_1 (\cos \theta + s_1 \sin \theta)^{1/2} \right] \right\} \end{aligned} \quad (3.20)$$

with material constants

$$\begin{aligned} p_\alpha &= a_{11} s_\alpha^2 + a_{12} - a_{13} s_\alpha \\ q_\alpha &= a_{12} s_\alpha + \frac{a_{22}}{s_\alpha} - a_{23} \end{aligned} \quad (3.21)$$

where

$$s_\alpha = a_\alpha + i b_\alpha, \quad b_\alpha > 0 \quad (3.22)$$

are two groups of conjugate roots of the eigen equation [97, 109] by Eq.(3.5) as

$$a_{11} s^4 - 2a_{13} s^3 + (2a_{12} + a_{33}) s^2 - 2a_{23} s + a_{22} = 0 \quad (3.23)$$

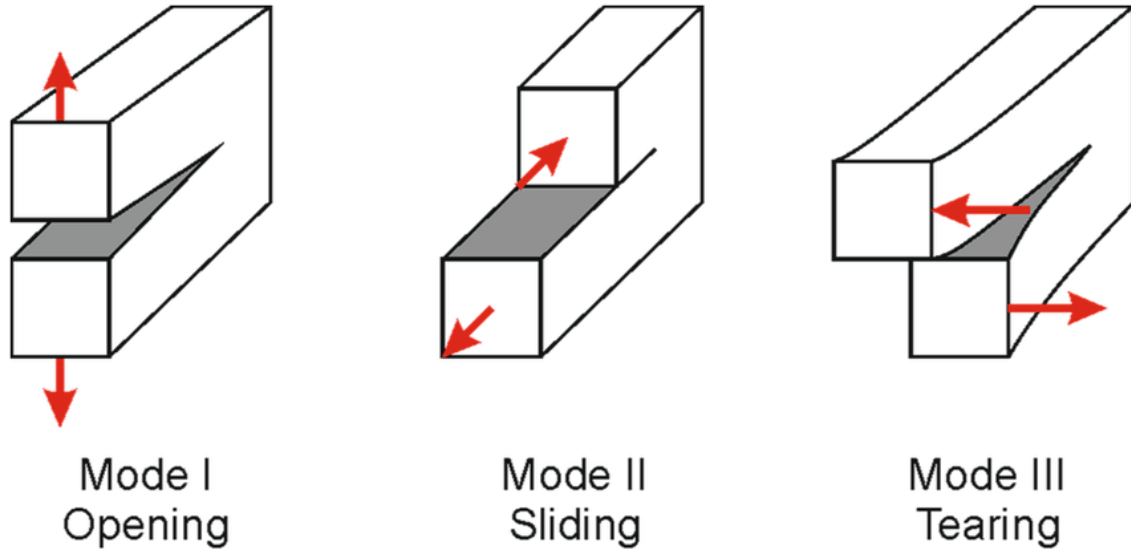


Fig. 3.2 Schematic diagram of the different modes (from [110]).

Following the similar approach by Westergaard, the potential function for Mode II is found by setting

$$\Phi_{II} = -y \operatorname{Re} \frac{\tau}{\sqrt{1 - \frac{a^2}{z^2}}} \quad (3.24)$$

And the Mode III crack opening induced by an anti-plane shear problem can also be obtained by a Williams expansion or by the complex theory for an easier harmonic compatibility equation [104, 105, 106, 108, 107]. For the general displacement of an isotropic material under biaxial loading, we use the solution by Theocaris [73, 74] for our system in the next subsection.

3.1.2 Analytical solution by Theocaris

Theocaris [73, 74] offers a full discussion for the planar crack opening within the linear limit. He uses Kolosov-Muskhelishvili relations [92] to obtain the solution in consideration of the orientation of the crack and the biaxial loading.

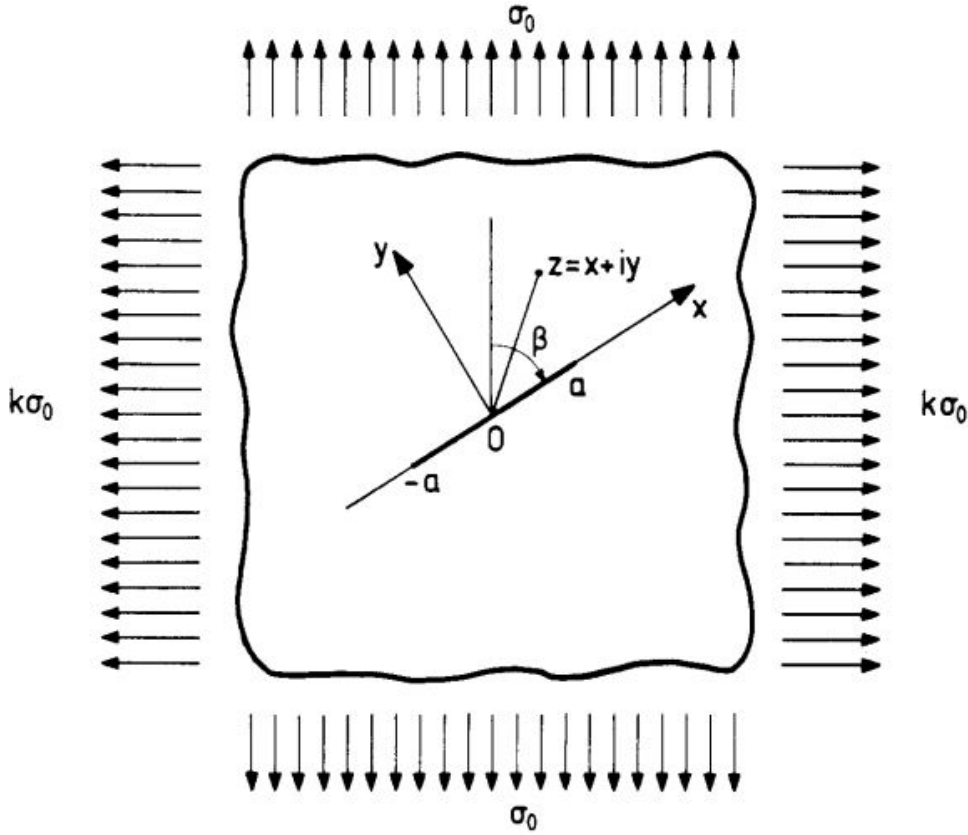


Figure 1. The geometry of a biaxially loaded internal inclined crack.

Fig. 3.3 Geometry of the inclined crack with boundary loading (from [74]): $2a$ is the initial crack length and k could be negative.

As demonstrated in Fig.(3.3), there is an initial tilting angle β which will generate a mix-mode solution with K_I and K_{II} . The displacements for the crack $-a < x < a$ are given as

$$\begin{aligned} u_{\pm}(x) &= C_{mat}\{(1-k)(\cos 2\beta)x \pm (1-k)(\sin 2\beta)\sqrt{a^2-x^2}\} \\ v_{\pm}(x) &= C_{mat}\{(1-k)(\sin 2\beta)x \pm [(1+k) - (1-k)\cos 2\beta]\sqrt{a^2-x^2}\} \end{aligned} \quad (3.25)$$

where the material constant C_{mat} is given by

$$C_{mat} = \frac{\sigma_0(1+\kappa_{mat})}{8\mu} = \begin{cases} \frac{\sigma_0}{E} & \text{plane-stress} \\ \frac{\sigma_0}{E}(1-\nu^2) & \text{plane-strain} \end{cases} \quad (3.26)$$

as well as the stress intensity factors (SIF)

$$\begin{aligned} K_I &= \frac{\sigma_0\sqrt{\pi a}}{2} [(1+k) - (1-k)\cos 2\beta] \\ K_{II} &= \frac{\sigma_0\sqrt{\pi a}}{2} (1-k)\sin 2\beta \end{aligned} \quad (3.27)$$

Here we suppose $C_{mat} > 0$ for a special convention which is different from the original work by Theocaris [74]. For the compressive case of $\sigma_0 < 0$, we could set $\beta = 0$ and $k < 0$. There is a geometry index for the elliptical crack as

$$\delta_{cr} = (1 + k) - C_{mat}(1 - k)^2 + \cos 2\beta(1 - k) [C_{mat}(1 + k) - 1] \quad (3.28)$$

The criterion gives an open crack with $\delta_{cr} > 0$ and two overlapped lips (branches) when $\delta_{cr} < 0$. We focus on the analysis with $0 < C_{mat} < 25\%$ where C_{mat} has the same order of strain and 25% is really large in the linear assumption.

- 1) Crack with perpendicular tension force: $\beta = \pi/2$ and $|kC_{mat}| < 25\%$

$$\begin{aligned} \delta_{cr} &= 2[1 - C_{mat}(1 - k)] > 0 \\ v_{\pm}(x = 0) &= \pm 2C_{mat} \cdot a \end{aligned} \quad (3.29)$$

and we find $v_{+}/a \sim 2\sigma_0/E$

- 2) Crack with perpendicular compressive force: $\beta = 0$ and $k < 0$

$$\begin{aligned} \delta_{cr} &= 2k(1 + C_{mat} - kC_{mat}) < 0 \\ v_{\pm}(x = 0) &= \mp 2|k| \cdot C_{mat} \cdot a \rightarrow \text{overlap} \end{aligned} \quad (3.30)$$

Besides, Theocaris also compares the method by Westergaard and Sih et al. He then gives the transform between the two potential functions ϕ^I and Z_I . He then proves the equivalence just when $\beta = 0$ and $\beta = \pi/2$. An extra constant term is necessary for the analysis of the slant crack. [73].

3.1.3 Modified formula for finite strain

In our case of *C. elegans* elongation, finite strain is considered with hyper-elasticity and fiber anisotropy. In addition, active stress, as well as initial strain, are also of the same order beyond the linear limit. So it is not easy to obtain an analytical solution for the crack shape in classical fracture mechanics. As far as we know, there is no formula of an open crack shape in anisotropic hyper-elasticity. Nevertheless, there is the basic picture of Eq.(3.29) that the crack opening length b is proportional to σ_0/E which is natural and also favored by biologists due to its simple form.

Following the work by Theocaris, we modify the original formula by replacing σ_0 and E respectively with the Cauchy stress $\sigma_{\alpha}(\mathbf{F})$ and the tangent stiffness modulus E_{α} in the opening direction. According to the experiment [8, 84], cuts are made in the current configuration and we use the superposition law to gain the total stress and calculate the tangent stiffness matrix with information of equivalent components E_{θ} and E_z . Here we make a simplification of pure Mode I crack opening which can be achieved by laser cuts along the special direction. Due to the biaxial tension state, a small tilting angle can be neglected. We give the relation between the measurable geometry factor \mathcal{F}_{α} and elastic quantities depicted in Fig.(3.4) as

$$\begin{aligned} \mathcal{F}_{\alpha} &= \frac{b_{\alpha}}{l_{\beta}} \approx \frac{2\sigma_{\alpha}}{E_{\alpha}} \\ \sigma_{\alpha} &= \sigma_{\alpha}^p(\mathbf{F}) + \sigma_{\alpha}^a(\mathbf{n}, \zeta) \\ E_{\alpha} &= K_{\alpha\alpha} - \frac{K_{\alpha\beta}^2}{K_{\beta\beta}} ; K_{\alpha\beta} = \frac{\partial \sigma_{\alpha}^p}{\partial \ln \lambda_{\beta}} = \lambda_{\beta} \frac{\partial \sigma_{\alpha}^p}{\partial \lambda_{\beta}} \end{aligned} \quad (3.31)$$

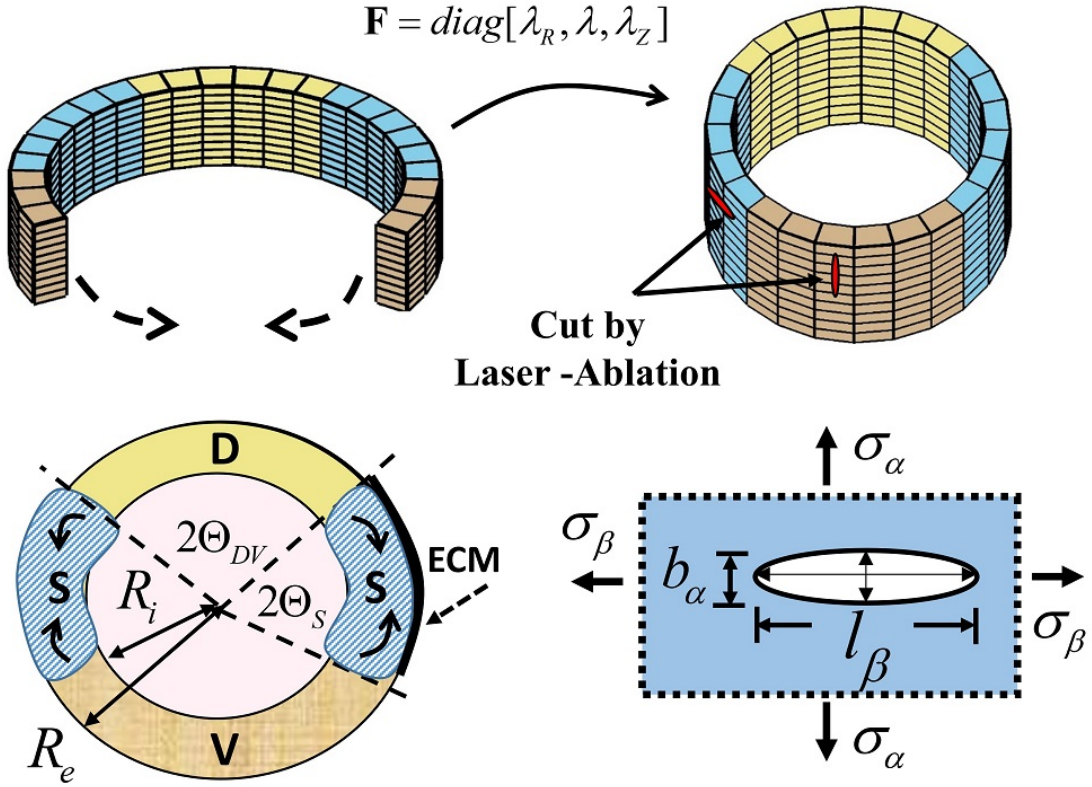


Fig. 3.4 Geometry of an open crack with initial length l_β and opening length b_α in the biaxial loading state.

where $\{\alpha, \beta\}$ takes $\{\theta, z\}$ or $\{z, \theta\}$ and there is no Einstein summation convention in Eq.(3.31). σ^p and σ^a are the passive and active stress defined in Chapter 3. We take for C. elegans

$$\sigma_\alpha^p(\mathbf{F}) = \frac{\partial \tilde{W}}{\partial \lambda_\alpha} \lambda_\alpha = \frac{\partial \tilde{W}}{\partial \ln \lambda_\alpha} \quad (3.32)$$

$$\tilde{W} = \frac{\mu}{2} \left[(\Lambda \Lambda_Z / \lambda_0 \lambda_{0z})^{-2} + (\Lambda / \lambda_0)^2 + (\Lambda_Z / \lambda_{0z})^{-2} - 3 \right] + \frac{\tau}{4} \left[(\Lambda / \lambda_0)^2 - 1 \right]^2$$

where λ_0 and λ_{0z} are unknown pre-strains. The active stress tensor is decomposed into a volumetric/spherical and a deformativ/deviatoric part

$$\sigma^a = -p^a \mathbf{I} + \zeta \text{diag}(0, 1, -1) \quad (3.33)$$

$$\zeta \approx \frac{2\alpha_1}{\pi} \tan^{-1} [\alpha_2 (\Lambda_Z - 1)]$$

with two unknown coefficients α_1 and α_2 for the empirical formula of ζ . The volumetric part will be eliminated just like the hydrostatic pressure Eq.(2.12) and Eq.(2.13). Hereafter, we can use the experimental data to identify all the parameters in Fig.(3.7) with continuous conditions on the interface of S and DV cells: $\sigma_\theta^S = \sigma_\theta^{DV}$.

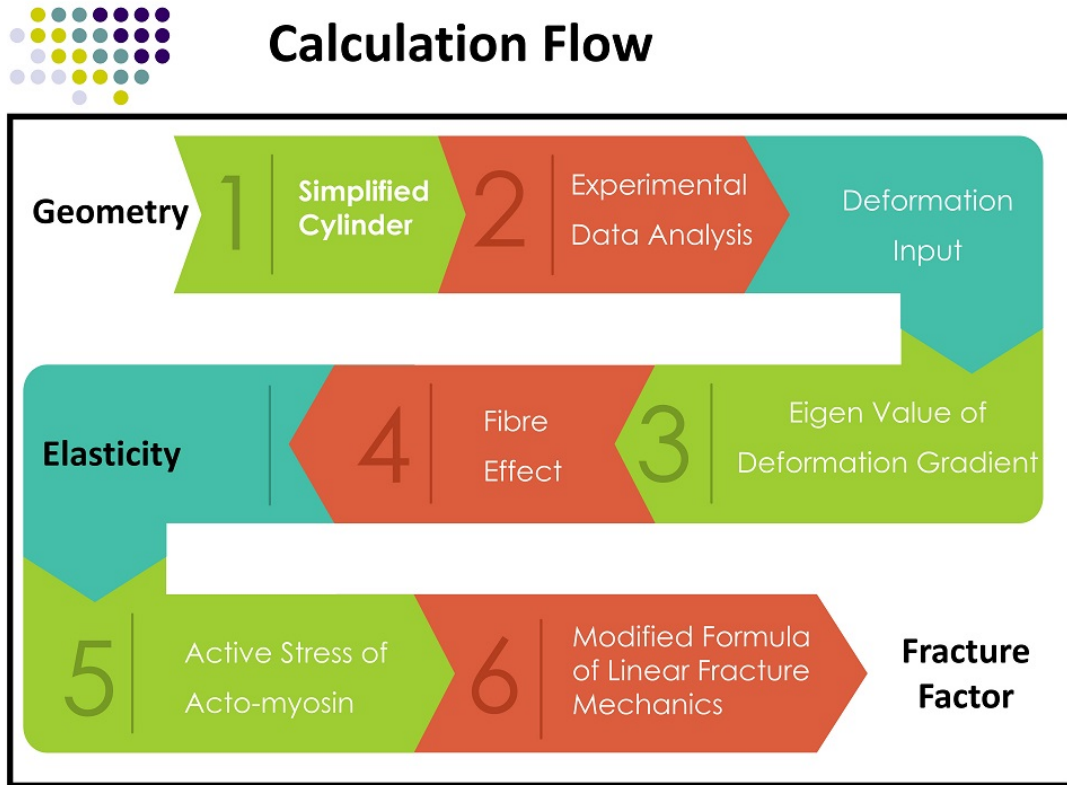


Fig. 3.5 Flow chart of fracture factor \mathcal{F} with stress in finite elasticity.

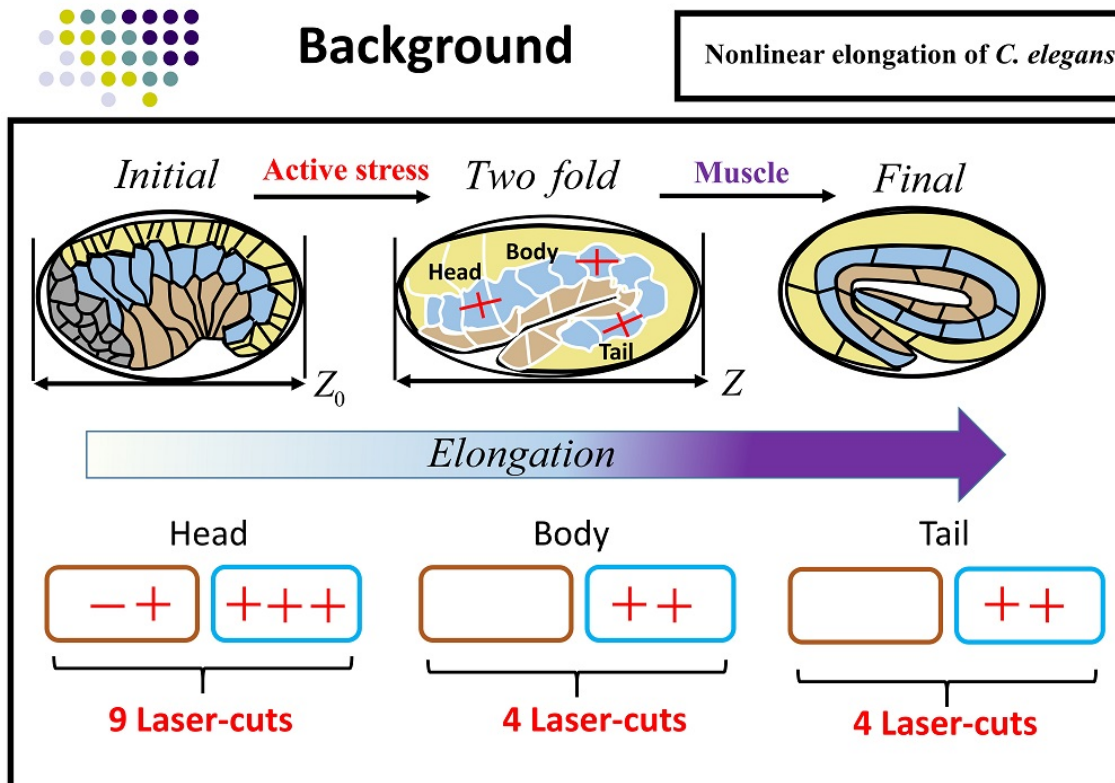


Fig. 3.6 Elongation by active stress with $Z/Z_0 = 1.3, 1.5, 1.7$.

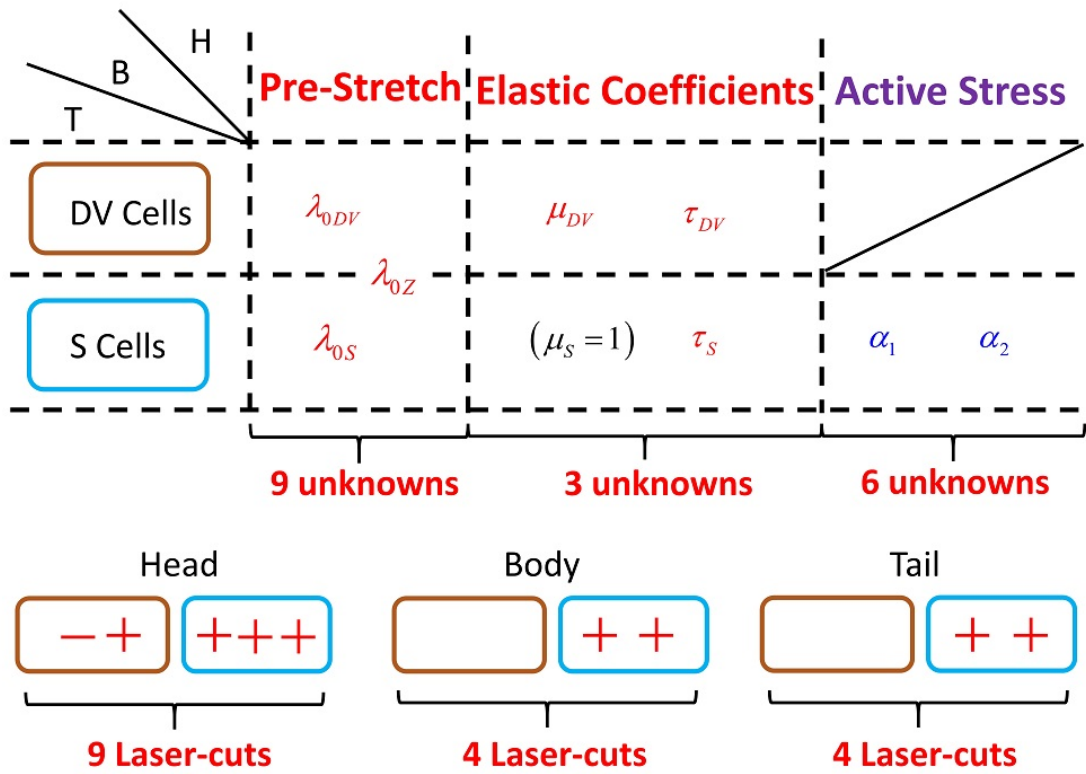


Fig. 3.7 List of parameters and available data from [8] concerning three positions in the embryo: head, body and tail and two different kinds of cells: S and DV. Number of unknowns: 18, measurements: 17 and continuity equations: 10.

We use the shear modulus of the seam cells, μ_S , as the unit for nondimensionalization. This allows us to get the table (3.2) of all material constants with the help of the crack factor \mathcal{F} Eq.(3.31) as well as the experimental measurement (see Fig.(2.3)).

	C_{0S} [μm]	C_{0DV} [μm]	λ_{0Z}	λ_{0S}	λ_{0DV}	α_1	α_2
Head	14.5	33.0	1.025	1.06	1.0326	2.2	1.27
Body	10.1	24.8	1.025	1.09	1.05	1.15	3.2
Tail	10.1	24.8	1.055	1.05	1.0232	1.25	2.9

Elastic coefficients: $\mu_{DV} = 1.44$, $\tau_S = 0.15$, $\tau_{DV} = 0.67$ with $\mu_S = 1$

Table 3.2: Geometry and material parameters

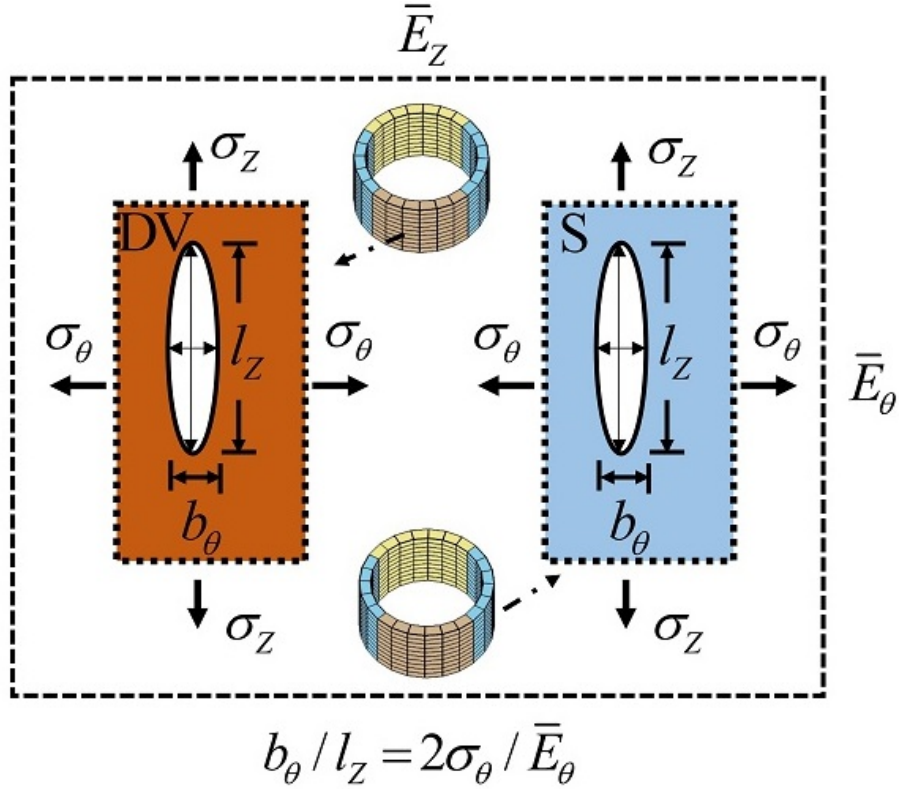


Fig. 3.8 Calculation map with equivalent Young's modulus defined by Eq.(3.31).

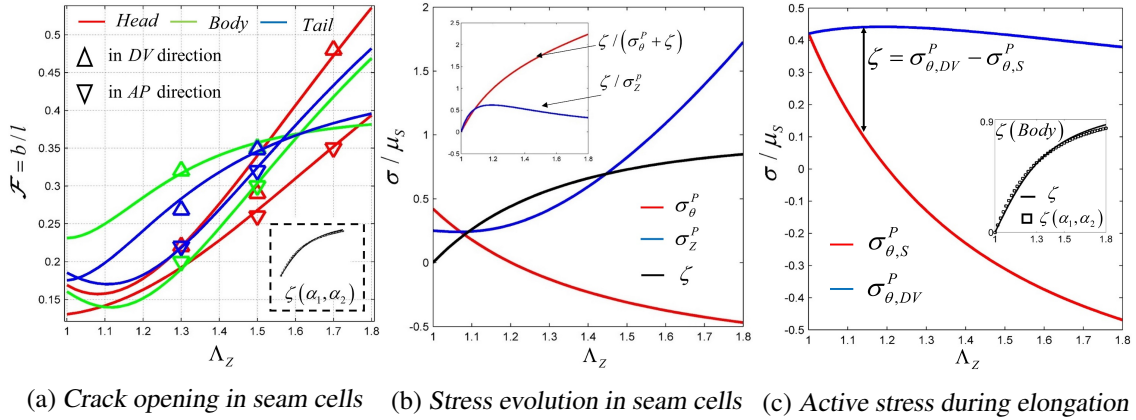


Fig. 3.9 Estimate of active stress: (a) Fitting curve for crack factor $\mathcal{F} = b/l \sim 2\sigma_\alpha/E_\alpha$ with experimental data; (b) Dimensionless passive stress versus elongation; (c) Estimate of active stress calculated by the connection equation $\sigma_\theta^S = \sigma_\theta^{DV}$.

Fig.(3.9) shows us some primary results through the calculation with our modified expression in seam cells. Our theoretical formulas (solid lines) meet well with the experimental data (hollow triangles). We can see that through solving a series of nonlinear constraint equations by Fig.(3.7) with the connecting condition $\sigma_\theta^S = \sigma_\theta^{DV}$, we can get the active stress ζ as a function of the

elongation Λ_Z by $\zeta(\Lambda_Z) = \sigma_\theta^P(DV) - \sigma_\theta^P(S)$ since molecular motors are mainly active in seam cells. Then we can identify two parameters α_1 and α_2 for an empirical fitting Eq.(3.33) for such a mechanism. However, we can just acquire an assessment of stress distribution and the absolute value of Young's modulus should be derived through other methods [10, 11, 12, 13, 14]. During the calculus, we assume stress and strain orthogonality by Eq.(2.5) and Eq.(2.11). Besides we provide the results of equivalent stiffness coefficients E_α of Eq.(3.31)

Cracks open in two orthogonal directions which implies a biaxial tension state of the epithelium. According to our analysis, there is no surprise for \mathcal{F}_Z but it might seem rather bizarre that the passive part σ_θ^p is negative in θ direction during elongation. So there ought to be an extra inner tensile stress. Thanks to laser ablation, we can first know the local sign of the total stress with open for positive and closed for negative. Furthermore, the shape factor reflects more or less the anisotropy in different orthogonal directions. With data analysis, we finally obtain some quantitative information about pre-strain and active contribution in mean average field. This technique can be used for other soft matter systems in elasticity. Moreover, we want to simulate the crack opening in a finite plane on purpose of mechanics. Besides, the real biological system has finite size. We shall use a numerical method in the next section.

3.2 Numerical simulations with XFEM in MATLAB

We could use the J integral [111] with a Newton iterative solver for the nonlinear problem. But here we still want to give a fast estimate of the crack opening factor with our modified formula. Therefore, we employ FEM with enriched node approximations [38, 112, 113, 114, 115, 116] because of its simple implementation. There are other numerical methods like BEM, phase field and MD [117, 118, 119] with techniques for the crack tip interpolation and reconstruction. In this section, we use the open source code in MATLAB [120]

3.2.1 Basic algorithm

Here we give a brief introduction on the extended-FEM (XFEM) in fracture mechanics. XFEM is developed to settle all kinds of discontinuities for classical continuum mechanics like material interfaces and cracks by singular elements and mesh-free interpolations. Essentially, it is a modification and extension on the basis of FEM. In this chapter, we shall focus on one of its applications in 2D, the crack problem by enriched elements within the Ritz-Galerkin frame.

We begin with the constitutive relation

$$\sigma_{ij} = \hat{D}_{ijkl}\varepsilon_{kl} \Rightarrow \{\sigma\} = [\hat{D}] \{\varepsilon\} \quad (3.34)$$

where the left equation is written in tensor components and the right in a matrix form. During the computation, we prefer the latter. Here $\hat{D} = D(\mathbf{u}, x)$ is related to deformation as well as positions for the general case and we make a strong assumption of Eq.(3.10) which means $[\hat{D}]$ is a constant matrix with only two material parameters. We limit our discussion to the linear isotropic case. We make a temporary convention: vectors are written in bold and matrices are labeled with square brackets or subscripts for the size.

The virtual work principle without inertial terms reads

$$\int_{\Omega} \delta \boldsymbol{\varepsilon}^T \boldsymbol{\sigma} - \int_{\Omega} \delta \mathbf{u}^T \mathbf{b} - \int_{\partial\Omega} \delta \mathbf{u}^T \mathbf{f}_{bc} = 0 \quad (3.35)$$

where b is the body force and f_{bc} is the known boundary force with the Cauchy relation. The stress-strain and strain-displacement relations in a matrix form were provided previously in Eq.(3.10). We use the Ritz-Galerkin method [63, 121, 122] with enriched degrees of freedom (DOFs) [38] as

$$\begin{aligned} \{u\} &= [N_{std}] \{q_{std}\} + [N_{enr}] \{q_{enr}\} \\ \{\varepsilon\} &= [L] \{u\} = [B_{std}] \{q_{std}\} + [B_{enr}] \{q_{enr}\} \end{aligned} \quad (3.36)$$

where $[N]$ is the shape function matrix, $\{q_{std}\}$ is the standard nodes in FEM, $\{q_{enr}\}$ represents the enriched part and $[L]$ is the linear partial differential operator matrix. In each element, we have the same piece-wise interpolation approximations

$$\begin{aligned} u^h(x) &= u^h(x; n_{std}) + u^h(x; n_H) + u^h(x; n_{cr}) \\ &= \sum_{I=1}^{n_{std}} N_I(x) q_I + \sum_{J=1}^{n_H} N_J(x) H(x) q_J + \sum_{K=1}^{n_{cr}} N_K(x) \sum_{m=1}^{n_{asy}} f_m(r, \theta) q_K^m \end{aligned} \quad (3.37)$$

where $\sum N_I = \sum N_J = \sum N_K = 1$, $H(x)$ gives displacement jumps between different phases and $f_m(r, \theta)$ are enriched functions for crack tips which are related to material properties [104, 112]. For the isotropic case, we can take the asymptotic basis

$$[f_1, f_2, f_3, f_4] = \left[\sqrt{r} \cos \frac{\theta}{2}, \sqrt{r} \sin \frac{\theta}{2}, \sqrt{r} \cos \frac{\theta}{2} \sin \theta, \sqrt{r} \sin \frac{\theta}{2} \sin \theta \right] \quad (3.38)$$

For the orthotropic or even anisotropic material, we shall modify the asymptotic basis to ensure completeness of the solution space. We have the general relationship between stress and SIF as

$$\begin{Bmatrix} \sigma_y \\ \tau_{xy} \\ \tau_{xz} \end{Bmatrix} = \frac{1}{\sqrt{2\pi r}} \begin{bmatrix} f_{11}^I(\theta) & f_{12}^{II}(\theta) & f_{13}^{III}(\theta) \\ f_{21}^I(\theta) & f_{22}^{II}(\theta) & f_{23}^{III}(\theta) \\ f_{31}^I(\theta) & f_{32}^{II}(\theta) & f_{33}^{III}(\theta) \end{bmatrix} \begin{Bmatrix} K_I \\ K_{II} \\ K_{III} \end{Bmatrix} \quad (3.39)$$

where $K_i = f(g) \sigma_i \sqrt{\pi a}$ and $f(g)$ is a parameter dependent of specimen, geometry and loading. Eq.(3.39) is employed for crack opening in an anisotropic material with the same definition of K_i in the isotropic hypothesis while the square root law has to be modified in other cases which will not be discussed here [105, 106, 123]. For orthotropic circumstances, it is suggested to use the following enriched interpolation [114, 115] as

$$\begin{aligned} f_i &\sim \sqrt{r} \left[\cos \frac{\theta_1}{2} \sqrt{g_1(\theta)}, \cos \frac{\theta_2}{2} \sqrt{g_2(\theta)}, \sin \frac{\theta_1}{2} \sqrt{g_1(\theta)}, \sin \frac{\theta_2}{2} \sqrt{g_2(\theta)} \right] \\ g_\alpha(\theta) &= \cos^2(\theta) + \frac{\sin^2(\theta)}{e_\alpha^2} ; \theta_\alpha = \tan^{-1} \left(\frac{\tan \theta}{e_\alpha} \right) \end{aligned} \quad (3.40)$$

where e_α are two material constants. The calculation framework in 3D is given in references [112, 124]. Back to Eq.(3.37), two level set functions ψ^n and ψ^t are used to divide the DOFs into three types. We assume an initial crack as a straight line in the center of an elastic body in Fig.(3.10). There are three kinds of elements necessary in Eq.(3.37): the standard element with $u^h(x) = u^h(x; n_{std})$, the Heaviside-enriched (H) element with $u^h(x) = u^h(x; n_{std}) + u^h(x; n_H)$ and finally the crack tip element with $u^h(x) = u^h(x; n_{std}) + u^h(x; n_{cr})$. For neighbor interface elements close to the crack body or tips, there is a criterion for whether it needs the Heaviside enrichment at the Gaussian integral point [123]. In practice, we initialize all the elements

with standard interpolations and then identify all crack tips one by one through the criterion in Fig.(3.11). We first provide the definition as

$$\begin{aligned}\psi^n(\mathbf{X}) &= \mathbf{d}(\mathbf{X}) \cdot \hat{\mathbf{n}} ; \hat{\mathbf{n}} = \mathbf{e}_3 \times (\mathbf{X}_1^{tip} - \mathbf{X}_2^{tip}) \\ \psi^t(\mathbf{X}; \mathbf{X}_\alpha^{tip}) &= (\mathbf{X} - \mathbf{X}_\alpha^{tip}) \cdot \mathbf{t}_\alpha ; \mathbf{t}_1 = -\mathbf{t}_2\end{aligned}\quad (3.41)$$

Now we shall give several explanations for these two functions on the straight line crack. The method can also be applied to multi-cracks in 2D and 3D. We define the left starting point as X_2^{tip} , the right end point as X_1^{tip} , unit tangent vectors \mathbf{t}_2 and \mathbf{t}_1 as well as tip normal vectors $\mathbf{n}_\alpha = \mathbf{e}_3 \times \mathbf{t}_\alpha$. There is a linear transform map between the global xy coordinates and the special center $x'y'$ coordinates as

$$\begin{Bmatrix} X' \\ Y' \end{Bmatrix} = \begin{bmatrix} \mathbf{t}_1^T \\ \hat{\mathbf{n}}^T \end{bmatrix} \begin{Bmatrix} X - X_0 \\ Y - Y_0 \end{Bmatrix}\quad (3.42)$$

For the definition of $\psi^n(\mathbf{X})$, we define the uniform normal vector in each crack segment as $\hat{\mathbf{n}} = \mathbf{n}_1$ and the distance vector \mathbf{d} from the given node point \mathbf{X} to the nearest point of the crack. It is obvious that ψ^n is positive above the crack line in Fig.(3.11) and negative below the crack. In the same way we can define another function ψ^t as the signed distance to the nearest crack tip in Eq.(3.41). In abbreviation, we take $\psi_\alpha^t = \psi^t(\mathbf{X}, \mathbf{X}_\alpha^{tip})$ for the illustration of Fig.(3.11).

It is easy to understand these definitions with the help of the local coordinate system in the center of the crack line.

$$\begin{aligned}\psi^n &\geq 0 \Leftrightarrow Y' \geq 0 \\ \psi_1^t &\geq 0 \Leftrightarrow (X' - X_1') \geq 0 ; \psi_2^t \geq 0 \Leftrightarrow (X' - X_2') \leq 0\end{aligned}\quad (3.43)$$

In the actual application, we can determine which tip is closer to the node point by a radius search algorithm and it is sufficient to decide which enrichment should be implemented for the concerning domain. The general rule is given by

$$\begin{aligned}\min(\psi_{N_i}^n)\max(\psi_{N_i}^n) < 0 , \min(\psi_{N_i}^t)\max(\psi_{N_i}^t) < 0 &\Rightarrow \text{Crack} \\ \min(\psi_{N_i}^n)\max(\psi_{N_i}^n) < 0 , \min(\psi_{N_i}^t)\max(\psi_{N_i}^t) > 0 &\Rightarrow \text{Heaviside} \\ \min(\psi_{N_i}^n)\max(\psi_{N_i}^n) > 0 , \min(\psi_{N_i}^t)\max(\psi_{N_i}^t) > 0 &\Rightarrow \text{Standard}\end{aligned}\quad (3.44)$$

where N_i is the node number of each element and ψ^t is calculated with respect to the nearest tip point. For example, in Fig.(3.11) the element $[a_2, b_2, c_2, d_2]$ is calculated with ψ_2^t and $[a_1, b_1, c_1, d_1]$ is judged by ψ_1^t . For crack propagation, we have to employ an updated algorithm with an empirical growth formula [120]. In practice we define two narrow bands to target a point.

With these definitions we can assemble the total stiffness matrix by substituting Eq.(3.36) into Eq.(3.35) as

$$\begin{aligned}[\hat{K}] &= \begin{bmatrix} [K_{std}] & [K_{coup}] \\ [K_{coup}]^T & [K_{enr}] \end{bmatrix} ; \{\hat{q}\} = \begin{Bmatrix} q_{std} \\ q_{enr} \end{Bmatrix} ; \{\hat{f}\} = \begin{Bmatrix} f_{std} \\ f_{enr} \end{Bmatrix} \\ [K_{std/enr}^{ie}] &\sim \int_{\Omega_e} [B_{std/enr}]^T [D] [B_{std/enr}] \, dV_e ; [K_{coup}^{ie}] \sim \int_{\Omega_e} [B_{coup}]^T [D] [B_{std}] \, dV_e\end{aligned}\quad (3.45)$$

where $[\hat{K}]$ is the final stiffness matrix with all DOFs, $\{\hat{q}\}$ is the generalized displacement vector after reordering and $\{\hat{f}\}$ is the force vector. For each element i_e , the local elastic energy with $[K^{i_e}]$ is calculated by the expanded B matrix.

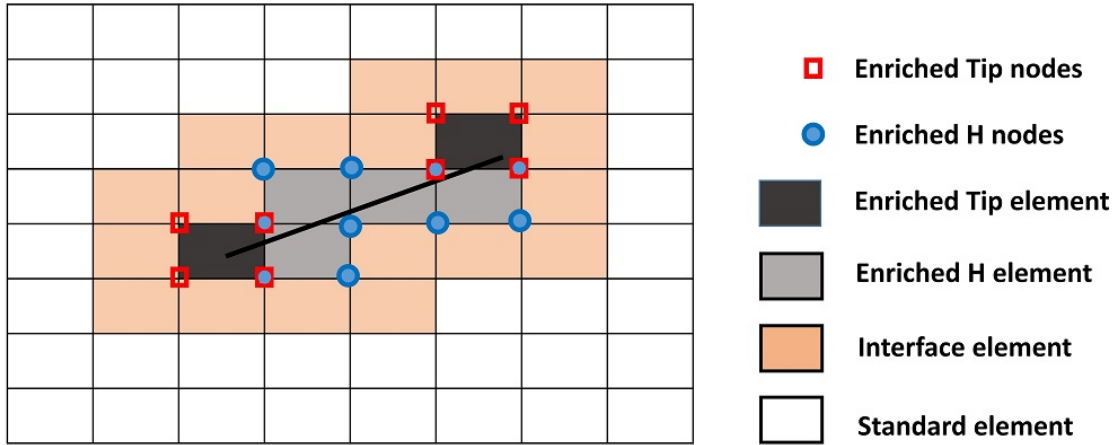


Fig. 3.10 Demonstration of enriched nodes and elements

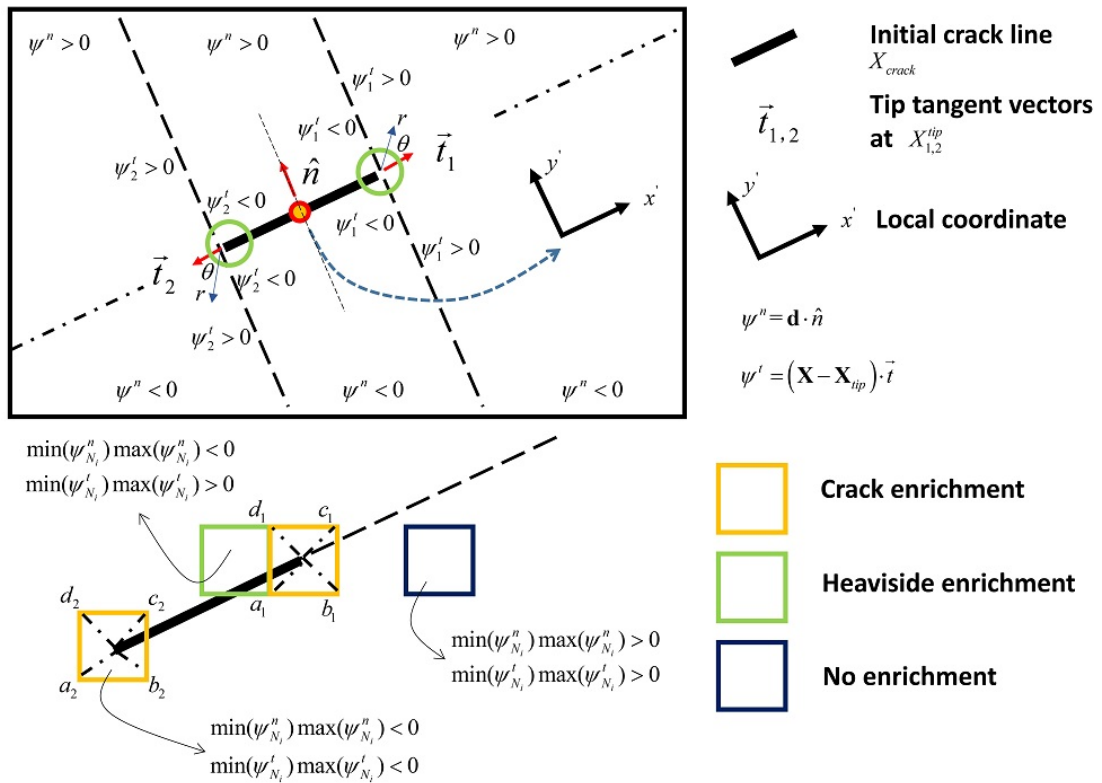


Fig. 3.11 Level Set functions ψ^n and ψ^t

We now proceed with a benchmark of the calculus and discuss the effect of the initial angle of the crack and biaxial loading.

3.3 Results and discussion

In this section we will apply the algorithm to the calculation. First we will use the theoretical formula with geometric modifications to verify the simulations. Then we use the XFEM to study the opening of the crack in consideration of different tilting angles with loading. In the following, we use the SI unit.

3.3.1 Geometry effects

For XFEM in finite size, we need to add a geometric factor for the SIF as [106, 107]

$$K_I^g = \beta_{geo} K_I \quad (3.46)$$

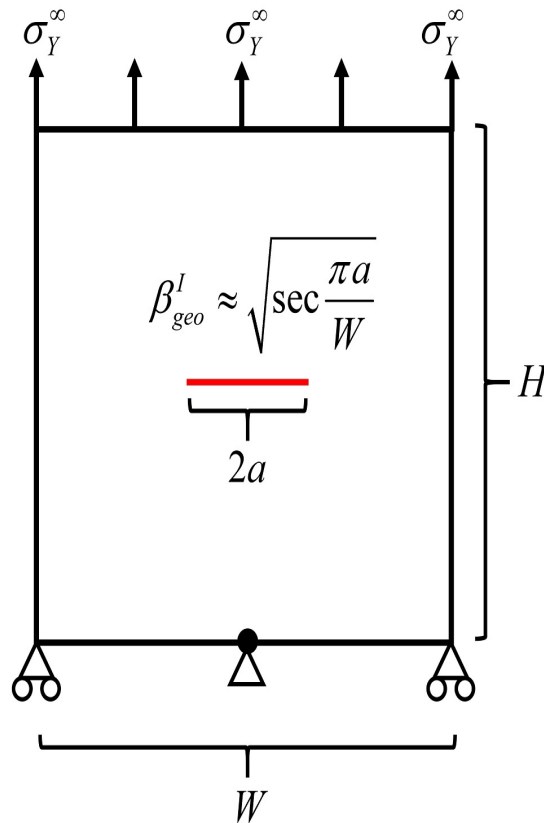


Fig. 3.12 Sketch of mode I opening with the geometric effect in full size

We neglect the crack propagation by setting a large value for the critical stress. Theoretically our geometry factor $\mathcal{F} \approx 2\sigma_Y^\infty/E$ can offer a priori estimate for an infinite plane where E is calculated by Eq.(3.31). However, the experiment might exhibit size effects which can be simulated

by XFEM. We fix the geometry with $W = H = 4$, $2a = 0.6$ and mesh size $\Delta x = \Delta y = 1/32$. We focus on the deformation and stress distribution when $\sigma_Y^\infty/E = 10\%$ and thus $\mathcal{F} \approx 0.2$. For the theoretical calculus of the stress intensity factors, we employ Eq.(3.27) and Eq.(3.46).

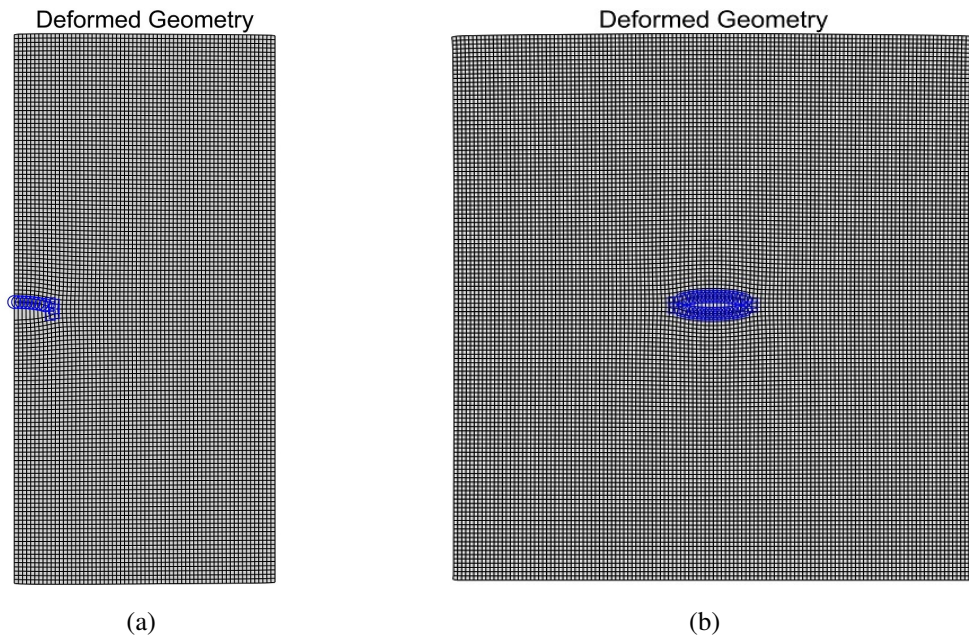


Fig. 3.13 $E = 10^5 \text{Pa}$, $\nu = 0.3$, $\sigma_Y^\infty = 10^4 \text{Pa}$, $K_I^g \approx 9.84 \times 10^3 \text{Pa}\sqrt{\text{m}}$ (a) *Open Crack (Half size) under uniaxial stretch with $\mathcal{F} \approx 0.22$, $K_I^{comp} = 9.72 \times 10^3 \text{Pa}\sqrt{\text{m}}$* ; (b) *Open Crack (Full size) under uniaxial stretch with $\mathcal{F} \approx 0.236$, $K_I^{comp} = 9.83 \times 10^3 \text{Pa}\sqrt{\text{m}}$*

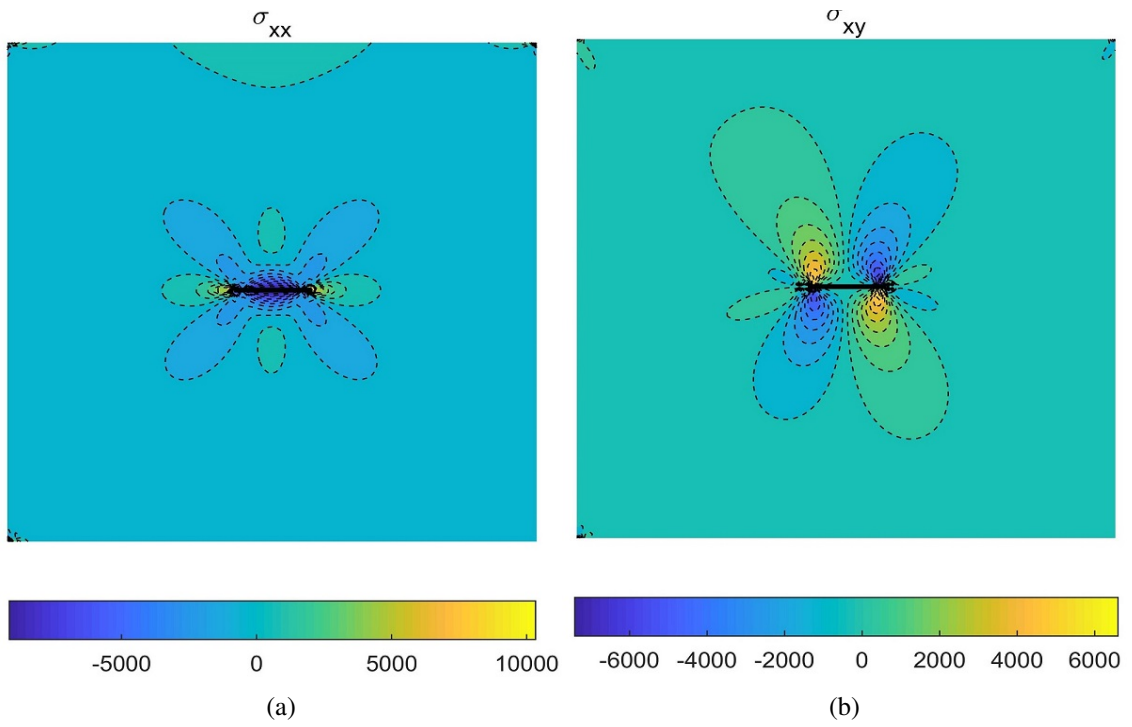


Fig. 3.14 Stress contour of components σ_{xx} and σ_{xy}

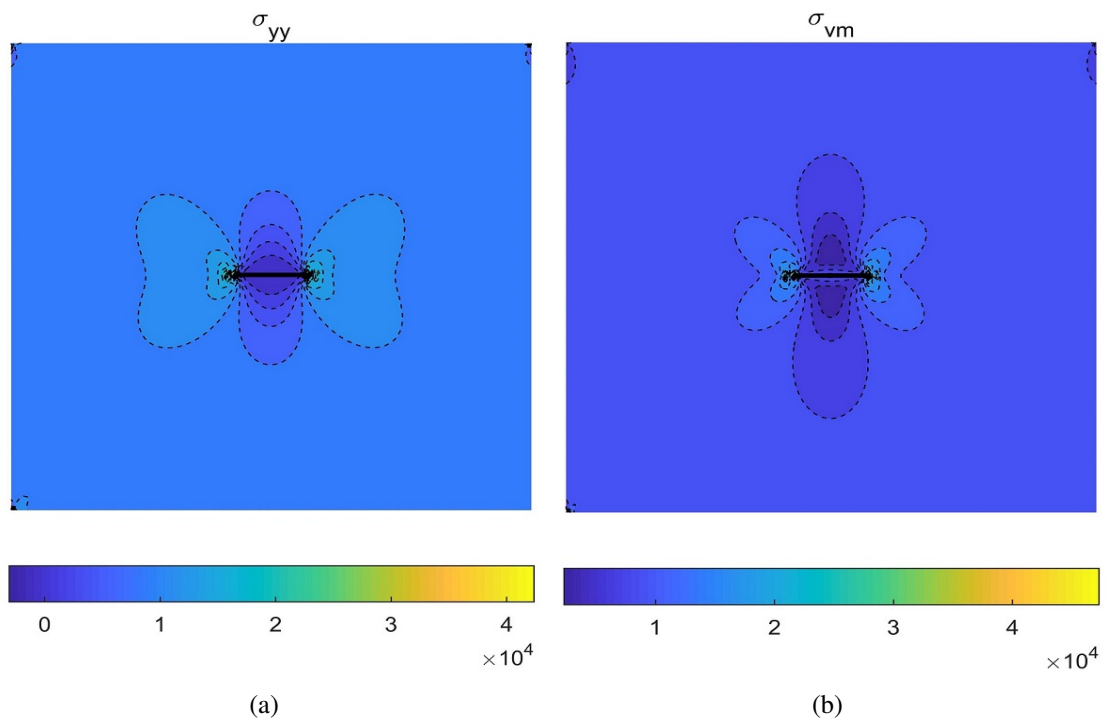


Fig. 3.15 Stress contour of components σ_{yy} and Von Mises value σ_{vm}

The code in MATLAB is verified by a simple benchmark study. With finite size modifications, the results of the numerical simulations are confirmed by the theoretical stress intensity factor.

3.3.2 Tilting angle in biaxial loading

In reality, we have the defect with a tilting angle and the membrane is under the biaxial tension state according to the experiments [8, 84] which means that the crack is under mixed mode loading. We again fix $W = H = 4$ and take $\Delta x = \Delta y = 1/128$.

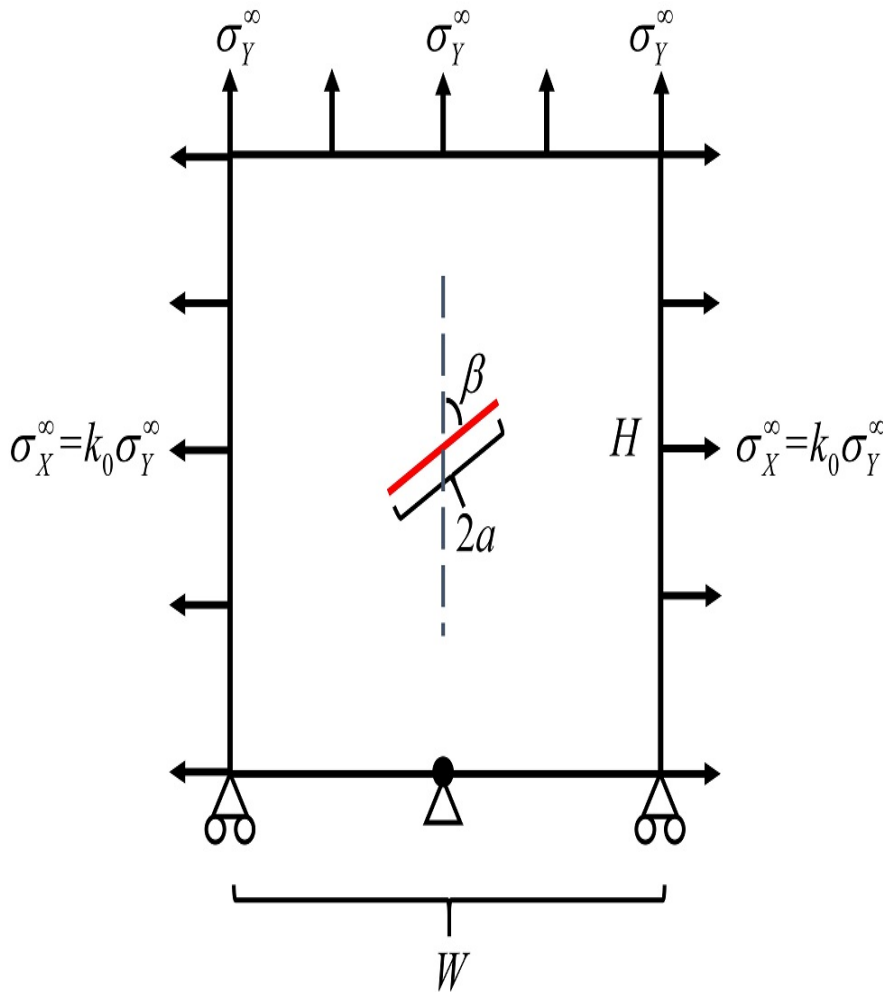


Fig. 3.16 Sketch of mixed mode crack opening with tilting angle $\delta\beta = \pi/2 - \beta$ and biaxial loading parameter k_0

In the following we will calculate the crack shape and stress distribution in two states: pure angle change of $\beta < 90^\circ$ in uniaxial loading with $k_0 = 0$ and tilting effect $\beta < 90^\circ$ in biaxial loading with $k_0 > 0$. First we increase $\delta\beta$ as $2^\circ, 5^\circ$ and 10° . Then for $\delta\beta = 5^\circ$ and $\delta\beta = 10^\circ$ respectively, we add the force in the X direction with $k_0 = 0.2, 0.5, 1.0$. The crack shape is described in blue. We provide the shape factor \mathcal{F} and stress intensity factors K_I, K_{II} of the mixed mode problem in each case. We use the MATLAB function `contourf(X, Y, Z, levels)` with 20

levels for the 2D stress contour plots in the undeformed configuration. The curve density and shape reflect the singularity near the crack tip and the solution in the total computational domain. In the experiment, we utilize the shape factor \mathcal{F} for the estimate of the far field stress perpendicular to the direction of laser cuts. This is our main concern in this part. We also provide the stress plots which might be useful for biologists. For example, the von Mises stress is connected with the plastic region. σ_{yy} is the most relevant component. We can see clearly from the contours how singularity decays with the radius. In this section, we neglect the crack growth as a simplification.

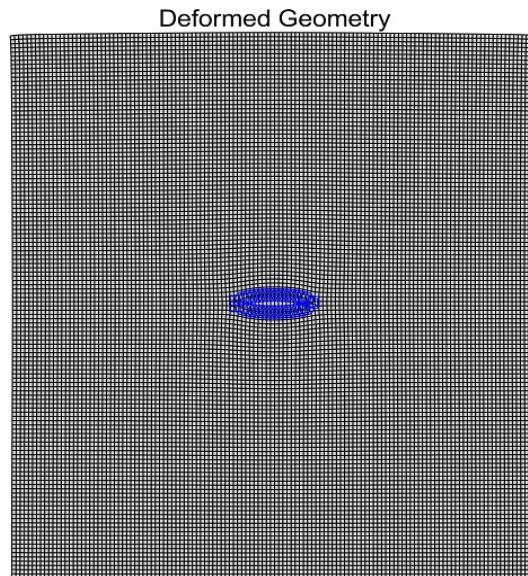


Fig. 3.17 $E = 10^5 \text{Pa}$, $\nu = 0.3$, $\sigma_Y^\infty = 10^4 \text{Pa}$, $\beta = 88^\circ$, $k_0 = 0$, $K_I^g \approx 9.83 \times 10^3 \text{Pa}\sqrt{\text{m}}$, $K_{II}^\beta \approx 0.34 \times 10^3 \text{Pa}\sqrt{\text{m}}$. Calculation results are $\mathcal{F} \approx 0.215$, $K_I^{comp} = 9.80 \times 10^3 \text{Pa}\sqrt{\text{m}}$, $K_{II}^{comp} = 0.32 \times 10^3 \text{Pa}\sqrt{\text{m}}$

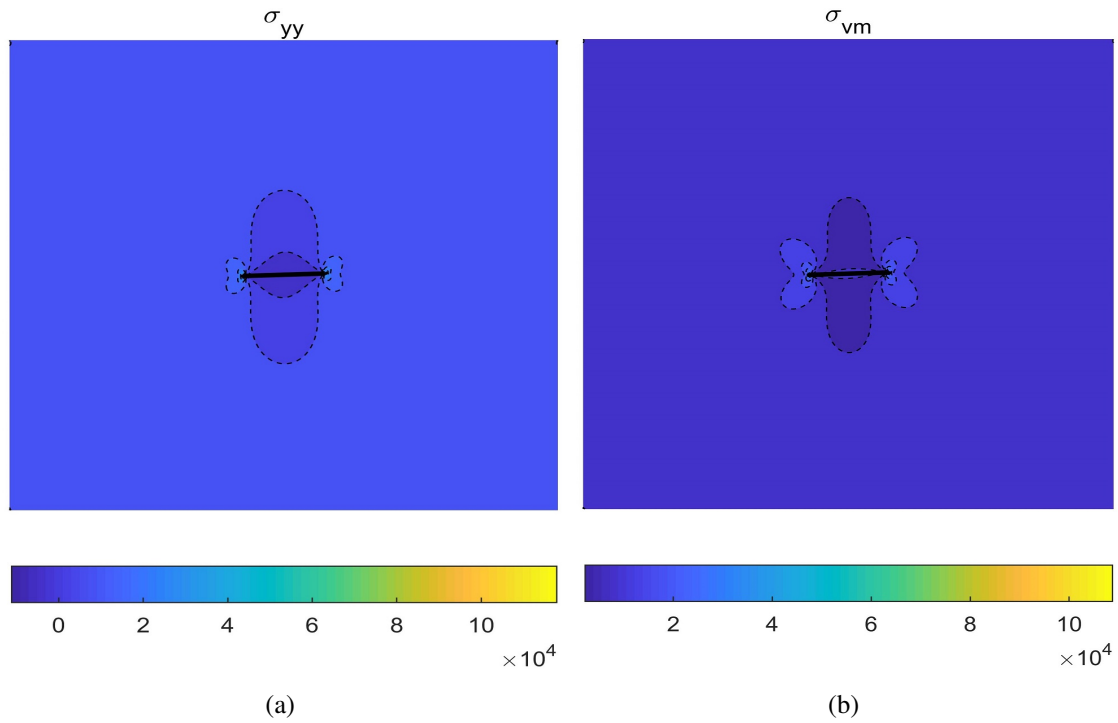


Fig. 3.18 Stress contour of components σ_{yy} and Von Mises value σ_{vm} with $\beta = 88^\circ$, $k_0 = 0$

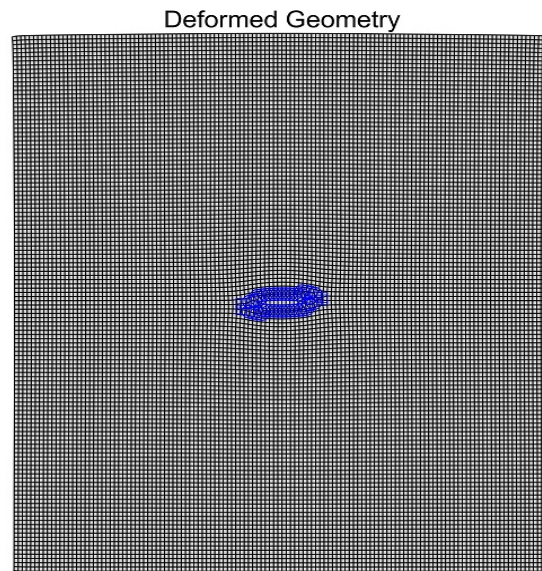


Fig. 3.19 $E = 10^5 \text{Pa}$, $\nu = 0.3$, $\sigma_Y^\infty = 10^4 \text{Pa}$, $\beta = 85^\circ$, $k_0 = 0$, $K_I^g \approx 9.77 \times 10^3 \text{Pa}\sqrt{\text{m}}$, $K_{II}^\beta \approx 0.85 \times 10^3 \text{Pa}\sqrt{\text{m}}$. Calculation results are $\mathcal{F} \approx 0.214$, $K_I^{comp} = 9.74 \times 10^3 \text{Pa}\sqrt{\text{m}}$, $K_{II}^{comp} = 0.85 \times 10^3 \text{Pa}\sqrt{\text{m}}$

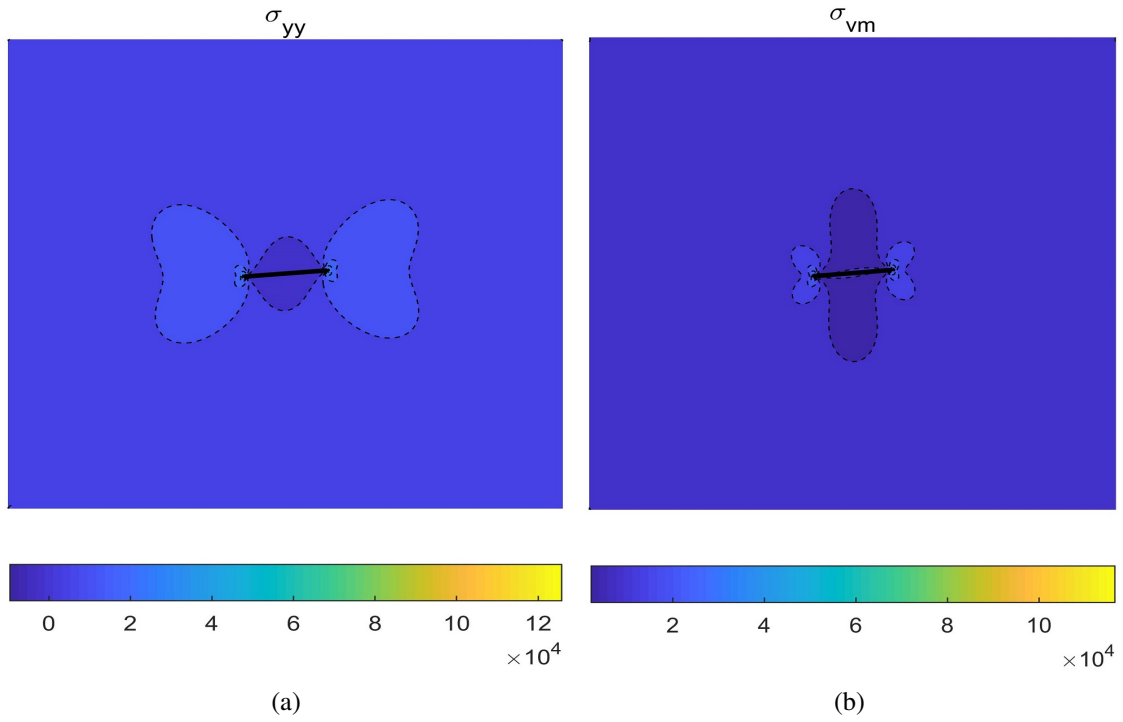


Fig. 3.20 Stress contour of components σ_{yy} and Von Mises value σ_{vm} with $\beta = 85^\circ$, $k_0 = 0$

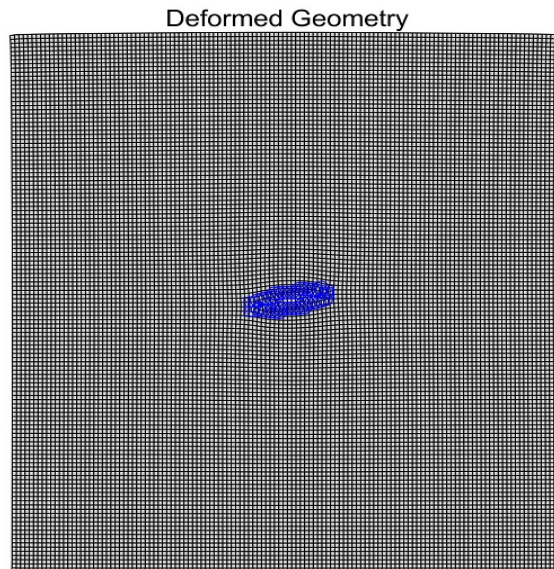


Fig. 3.21 $E = 10^5 \text{Pa}$, $\nu = 0.3$, $\sigma_Y^\infty = 10^4 \text{Pa}$, $\beta = 80^\circ$, $k_0 = 0$, $K_I^g \approx 9.55 \times 10^3 \text{Pa}\sqrt{\text{m}}$, $K_{II}^\beta \approx 1.68 \times 10^3 \text{Pa}\sqrt{\text{m}}$. Calculation results are $\mathcal{F} \approx 0.207$, $K_I^{comp} = 9.58 \times 10^3 \text{Pa}\sqrt{\text{m}}$, $K_{II}^{comp} = 1.69 \times 10^3 \text{Pa}\sqrt{\text{m}}$

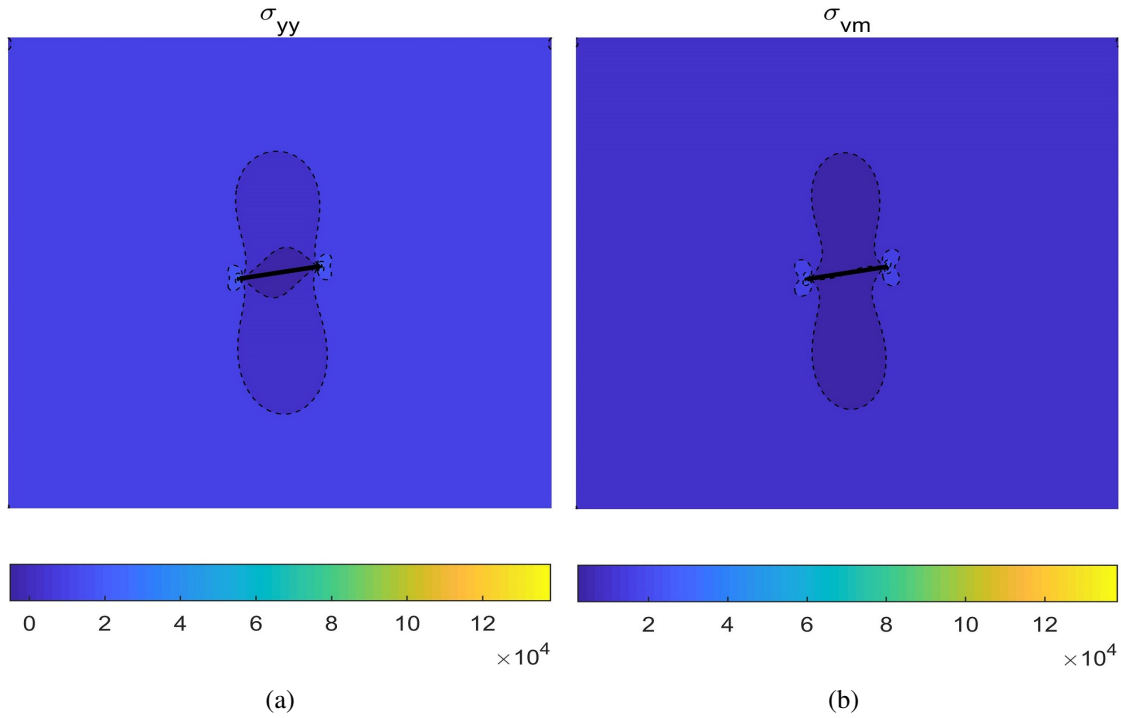


Fig. 3.22 Stress contour of components σ_{yy} and Von Mises value σ_{vm} with $\beta = 80^\circ$, $k_0 = 0$

From Fig.(3.17) to Fig.(3.22), we find that the crack factor \mathcal{F} decreases slightly compared to the theoretical value $\mathcal{F} = 0.2$. Mixed mode crack opening happens as expected with a rising value of K_{II} . We notice the dark region in σ_{yy} and σ_{vm} which reflects the small-stress area. Compare the results for different tilting angles, we find that the domain expands along the y direction. For the small tilting angle $\delta\beta \leq 10^\circ$ which is observed in the experiment [8], the simulation with given parameters prove the validity of our modified formula with respect to \mathcal{F} . The stress distribution almost keeps its symmetry despite the rotation of singularity tips. The affected area of the local stress state due to the cut is described by contour plots.

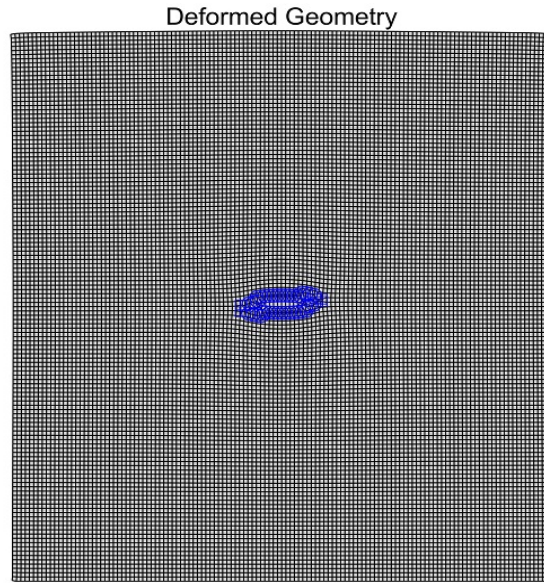


Fig. 3.23 $E = 10^5 \text{Pa}$, $\nu = 0.3$, $\sigma_Y^\infty = 10^4 \text{Pa}$, $\beta = 85^\circ$, $k_0 = 0.2$, $K_I^g \approx 9.78 \times 10^3 \text{Pa}\sqrt{\text{m}}$, $K_{II}^\beta \approx 0.68 \times 10^3 \text{Pa}\sqrt{\text{m}}$. Calculation results are $\mathcal{F} \approx 0.205$, $K_I^{comp} = 9.76 \times 10^3 \text{Pa}\sqrt{\text{m}}$, $K_{II}^{comp} = 0.68 \times 10^3 \text{Pa}\sqrt{\text{m}}$

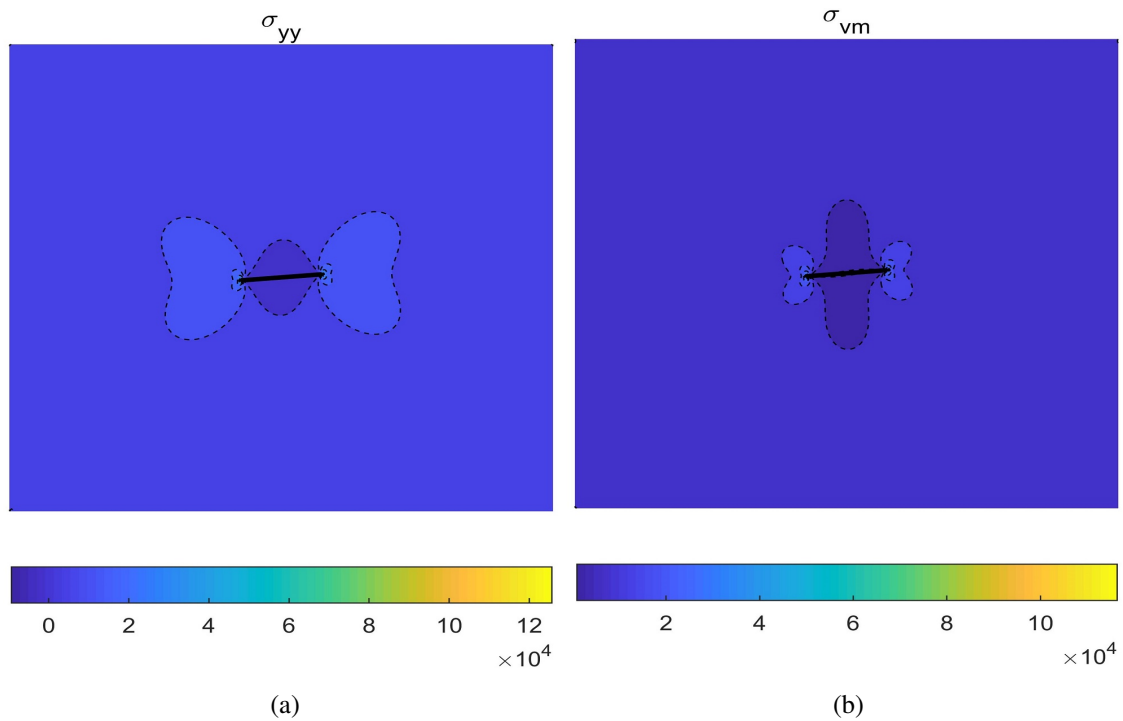


Fig. 3.24 Stress contour of components σ_{yy} and Von Mises value σ_{vm} with $\beta = 85^\circ$, $k_0 = 0.2$

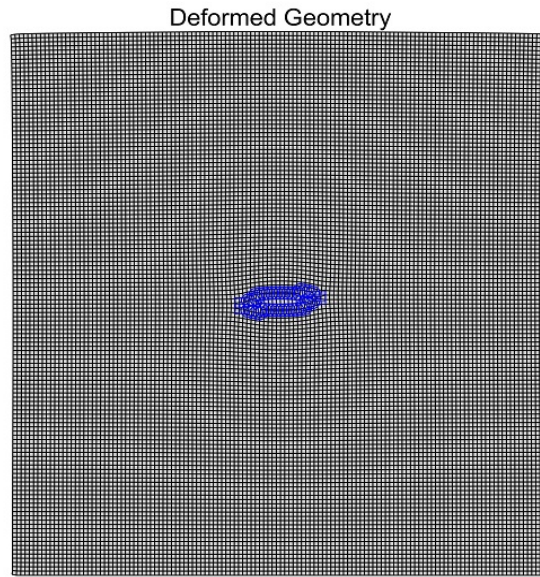


Fig. 3.25 $E = 10^5 \text{Pa}$, $\nu = 0.3$, $\sigma_Y^\infty = 10^4 \text{Pa}$, $\beta = 85^0$, $k_0 = 0.5$, $K_I^g \approx 9.81 \times 10^3 \text{Pa}\sqrt{\text{m}}$, $K_{II}^\beta \approx 0.43 \times 10^3 \text{Pa}\sqrt{\text{m}}$. Calculation results are $\mathcal{F} \approx 0.201$, $K_I^{\text{comp}} = 9.78 \times 10^3 \text{Pa}\sqrt{\text{m}}$, $K_{II}^{\text{comp}} = 0.42 \times 10^3 \text{Pa}\sqrt{\text{m}}$

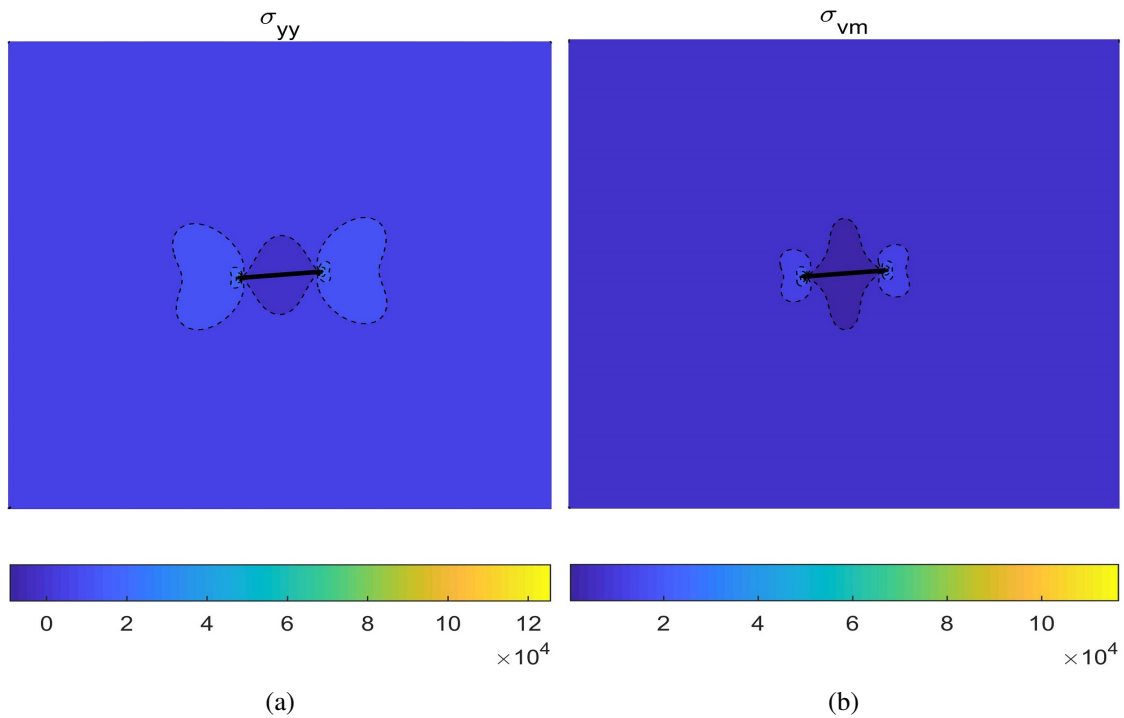


Fig. 3.26 Stress contour of components σ_{yy} and Von Mises value σ_{vm} with $\beta = 85^0$, $k_0 = 0.5$

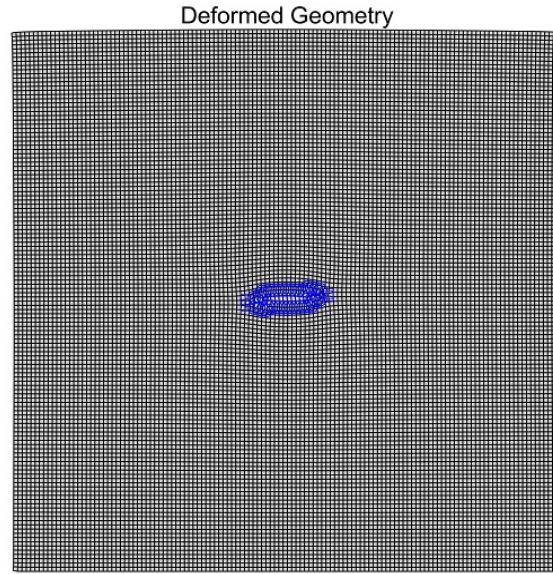


Fig. 3.27 $E = 10^5 \text{Pa}$, $\nu = 0.3$, $\sigma_Y^\infty = 10^4 \text{Pa}$, $\beta = 85^\circ$, $k_0 = 1.0$, $K_I^g \approx 9.85 \times 10^3 \text{Pa}\sqrt{\text{m}}$, $K_{II}^\beta \approx 0 \text{Pa}\sqrt{\text{m}}$. Calculation results are $\mathcal{F} \approx 0.186$, $K_I^{comp} = 9.82 \times 10^3 \text{Pa}\sqrt{\text{m}}$, $K_{II}^{comp} = -7 \times 10^{-3} \text{Pa}\sqrt{\text{m}}$

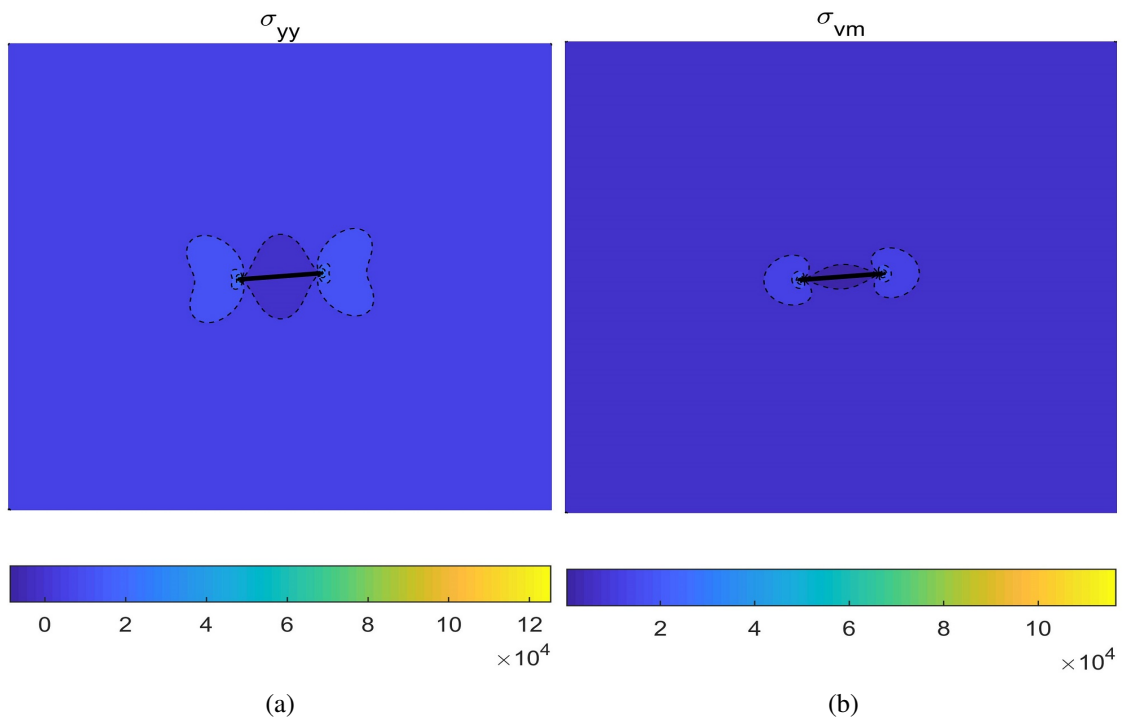


Fig. 3.28 Stress contour of components σ_{yy} and Von Mises value σ_{vm} with $\beta = 85^\circ$, $k_0 = 1.0$

With a fixed small angle $\delta\beta = 5^\circ$, the shape factor \mathcal{F} decreases as k_0 increases. Because of

finite strain, the stretch along the crack will increase the displacement of the tips, which is not considered by our formula. The stress distribution σ_{yy} does not change too much with the loading along the x direction. But the large-stress domain grows with the external stretch.

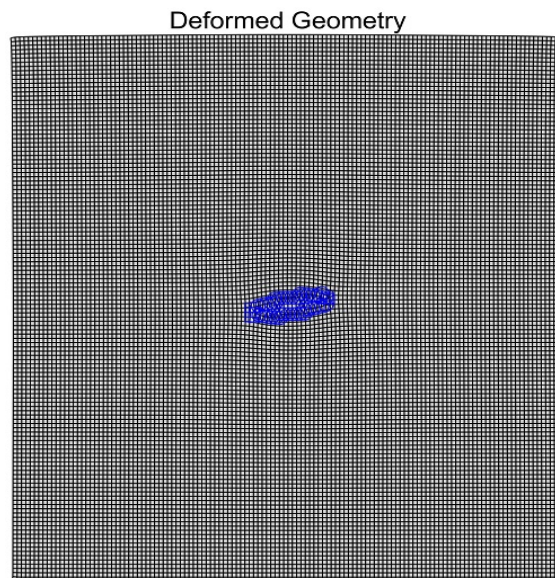


Fig. 3.29 $E = 10^5 \text{Pa}$, $\nu = 0.3$, $\sigma_Y^\infty = 10^4 \text{Pa}$, $\beta = 80^0$, $k_0 = 0.2$, $K_I^g \approx 9.61 \times 10^3 \text{Pa}\sqrt{\text{m}}$, $K_{II}^\beta \approx 1.35 \times 10^3 \text{Pa}\sqrt{\text{m}}$. Calculation results are $\mathcal{F} \approx 0.204$, $K_I^{comp} = 9.64 \times 10^3 \text{Pa}\sqrt{\text{m}}$, $K_{II}^{comp} = 1.34 \times 10^3 \text{Pa}\sqrt{\text{m}}$

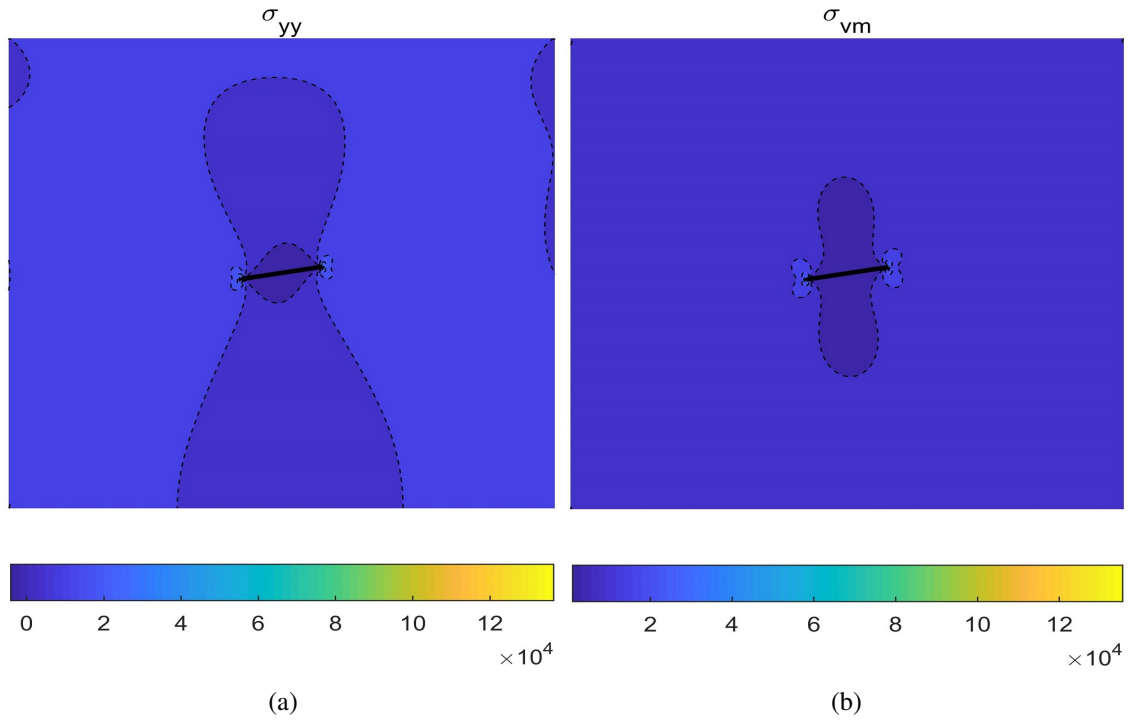


Fig. 3.30 Stress contour of components σ_{yy} and Von Mises value σ_{vm} with $\beta = 80^0$, $k_0 = 0.2$

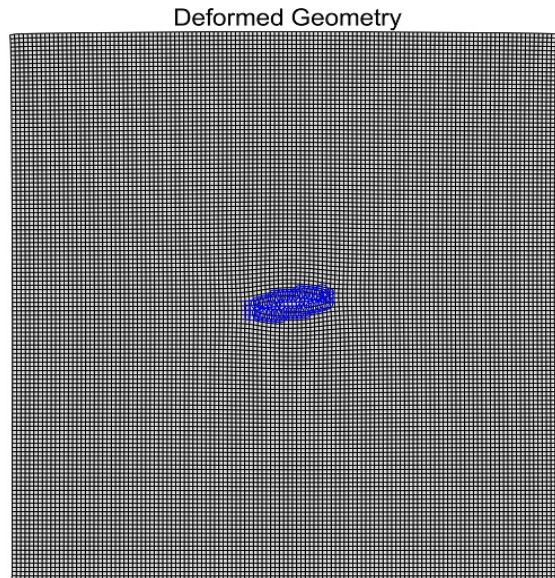


Fig. 3.31 $E = 10^5 \text{Pa}$, $\nu = 0.3$, $\sigma_Y^\infty = 10^4 \text{Pa}$, $\beta = 80^0$, $k_0 = 0.5$, $K_I^g \approx 9.70 \times 10^3 \text{Pa}\sqrt{\text{m}}$, $K_{II}^\beta \approx 0.84 \times 10^3 \text{Pa}\sqrt{\text{m}}$. Calculation results are $\mathcal{F} \approx 0.202$, $K_I^{comp} = 9.73 \times 10^3 \text{Pa}\sqrt{\text{m}}$, $K_{II}^{comp} = 0.82 \times 10^3 \text{Pa}\sqrt{\text{m}}$

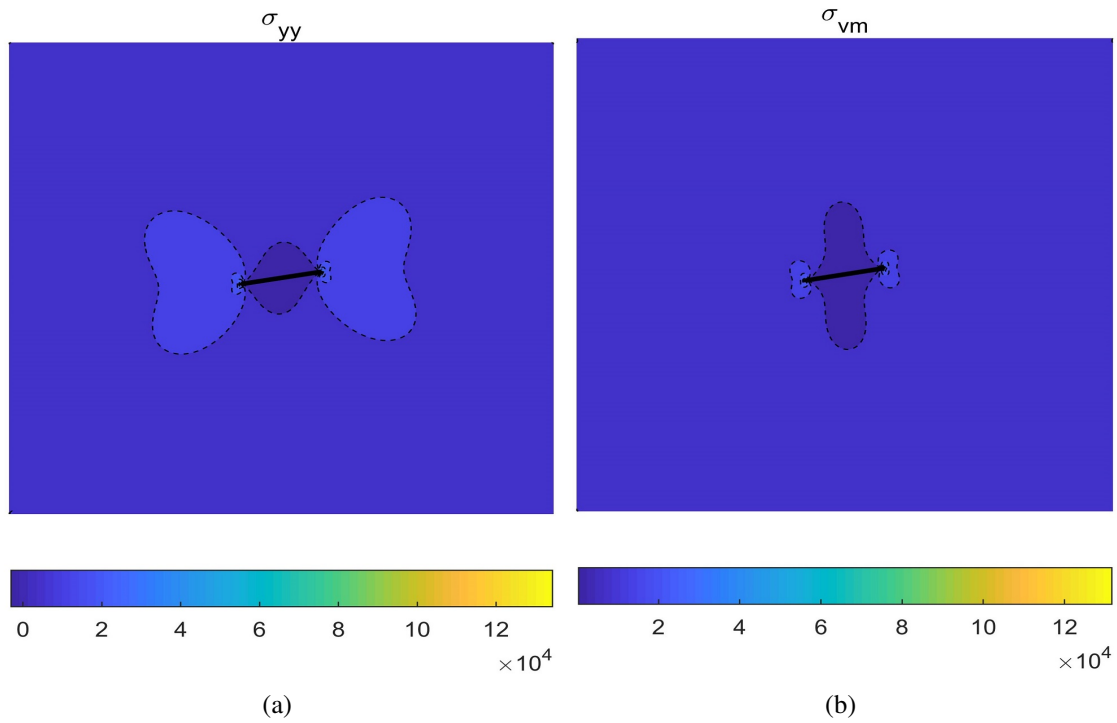


Fig. 3.32 Stress contour of components σ_{yy} and Von Mises value σ_{vm} with $\beta = 80^0$, $k_0 = 0.5$

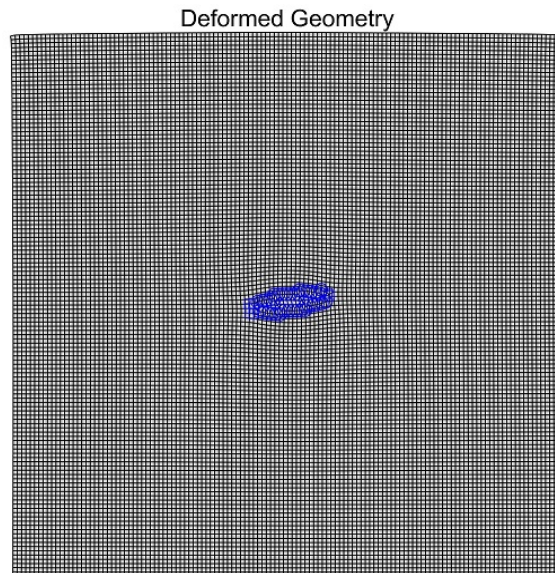


Fig. 3.33 $E = 10^5 \text{Pa}$, $\nu = 0.3$, $\sigma_Y^\infty = 10^4 \text{Pa}$, $\beta = 80^0$, $k_0 = 1.0$, $K_I^g \approx 9.85 \times 10^3 \text{Pa}\sqrt{\text{m}}$, $K_{II}^\beta \approx 0 \text{Pa}\sqrt{\text{m}}$. Calculation results are $\mathcal{F} \approx 0.189$, $K_I^{comp} = 9.88 \times 10^3 \text{Pa}\sqrt{\text{m}}$, $K_{II}^{comp} = 7.8 \times 10^{-3} \text{Pa}\sqrt{\text{m}}$

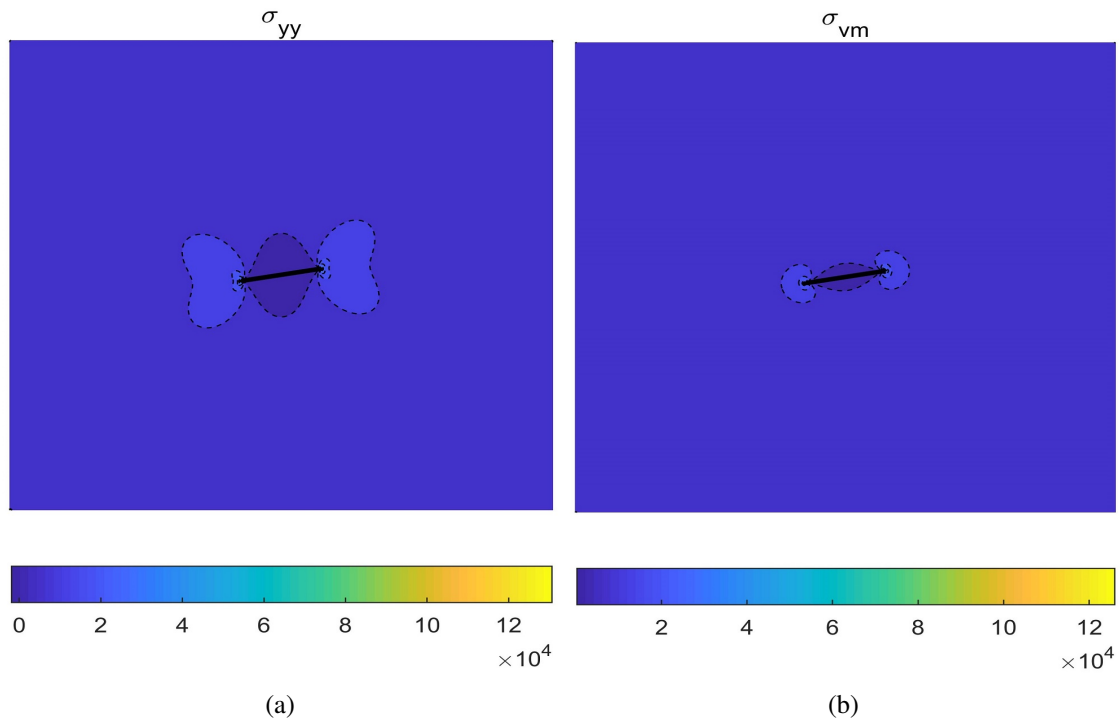


Fig. 3.34 Stress contour of components σ_{yy} and Von Mises value σ_{vm} with $\beta = 80^\circ$, $k_0 = 1.0$

Now we compare the figure groups Fig.(3.23 to 3.28) and Fig.(3.29 to 3.34). First, the shape factor is almost the same with given parameters and boundary conditions. Second, the stress intensity factors K_I and K_{II} satisfy Eq.(3.27) with the same geometric modification Eq.(3.46) for finite size. Last but not least, the stress contours of σ_{yy} and σ_{vm} are also quite similar when $k_0 = 0.5, 1.0$. Biaxial loading will decrease the effect of the crack orientation when $\delta\beta \leq 10^\circ$. In conclusion, our modified formula works in all situations above. But the local stress distribution depends on the angle change and loading condition.

3.4 Conclusion

In this chapter, a modified crack opening factor is suggested by substituting the original Young's modulus in the linear instance with an equivalent one from the tangent stiffness matrix. The tilting angle of a crack under biaxial loading is considered. Stress intensity factors and the crack opening factor are acquired by both theoretical and numerical methods. For a tilting angle $\delta\beta \leq 10^\circ$ and biaxial loading $k_0 \leq 1$, formula $\mathcal{F}_\alpha = 2\sigma_\alpha/E_\alpha$, Eq.(3.31), gives a relatively accurate estimate. For finite size with irregular geometry, XFEM could help us recognize the displacement and stress distribution even in anisotropic systems. Results in Fig.(3.9) demonstrate that active stress is of the same order as the passive one during *C. elegans* elongation which could explain the crack opening in both orthogonal directions in the experiment. Laser ablation technique is verified as a powerful tool for biologists for tissue scale mechanical measurement.

In this part, we have employed finite elasticity with fracture mechanics to deal with our biological problem. We have given a theoretical analysis for the deformation of *C. elegans* elonga-

tion. We have also provided the stress-strain relationship in consideration of the active network in the seam cells. Finally we have derived a simple formula for a stress estimate by laser ablation. Theoretical and numerical solutions explain the experimental results very convincingly.

Part II

Buckling of *Drosophila* wing disc

We study the buckling of the *Drosophila* wing disc by nonlinear elasticity. We model the system as a bilayer composed of a soft substrate and a stiffer and thinner extracellular matrix (ECM). We find two deformation scales shown in Fig.(0.6). In this part, we focus on the bending at the tissue scale. Meanwhile, 3D solid finite element simulations are time-consuming for thin bilayers. So we choose two kinds of methods in chapter 4 and chapter 5 respectively. First we treat the bilayer structure as a whole slender plate in chapter 4 because both layers are still thin compared to other length scales. We use the homogenization method to get the equivalent monolayer equations with inner bending induced by growth and active networks. We discuss the 1D case and present an analytical solution. We find that an extra nonlinear term will break the symmetry of the buckling shape. We consider the defect of the ECM in the bending stiffness. Then we use COMSOL for 3D shell simulations. In chapter 5, we model the bilayer system as a 3D solid with nonlinear Euler beam elements. Geometrically nonlinear elasticity is considered in finite element simulations. Growth in beams and solids is included by inner stress. A platform in MATLAB is used for the simulations with a friendly interface for secondary development. Finally, we study 2D wrinkling and folding simulations with viscoelasticity.

Chapter 4

Bilayer Fvk model with growth

Growth of thin layers can explain the shape diversity observed in nature such as in flowers, leaves or algae. A decade ago, the formalism of a growing plate [125] has been established and has shown that inhomogeneous growth inside a thin layer may induce buckling, generating simultaneously the so-called Gaussian and the average curvature in the FvK equations. Whereas, many thin living objects are made of several layers which have varying elastic properties and also follow different rules of growth. The scope here is to extend the analysis from a single layer to a bilayer [126, 127] with distinct moduli and growth but remaining thin. Besides, we also consider the role of the extracellular matrix (ECM). Biologists can modify this layer which, in our case, changes the bending stiffness, growth and even active momentum in the model.

FvK equations are the preferred tool for us: assuming an initially planar plate, the order of magnitude of the vertical deflection ζ may be much larger than that of the thickness h of the plate but smaller compared with the horizontal length L . These restrictions concern also the bilayer specimen. We shall employ the same method in Chapter 1 to obtain governing equations for the thin bilayer plate in section (4.1) with discussion of the 1D case. We consider 3D simulations with complex geometry in section(4.2).

4.1 Governing equations with growth

In this section, we will derive the bilayer Fvk model with growth. Then we will introduce the bending contribution induced by bilayer growth and the active network. In order to determine the neutral surface for the equivalent monolayer model, we minimize the corresponding elastic energy in 1D. We also analyze the 1D case with the ECM defects and a new quadratic term.

We start from the elastic strain in finite deformation theory. According to the famous *Kroner-Lee* decomposition [128], the deformation gradient tensor \mathbf{F} results from both the elastic tensor \mathbf{A} and the inelastic growth part \mathbf{G} in a simple way:

$$\mathbf{F} = \mathbf{A}\mathbf{G} \quad (4.1)$$

When growth is relatively small, we can linearize the matrix as $G_{ij} \simeq \delta_{ij} + \tilde{g}_{ij}$ with $|\tilde{g}_{ij}| \ll 1$. And thus

$$\mathbf{A} = \mathbf{F}\mathbf{G}^{-1} \approx \mathbf{F}(\mathbf{I} - \tilde{\mathbf{g}}) \quad (4.2)$$

To calculate \mathbf{F} , we use the kinematic relations Eq.(1.32,1.33,1.34) and neglect higher order terms within the Fvk limit

The elastic strain tensor becomes

$$\begin{aligned} \mathbf{E} &= \frac{1}{2}(\mathbf{A}^T \mathbf{A} - \mathbf{I}) \Rightarrow \\ E_{ij} &\approx \frac{1}{2} \left(\frac{\partial u_i^0}{\partial x_j} + \frac{\partial u_j^0}{\partial x_i} - g_{ij} + \frac{\partial \zeta}{\partial x_i} \frac{\partial \zeta}{\partial x_j} \right) - \frac{\partial \zeta}{\partial x_\gamma} \tilde{g}_{\gamma 3} \delta_{3i} \delta_{3j} + \frac{1}{2} (u_j^1 \delta_{3i} + u_i^1 \delta_{3j}) \\ &\quad + \frac{Z - Z_n}{2} \left(\frac{\partial u_i^1}{\partial x_j} + \frac{\partial u_j^1}{\partial x_i} \right) \end{aligned} \quad (4.3)$$

where \mathbf{g} equals two times the symmetric part of the linearized growth tensor, i.e. $g_{ij} = (\tilde{g}_{ij} + \tilde{g}_{ji})$. This notation shall be used for the following discussion.

In this thesis within the Fvk limit, we use the homogenization method by taking the integral over the thickness and consider the difference in each layer as a kind of inner angular momentum or extra force on the neutral surface. Due to small but finite strain for such biological systems, we still apply Hooke's law. We also take the standard membrane hypothesis: $\sigma_{i3} = 0$ as we have demonstrated in the monolayer model. Then, for every layer, the in-plane stress-strain relation in the isotropic situation reads $\sigma_{\alpha\beta} = \frac{E}{1-\nu^2} ((1-\nu)\varepsilon_{\alpha\beta} + \nu\varepsilon_{\gamma\gamma}\delta_{\alpha\beta})$ where $\varepsilon_{\alpha\beta} = \varepsilon_{\alpha\beta}^0 + (Z - Z_n)\varepsilon_{\alpha\beta}^1$. With $E_{i3} = 0$, the first-order bending part (Eq.1.37) related to $\varepsilon_{\alpha\beta}^1$ becomes

$$U^1(x, y) \approx \left(-\frac{\partial}{\partial x}\zeta + g_{13}\right); \quad V^1(x, y) \approx \left(-\frac{\partial}{\partial y}\zeta + g_{23}\right) \quad (4.4)$$

So the zero and first order membrane strain are given by

$$\varepsilon_{\alpha\beta}^0 \approx \frac{1}{2} \left(\frac{\partial u_\alpha}{\partial x_\beta} + \frac{\partial u_\beta}{\partial x_\alpha} + \frac{\partial \zeta}{\partial x_\alpha} \frac{\partial \zeta}{\partial x_\beta} \right) - \frac{1}{2} g_{\alpha\beta}; \quad \varepsilon_{\alpha\beta}^1 \approx -\partial_{\alpha\beta}\zeta + \frac{1}{2} \left(\frac{\partial g_{\beta 3}}{\partial x_\alpha} + \frac{\partial g_{\alpha 3}}{\partial x_\beta} \right) = -\partial_{\alpha\beta}\zeta + \varepsilon_{\alpha\beta}^{1,g} \quad (4.5)$$

It is not difficult to obtain the Euler-Lagrange equations with growth as

$$\begin{aligned} \Delta D(\Delta\zeta - C_M) - \partial_\alpha(N_{\alpha\beta}\partial_\beta\zeta) + \partial_{\alpha\beta}M_{\alpha\beta}^g &= 0 \\ \frac{\partial}{\partial x_\beta} \left(\int \sigma_{\alpha\beta} dZ \right) &= \frac{\partial}{\partial x_\beta} (N_{\alpha\beta}) = 0 \end{aligned} \quad (4.6)$$

The first equation represents the out-of-plane bending equilibrium and the second one stands for the in-plane stress equilibrium with the following definitions

$$\begin{aligned} D &= \int \frac{E}{1-\nu^2} (Z - Z_n)^2 dZ \\ C_M &= \frac{1}{D} \int \frac{E}{1-\nu^2} (Z - Z_n)^2 \frac{\partial g_{\gamma 3}}{\partial x_\gamma} dZ \\ M_{\alpha\beta}^g &= - \int (Z - Z_n) \sigma_{\alpha\beta}^0 dZ \sim \int (Z - Z_n) \frac{E}{1-\nu^2} \left[(1-\nu) \frac{1}{2} g_{\alpha\beta} + \frac{1}{2} \nu g_{\gamma\gamma} \delta_{\alpha\beta} \right] dZ \end{aligned} \quad (4.7)$$

where $M_{\alpha\beta}^g$ is the inner angular momentum due to the growth gradient. We consider the bilayer with the volume set $\Omega = S_0(x, y) \times [-h_S, h_f]$. Here we set the coordinate system on the interface S_0 , which is a plane for the moment i.e. $Z = 0$. h_S is the thickness of the bottom layer (substrate) and h_f stands for the top one (film). We assume that these two layers connect each other, do not separate during the deformation and share the same Poisson coefficient.

The total free energy is the sum of the upper film and the lower substrate (without debonding surface energy [129]).

$$\mathcal{E} = \int_0^{h_f} dZ \int_{S_0(x,y)} \frac{1}{2} \sigma_{ij}^f \varepsilon_{ij}^f dx dy + \int_{-h_s}^0 dZ \int_{S_0(x,y)} \frac{1}{2} \sigma_{ij}^S \varepsilon_{ij}^S dx dy \quad (4.8)$$

On the binding surface $S_0(x, y)$, we have the continuity of the interface (at $Z = 0$)

$$\{U^+, V^+, \zeta^+\} = \{U^-, V^-, \zeta^-\} = \{U^0, V^0, \zeta\}(x, y) \quad (4.9)$$

The principle of minimum potential energy of a conservative system states

$$\delta\Pi = \delta\mathcal{E} - \int_{S_0} p \delta\zeta dS - \int_{\partial S_0} N_{\alpha\beta} n_\beta \delta u_\alpha dl - \int_{\partial S_0} \bar{Q}_\alpha \delta\zeta_\alpha dl - \int_{\partial S_0} \bar{M}_{\alpha\beta} \delta\zeta_{\alpha\beta} dl = 0 \quad (4.10)$$

Here p is the out-of-plane deflection force; \bar{Q} is the edge shear force and \bar{M} is the edge bending momentum on the boundary of S_0 . For the variation of \mathbf{u}^0 , we have the in-plane force equilibrium equation about the plate.

$$N_{\alpha\beta,\beta} = 0 ; N_{\alpha\beta} := \int \sigma_{\alpha\beta}^0 dZ = h_f \sigma_{\alpha\beta}^{0,f} + h_s \sigma_{\alpha\beta}^{0,S} \quad (4.11)$$

where we use $\int (Z - Z_n) \sigma_{\alpha\beta}^1 dZ = 0$ due to minimization of the potential energy which will later be presented by a 1D case study. We neglect the higher order bending terms in the classical Fvk limit.

In principle we can assume all kinds of boundary conditions for the degree of bending ζ . For a clamped membrane

$$\zeta = \zeta_{,\alpha} = 0 \quad (4.12)$$

And for a "free boundary", classically it reads with Kirchhoff conditions [130]

$$\bar{M}_{nn} = 0 ; \bar{Q}_n + \frac{\partial \bar{M}_{ns}}{\partial x_s} = 0 \quad (4.13)$$

where n and s are, respectively, the normal and tangent direction of the boundary. For simplification we just consider the main linear part of the boundary conditions.

4.1.1 Active momentum by ECM and initial curvatures

We could also reckon that the inner bending is induced by the ECM. As a simple implementation, we assume that the elastic curvature tensor equals

$$\kappa_{\alpha\beta}^e = \kappa_{\alpha\beta} - \kappa_{\alpha\beta}^a \quad (4.14)$$

where $\kappa_{\alpha\beta}^a$ is the momentum contribution by the active network. The bending energy with the Kirchhoff assumption reads

$$\mathcal{E}_{bend} = \frac{1}{2} D_{\alpha\beta\gamma\delta} (\kappa_{\alpha\beta} - \kappa_{\alpha\beta}^a) (\kappa_{\gamma\delta} - \kappa_{\gamma\delta}^a) ; \kappa_{\alpha\beta} = \zeta_{\alpha\beta} \quad (4.15)$$

Thus we can obtain the modified governing equations (see Eq.(4.7)) as

$$\begin{aligned} \Delta D(\Delta\zeta - C_M) - \partial_\alpha (N_{\alpha\beta} \partial_\beta \zeta) + \partial_{\alpha\beta} M_{\alpha\beta}^g &= \partial_{\alpha\beta} (D \kappa_{\alpha\beta}^a) \\ \frac{\partial}{\partial x_\beta} \left(\int \sigma_{\alpha\beta} dZ \right) &= \frac{\partial}{\partial x_\beta} (N_{\alpha\beta}) = 0 \end{aligned} \quad (4.16)$$

For the effect of an initially curved shape $w^0(x, y)$, we use the shallow shell approximation of chapter 1. The equations become

$$\begin{aligned} \Delta D(\Delta\zeta - C_M) - \partial_\alpha(N_{\alpha\beta}\partial_\beta\zeta) + \partial_{\alpha\beta}M_{\alpha\beta}^g &= \partial_{\alpha\beta}(D\kappa_{\alpha\beta}^a) + N_{\alpha\beta}\partial_{\alpha\beta}w^0 \\ \frac{\partial}{\partial x_\beta}\left(\int \sigma_{\alpha\beta}dZ\right) &= \frac{\partial}{\partial x_\beta}(N_{\alpha\beta}) = 0 \end{aligned} \quad (4.17)$$

Furthermore, we can use a term $p^{ag}(x, y)$ to combine the contribution of an active momentum and growth differences as

$$\begin{aligned} \Delta D(\Delta\zeta - C_M) - \partial_\alpha(N_{\alpha\beta}\partial_\beta\zeta) &= N_{\alpha\beta}\partial_{\alpha\beta}w^0 + p^{ag}(x, y) \\ p^{ag}(x, y) &= \partial_{\alpha\beta}(D\kappa_{\alpha\beta}^a - M_{\alpha\beta}^g) \\ \frac{\partial}{\partial x_\beta}\left(\int \sigma_{\alpha\beta}dZ\right) &= \frac{\partial}{\partial x_\beta}(N_{\alpha\beta}) = 0 \end{aligned} \quad (4.18)$$

While the governing equations are not closed with the unknown Z_n in Eq.(4.7). We have to make sure that our theory reduces to the composite Euler beam formulation with Kirchhoff hypothesis in 1D. Next we will discuss the 1D case and determine the neutral surface Z_n via a minimization of the strain energy.

4.1.2 Reduced 1D case with clamped boundary

We use Eq(4.8) and assume uniaxial deformation by taking $\sigma_{22}^0 = 0$ and $\varepsilon_{22}^1 = 0$. The free energy in 1D is then given by

$$\mathcal{E} = \int \frac{1}{2}\sigma^0\varepsilon^0 - (Z - Z_n)\sigma^0\left(\frac{d^2\zeta}{dx^2} - C_M\right) + \frac{E(Z - Z_n)^2}{2(1 - \nu^2)}\left(\frac{d^2\zeta}{dx^2} - C_M\right)^2 dZdS \quad (4.19)$$

where C_M is defined by Eq.(4.7).

The elastic strain components reduce to $\varepsilon^0 = \frac{dU^0}{dx} - g_{11} + \frac{1}{2}\left(\frac{d\zeta}{dx}\right)^2$; $\varepsilon^1 = -\frac{d^2\zeta}{dx^2} + \frac{dg_{13}}{dx}$ and the stress components of different orders tend to $\sigma^0 = E\varepsilon^0$; $\sigma^1 = \frac{E}{1 - \nu^2}\varepsilon^1$.

Next we minimize the elastic energy with constant Z_n

$$\frac{\delta\mathcal{E}}{\delta Z_n} = 0 \Rightarrow N\left(\frac{d^2\zeta}{dx^2} - C_M\right) - \left(\frac{d^2\zeta}{dx^2} - C_M\right)^2 \int_{-h_S}^{h_f} \frac{E}{1 - \nu^2}(Z - Z_n)dZ = 0 \quad (4.20)$$

where $N = \int \sigma^0 dZ = N_{11}$. To be consistent with the pure bending of the small-strain case, we take $\nu_f = \nu_S = \nu$ and

$$\int E(Z - Z_n)/(1 - \nu^2)dZ = 0 \quad (4.21)$$

which gives the bending stiffness for Eq.(4.6)

$$D = \frac{1}{12(1 - \nu^2)} \frac{E_f^2 h_f^4 + 4E_f E_S h_f^3 h_S + 6E_f E_S h_f^2 h_S^2 + 4E_f E_S h_f h_S^3 + E_S^2 h_S^4}{E_f h_f + E_S h_S} = \frac{1}{12(1 - \nu^2)} \tilde{D} \quad (4.22)$$

In addition, we can get the expression of $M_{\alpha\beta}^g$ in Eq.(4.7) since u, v, ζ are independent of Z .

We take the bending stiffness for the incompressible case as $D(\nu = 1/2) = D_{1/2} = \frac{1}{9}\tilde{D}$. The formula is verified by the composite beam theory with $D(\nu = 0) = D_0 = \frac{1}{12}\tilde{D}$ where $Z_n = \frac{E_f h_f^2 - E_S h_S^2}{2(E_f h_f + E_S h_S)}$ from Eq.(4.21) by taking the integral over the thickness from $-h_S$ to h_f .

Stress equilibrium gives a simple result in 1D as

$$N = \int E(Z)\varepsilon_0 dZ = N_{11} = Const. \quad (4.23)$$

Bending equilibrium now reads

$$\frac{d^2}{dx^2} \left(D \frac{d^2 \zeta}{dx^2} - D \frac{dg_{13}}{dx} \right) + \frac{d^2}{dx^2} M_{11}^g - N \frac{d^2 \zeta}{dx^2} = N w_{xx}^0 + p(x) \quad (4.24)$$

where

$$M_{11}^g = \int_{-h_S}^{h_f} \frac{E(Z - Z_n)}{1 - \nu^2} g_{11} dZ = \int_0^{h_f} \frac{E(Z - Z_n)}{1 - \nu^2} g_f dZ + \int_{-h_S}^0 \frac{E(Z - Z_n)}{1 - \nu^2} g_S dZ \quad (4.25)$$

For the moment we assume that each layer has uniform growth $g_{f,S}$, so M_{11}^g equals a constant in the bending equation but acts as an extra angular momentum on the boundary. And w_{xx}^0 is the initial curvature of the stripe by the shallow shell approximation.

With Eq.4.24 divided by E_S , we obtain the dimensionless equation as

$$\frac{d^2}{dx^2} \left(D^* \frac{d^2 \zeta}{dx^2} - D^* \frac{dg_{13}}{dx} \right) - N^* \frac{d^2 \zeta}{dx^2} = N^* w_{xx}^{0*} + p^*(x) \quad (4.26)$$

where the dimensionless bending stiffness D^* is

$$D^* = \frac{\eta_S^3}{12(1 - \nu^2)} \frac{\alpha^2 \beta^4 + 4\alpha \beta^3 + 6\alpha \beta^2 + 4\alpha \beta + 1}{\alpha \beta + 1} \quad (4.27)$$

with the following scaled quantities

$$\begin{aligned} \alpha &= E_f/E_S, \quad 0 < \alpha < 1 \\ \eta_f &= h_f/L, \quad 0 < \eta_f \ll 1 \\ \eta_S &= h_S/L, \quad 0 < \eta_S \ll 1 \\ \beta &= h_f/h_S = \eta_f/\eta_S \\ x &= x/L, \quad -1/2 \leq x \leq 1/2 \\ \zeta &= \zeta/L, \quad 0 \leq |\zeta| \leq |\zeta_0| \\ w^* &= w/L \\ N^* &= N_0/E_S L \\ p^* &= p/E_S \end{aligned} \quad (4.28)$$

Next we try to find the buckling solution with MATLAB and MANLAB in 1D [131]. We focus on buckling phenomena induced by the inner stress N due to growth in Eq.(4.23). Furthermore,

we take COMSOL [132] for the complicated situation in 3D. We employ Matlab to deal with the bending equation with constant growth in Eq.(4.25).

$$\frac{d^2}{dx^2}(D^* \frac{d^2\zeta}{dx^2}) - N^* \frac{d^2\zeta}{dx^2} = N^* w_{xx}^{0*} + p^*(x, g, N) \quad (4.29)$$

where p^* includes the active momentum and growth in Eq.(4.18) with the shear effect g_{13} from C_M in Eq.(4.7,4.26). Since the real bilayer system is not perfectly uniform and the inner membrane force N will also change the location of the neutral surface in Eq.(4.20), we attempt to take this into account in the next section.

4.1.3 Solution with nonlinear effects

In this section, we will describe the nonlinear effect stemming from the location change of the neutral surface Z_n with an analytical solution. We perturbate the neutral surface as $Z_n = Z_n + \epsilon_b h_f$. The dimensionless bending equation becomes

$$\frac{d^2}{dx^2}(D^* \frac{d^2\zeta}{dx^2}) + \frac{b^*}{2} \frac{d^2}{dx^2}(\frac{d\zeta}{dx})^2 + (-N^* + b^* w_{xx}^{0*}) \frac{d^2\zeta}{dx^2} = N^* w_{xx}^{0*} + p^* \quad (4.30)$$

where

$$b^* = -\frac{\epsilon_b}{2} \eta_S^2 (\alpha \beta^2 + \beta) \quad (4.31)$$

The change of Z_n induces a nonlinear term of order $O(b\zeta^2)$. We want to find an analytical solution to show the role of this nonlinear effect. With $dD/dx = 0, p(x) = 0, w^0 = 0$ as well as constant growth, the bending equilibrium is integrable as

$$D^* \frac{d^2\zeta}{dx^2} + \frac{b^*}{2} (\frac{d\zeta}{dx})^2 = N^* \zeta + Ax + B \quad (4.32)$$

where D^*, b^* are defined according to Eq.(4.27,4.31) and A, B are integral constants. Furthermore, we assume $\zeta(x)$ is an even function and thus we have $A = 0$. So we have the implicit analytical solution with $\zeta(\pm \frac{1}{2}) = \zeta'(\pm \frac{1}{2}) = 0$

$$(\frac{d\zeta}{dx})^2 = -\frac{2N^*\zeta_0}{b^*} \left(\frac{e^{-\frac{b^*}{D^*}\zeta} - 1}{e^{-\frac{b^*}{D^*}\zeta_0} - 1} - \frac{\zeta}{\zeta_0} \right) \geq 0, -1/2 \leq x \leq 1/2 \quad (4.33)$$

where N^* is supposed negative (compression stress to assure the right hand side is always positive), ζ_0 is the peak/valley deflection of the plate and it can be solved by $\zeta(0) = \zeta_0$. Finally we can get the solution with the integral of Eq.(4.33).

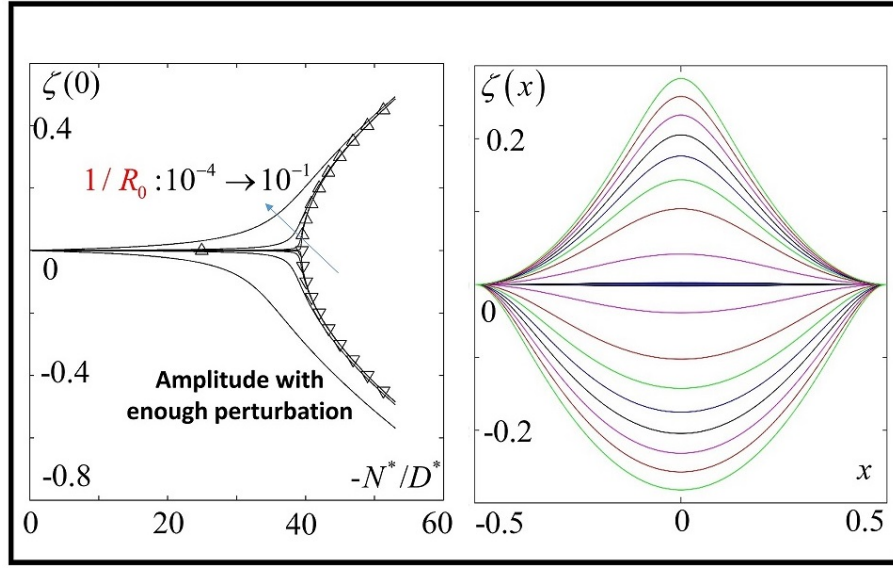


Fig. 4.1 Analytical solution with $\nu = 0.5, \alpha = 50, \eta_f = 0.0005, \eta_S = 0.01, \epsilon_b = 1, b^*/D^* \approx O(10)$: (a) bifurcation map (b) deflection shape of two branches with increasing N

Fig.(4.1) shows the bifurcation diagram (left) and the buckling shape of two branches (right) due to the nonlinear effect. ζ is the nondimensional deflection with $\zeta = \zeta/L$, x is the nondimensional position. $\zeta(0)$ is the peak value at the middle point $x = 0$. In order to increase the numerical convergence, we suppose $w_0 = -\delta(x - 0.5)(x + 0.5)$ with an initial curvature $1/R_0 \approx w_{xx}^{0*} = -2\delta$ where δ is a small quantity. There is a symmetry breaking due to the square term of ζ . But when ζ is not large, $\zeta(0) < 0.1$, one finds that the shapes of the two branches are quite similar. After we should consider defects of the extracellular matrix.

4.1.4 Solution with ECM defect

In the experiment, biologists can remove a part of the ECM during morphogenesis of the wing disc. In mechanics, this reduces the bending stiffness D directly in Eq.(4.22). We use the following form

$$\begin{aligned} D^*(x) &= D_0 - (D_0 - D_d) \exp \left[\epsilon_w (x - x_m)^2 / dw^2 \right] > 0 \\ b^*(x) &= b^* (1 - \exp \left[\epsilon_w (x - x_m)^2 / dw^2 \right]) \end{aligned} \quad (4.34)$$

where x_m is the position of the defect, dw reflects the removed length and we take $\epsilon_w \approx -10$ for this experimental formula. It is obvious that when $dw \rightarrow 0$, we have $D^* = D_0$. Near x_m , $D = D_d(E_S, h_S) > 0$ and far away from the defect domain, $D = D_0(E_f, h_f, E_S, h_S) > D_d$.

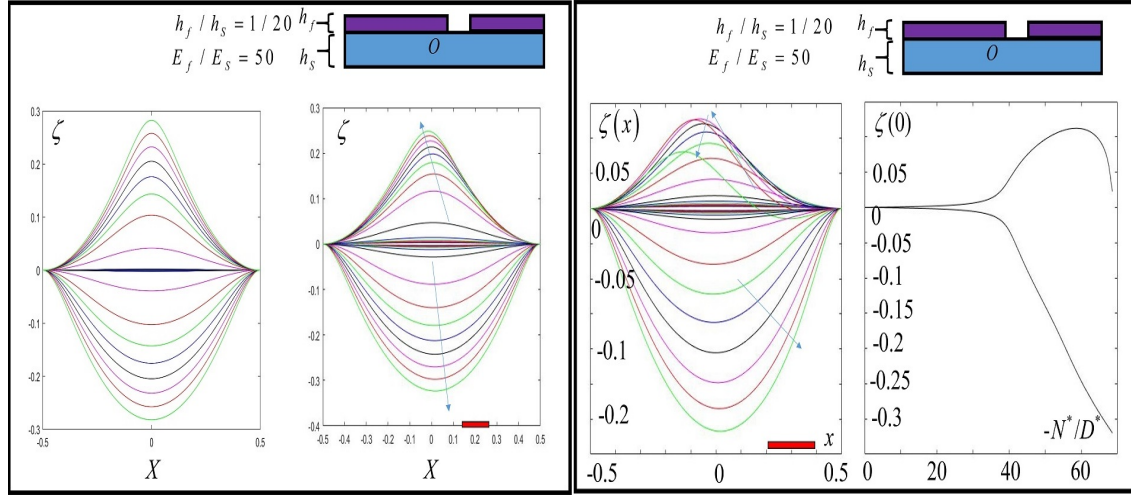
(a) ECM defect: $x_m = 0.2, dw = 0.1$ (b) ECM defect: $x_m = 0.3, dw = 0.2$

Fig. 4.2 Defects with $D(x)$. (a) Different buckling shapes between analytical solutions (left) and results in consideration of bending stiffness distribution (right); (b) buckling shapes and the bifurcation diagram with given parameters. Arrows point out the rise of the membrane force N induced by constant growth in Eq.(4.23)

In Fig.(4.2a), we remove the ECM near $x_m = 0.2$ with $dw = 0.1$. It does not change the shape of the solution compared with Fig.(4.1) but the position of the peak. In Fig.(4.2b), we take $x_m = 0.3$ and raise dw to 0.2. We find it generates a buckling mode shift for one branch. Moreover, there is an instability shown in the figure. We suppose a buckling shape controlled by growth together with the ECM defect.

In the following, we want to simplify the nonlinear effect by replacing it with a simple quadratic term.

4.1.5 Quadratic effect calculated in MANLAB

We substitute the nonlinear term referred to $(\frac{d\zeta}{dx})^2$ in Eq.(4.30) with ζ^2 in the toolbox MANLAB [131] for the calculation. The governing equation becomes

$$\frac{d^2}{dx^2}(D^* \frac{d^2\zeta}{dx^2}) - N^* \frac{d^2\zeta}{dx^2} = N^* w_{xx}^{0*} + k_1 \zeta + \frac{k_2}{2} \zeta^2 - N^* p(x) + p_0(x) \quad (4.35)$$

where k_2 is in our concern and k_1 behaves like a linear Winkler foundation [133]. $-Np(x)$ is a term proportional to growth, $p_0(x)$ is the initial deflection force and Nw_{xx}^{0*} reflects the effect of the initial curvature. We write the general model in MANLAB but we focus on the role of k_2 . After the finite difference procedure, the discrete governing equation can be generalized as a constant part L_0 , a linear operator $L(U)$ and a quadratic term $Q(U, U)$.

$$R(U) = L_0 + L(U) + Q(U, U) = 0$$

$$U = \begin{bmatrix} \zeta_i \\ N \\ \lambda \end{bmatrix} \quad (4.36)$$

where

$$\begin{aligned}
 L_0 &= \begin{bmatrix} -p_0(x_i) \\ 0 \end{bmatrix} \\
 L(\mathbf{U}) &= \begin{bmatrix} \frac{d^2}{dx^2} \left(D \frac{d^2}{dx^2} \zeta_i \right) - k_1 \zeta_i - \lambda p(x_i) \\ -N - \lambda \end{bmatrix} \\
 Q(\mathbf{U}) &= \begin{bmatrix} -N \frac{d^2}{dx^2} \zeta_i - \frac{k_2}{2} \zeta_i^2 \\ 0 \end{bmatrix}
 \end{aligned} \tag{4.37}$$

We use $D = 1$, $x = x/L$, $\zeta = \zeta/L$ to normalize the equation Eq.(4.35) with the ECM defect defined by Eq.(4.34). $p(x)$ is a force system for the test of the quadratic term ζ^2 with no significant physical meanings. With Eq.(4.36,4.37), $\lambda = -N$ is positive and it is assumed to be a continuous loading parameter in the buckling analysis. After we define $0 \leq x \leq 1$ and we take the deflection value at the middle point $\zeta(0.5)$ for the phase diagram. The results are as follows

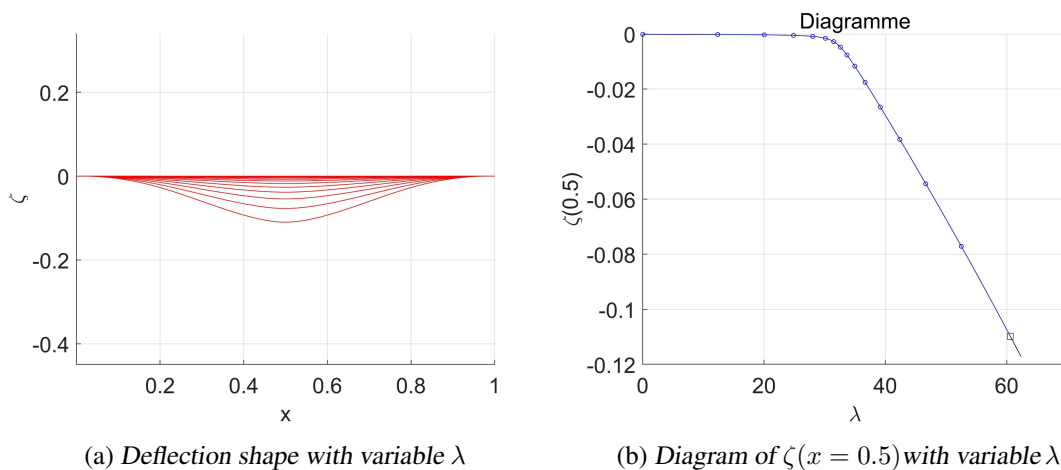


Fig. 4.3 Results with $D_0 = 1$, $D_d = 0.5$, $x_m = 0.5$, $dw = 0.2$, $k_1 = 0$, $k_2 = 10000$, $p(x) = 0$. (a) Buckling shape with ECM defect; (b) diagram with given parameters

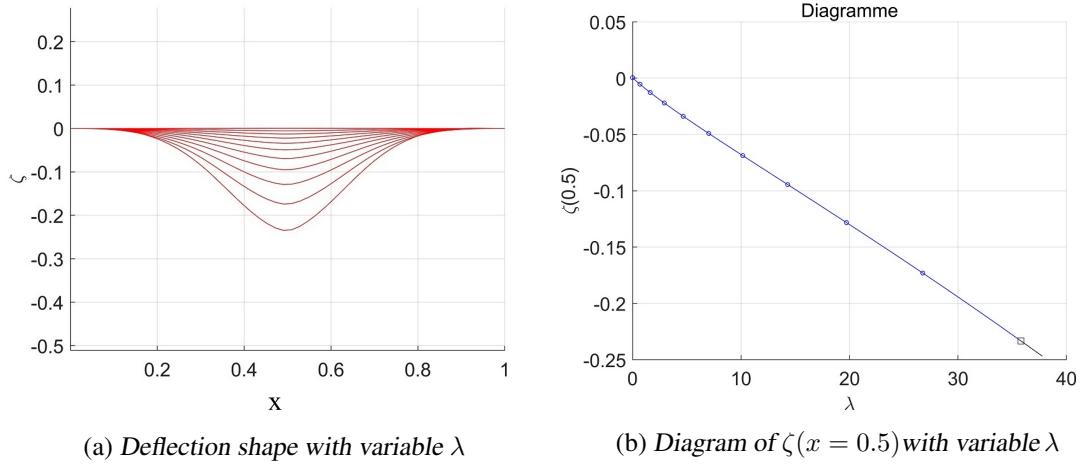


Fig. 4.4 Results with $D_0 = 1, D_d = 0.5, x_m = 0.5, dw = 0.1, k_1 = 0, k_2 = 10000, p(x) = 100\delta(0.5) - 100\delta(0.3) - 100\delta(0.7)$. (a) Buckling shape with ECM defect; (b) diagram with given parameters

In Fig.(4.3), we can see the buckling shape (one branch) and the diagram with the loading parameter λ versus deflection value at $x = 0.5$. There is a continuous phase transition with no external deflection force. In Fig.(4.4), phase transition disappears due to $p(x)$.

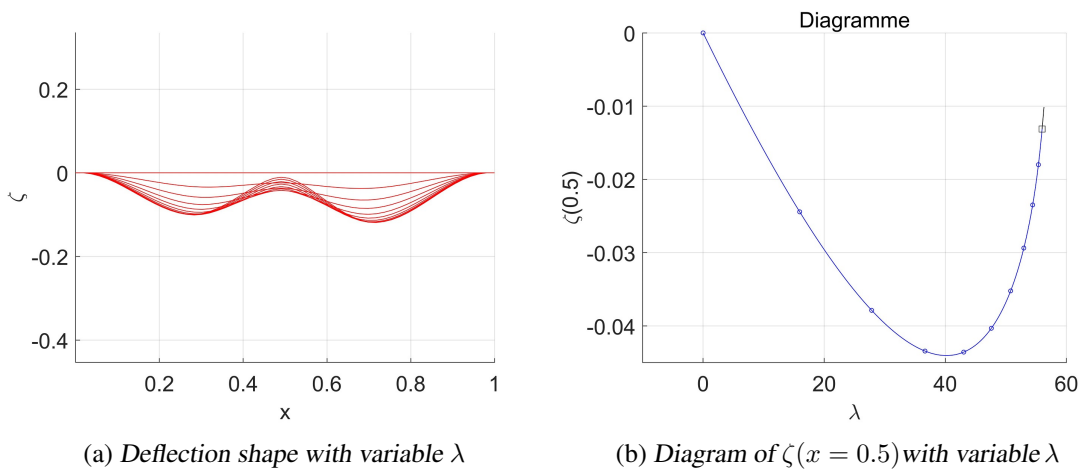


Fig. 4.5 Results with $D_0 = 1, D_d = 0.5, x_m = 0.5, dw = 0.2, k_1 = 0, k_2 = 10000, p(x) = 100\delta(0.5) - 100\delta(0.3) - 100\delta(0.7)$. (a) Buckling shape with ECM defect; (b) diagram with given parameters

We increase the defect area from $dw = 0.1$ in Fig.(4.4) to $dw = 0.2$ in Fig.(4.5). One observes shape change similar to Fig.(4.2). In addition, there is a critical point in Fig.(4.5b).

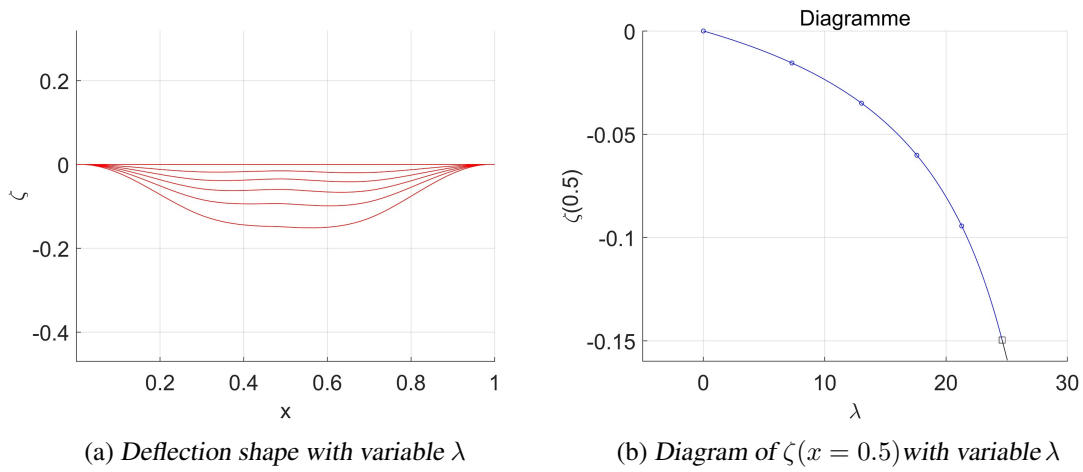


Fig. 4.6 Results with $D_0 = 1, D_d = 0.5, x_m = 0.5, dw = 0.2, k_1 = 0, k_2 = 100, p(x) = 100\delta(0.5) - 100\delta(0.3) - 100\delta(0.7)$. (a) Buckling shape with ECM defect; (b) diagram with given parameters

We then decrease the quadratic effect by k_2 in Fig.(4.6) compared to Fig.(4.5). We observe a different bending shape with loading.

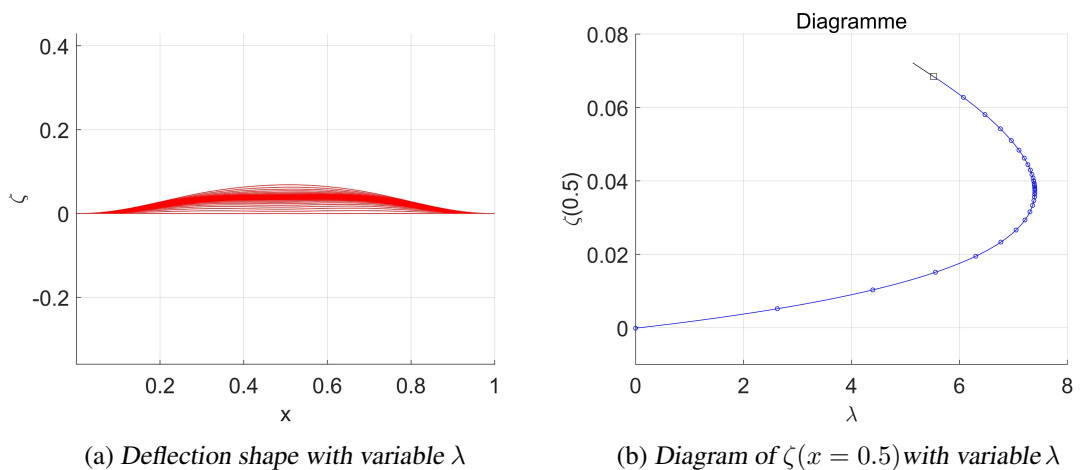


Fig. 4.7 Results with $D_0 = 1, D_d = 0.5, x_m = 0.5, dw = 0.2, k_1 = 0, k_2 = 10000, p(x) = -100\delta(0.5) + 100\delta(0.3) + 100\delta(0.7)$. (a) Buckling shape with ECM defect; (b) diagram with given parameters

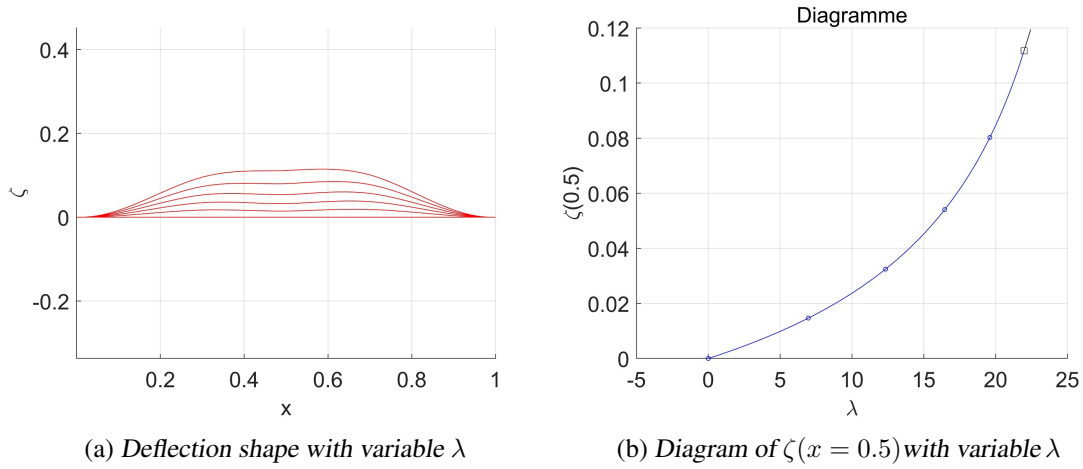


Fig. 4.8 Results with $D_0 = 1, D_d = 0.5, x_m = 0.5, dw = 0.2, k_1 = 0, k_2 = 100, p(x) = -100\delta(0.5) + 100\delta(0.3) + 100\delta(0.7)$. (a) Buckling shape with ECM defect; (b) diagram with given parameters

Finally we show the symmetry breaking due to k_2 . We compare Fig.(4.7,4.8) with Fig.(4.5,4.6). Difference increases as the rise of k_2 . In addition, we find an unstable point in Fig.(4.7).

In conclusion, the quadratic term associated to k_2 will break the symmetry of the solution like the nonlinear effect b^* in Eq.(4.32). Buckling shapes induced by growth with different parameters were found numerically by writing a self-defined class document in MANLAB. We have assumed constant growth in each layer in the calculation (see Eq.(4.25)). We will use the COMSOL shell to calculate more complicated situations referred to differential growth and complex geometry in 3D.

4.2 Numerical implementation in COMSOL

We employ the COMSOL shell [46, 134, 135] for 3D simulations referred to Eq.(4.18). First we will discuss the inner bending induced by growth and the active network in section(4.2.1). We then set up the geometry for a thin wing disc and add in-plane growth in section (4.2.2). Afterwards we consider the additional bilayer bending and the ECM defect in section(4.2.3) and (4.2.4). Finally, we introduce the nonlinear term in section (4.2.5).

COMSOL uses the SI unit system as default. Particularly, we use the unit [m] for the length scale. It does not change the strain and final deflection results during the simulations. But we should be careful about the loading.

4.2.1 Active bending with growth

First we imagine a bilayer plate with parameters in Fig.(4.9)

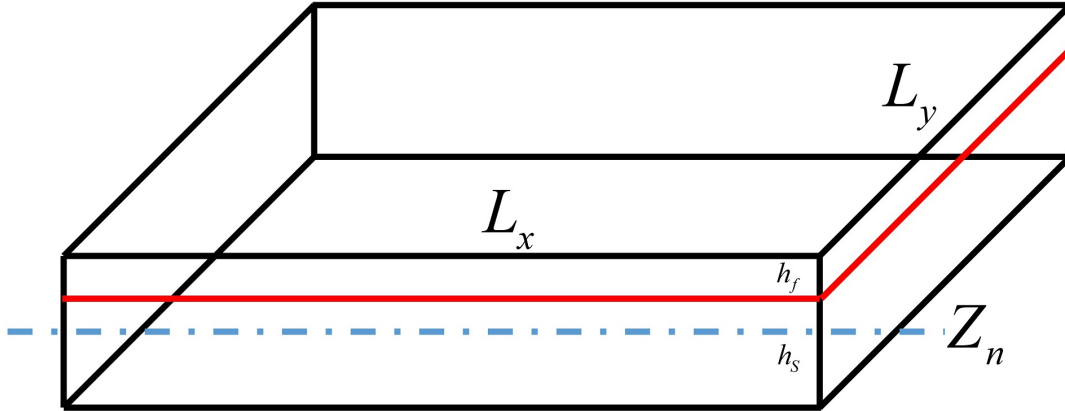


Fig. 4.9 Sketch of bilayer: $L_x = 1, L_y = 0.5, h_S = 0.01, h_f = h_S/20, E_S = 1\text{Kpa}, E_f = 50\text{Kpa}, \nu = 0.3, Z_n = -0.00125, D = 3 * 10^{-4}\text{Pa} \cdot \text{m}^3, \bar{E} = 2.9\text{Kpa}$

The coordinate system is set on the interface of two layers with $Z = 0$. The diagram also provides material parameters and geometry size.

We assume growth only in the soft substrate as $g_{\alpha\beta}^f = 0$ and neglect the membrane force with $N_{\alpha\beta} = 0$. Furthermore we take growth as a function of position $g_{\alpha\beta}^S(x, y)$. Then the governing equations Eq.(4.18) with definitions Eq.(4.7) read

$$\begin{aligned} \Delta D(\Delta\zeta - C_M) &= \partial_{\alpha\beta}(D\kappa_{\alpha\beta}^a - M_{\alpha\beta}^g) \\ M_{\alpha\beta}^g &= -\frac{1}{2}(h_S^2 + 2h_S Z_n) \frac{E_S}{1-\nu^2} \left[(1-\nu) \frac{1}{2} g_{\alpha\beta}^S + \frac{1}{2} \nu g_{\gamma\gamma}^S \delta_{\alpha\beta} \right] \end{aligned} \quad (4.38)$$

where the second equation can be deduced by taking the integral over the thickness from $-h_S$ to h_f . Moreover we assume a constant D and neglect the shear effect C_M , so we have

$$\begin{aligned} D\Delta\Delta\zeta &= D\Delta\Delta w^a + q_S^g \\ \partial_{\alpha\beta} w^a &= \kappa_{\alpha\beta}^a \\ q_S^g &= \frac{1}{2} \frac{E_S h_S^2}{1-\nu^2} \left(1 + 2 \frac{Z_n}{h_S} \right) \cdot \partial_{\alpha\beta} \left[(1-\nu) \frac{1}{2} g_{\alpha\beta}^S + \frac{1}{2} \nu g_{\gamma\gamma}^S \delta_{\alpha\beta} \right] \end{aligned} \quad (4.39)$$

We have to be careful about the definition of the growth tensor in Eq.(4.3) as $g_{\alpha\beta} = \tilde{g}_{\alpha\beta} + \tilde{g}_{\beta\alpha}$. If we assume $\tilde{g}_{12} = 0$ and $D = \frac{\bar{E}}{12(1-\nu^2)}$, we get the expression of q_S^g as

$$q_S^g = D \cdot \frac{6E_S h_S^2}{E h^3} \left(1 + 2 \frac{Z_n}{h_S} \right) [\partial_{xx} \tilde{g}_{11}^S + \partial_{yy} \tilde{g}_{22}^S + \nu(\partial_{xx} \tilde{g}_{22}^S + \partial_{yy} \tilde{g}_{11}^S)] \quad (4.40)$$

After we run simulations in COMSOL with the parameters of Fig.(4.9). We take $g_{\alpha\beta}^S = 0$ and $w^a(x) = x^2(1-x)^2$ leading to $\kappa_{11}^a = 12x^2 - 12x + 2$ with the following results.

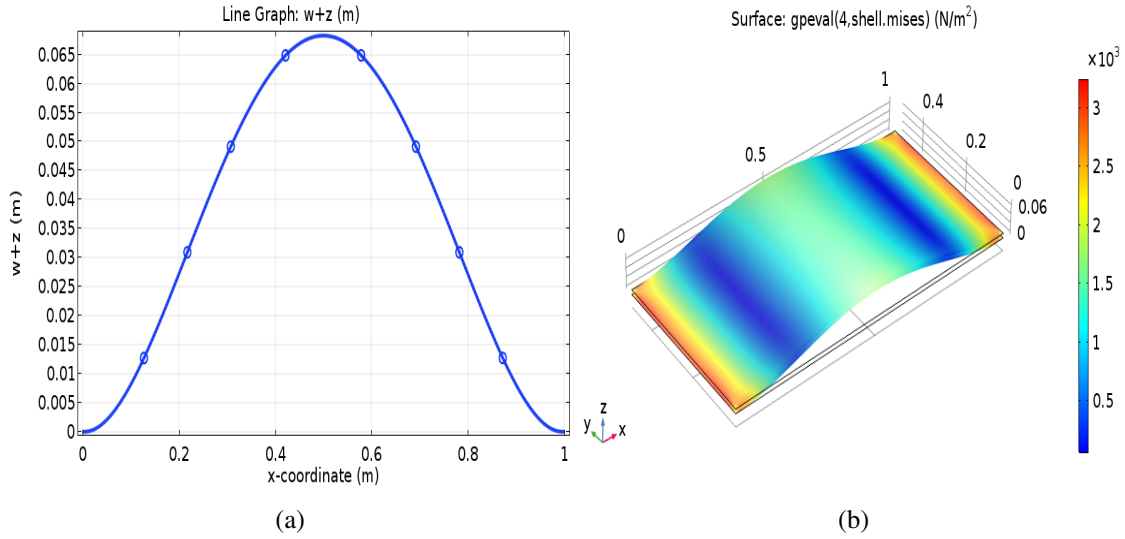


Fig. 4.10 Deformation by active bending in clamped-clamped boundary condition: (a) deflection curve: vertical displacement w versus x with $L_x = 1, L_y = 0.5$ in Fig.(4.9); (b) Von Mises stress contour

The deflection curve in Fig.(4.10a) meets well with the 1D approximation $\zeta \approx w^a = x^2(x - 1)^2$. Then we take $w^a = 0$ and $\tilde{g}_{11}^S = \delta \exp[-\gamma(x - x_m)^2]$ resulting in $q_S^g \sim \delta \exp[-\gamma(x - x_m)^2] * [4\gamma^2(x - x_m)^2 - 2\gamma]$.

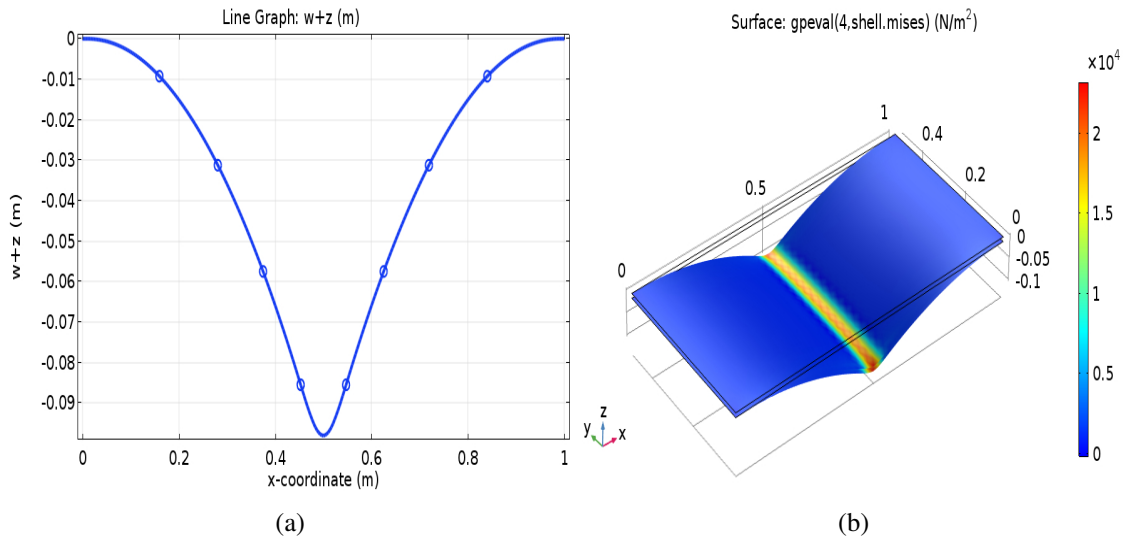


Fig. 4.11 Deformation by differential growth along the x axis in clamped-clamped boundary condition: $\delta = 0.1, \gamma = 1000, x_m = 0.5$ (a) deflection curve: vertical displacement w versus x with $L_x = 1, L_y = 0.5$ in Fig.(4.9); (b) Von Mises stress contour

In this case q_S^g behaves like a special force with an exponential rate γ . Both results in Fig.(4.10) and Fig.(4.11) demonstrate that global bending can be induced by active networks

and differential growth.

Then we add growth directly in the membrane strain with the linear decomposition $\varepsilon = \varepsilon^e + \varepsilon^{th}$ [88] which means that the total strain is composed of an elastic and an inelastic part. We focus on the buckling by in-plane loading. In the following simulations, we suppose that the thin ECM only contributes to the bending stiffness and active momentum.

4.2.2 Equivalent monolayer shell with in-plane growth

We simplify the real complex geometry of the wing disc as an ellipsoidal shell (see Fig.(4.12)). We assume the structure is very thin with in-plane expansion. The boundary is fixed. We want to use the bilayer plate/shell model to offer some predictions for the biological system.

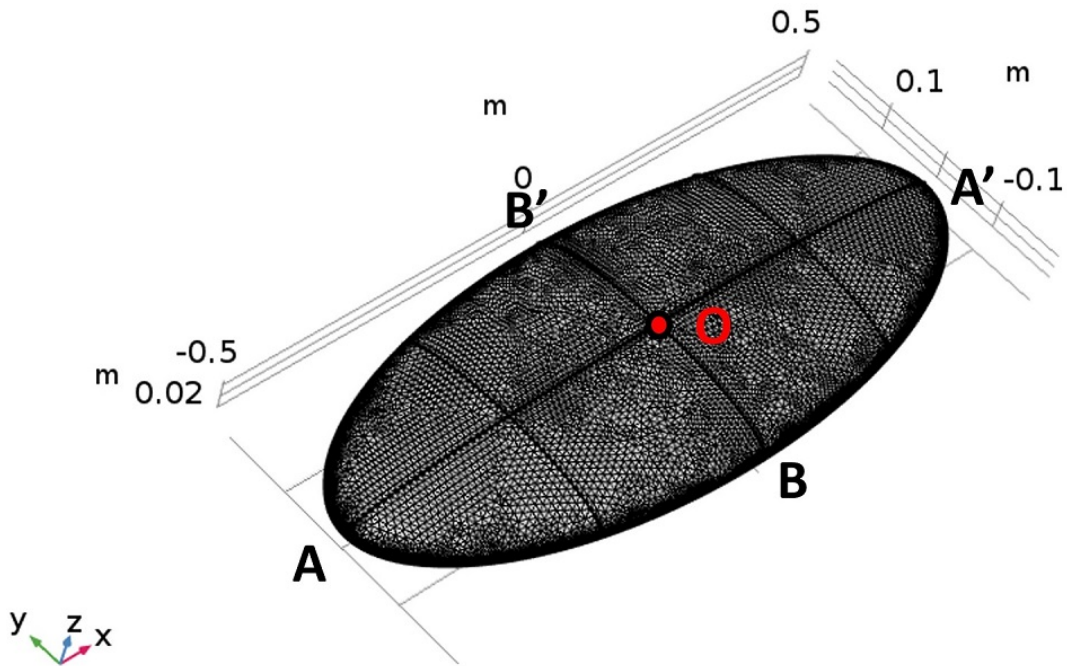


Fig. 4.12 Sketch of geometry in COMSOL: Ellipsoid surface $(\frac{x}{R_x})^2 + (\frac{y}{R_y})^2 + (\frac{z}{R_z})^2 = 1$, $-R_x \leq x \leq R_x$, $-R_y \leq y \leq R_y$, $z(x, y) \geq 0$ with $R_x = 0.5$, $R_y = 0.2$, $R_z = 0.05$ and thickness $d = 0.001$; $E = 1Kpa$, $\nu = 0.33$. Initially all boundaries are fixed.

After the homogenization process, we can set the equivalent Young's modulus and thickness for the shell and choose arbitrary functions respectively. In this section, we assume a uniform growth with a Gaussian distribution for the local difference as

$$\tilde{\varepsilon}_{\alpha\beta}^g = \begin{bmatrix} \varepsilon^{th}(x) & 0 \\ 0 & \varepsilon^{th}(x) \end{bmatrix} \quad (4.41)$$

$$\varepsilon^{th}(x) = \alpha^{th}(1 + \beta^{th} \exp[-\gamma^{th}(x - x_m)^2]) * \lambda^{th} \quad -R_x \leq x \leq R_x, 0 \leq \lambda^{th} \leq 1$$

where α^{th} is the value of uniform growth over the domain, β^{th} is the amplitude of extra growth, γ^{th} stands for the decay rate, x_m is the center of this gradient distribution and λ^{th} is the loading

parameter ranging from 0 to 1. Special attention is paid on the final buckling shape which is important for biology. We study how different deformation arises with the controlling parameters.

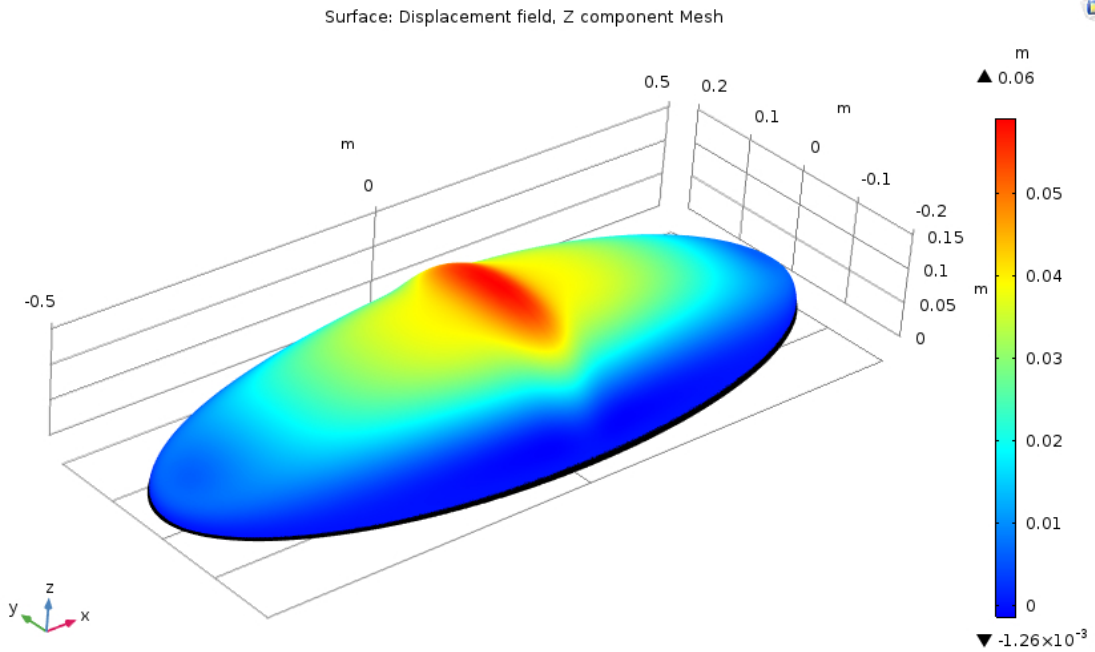


Fig. 4.13 Buckling shape with $x_m = 0, \alpha^{th} = 0.03, \beta^{th} = 1, \gamma^{th} = 1000, d = 0.001$

The in-plane growth of a thin shell can generate local buckling (see Fig.(4.13) with displacement contour). We set maximum growth $\alpha^{th} * (1 + \beta^{th}) = 6\%$ within the linear limit.

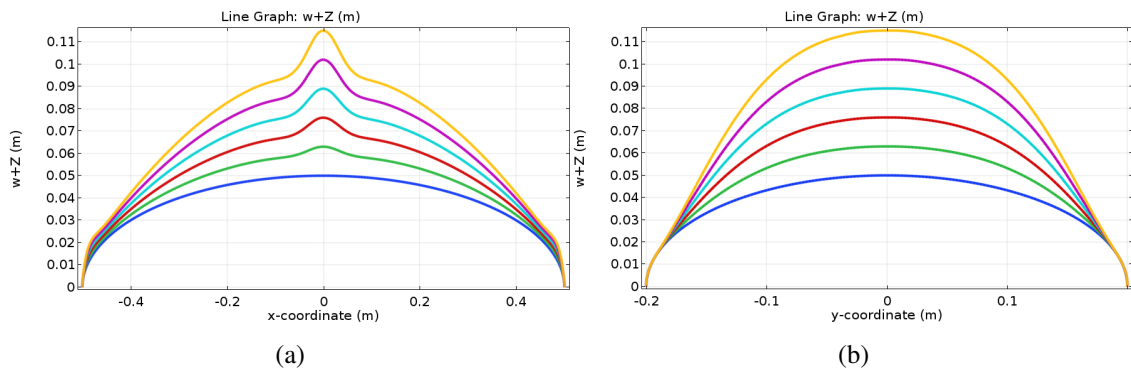


Fig. 4.14 Deflection shape $w + Z$ in Fig.(4.13) for $\lambda^{th} = 0, 0.2, 0.4, 0.6, 0.8, 1.0$ with given parameters: (a) along path AOA' ; (b) along path BOB'

Fig.(4.14a) shows the buckling curve along AA' as $y = 0$. We see that there is a bulge due to the localized in-plane expansion difference in Eq.(4.41). Since the center point grows more, it buckles more. But in the perpendicular direction, deformation is smooth (see Fig.(4.14b)). Here λ^{th} is the loading parameter defined in Eq.(4.41).

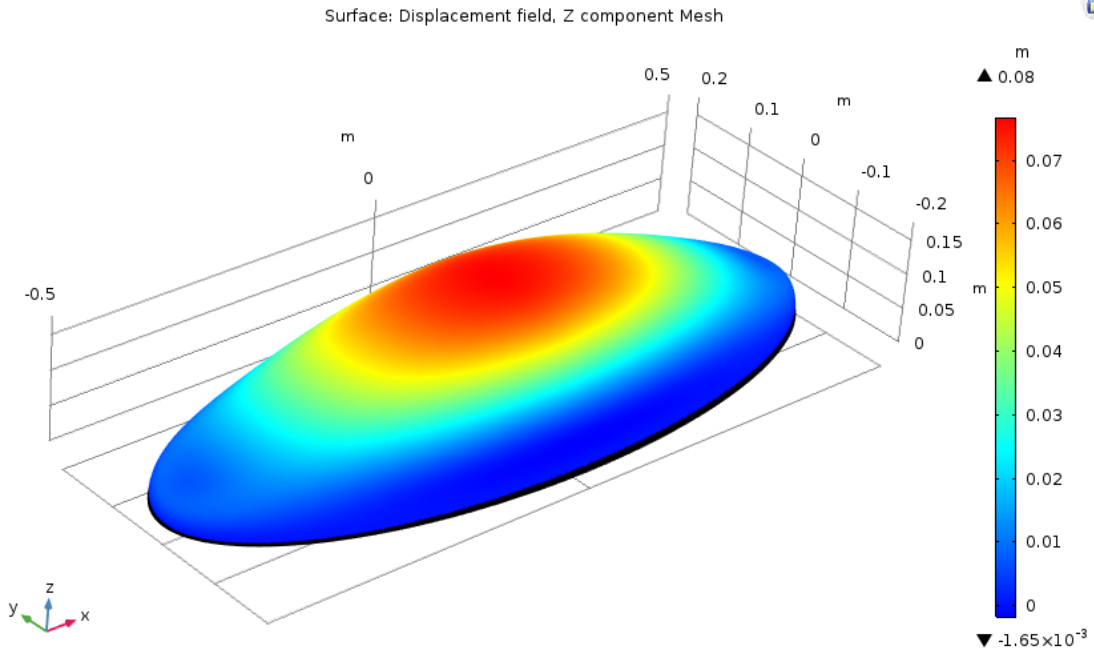


Fig. 4.15 Buckling shape with $x_m = 0, \alpha^{th} = 0.03, \beta^{th} = 1, \gamma^{th} = 10, d = 0.001$

We lower the coefficient γ^{th} in Eq.(4.41) from 1000 to 10. The solutions become smoother near the center. The bulge of the previous case disappears while the total displacement increases in Fig.(4.16) compared to Fig.(4.14).

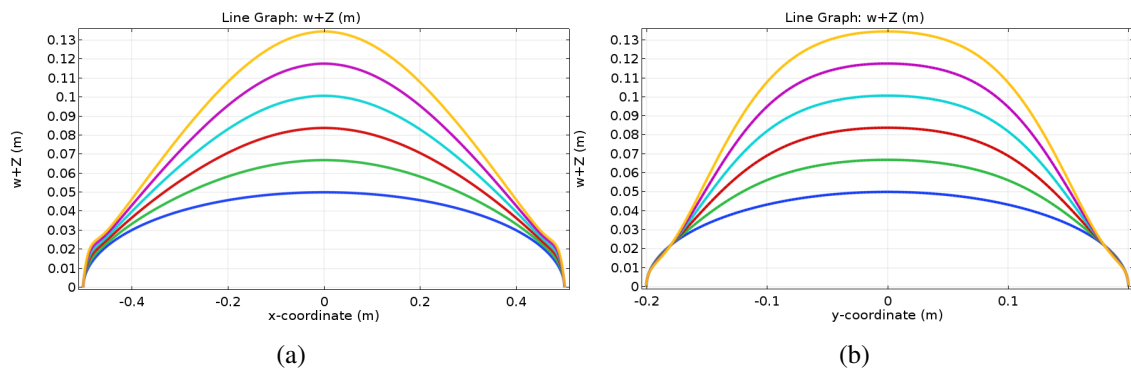


Fig. 4.16 Deflection shape $w + Z$ in Fig.(4.15) for $\lambda^{th} = 0, 0.2, 0.4, 0.6, 0.8, 1.0$ with given parameters: (a) along path AOA' ; (b) along path BOB'

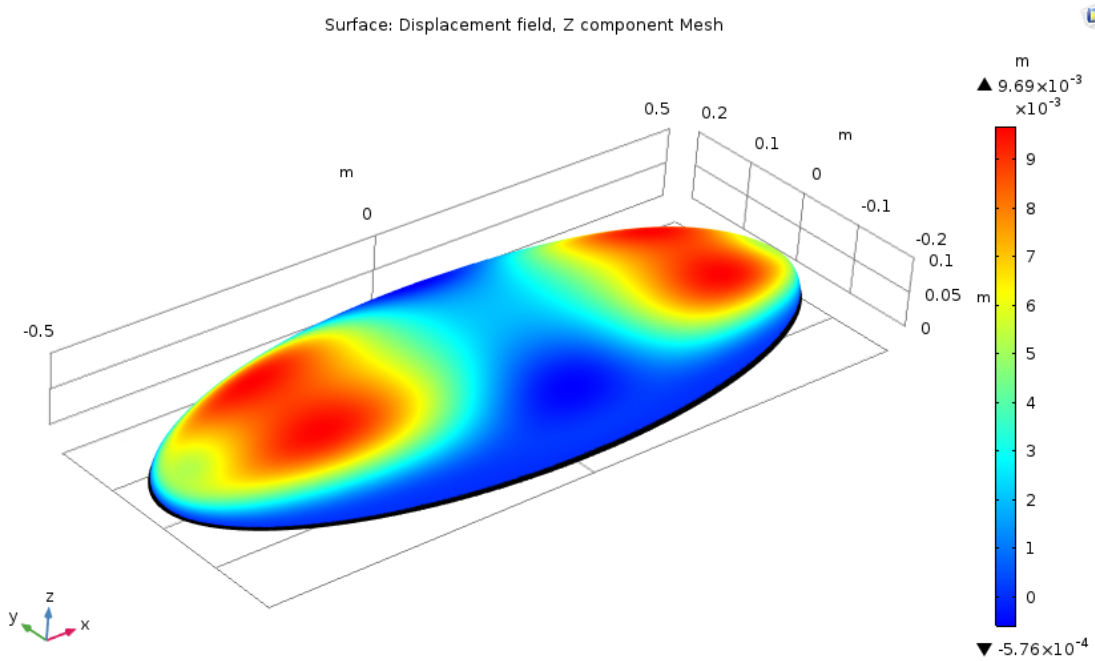


Fig. 4.17 Buckling shape with $x_m = 0, \alpha^{th} = 0.03, \beta^{th} = -1, \gamma^{th} = 10, d = 0.001$

Then we suppose less growth in the center part by setting $\beta^{th} = -1$ with $\gamma^{th} = 10$. In the experiment, this translates to a low dividing activity in the middle. Fig.(4.17) and Fig.(4.18) demonstrate the deformation. In comparison with the previous solution, the buckling shape is quite flat.

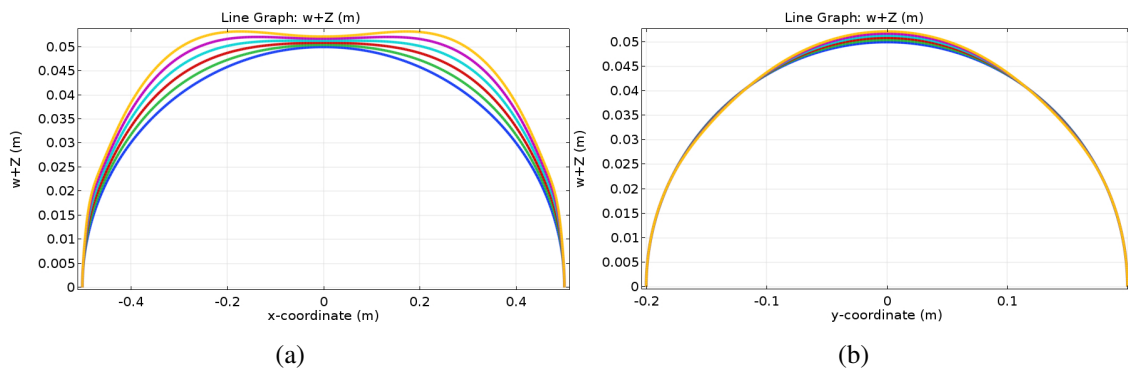


Fig. 4.18 Deflection shape $w + Z$ in Fig.(4.17) for $\lambda^{th} = 0, 0.2, 0.4, 0.6, 0.8, 1.0$ with given parameters: (a) along path AOA' ; (b) along path BOB'

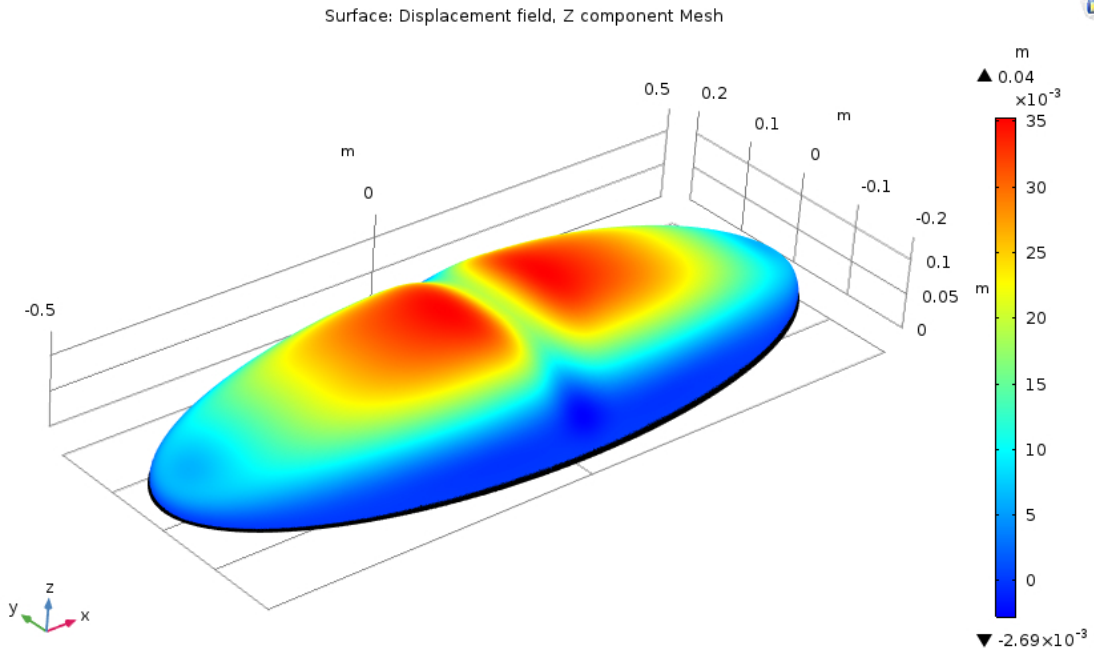


Fig. 4.19 Buckling shape with $x_m = 0, \alpha^{th} = 0.03, \beta^{th} = -1, \gamma^{th} = 1000, d = 0.001$

Finally we increase γ^{th} compared to Fig.(4.17,4.18) and we find a new buckling shape. We focus on Fig.(4.20a) and there is an obvious indentation as opposed to Fig.(4.14a).

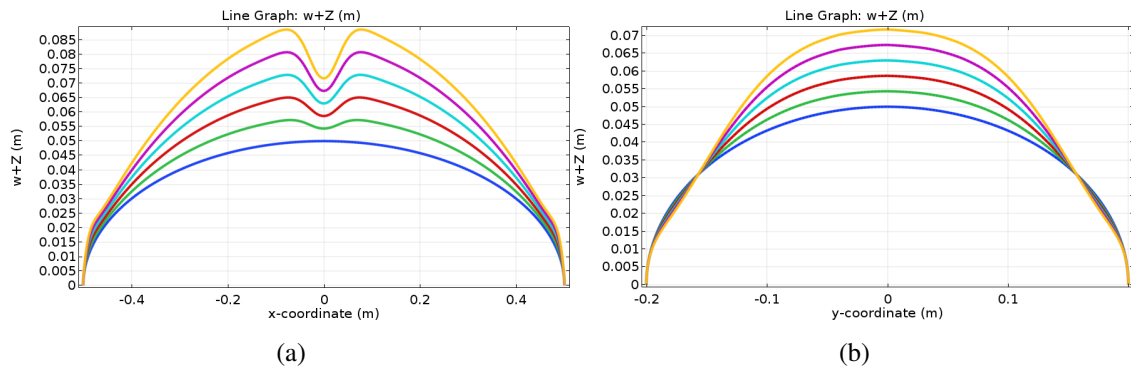


Fig. 4.20 Deflection shape $w + Z$ in Fig.(4.19) for $\lambda^{th} = 0, 0.2, 0.4, 0.6, 0.8, 1.0$ with given parameters: (a) along path AOA' ; (b) along path BOB'

The results demonstrate that within the linear limit, i.e $\epsilon^{th} \leq 0.06$ in our case, exponential growth can generate local buckling phenomena in complex geometry.

4.2.3 Additional bending

We introduce an additional deflection force for the bilayer with growth only in the substrate as

$$q_S^g = \frac{1}{2} \frac{E_S h_S^2}{1 - \nu^2} \left(1 + 2 \frac{Z_n}{h_S}\right) \cdot \partial_{xx} (1 + \nu) \varepsilon^{th} \quad (4.42)$$

$$\partial_{xx} \varepsilon^{th}(x) = \alpha^{th} \beta^{th} \exp[-\gamma^{th} (x - x_m)^2] [4(\gamma^{th})^2 (x - x_m)^2 - 2\gamma^{th}] * \lambda^{th}$$

with the definitions of section 4.2.1. Z_n in Fig.(4.9) can affect the extra bending part ascribed to varying expansion of the two layers. For a monolayer or $h_f/h_S \ll 1$, $Z_n = -h_S/2$ and thus $q_S^g = 0$. We take $Z_n = 0$, $h_S = d$ for simplification in this section.

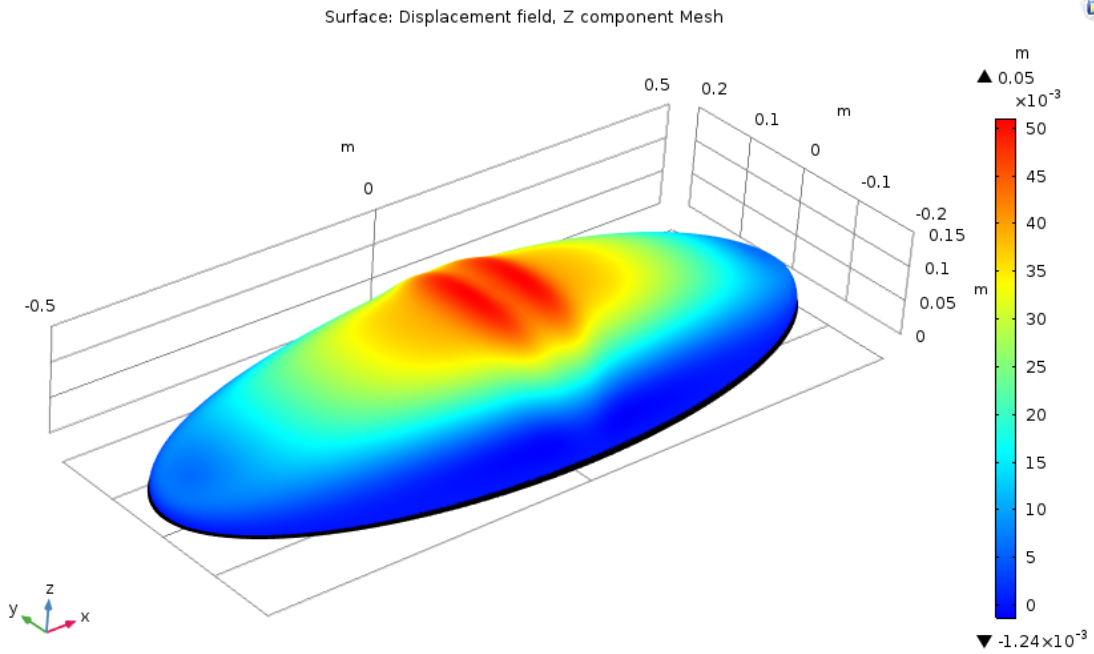


Fig. 4.21 Buckling shape with $x_m = 0$, $\alpha^{th} = 0.03$, $\beta^{th} = 1$, $\gamma^{th} = 1000$, $d = 0.001$, $Z_n = 0$

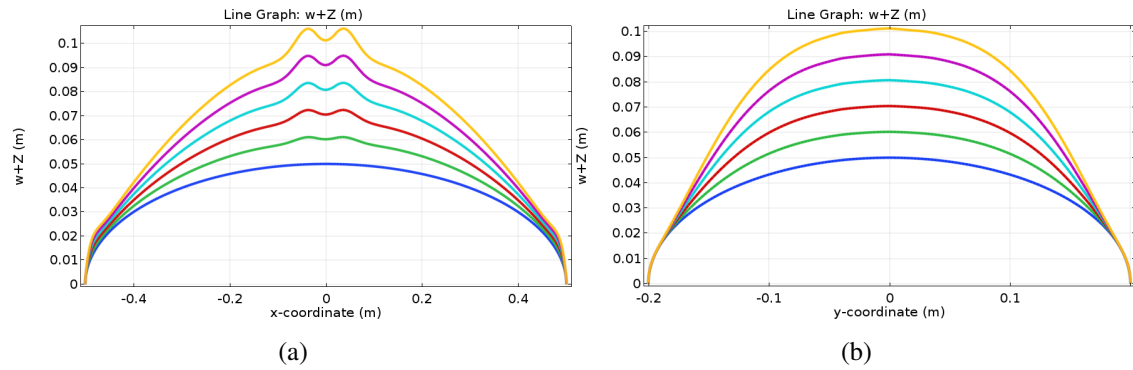


Fig. 4.22 Deflection shape $w + Z$ in Fig.(4.21) for $\lambda^{th} = 0, 0.2, 0.4, 0.6, 0.8, 1.0$ with given parameters: (a) along path AOA' ; (b) along path BOB'

Compared to Fig.(4.14a), there is a buckling shape change in Fig.(4.22a) due to Eq.(4.42).

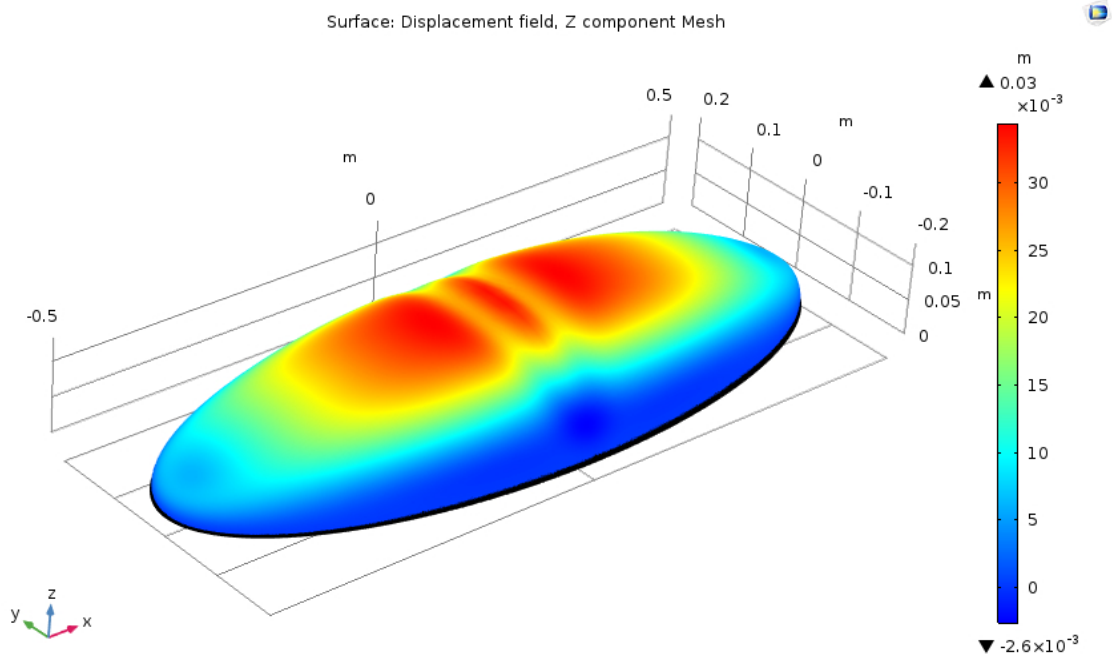


Fig. 4.23 Buckling shape with $x_m = 0, \alpha^{th} = 0.03, \beta^{th} = -1, \gamma^{th} = 1000, d = 0.001Z_n = 0$

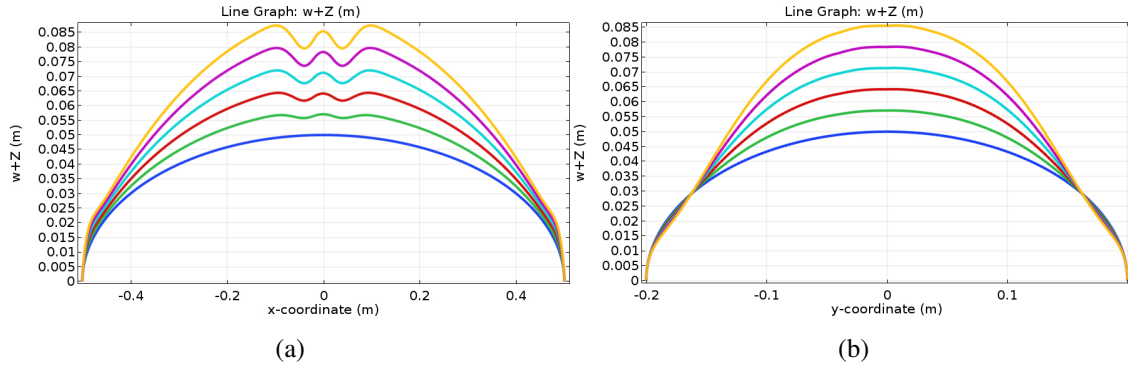


Fig. 4.24 Deflection shape $w + Z$ in Fig.(4.23) for $\lambda^{th} = 0, 0.2, 0.4, 0.6, 0.8, 1.0$ with given parameters: (a) along path AOA' ; (b) along path BOB'

Then we set $\beta^{th} = 1$ leading to another buckling deformation near the middle part demonstrated in Fig.(4.23,4.24).

We consider the effect of active bending by networks with Eq.(4.39). For example we take $w^a = \delta_a(x + 0.5)^2(x - 0.5)^2$ which will give rise to a uniform deflection force of $24\delta \cdot D$ (see Fig.(4.10)). This effect can be absorbed by bending due to growth. So we do not provide more simulations here.

In this section, we have considered the bending contribution from bilayer differential growth. Next we try to take an ECM defect into account.

4.2.4 ECM stiffness contribution

In reality, biologists can remove the extracellular matrix (ECM) in order to modify the material and the geometry. For stiffness contribution, this can be described easily with the help of a distribution function of thickness $d(x)$ as

$$\begin{aligned}
 d(x) &= d(1 - \beta_d * \delta_d(x, x_d, w_d)) \quad -R_x \leq x \leq R_x \\
 \delta_d(x, x_d, w_d) &= H(x - x_d + \frac{w_d}{2}) - H(x - x_d - \frac{w_d}{2})
 \end{aligned} \tag{4.43}$$

where β_d reflects the bending stiffness by the ECM, δ_d is a square wave distribution defined by the Heaviside function $H(x)$, x_d is the location of the defect and w_d is the band of the removed area.

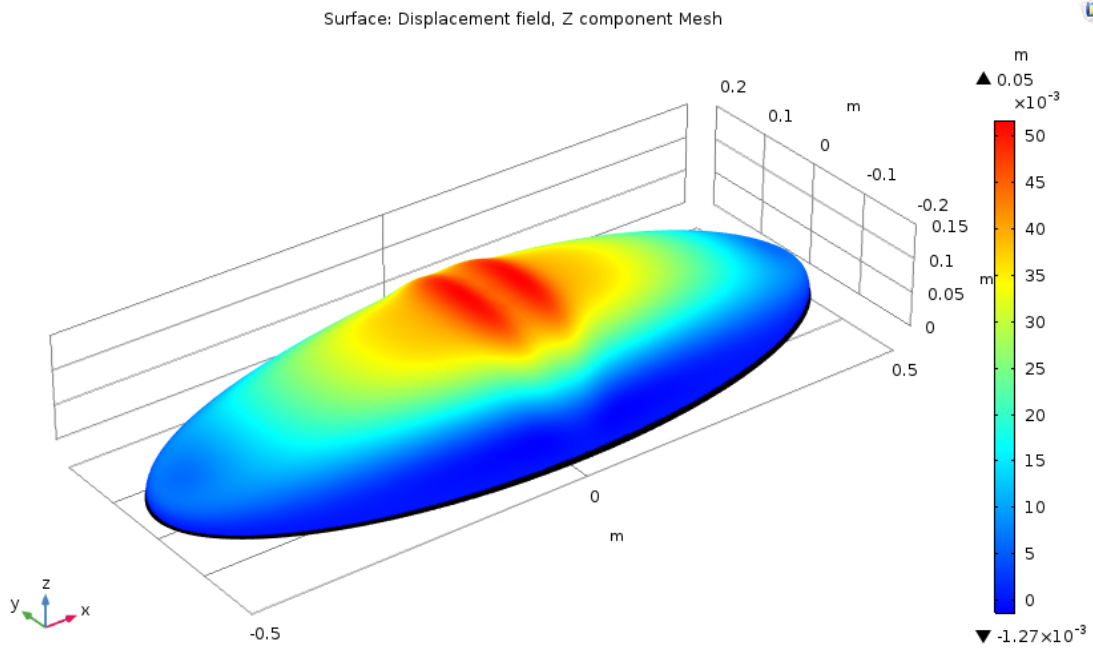


Fig. 4.25 Buckling shape with $x_m = 0, \alpha^{th} = 0.03, \beta^{th} = 1, \gamma^{th} = 1000, d = 0.001, Z_n = 0, \beta_d = 0.1, x_d = 0, w_d = 0.1$

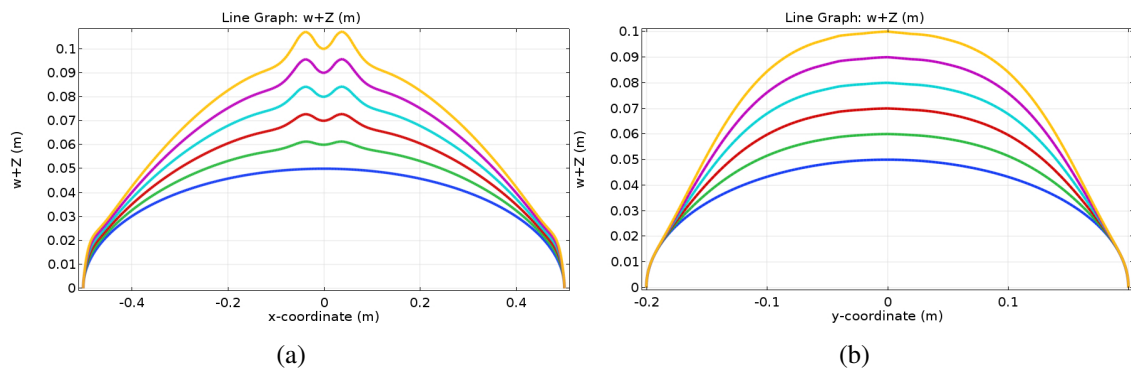


Fig. 4.26 Deflection shape $w + Z$ in Fig.(4.25) for $\lambda^{th} = 0, 0.2, 0.4, 0.6, 0.8, 1.0$ with given parameters: (a) along path AOA' ; (b) along path BOB'

We first take $\beta_d = 0.1, x_d = 0, w_d = 0.1$ for the original case in Fig.(4.21). There is almost no change of the buckling shape according to the results in Fig.(4.25,4.26).

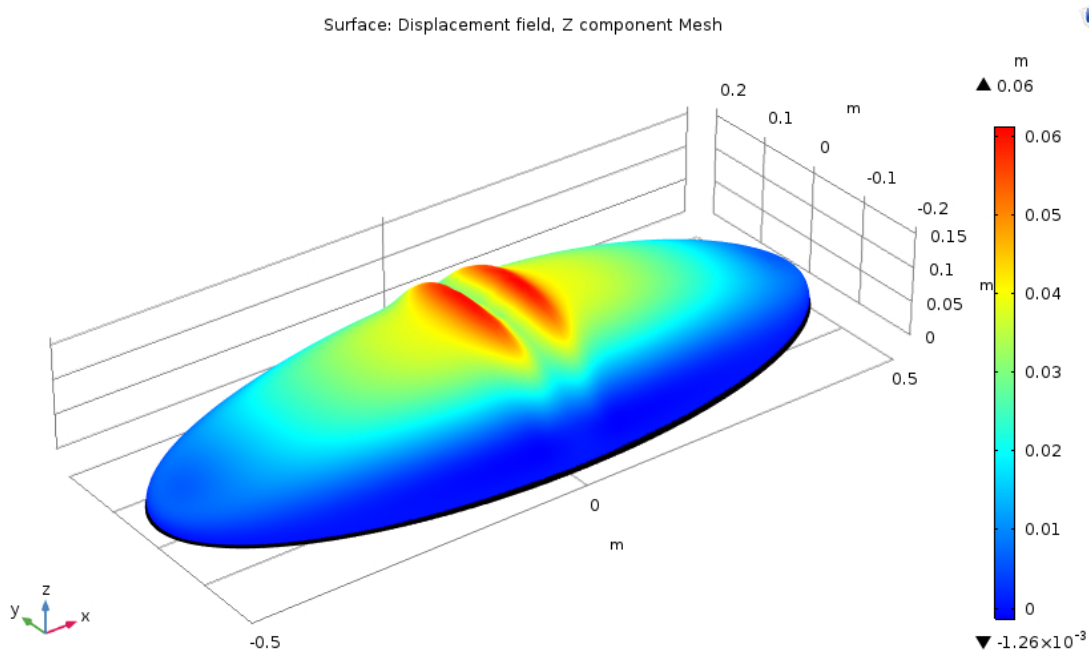


Fig. 4.27 Buckling shape with $x_m = 0, \alpha^{th} = 0.03, \beta^{th} = 1, \gamma^{th} = 1000, d = 0.001, Z_n = 0, \beta_d = 0.5, x_d = 0, w_d = 0.1$

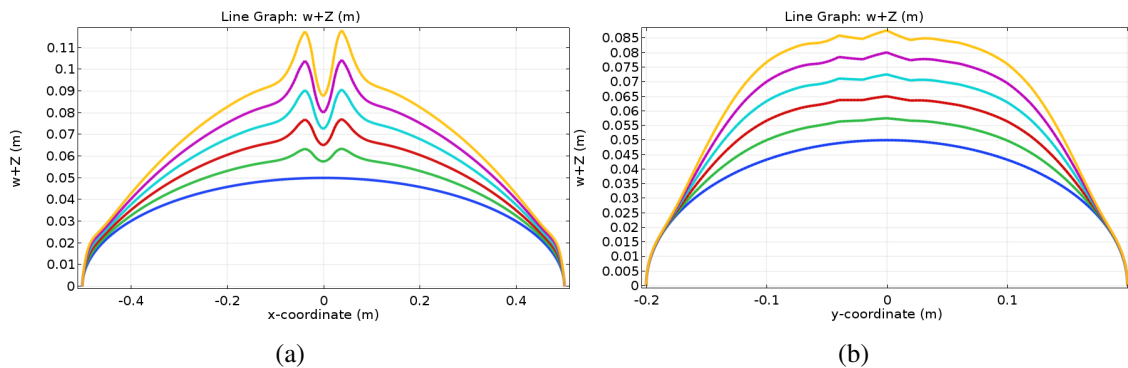


Fig. 4.28 Deflection shape $w + Z$ in Fig.(4.27) for $\lambda^{th} = 0, 0.2, 0.4, 0.6, 0.8, 1.0$ with given parameters: (a) along path AOA' ; (b) along path BOB'

We then lower the bending stiffness D with $\beta_d = 0.5$. The buckling near the center point increases as shown in Fig.(4.28) compared to the solution in Fig.(4.26). In this context we should bear in mind that β_d depends on the material properties and thickness of the ECM and the soft substrate. In addition, destroying the ECM might affect the active momentum by networks in the previous discussion. In this section, We focus on the stiffness contribution by the ECM with Eq.(4.43). Finally we will study the nonlinear effect in the following part.

4.2.5 Nonlinear effects

We take the weak form in COMSOL as

$$\begin{aligned} \delta \mathcal{E}_{bi}^{\text{II}} &= -\tilde{\varepsilon}_b^{\text{II}} \int Z \zeta_{,\alpha} \sigma_{\alpha\beta}^b \delta \zeta_{,\beta} dV * \lambda^{th} \approx -\tilde{\varepsilon}_b^{\text{II}} \int Z \Delta \theta_{\alpha} \sigma_{\alpha\beta}^b \delta \Delta \theta_{\beta} dV * \lambda^{th} \\ &\approx -\lambda_b^{\text{II}} \int \Delta \theta_{\alpha} \left(\frac{1}{1+\nu} \varepsilon_{\alpha\beta}^b + \frac{\nu}{1-\nu^2} \varepsilon_{\gamma\gamma}^b \delta_{\alpha\beta} \right) \delta \Delta \theta_{\beta} dS * \lambda^{th} \end{aligned} \quad (4.44)$$

where the nonlinear term takes into account the coupling of angle change and curvatures in Eq.(4.30) as $-\zeta_{,x} \zeta_{,xx} \delta \zeta_{,x}$. It stems from the higher order effect of neutral surface change. λ_b is assumed of the same order as $E_b d^2$, $\varepsilon_{\alpha\beta}^b$ are out-of-plane bending components, $\Delta \theta$ is correlated to the angle change of the shell normal vector.

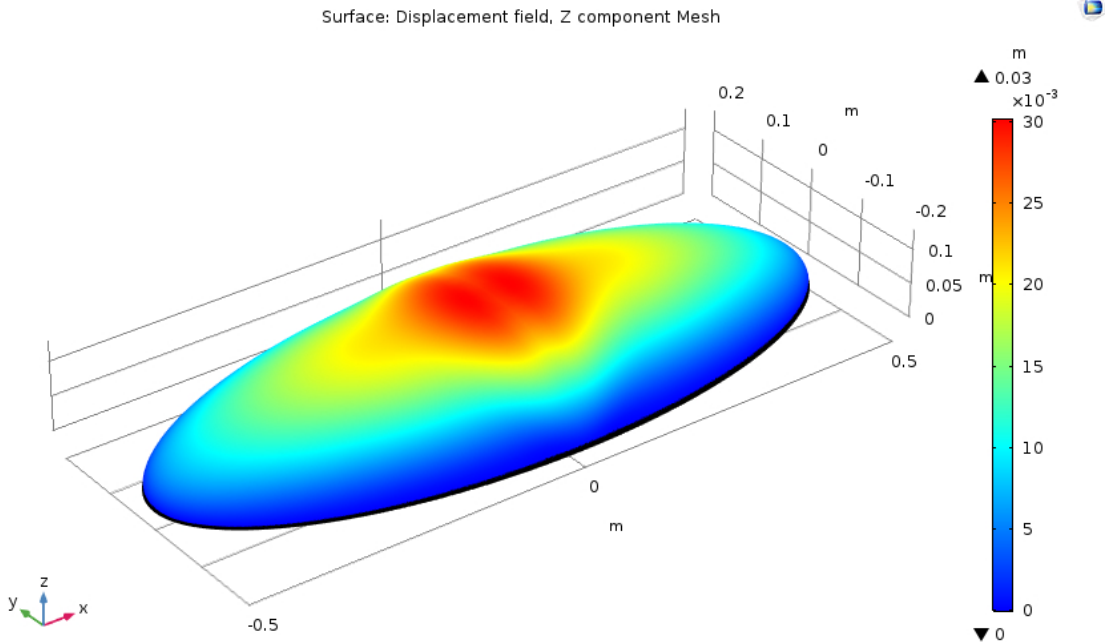


Fig. 4.29 Buckling shape with $x_m = 0$, $\alpha^{th} = 0.03$, $\beta^{th} = 1$, $\gamma^{th} = 1000$, $d = 0.001$, $Z_n = 0$, $\lambda_b^{\text{II}} = 0.001$

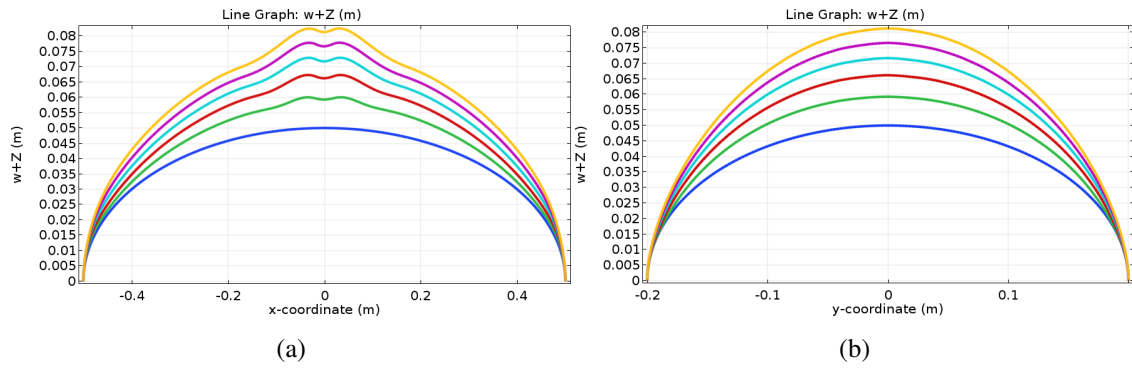


Fig. 4.30 Deflection shape $w + Z$ in Fig.(4.29) for $\lambda^{th} = 0, 0.2, 0.4, 0.6, 0.8, 1.0$ with given parameters: (a) along path AOA' ; (b) along path BOB'

We take $\lambda_b^{II} = 0.001$ with the same sign of ζ and we find it behaves like a global negative deflection force when ζ is not too large. Buckling shape turns to be steady with the nonlinear effect.

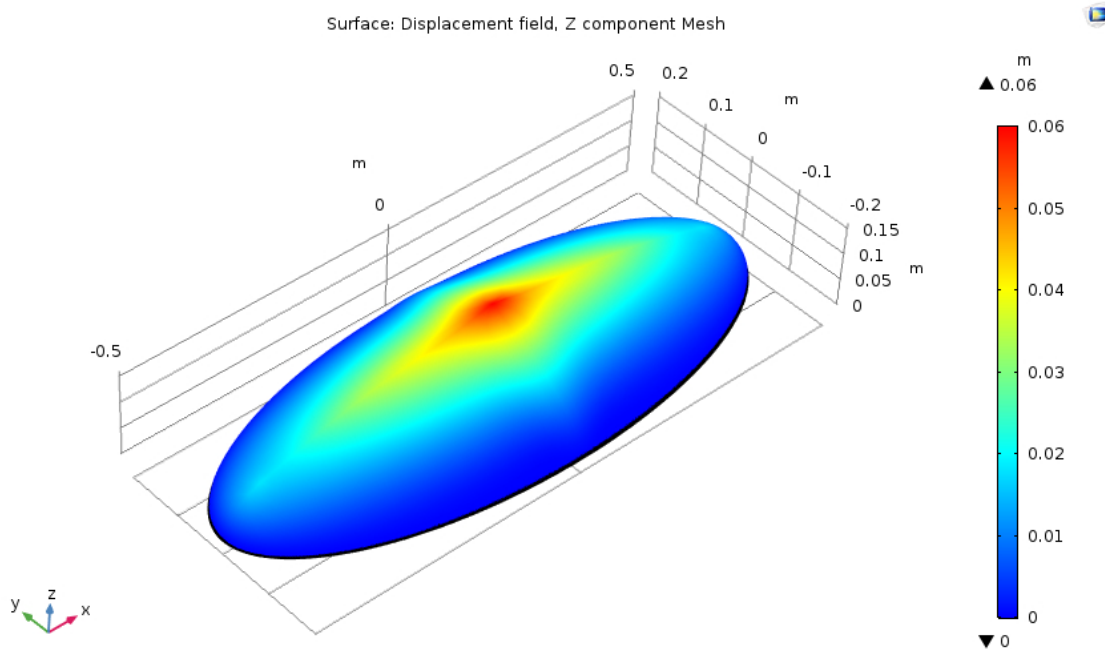


Fig. 4.31 Buckling shape with $x_m = 0, \alpha^{th} = 0.03, \beta^{th} = 1, \gamma^{th} = 1000, d = 0.001, Z_n = 0, \lambda_b^{II} = -0.001$

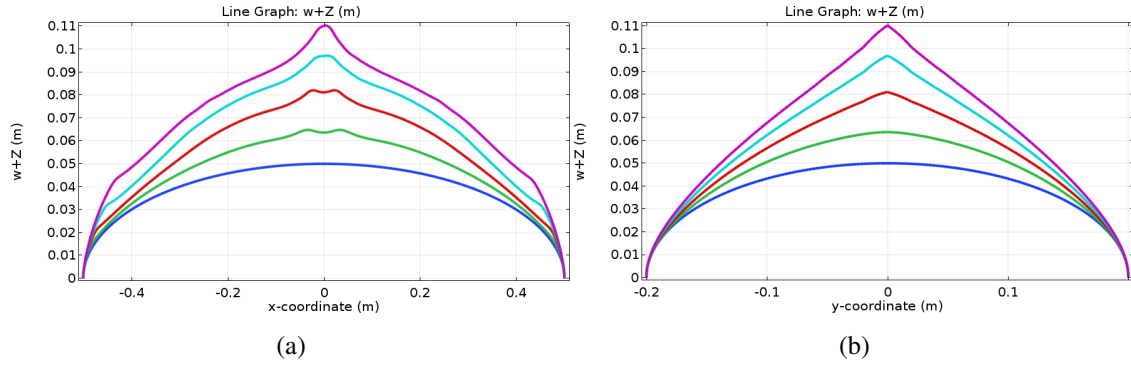


Fig. 4.32 Deflection shape $w + Z$ in Fig.(4.31) for $\lambda^{th} = 0, 0.2, 0.4, 0.6, 0.8$ with given parameters: (a) along path AOA' ; (b) along path BOB'

The simulation with negative λ_b^{II} shows that the quadratic term makes the buckling shape steeper (see Fig.(4.31,4.32)).

4.2.6 Conclusion

Results	Description
	Buckling shape with $x_m = 0, \alpha^{th} = 0.03, \beta^{th} = 1, \gamma^{th} = 1000, d = 0.001$
	Buckling shape with $x_m = 0, \alpha^{th} = 0.03, \beta^{th} = 1, \gamma^{th} = 10, d = 0.001$
	Buckling shape with $x_m = 0, \alpha^{th} = 0.03, \beta^{th} = -1, \gamma^{th} = 10, d = 0.001$
	Buckling shape with $x_m = 0, \alpha^{th} = 0.03, \beta^{th} = -1, \gamma^{th} = 1000, d = 0.001$
	Buckling shape with $x_m = 0, \alpha^{th} = 0.03, \beta^{th} = 1, \gamma^{th} = 1000, d = 0.001, Z_n = 0$
	Buckling shape with $x_m = 0, \alpha^{th} = 0.03, \beta^{th} = -1, \gamma^{th} = 1000, d = 0.001, Z_n = 0$
	Buckling shape with $x_m = 0, \alpha^{th} = 0.03, \beta^{th} = 1, \gamma^{th} = 1000, d = 0.001, Z_n = 0, \beta_d = 0.1, x_d = 0, w_d = 0.1$
	Buckling shape with $x_m = 0, \alpha^{th} = 0.03, \beta^{th} = 1, \gamma^{th} = 1000, d = 0.001, Z_n = 0, \beta_d = 0.5, x_d = 0, w_d = 0.1$
	Buckling shape with $x_m = 0, \alpha^{th} = 0.03, \beta^{th} = 1, \gamma^{th} = 1000, d = 0.001, Z_n = 0, \lambda_b^{II} = 0.001$
	Buckling shape with $x_m = 0, \alpha^{th} = 0.03, \beta^{th} = 1, \gamma^{th} = 1000, d = 0.001, Z_n = 0, \lambda_b^{II} = -0.001$

Table 4.1: Summary of computational results with COMSOL shell

With linear decomposition, 3D shell buckling is calculated in COMSOL. An equivalent monolayer method is taken for the modeling. Special concern is paid on the local growing process for genetic control in the experiment. Active bending by growth and networks is covered in the numerical implementation. ECM defect is introduced in the bending contribution. Finally, the nonlinear effect is considered with the weak form toolbox of COMSOL.

4.3 Conclusion

A bilayer FvK model with growth is derived using a variational method. Neutral surface and equivalent bending stiffness are acquired by the minimization of the elastic energy. In a second step, general FEM simulations with the additional bending and nonlinear effect are implemented in the software COMSOL. In this chapter we utilize the theory of plates and shells to explain the buckling of the bilayer membrane in biological systems such as the *Drosophila* wing disc. We attempt to set up a general model to explain the experimental phenomena. Local exponential growth with an ECM defect is discussed as well. Different buckling shapes at the tissue scale can be controlled with appropriate parameters of the system.

Chapter 5

Finite element simulations with beams and solids

In this chapter, we want to use the traditional finite element method (FEM) for the bilayer structure simulation. For research purpose, we employ a numerical platform in MATLAB equipped with nonlinear Euler beam elements and isoparametric solid elements. The Riks method is taken for the solver of the buckling analysis. During the simulation, we first suggest our system as a solid stripe coupled with bending beams. Growth in different parts is implemented as the inner stress with an updated algorithm. The ECM defect and the initial curvature are considered during the study. The toolbox is written in a general form with an interface of input files, which could be applied to other problems. Finally, we consider the 2D wrinkling and folding simulations with viscoelasticity.

5.1 Algorithm of geometrical nonlinearity

We employ beam and solid elements for the geometrically nonlinear problem [30, 31, 38]. We start with the decomposition of the Green-Lagrange strain measurement

$$\begin{aligned} E_{IJ} &= \frac{1}{2}(F_{KI}F_{KJ} - \delta_{IJ}) = e_{IJ} + \eta_{IJ} \\ e_{IJ} &= \frac{1}{2}\left(\frac{\partial u_I}{\partial X_J} + \frac{\partial u_J}{\partial X_I}\right), \quad \eta_{IJ} = \frac{1}{2}\frac{\partial u_K}{\partial X_I}\frac{\partial u_K}{\partial X_J} \end{aligned} \quad (5.1)$$

as well as the variation of the elastic energy in Chapter 1

$$\delta\mathcal{E} = \int_{tV} \sigma_{ij}\delta\varepsilon_{ij}d^tV = \int_{0V} S_{iJ}^I\delta F_{iJ}d^0V = \int_{0V} S_{IJ}^{II}\delta E_{IJ}d^0V \quad (5.2)$$

In FEM, matrices are preferred due to the numerical implementation. We thus need to introduce a vector form of the strain $\boldsymbol{\gamma}$ and the stress $\boldsymbol{\tau}$ as

$$\boldsymbol{\gamma} = \boldsymbol{e} + \boldsymbol{\eta} = \begin{Bmatrix} e_{11} \\ e_{22} \\ e_{33} \\ 2e_{12} \\ 2e_{23} \\ 2e_{31} \end{Bmatrix} + \begin{Bmatrix} \eta_{11} \\ \eta_{22} \\ \eta_{33} \\ 2\eta_{12} \\ 2\eta_{23} \\ 2\eta_{31} \end{Bmatrix}, \quad \boldsymbol{\tau} = \begin{Bmatrix} \tau_{11} \\ \tau_{22} \\ \tau_{33} \\ \tau_{12} \\ \tau_{23} \\ \tau_{31} \end{Bmatrix} \quad (5.3)$$

For geometrical nonlinearity, we do the variation in a Lagrangian formulation

$$\int_{0V} \delta \boldsymbol{\gamma}^T \boldsymbol{\tau}^{t+\Delta t} dV = \int_{0S} \delta \mathbf{u}^T \mathbf{f}_{bc} dS + \int_{0V} \delta \mathbf{u}^T \mathbf{b} dV \quad (5.4)$$

where $\boldsymbol{\tau}$ is an unknown stress vector, \mathbf{f}_{bc} is a boundary force and \mathbf{b} is a body force. In order to obtain the incremental procedure with the field variables, two decompositions should be employed as

$$\begin{aligned} \boldsymbol{\tau}^{t+\Delta t} &= \boldsymbol{\tau}^t + \Delta \boldsymbol{\tau} = \boldsymbol{\tau}^t + \mathbf{D}^t \cdot \Delta \boldsymbol{\gamma} \\ \Delta \boldsymbol{\gamma} &= \Delta \mathbf{e} + \Delta \boldsymbol{\eta} \end{aligned} \quad (5.5)$$

where

$$\begin{aligned} \Delta \mathbf{e} &= \frac{1}{2} (\mathbf{F}^T \cdot (\Delta \mathbf{u}) \nabla_{\mathbf{X}} + \nabla_{\mathbf{X}} (\Delta \mathbf{u}) \cdot \mathbf{F}) \\ \Delta \boldsymbol{\eta} &= \frac{1}{2} \nabla_{\mathbf{X}} (\Delta \mathbf{u}) \cdot (\Delta \mathbf{u}) \nabla_{\mathbf{X}} \end{aligned} \quad (5.6)$$

Under the assumption of small strains, we can take the tangent stiffness \mathbf{D}^t as a constant matrix \mathbf{D} and $\boldsymbol{\tau}^t \approx \mathbf{D} \cdot \boldsymbol{\gamma}^t$. After linearisation with $\delta \boldsymbol{\gamma} = \delta \Delta \boldsymbol{\gamma}$, Eq.(5.4) becomes

$$\int_{0V} \delta \Delta \mathbf{e}^T \mathbf{D} \Delta \mathbf{e} dV + \int_{0V} \delta \Delta \boldsymbol{\eta}^T \boldsymbol{\tau}^t dV = \int_{0S} \delta \mathbf{u}^T \mathbf{f}_{bc} dS + \int_{0V} \delta \mathbf{u}^T \mathbf{b} dV - \int_{0V} \delta \Delta \mathbf{e}^T \boldsymbol{\tau}^t dV \quad (5.7)$$

In a discrete form, Eq.(5.7) reduces to

$$\delta \Delta \mathbf{a}^T (\mathbf{K}_L + \mathbf{K}_{NL}) \Delta \mathbf{a} = \delta \Delta \mathbf{a}^T (\mathbf{f}_{ext}^{t+\Delta t} - \mathbf{f}_{int}^t) \quad (5.8)$$

The full derivation is as follows.

First, the displacement field is given by $\mathbf{u} = \mathbf{H} \mathbf{a}$ where \mathbf{a} is the total discrete nodal vector of degrees n and \mathbf{H} is the interpolation matrix for all degrees of freedom. For a three-dimensional configuration \mathbf{H} has the size of $3 \times 3n$ as

$$\mathbf{H} = \begin{bmatrix} h_1 & 0 & 0 & h_2 & 0 & 0 & \cdots & h_n & 0 & 0 \\ 0 & h_1 & 0 & 0 & h_2 & 0 & \cdots & 0 & h_n & 0 \\ 0 & 0 & h_1 & 0 & 0 & h_2 & \cdots & 0 & 0 & h_n \end{bmatrix} \quad (5.9)$$

Then comes to the relation between the linear strain increment and the nodal displacement increment

$$\Delta \mathbf{e} = \mathbf{L} \Delta \mathbf{u} \quad (5.10)$$

where in 3D

$$\mathbf{L} = \begin{bmatrix} F_{11} \frac{\partial}{\partial X_1} & F_{21} \frac{\partial}{\partial X_1} & F_{31} \frac{\partial}{\partial X_1} \\ F_{12} \frac{\partial}{\partial X_2} & F_{22} \frac{\partial}{\partial X_2} & F_{32} \frac{\partial}{\partial X_2} \\ F_{13} \frac{\partial}{\partial X_3} & F_{23} \frac{\partial}{\partial X_3} & F_{33} \frac{\partial}{\partial X_3} \\ F_{11} \frac{\partial}{\partial X_2} + F_{12} \frac{\partial}{\partial X_1} & F_{21} \frac{\partial}{\partial X_2} + F_{22} \frac{\partial}{\partial X_1} & F_{31} \frac{\partial}{\partial X_2} + F_{32} \frac{\partial}{\partial X_1} \\ F_{12} \frac{\partial}{\partial X_3} + F_{13} \frac{\partial}{\partial X_2} & F_{22} \frac{\partial}{\partial X_3} + F_{23} \frac{\partial}{\partial X_2} & F_{32} \frac{\partial}{\partial X_3} + F_{33} \frac{\partial}{\partial X_2} \\ F_{13} \frac{\partial}{\partial X_1} + F_{11} \frac{\partial}{\partial X_3} & F_{23} \frac{\partial}{\partial X_1} + F_{21} \frac{\partial}{\partial X_3} & F_{33} \frac{\partial}{\partial X_1} + F_{31} \frac{\partial}{\partial X_3} \end{bmatrix} \quad (5.11)$$

So we have $\Delta \mathbf{e} = \mathbf{LH}\Delta \mathbf{a} = \mathbf{B}_L \Delta \mathbf{a}$ and

$$\int_{0_V} \delta \Delta \mathbf{e}^T \mathbf{D} \Delta \mathbf{e} dV = \delta \Delta \mathbf{a}^T \mathbf{K}_L \delta \Delta \mathbf{a}$$

$$\mathbf{K}_L = \int_{0_V} \mathbf{B}_L^T \mathbf{D} \mathbf{B}_L dV$$
(5.12)

as well as

$$\int_{0_V} \delta \Delta \boldsymbol{\eta}^T \boldsymbol{\tau}^t dV = \Delta \mathbf{a}^T \mathbf{K}_{NL} \delta \Delta \mathbf{a}$$

$$\mathbf{K}_{NL} = \int_{0_V} \mathbf{B}_{NL}^T \boldsymbol{\mathfrak{T}} \mathbf{B}_{NL} dV$$
(5.13)

where

$$\mathbf{B}_{NL} = \begin{bmatrix} \frac{\partial h_1}{\partial X_1} & 0 & 0 & \frac{\partial h_2}{\partial X_1} & 0 & 0 & \dots \\ \frac{\partial h_1}{\partial X_2} & 0 & 0 & \frac{\partial h_2}{\partial X_2} & 0 & 0 & \dots \\ \frac{\partial h_1}{\partial X_3} & 0 & 0 & \frac{\partial h_2}{\partial X_3} & 0 & 0 & \dots \\ 0 & \frac{\partial h_1}{\partial X_1} & 0 & 0 & \frac{\partial h_2}{\partial X_1} & 0 & \dots \\ 0 & \frac{\partial h_1}{\partial X_2} & 0 & 0 & \frac{\partial h_2}{\partial X_2} & 0 & \dots \\ 0 & \frac{\partial h_1}{\partial X_3} & 0 & 0 & \frac{\partial h_2}{\partial X_3} & 0 & \dots \\ 0 & 0 & \frac{\partial h_1}{\partial X_1} & 0 & 0 & \frac{\partial h_2}{\partial X_1} & \dots \\ 0 & 0 & \frac{\partial h_1}{\partial X_2} & 0 & 0 & \frac{\partial h_2}{\partial X_2} & \dots \\ 0 & 0 & \frac{\partial h_1}{\partial X_3} & 0 & 0 & \frac{\partial h_2}{\partial X_3} & \dots \end{bmatrix}$$
(5.14)

and

$$\boldsymbol{\mathfrak{T}} = \begin{bmatrix} \tau_{xx} & \tau_{xy} & \tau_{xz} & 0 & 0 & 0 & 0 & 0 & 0 \\ \tau_{xy} & \tau_{yy} & \tau_{yz} & 0 & 0 & 0 & 0 & 0 & 0 \\ \tau_{xz} & \tau_{yz} & \tau_{zz} & 0 & 0 & 0 & 0 & 0 & 0 \\ 0 & 0 & 0 & \tau_{xx} & \tau_{xy} & \tau_{xz} & 0 & 0 & 0 \\ 0 & 0 & 0 & \tau_{xy} & \tau_{yy} & \tau_{yz} & 0 & 0 & 0 \\ 0 & 0 & 0 & \tau_{xz} & \tau_{yz} & \tau_{zz} & 0 & 0 & 0 \\ 0 & 0 & 0 & 0 & 0 & 0 & \tau_{xx} & \tau_{xy} & \tau_{xz} \\ 0 & 0 & 0 & 0 & 0 & 0 & \tau_{xy} & \tau_{yy} & \tau_{yz} \\ 0 & 0 & 0 & 0 & 0 & 0 & \tau_{xz} & \tau_{yz} & \tau_{zz} \end{bmatrix}$$
(5.15)

Finally we have $\mathbf{f}_{ext}^{t+\Delta t}$ and \mathbf{f}_{int}^t for Eq.(5.8) as

$$\mathbf{f}_{ext}^{t+\Delta t} = \int_{0_S} \mathbf{H}^T \mathbf{f}_{bc} dS + \int_{0_V} \mathbf{H}^T \mathbf{b} dV$$

$$\mathbf{f}_{int}^t = \int_{0_V} \mathbf{B}_L^T \boldsymbol{\tau}^t dV$$
(5.16)

We can now apply the algorithm in MATLAB.

5.2 Finite element simulations in MATLAB

A simple toolbox is established for the numerical simulation. It contains a general framework of FEM and it is ready for secondary development. We could use this toolbox for an arbitrary geometry once the mesh information is provided with boundary conditions and loading history. There are many advantages of the self-written environment. We could easily change the element data and get the information of the global stiffness matrix in comparison with the commercial FEM software.

Parametric modeling is founded in the platform and we could add new element types if necessary. As shown in Fig.(5.1), the Riks method [31] is used for the numerical solver.

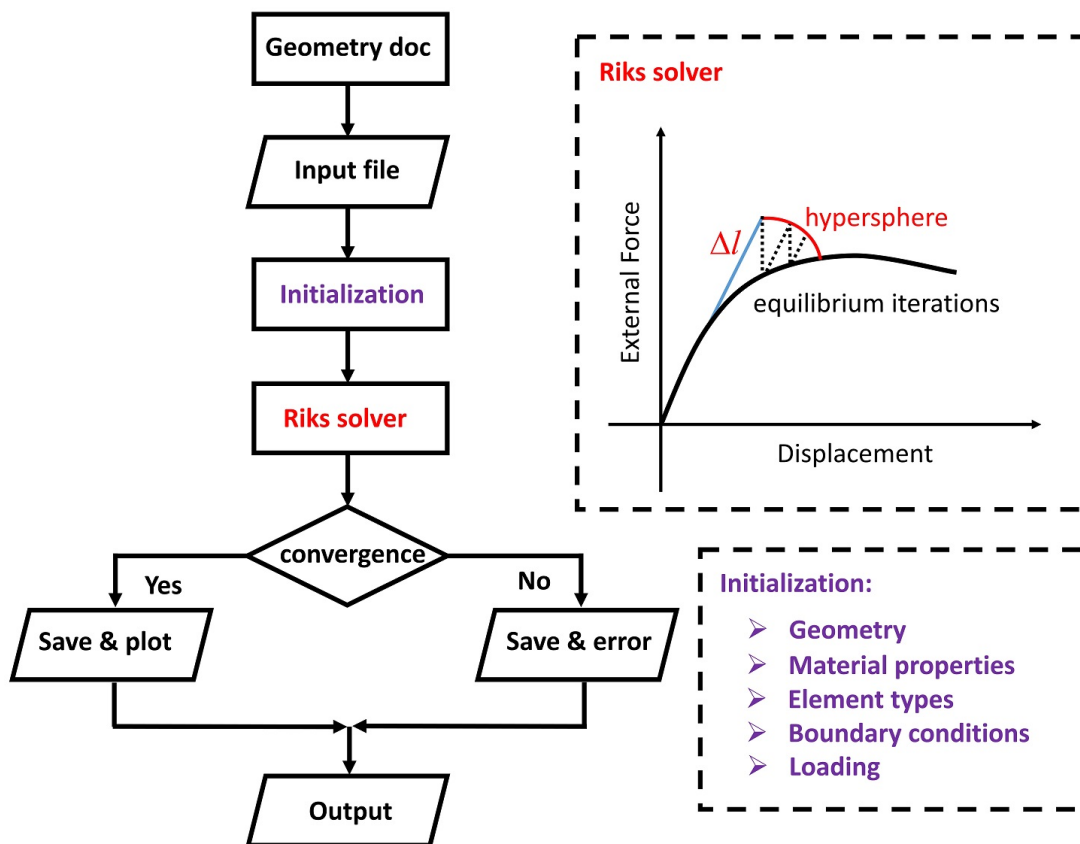


Fig. 5.1 Flow chart of calculation

A bi-material biological system is always of great interest. We will employ FEM in 1D, 2D and 3D to study buckling phenomena with growth. In the following, we will first come back to the original problem discussed in chapter 4. We use beam elements to describe the thinner and stiffer ECM and employ a 3D solid for the soft tissue layer. According to our knowledge, the beam elements includes the contribution of bending stiffness. Active stress is achieved by setting growth along the beam axis. Then in 2D, we use viscoelasticity to explain different buckling shapes in the same morphogenesis process.

5.2.1 Nonlinear Euler-Bernouli beam

Before coupling of different elements, we first introduce the buckling of the beam. In our toolbox, first-order nonlinear Euler-Bernouli elements (called B31 after) [61, 136, 137] are employed for 3D simulations. Shear is neglected and the elastic axial strain induced by growth reads

$$\varepsilon_g = -\lambda_g * \Delta T \quad (5.17)$$

where λ_g is the loading variable and ΔT is a known non-dimensional parameter.

We firstly consider a straight cylindrical beam oriented along the x-axis as a patch test with length a , section area A , moment along the y-axis I_y , moment along the z-axis I_z , torsion moment along the x-axis J_t , Young's modulus E and Poisson coefficient ν . The left end is fixed and the right end is under compression parallel to the x-axis with prescribed displacement $u = -\lambda_g * u_0$.

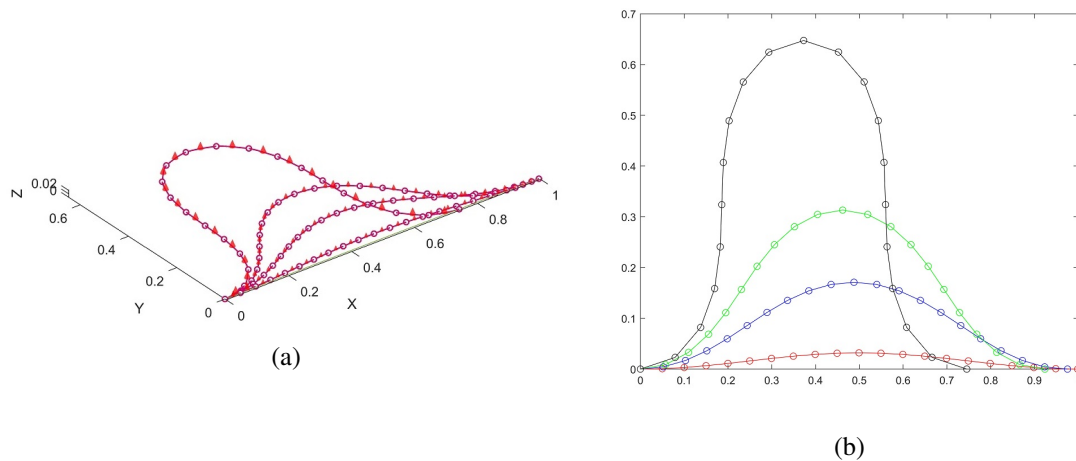


Fig. 5.2 Deflection shapes for $\lambda_g = 0.002, 0.04, 0.15, 0.5$ with $\Delta T = 1$, $u_0 = 0.5$

Fig.(5.2) demonstrates the final deflection curve induced by axial compression u_0 and inner growth ΔT . There are literatures for the more sophisticated situations [138, 139]. Next we suppose a honeycomb structure with the same geometry and material properties for each element.

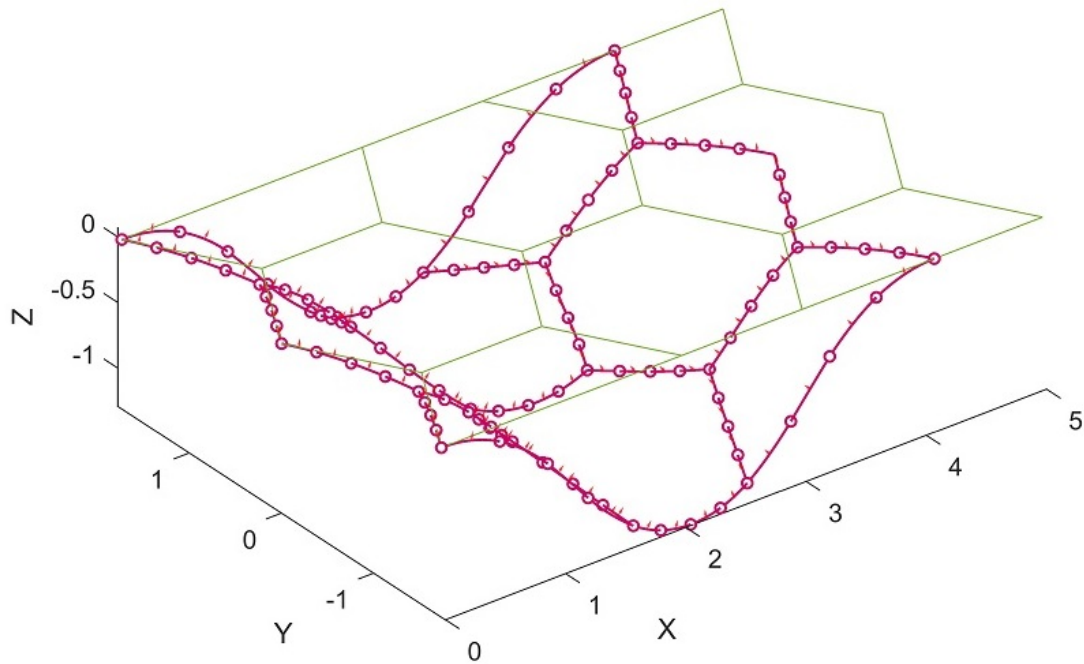


Fig. 5.3 *Buckling shape of the structure*

We observe in Fig.(5.3) a buckling mode due to the external loading. We apply a defect such as a small force to achieve a out-of-plane deflection. Hereafter, we focus on the simulation of a 3D stripe case.

5.2.2 3D Solids with beams

In this section, 3D isoparametric solid elements (called S38 after) are used for a monolayer epithelium with nonlinear beam elements B31 for extra bending stiffness. We try to explain our problem as simple as possible. The geometry is sketched in Fig.(5.4)

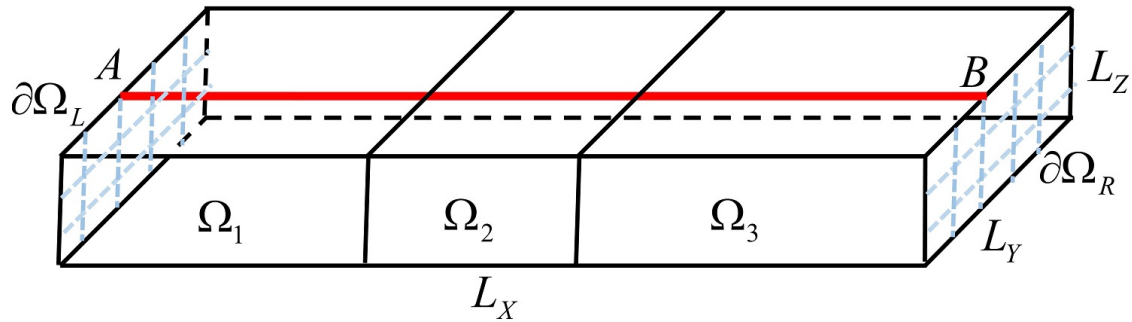


Fig. 5.4 Geometry of 3D stripe

where the size of the Volume $\Omega = \Omega_1 \cup \Omega_2 \cup \Omega_3$ is $L_X \times L_Y \times L_Z$. There is a section of the beam AB which could be initially curved. In this case, the left and the right side of the stripe noted as $\partial\Omega_L$ and $\partial\Omega_R$ are fixed by the boundary condition. Local growth happens in domain Ω_2 and initial shape AB might determine the final resolution. Mesh information is labeled as follows

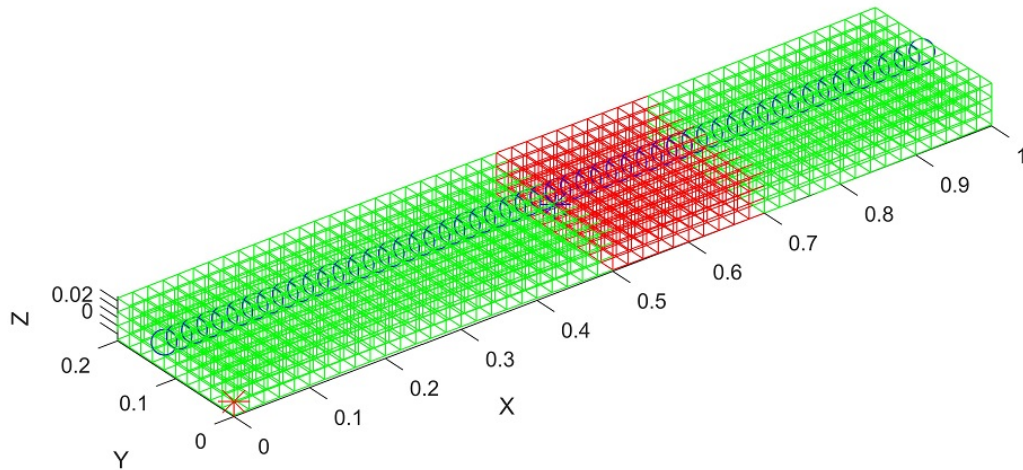


Fig. 5.5 Mesh diagram of the system: The region in green is the normal part without growth and the piece in red has isotropic growth with a loading parameter λ_g . Blue circles represent stiffer beam elements which have additional bending energy

We use the notation λ_g for a loading parameter of Eq.(5.17) and N_{step} for the calculation step. We try to use the initial curvature AB to control the final buckling shape. We suggest growth only in the red domain of Fig.(5.5) for simplification. We set different Young's moduli in different areas. The SI unit system is applied and the color bar represents the value of the displacement. We obtain the following results

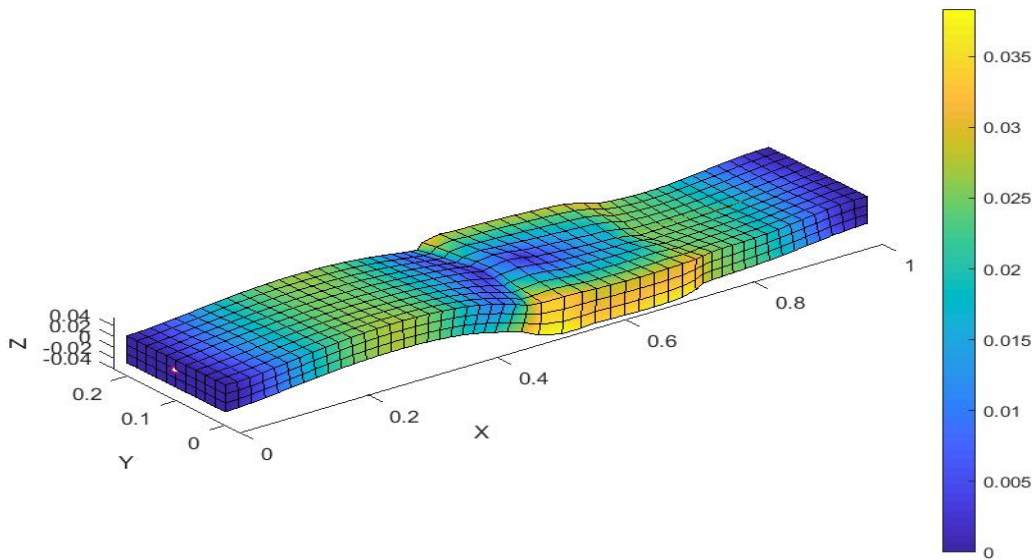


Fig. 5.6 $L_X = 1, L_Y = 0.2, L_Z = 0.05, \Omega_2 : 0.5 \leq X \leq 0.7, AB \approx \delta \sin(2\pi X), E_1 = E_3 = 10^3 \text{Pa}, E_2 = 0.5 \times 10^3 \text{Pa}, E_{beam} = 50 * E_1, \nu_1 = \nu_2 = \nu_3 = 0.3, \Delta T = 1, N_{step} = 5, \lambda_g = 0.2$

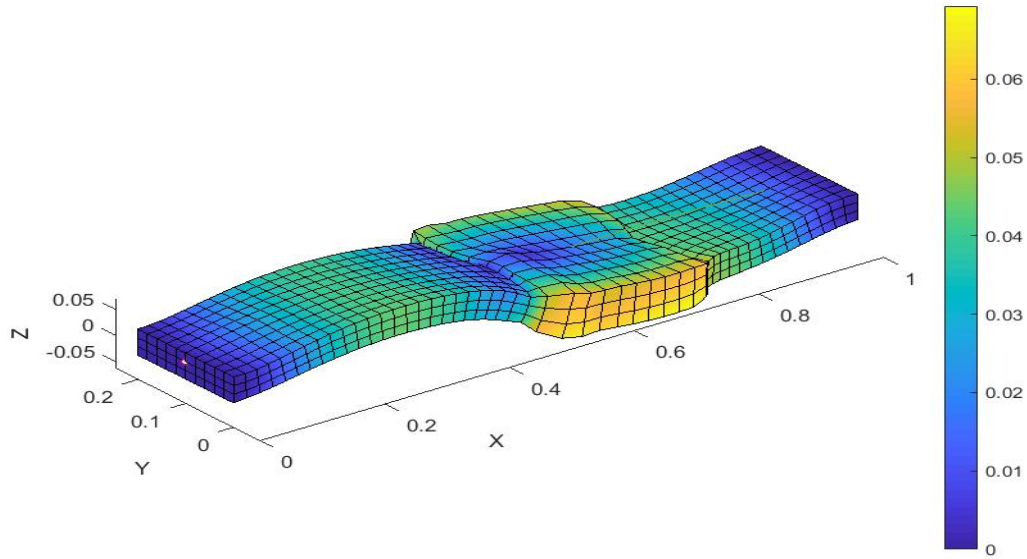


Fig. 5.7 $L_X = 1, L_Y = 0.2, L_Z = 0.05, \Omega_2 : 0.5 \leq X \leq 0.7, AB \approx \delta \sin(2\pi X), E_1 = E_3 = 10^5 \text{Pa}, E_2 = 0.5 \times 10^5 \text{Pa}, E_{beam} = 50 * E_1, \nu_1 = \nu_2 = \nu_3 = 0.3, \Delta T = 1, N_{step} = 8, \lambda_g = 0.5$

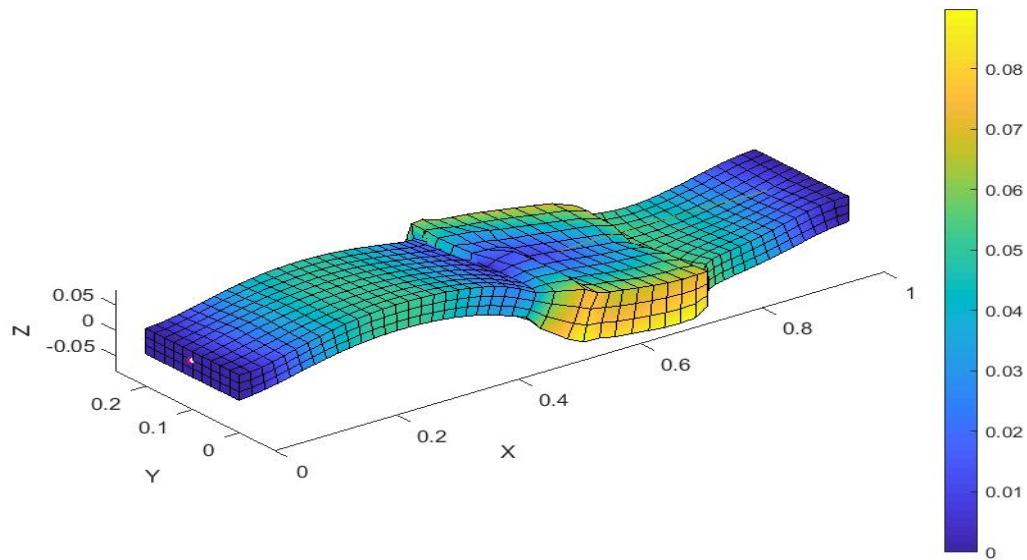


Fig. 5.8 $L_X = 1, L_Y = 0.2, L_Z = 0.05, \Omega_2 : 0.5 \leq X \leq 0.7, AB \approx \delta \sin(2\pi X), E_1 = E_3 = 10^5 \text{Pa}, E_2 = 0.5 \times 10^5 \text{Pa}, E_{beam} = 50 * E_1, \nu_1 = \nu_2 = \nu_3 = 0.3, \Delta T = 1, N_{step} = 10, \lambda_g = 0.8$

Fig.(5.6) to Fig.(5.8) is a group of results with AB in Fig.(5.4) initially curved as $\delta \sin(2\pi X)$. Loading parameter λ_g varies from 0.1 to 1.3 with an adaptive step size. We find that the domain of growth expands isotropically in 3D leading to the global buckling of the total length.

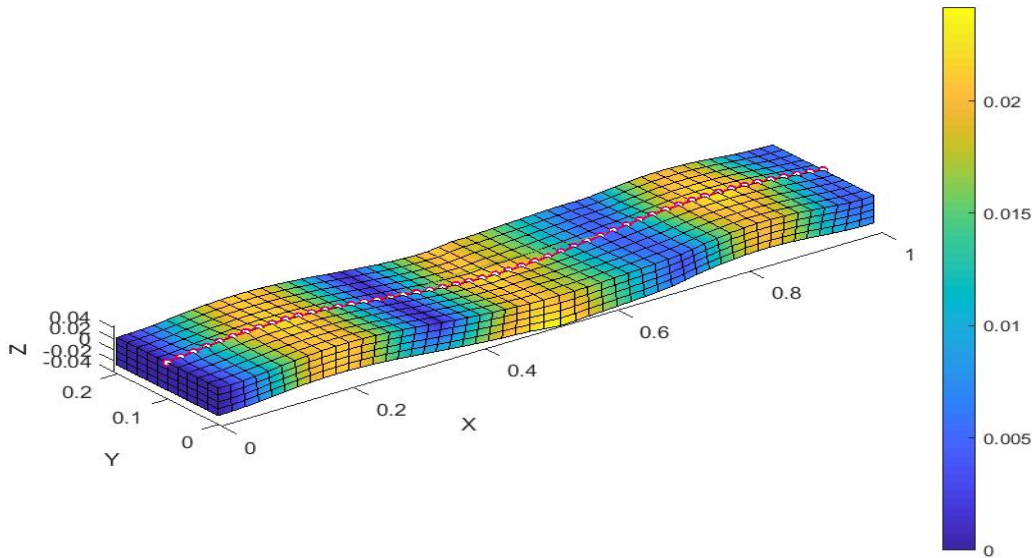


Fig. 5.9 $L_X = 1, L_Y = 0.2, L_Z = 0.05, \Omega_2 : 0.5 \leq X \leq 0.7, AB \approx \delta \sin(3\pi X), E_1 = E_3 = 10^3 \text{Pa}, E_2 = 0.5 \times 10^3 \text{Pa}, E_{beam} = 50 * E_1, \nu_1 = \nu_2 = \nu_3 = 0.3, \Delta T = 1, N_{step} = 3, \lambda_g = 0.02$

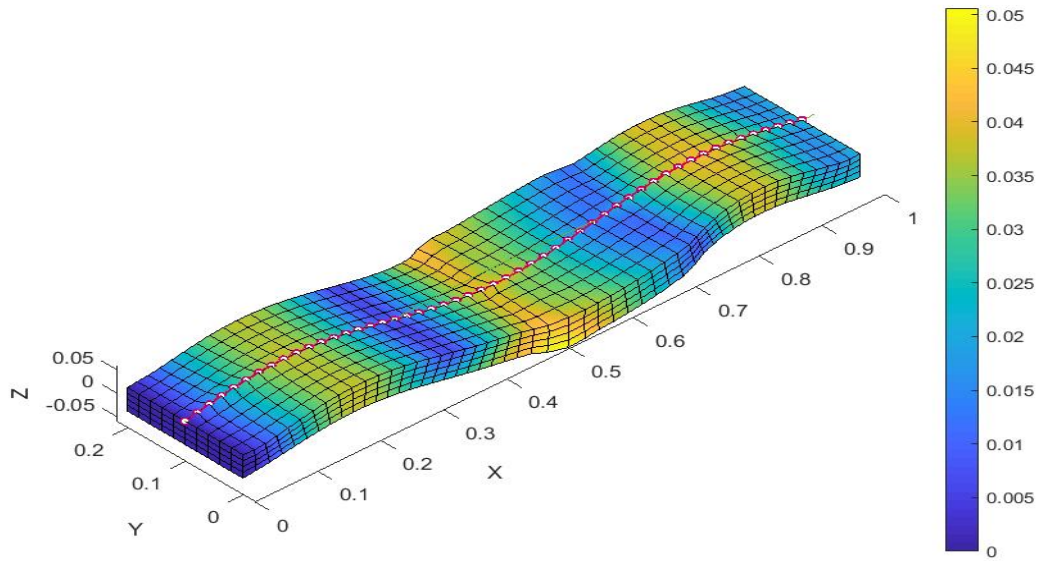


Fig. 5.10 $L_X = 1, L_Y = 0.2, L_Z = 0.05, \Omega_2 : 0.5 \leq X \leq 0.7, AB \approx \delta \sin(3\pi X), E_1 = E_3 = 10^3 \text{Pa}, E_2 = 0.5 \times 10^3 \text{Pa}, E_{beam} = 50 * E_1, \nu_1 = \nu_2 = \nu_3 = 0.3, \Delta T = 1, N_{step} = 5, \lambda_g = 0.1$

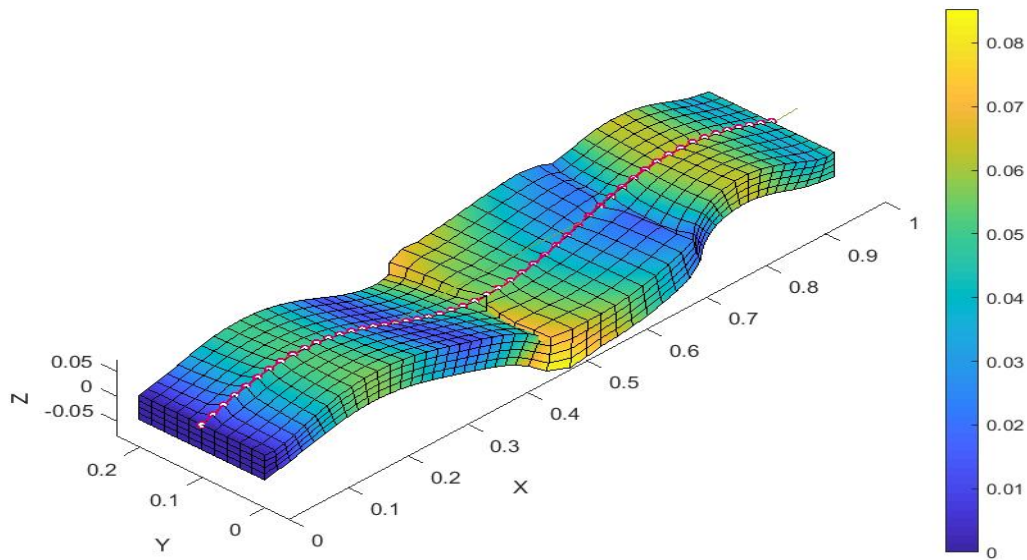


Fig. 5.11 $L_X = 1, L_Y = 0.2, L_Z = 0.05, \Omega_2 : 0.5 \leq X \leq 0.7, AB \approx \delta \sin(3\pi X), E_1 = E_3 = 10^3 \text{Pa}, E_2 = 0.5 \times 10^3 \text{Pa}, E_{beam} = 50 * E_1, \nu_1 = \nu_2 = \nu_3 = 0.3, \Delta T = 1, N_{step} = 7, \lambda_g = 0.3$

Fig.(5.9) to Fig.(5.11) show a similar phenomenon as expected with the given parameters. After we change the geometry by increasing the total length. We also move the growing area from the right to the middle part.

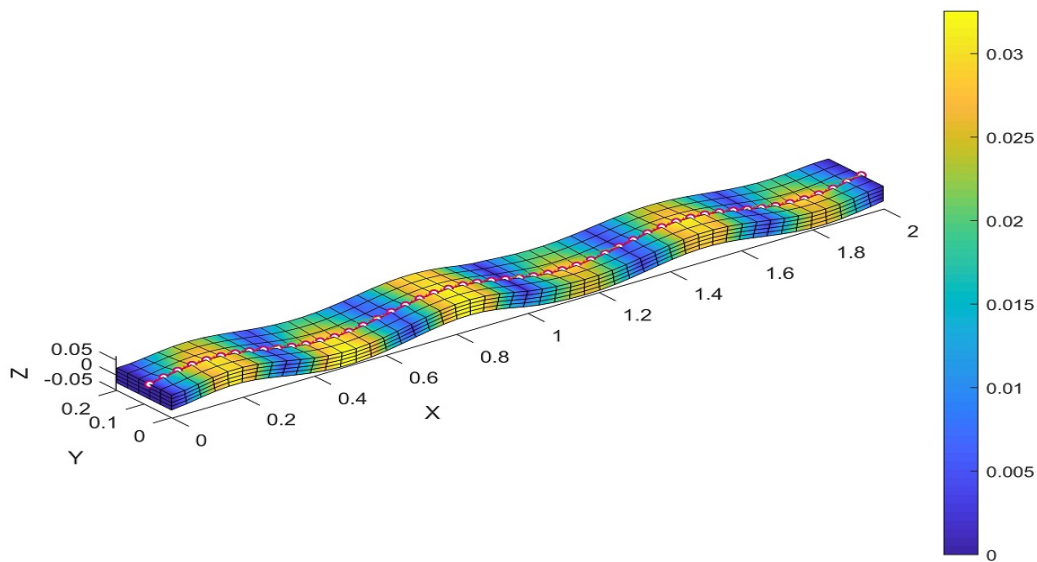


Fig. 5.12 $L_X = 2, L_Y = 0.2, L_Z = 0.05, \Omega_2 : 0.5 \leq X \leq 1.5, AB \approx \delta \sin(6\pi X), E_1 = E_3 = 10^3 \text{Pa}, E_2 = 0.5 \times 10^3 \text{Pa}, E_{beam} = 50 * E_1, \nu_1 = \nu_2 = \nu_3 = 0.3, \Delta T = 1, N_{step} = 5, \lambda_g = 0.01$

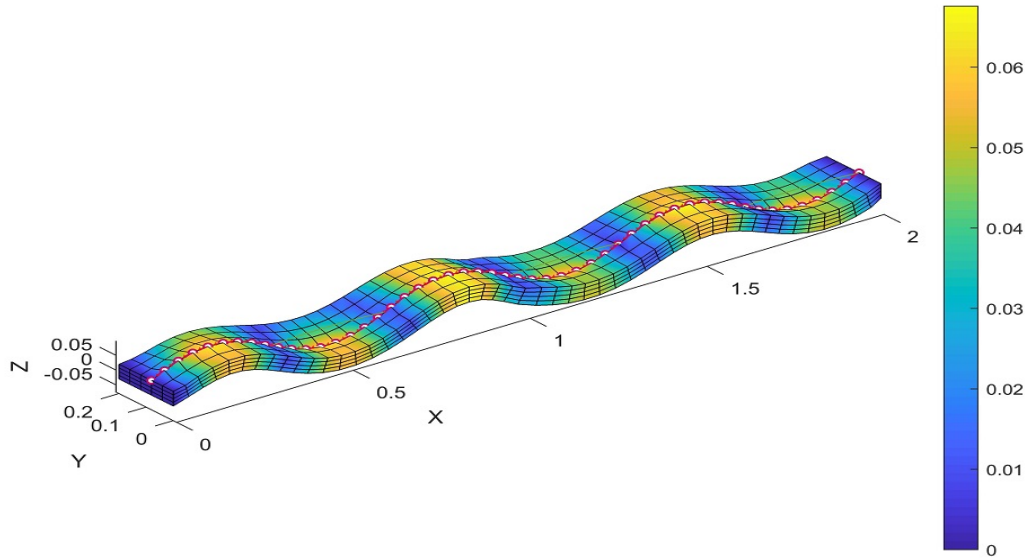


Fig. 5.13 $L_X = 2, L_Y = 0.2, L_Z = 0.05, \Omega_2 : 0.5 \leq X \leq 1.5, AB \approx \delta \sin(6\pi X), E_1 = E_3 = 10^3 \text{Pa}, E_2 = 0.5 \times 10^3 \text{Pa}, E_{beam} = 50 * E_1, \nu_1 = \nu_2 = \nu_3 = 0.3, \Delta T = 1, N_{step} = 10, \lambda_g = 0.06$

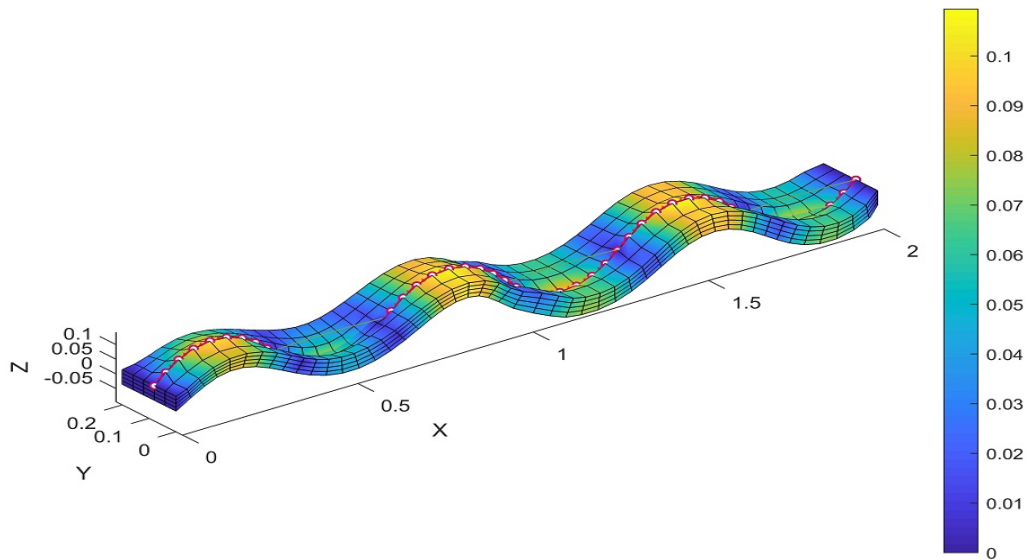


Fig. 5.14 $L_X = 2, L_Y = 0.2, L_Z = 0.05, \Omega_2 : 0.5 \leq X \leq 1.5, AB \approx \delta \sin(6\pi X), E_1 = E_3 = 10^3 \text{Pa}, E_2 = 0.5 \times 10^3 \text{Pa}, E_{beam} = 50 * E_1, \nu_1 = \nu_2 = \nu_3 = 0.3, \Delta T = 1, N_{step} = 15, \lambda_g = 0.16$

We find that the final buckling shape follows the same rule as discussed before. The system prefers to bend instead of expanding laterally.

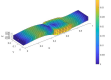
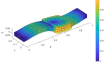
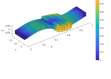
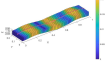
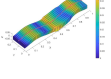
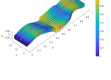
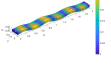
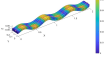
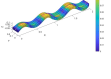
Results	Description
	$L_X = 1, L_Y = 0.2, L_Z = 0.05, \Omega_2 : 0.5 \leq X \leq 0.7, AB \approx \delta \sin(2\pi X), E_1 = E_3 = 10^3 \text{Pa}, E_2 = 0.5 \times 10^3 \text{Pa}, E_{beam} = 50 * E_1, \nu_1 = \nu_2 = \nu_3 = 0.3, \Delta T = 1, N_{step} = 5, \lambda_g = 0.2$
	$L_X = 1, L_Y = 0.2, L_Z = 0.05, \Omega_2 : 0.5 \leq X \leq 0.7, AB \approx \delta \sin(2\pi X), E_1 = E_3 = 10^5 \text{Pa}, E_2 = 0.5 \times 10^5 \text{Pa}, E_{beam} = 50 * E_1, \nu_1 = \nu_2 = \nu_3 = 0.3, \Delta T = 1, N_{step} = 8, \lambda_g = 0.5$
	$L_X = 1, L_Y = 0.2, L_Z = 0.05, \Omega_2 : 0.5 \leq X \leq 0.7, AB \approx \delta \sin(2\pi X), E_1 = E_3 = 10^5 \text{Pa}, E_2 = 0.5 \times 10^5 \text{Pa}, E_{beam} = 50 * E_1, \nu_1 = \nu_2 = \nu_3 = 0.3, \Delta T = 1, N_{step} = 10, \lambda_g = 0.8$
	$L_X = 1, L_Y = 0.2, L_Z = 0.05, \Omega_2 : 0.5 \leq X \leq 0.7, AB \approx \delta \sin(3\pi X), E_1 = E_3 = 10^3 \text{Pa}, E_2 = 0.5 \times 10^3 \text{Pa}, E_{beam} = 50 * E_1, \nu_1 = \nu_2 = \nu_3 = 0.3, \Delta T = 1, N_{step} = 3, \lambda_g = 0.02$
	$L_X = 1, L_Y = 0.2, L_Z = 0.05, \Omega_2 : 0.5 \leq X \leq 0.7, AB \approx \delta \sin(3\pi X), E_1 = E_3 = 10^3 \text{Pa}, E_2 = 0.5 \times 10^3 \text{Pa}, E_{beam} = 50 * E_1, \nu_1 = \nu_2 = \nu_3 = 0.3, \Delta T = 1, N_{step} = 5, \lambda_g = 0.1$
	$L_X = 1, L_Y = 0.2, L_Z = 0.05, \Omega_2 : 0.5 \leq X \leq 0.7, AB \approx \delta \sin(3\pi X), E_1 = E_3 = 10^3 \text{Pa}, E_2 = 0.5 \times 10^3 \text{Pa}, E_{beam} = 50 * E_1, \nu_1 = \nu_2 = \nu_3 = 0.3, \Delta T = 1, N_{step} = 7, \lambda_g = 0.3$
	$L_X = 2, L_Y = 0.2, L_Z = 0.05, \Omega_2 : 0.5 \leq X \leq 1.5, AB \approx \delta \sin(6\pi X), E_1 = E_3 = 10^3 \text{Pa}, E_2 = 0.5 \times 10^3 \text{Pa}, E_{beam} = 50 * E_1, \nu_1 = \nu_2 = \nu_3 = 0.3, \Delta T = 1, N_{step} = 5, \lambda_g = 0.01$
	$L_X = 2, L_Y = 0.2, L_Z = 0.05, \Omega_2 : 0.5 \leq X \leq 1.5, AB \approx \delta \sin(6\pi X), E_1 = E_3 = 10^3 \text{Pa}, E_2 = 0.5 \times 10^3 \text{Pa}, E_{beam} = 50 * E_1, \nu_1 = \nu_2 = \nu_3 = 0.3, \Delta T = 1, N_{step} = 10, \lambda_g = 0.06$
	$L_X = 2, L_Y = 0.2, L_Z = 0.05, \Omega_2 : 0.5 \leq X \leq 1.5, AB \approx \delta \sin(6\pi X), E_1 = E_3 = 10^3 \text{Pa}, E_2 = 0.5 \times 10^3 \text{Pa}, E_{beam} = 50 * E_1, \nu_1 = \nu_2 = \nu_3 = 0.3, \Delta T = 1, N_{step} = 15, \lambda_g = 0.16$

Table 5.1: Summary of computational results with beams and solids

In this section, we have studied the buckling of a bilayer stripe with coupling beam and solid elements. We use the initial curvature to control the final buckling shape with given parameters. When the ECM is much thinner than the soft substrate, this method can help to save computational resources. In the final section we perform 2D simulations with viscoelasticity for local pattern formation.

5.2.3 2D wrinkling and folding simulations

Two cell population with different growth rates could create in-plane compression leading to out-of-plane buckling during the morphological process. In this section, we transfer the growth competition as boundary compression. There are references for elastic problems of bilayer systems [140, 141, 142]. Nevertheless, we try to consider viscosity in this part.

We study a bilayer of the viscoelastic material [143] with different Young's moduli E_α , Poisson coefficients ν_α , shear viscosity η_α and thickness h_α . We assume that the deviatoric part of the strain is governed by the Maxwell model with $\dot{\epsilon}_{\alpha\beta}^d = \frac{1}{2\mu}\dot{\sigma}_{\alpha\beta}^d + \frac{1}{2\eta}\sigma_{\alpha\beta}^d$ where μ is the shear modulus and η is the shear viscosity. The length and the width of the system are L_X and L_Y respectively. In practice, we assume an initial boundary velocity v_X to shorten the soft material and wait long enough until the boundary side approaches the value we want. A defect point is preset in the initial configuration and the mesh is perturbed for non-trivial solutions. Different case studies are shown below. We assume the length scale is $L_X = 100\mu\text{m}$, $L_Y = 10\mu\text{m}$ and $v_X \approx 1\mu\text{m/s}$ in Fig.(5.15). We employ a simple explicit method for the time step with $\Delta t = 0.01\text{s}$.

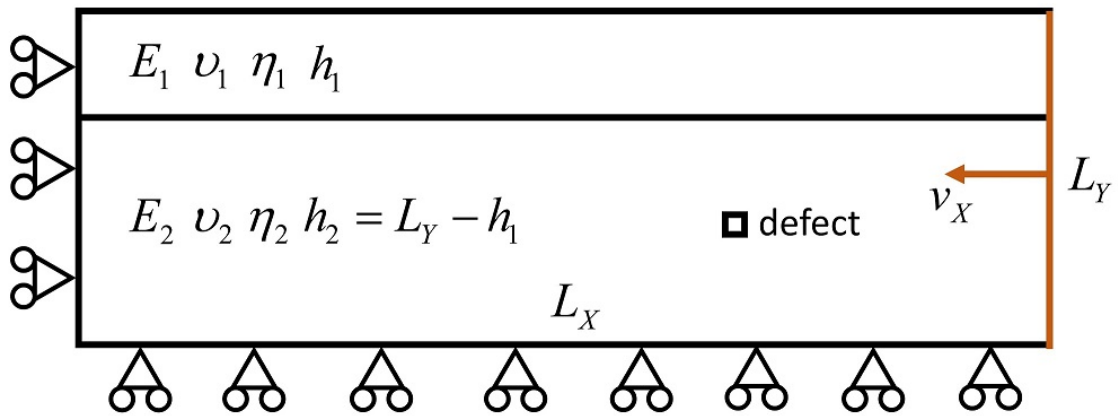


Fig. 5.15 Mechanical sketch of the simulation with boundary conditions: $X = 0, v_1 = 0$; $X = L_X, v_1 = -v_X$; $Y = 0, v_2 = 0$

Fig.(5.15) shows the bilayer system with a roller constraint on the left and a constant compression rate on the right. The Maxwell model can result in different buckling shapes in plane strain with low stress.

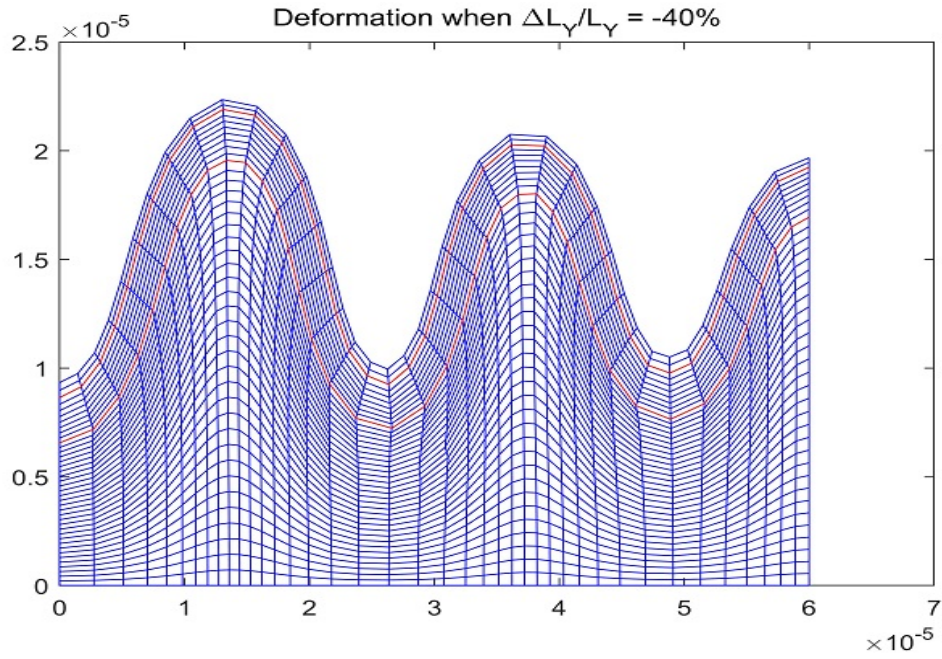


Fig. 5.16 *Wrinkling deformation with $E_1 = 50\text{KPa}$, $E_2 = 1\text{KPa}$, $\nu_1 = 0.3$, $\nu_2 = 0.49$, $\eta_1 = 10^5\text{Pa} \cdot \text{s}$, $\eta_2 = 10^3\text{Pa} \cdot \text{s}$, $L_X = 100\mu\text{m}$, $L_Y = 10\mu\text{m}$, $h_1/L_Y = 0.25$*

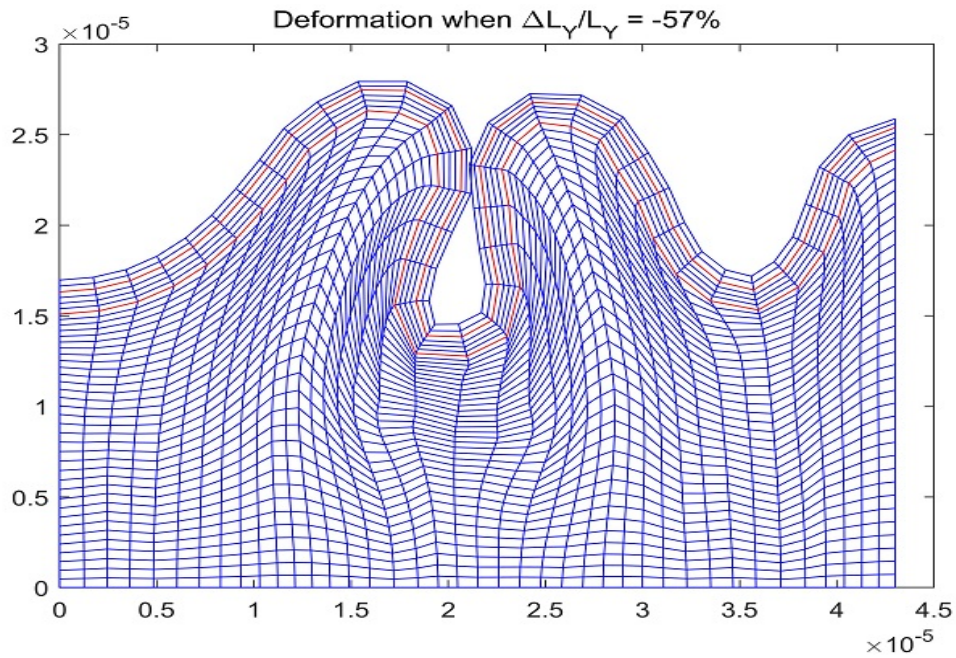


Fig. 5.17 *Folding deformation with $E_1 = 1\text{KPa}$, $E_2 = 50\text{KPa}$, $\nu_1 = 0.3$, $\nu_2 = 0.3$, $\eta_1 = 10^3\text{Pa} \cdot \text{s}$, $\eta_2 = 10\text{Pa} \cdot \text{s}$, $L_X = 100\mu\text{m}$, $L_Y = 10\mu\text{m}$, $h_1/L_Y = 0.15$*

Fig.(5.16) represents a wrinkle-like buckling with given parameters. Fig.(5.17) exhibits fold-

ing. We use the explicit time algorithm for the buckling mode but we do not consider some effects like contact mechanics. In this section, we try to solve the solution with different geometry and material properties which might be controlled in morphology.

a) Geometry effects

We could tune the length L_X and the thickness h_1 to achieve the corresponding shape change.

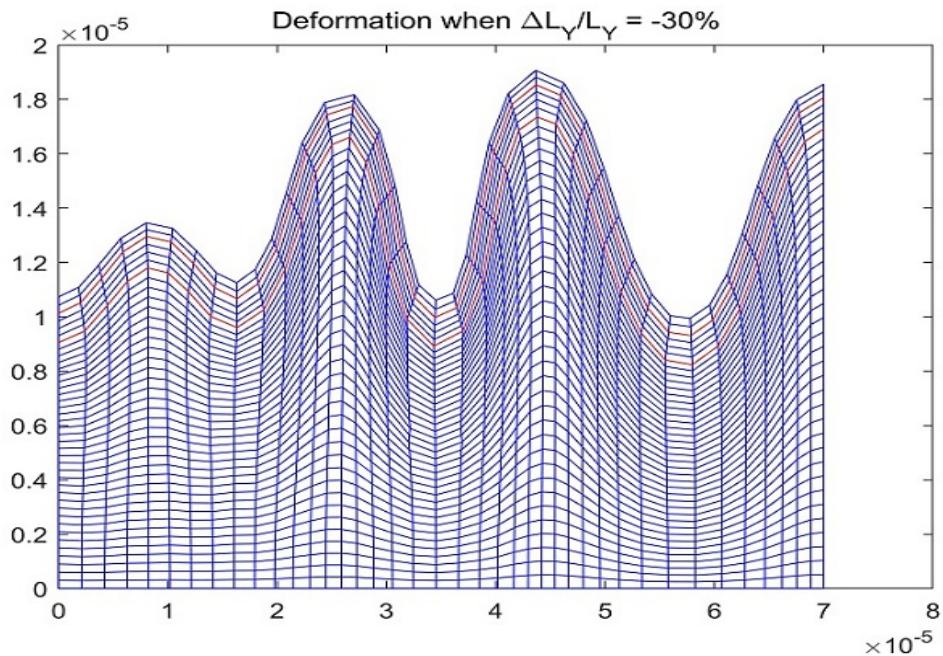


Fig. 5.18 Deformation with $E_1 = 50\text{KPa}$, $E_2 = 1\text{KPa}$, $\nu_1 = 0.3$, $\nu_2 = 0.49$, $\eta_1 = 10^5\text{Pa} \cdot \text{s}$, $\eta_2 = 10^3\text{Pa} \cdot \text{s}$, $L_X = 100\mu\text{m}$, $L_Y = 10\mu\text{m}$, $h_1/L_Y = 0.15$

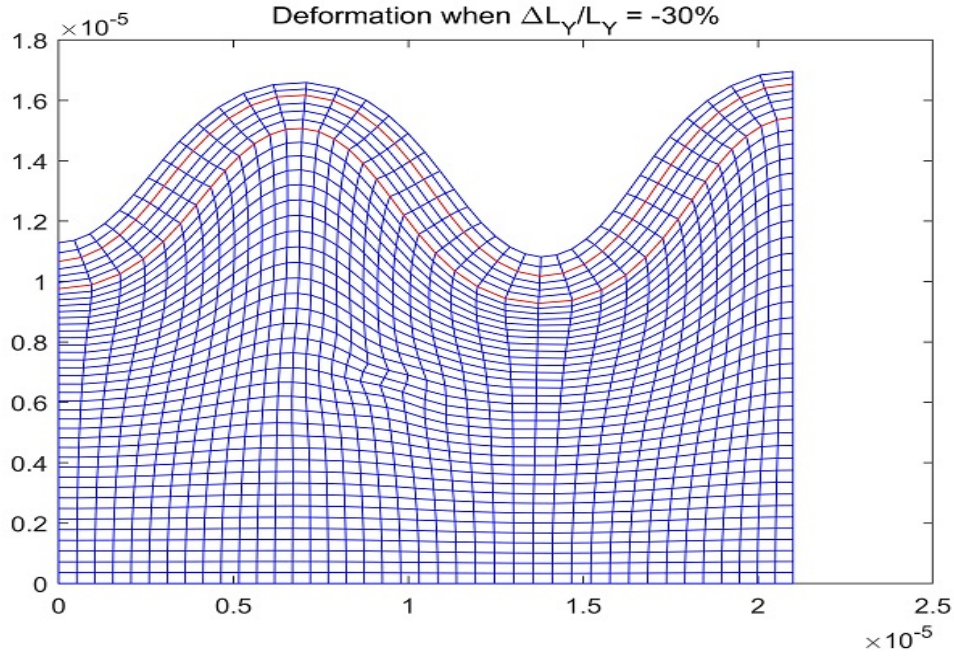


Fig. 5.19 Deformation with $E_1 = 50\text{KPa}$, $E_2 = 1\text{KPa}$, $\nu_1 = 0.3$, $\nu_2 = 0.49$, $\eta_1 = 10^5\text{Pa} \cdot \text{s}$, $\eta_2 = 10^3\text{Pa} \cdot \text{s}$, $L_X = 30\mu\text{m}$, $L_Y = 10\mu\text{m}$, $h_1/L_Y = 0.15$

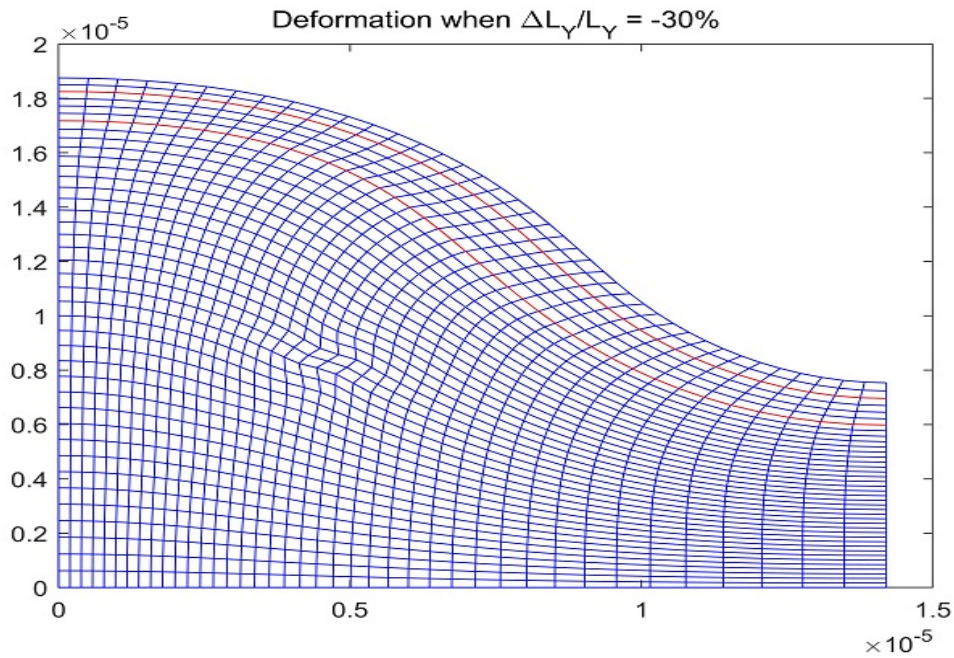


Fig. 5.20 Deformation with $E_1 = 50\text{KPa}$, $E_2 = 1\text{KPa}$, $\nu_1 = 0.3$, $\nu_2 = 0.49$, $\eta_1 = 10^5\text{Pa} \cdot \text{s}$, $\eta_2 = 10^3\text{Pa} \cdot \text{s}$, $L_X = 20\mu\text{m}$, $L_Y = 10\mu\text{m}$, $h_1/L_Y = 0.15$

From Fig.(5.18) to Fig.(5.20), we change the length L_X from 100 to 20. We find that the

wave number of the wrinkle-like solution decreases when the ratio L_X/L_Y drops as predicted in elasticity. However, there is a decay of the peak amplitude from right to left in Fig.(5.18) due to viscosity. In addition, in Fig.(5.20), material accumulates at the left side. It can be explained by the dynamic loading together with the chosen boundary conditions.

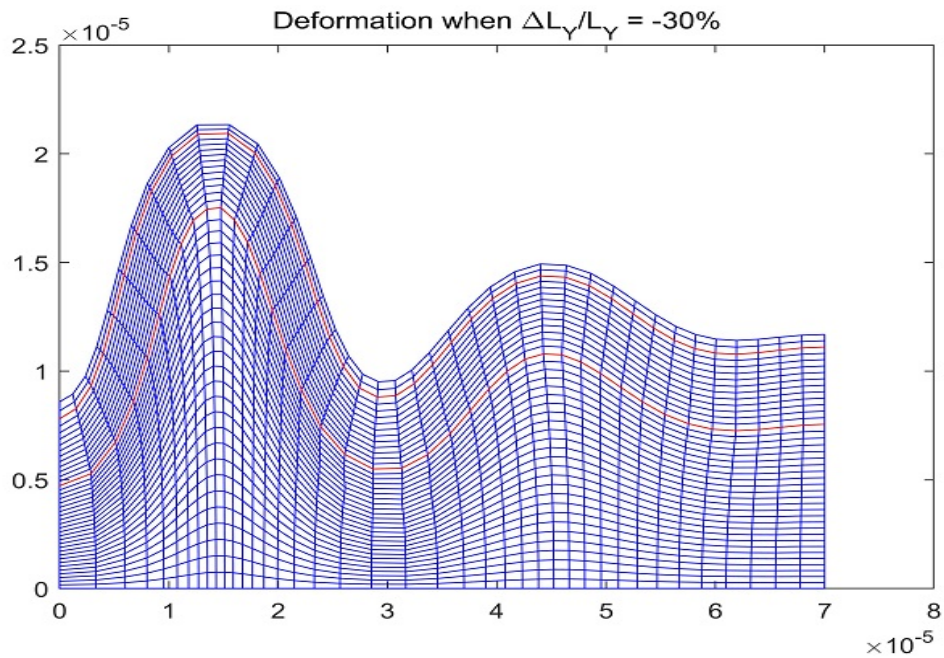


Fig. 5.21 Deformation with $E_1 = 50\text{KPa}$, $E_2 = 1\text{KPa}$, $\nu_1 = 0.3$, $\nu_2 = 0.49$, $\eta_1 = 10^5\text{Pa} \cdot \text{s}$, $\eta_2 = 10^3\text{Pa} \cdot \text{s}$, $L_X = 100\mu\text{m}$, $L_Y = 10\mu\text{m}$, $h_1/L_Y = 0.35$

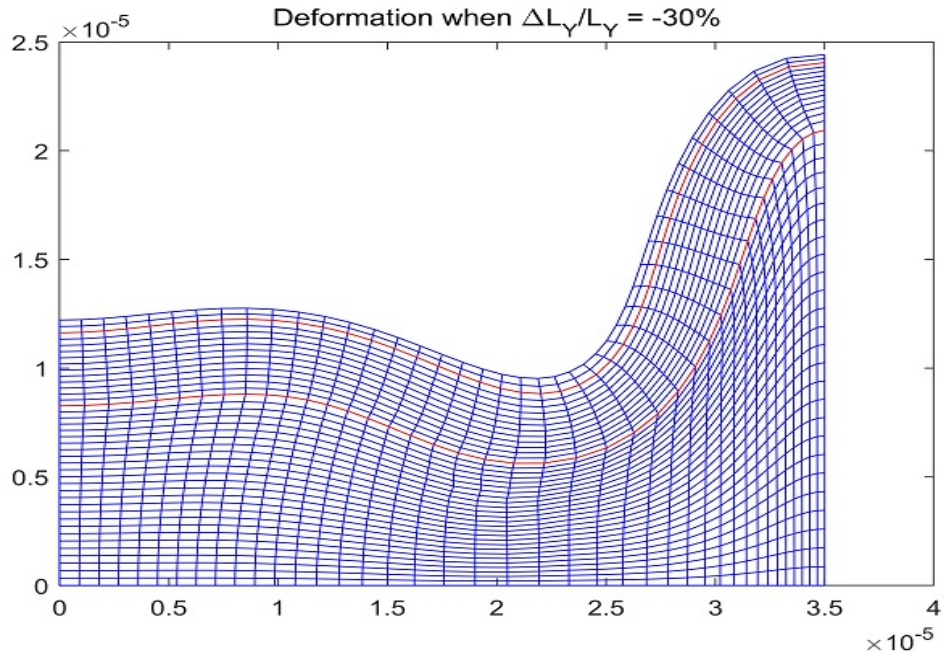


Fig. 5.22 Deformation with $E_1 = 50\text{KPa}$, $E_2 = 1\text{KPa}$, $\nu_1 = 0.3$, $\nu_2 = 0.49$, $\eta_1 = 10^5\text{Pa} \cdot \text{s}$, $\eta_2 = 10^3\text{Pa} \cdot \text{s}$, $L_X = 50\mu\text{m}$, $L_Y = 10\mu\text{m}$, $h_1/L_Y = 0.35$

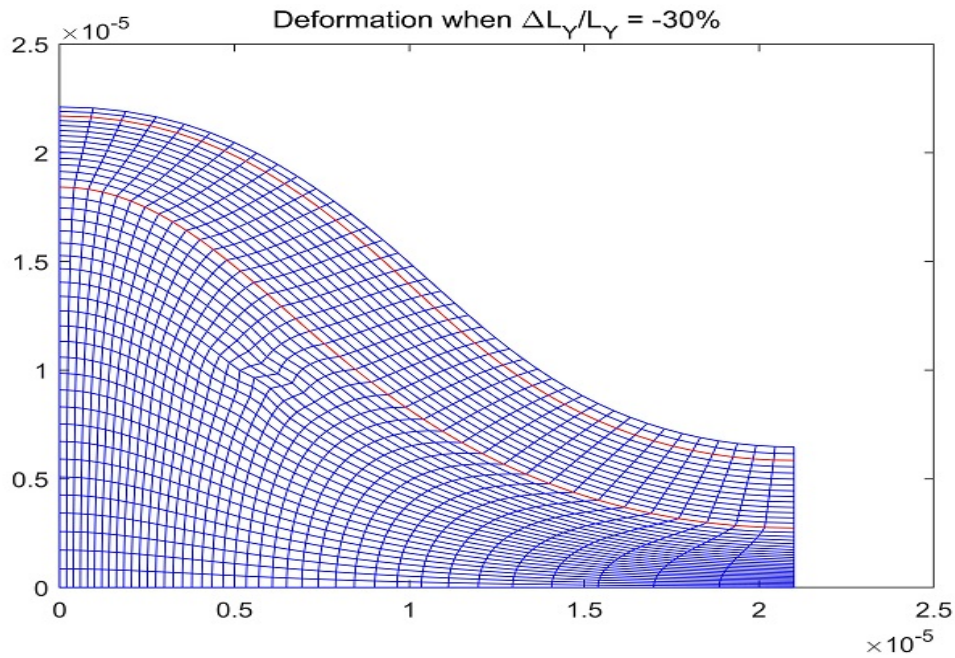


Fig. 5.23 Deformation with $E_1 = 50\text{KPa}$, $E_2 = 1\text{KPa}$, $\nu_1 = 0.3$, $\nu_2 = 0.49$, $\eta_1 = 10^5\text{Pa} \cdot \text{s}$, $\eta_2 = 10^3\text{Pa} \cdot \text{s}$, $L_X = 30\mu\text{m}$, $L_Y = 10\mu\text{m}$, $h_1/L_Y = 0.35$

Then we increase the ratio h_1/L_Y which corresponds to an increase of the thickness of the

upper layer. Two unusual buckling shapes appear in Fig.(5.21) and Fig.(5.22) due to the time effect. In this section, we find that the geometry as well as the dynamics can generate different buckling shapes. Next we will discuss the role of material parameters.

b) Material properties

Material properties like Young's modulus and viscosity can also determine the final buckling shape as follows

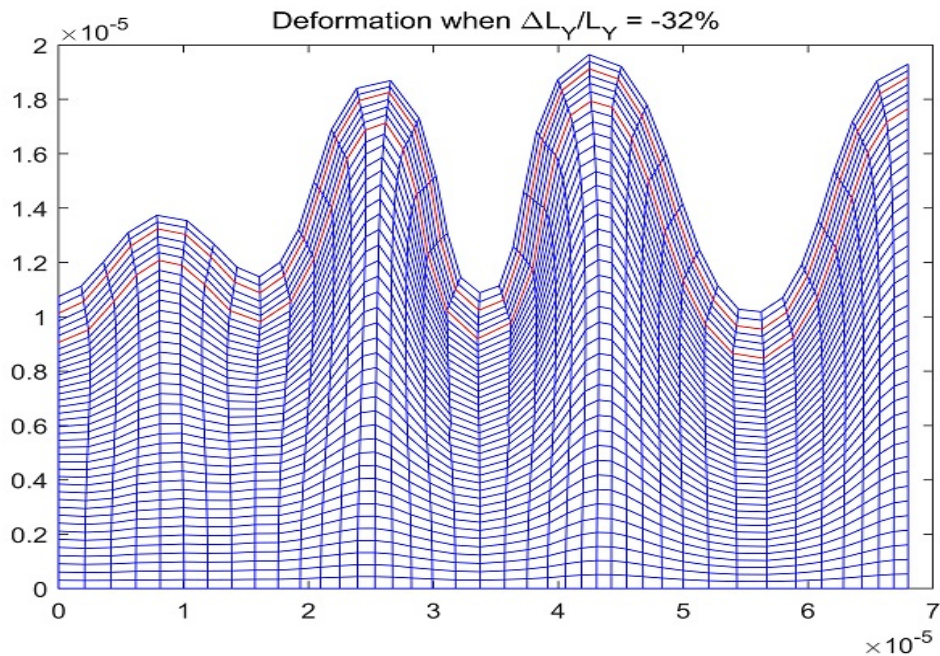


Fig. 5.24 Deformation with $E_1 = 50\text{KPa}$, $E_2 = 1\text{KPa}$, $\nu_1 = 0.3$, $\nu_2 = 0.49$, $\eta_1 = 10^5\text{Pa} \cdot \text{s}$, $\eta_2 = 10^3\text{Pa} \cdot \text{s}$, $L_X = 100\mu\text{m}$, $L_Y = 10\mu\text{m}$, $h_1/L_Y = 0.15$

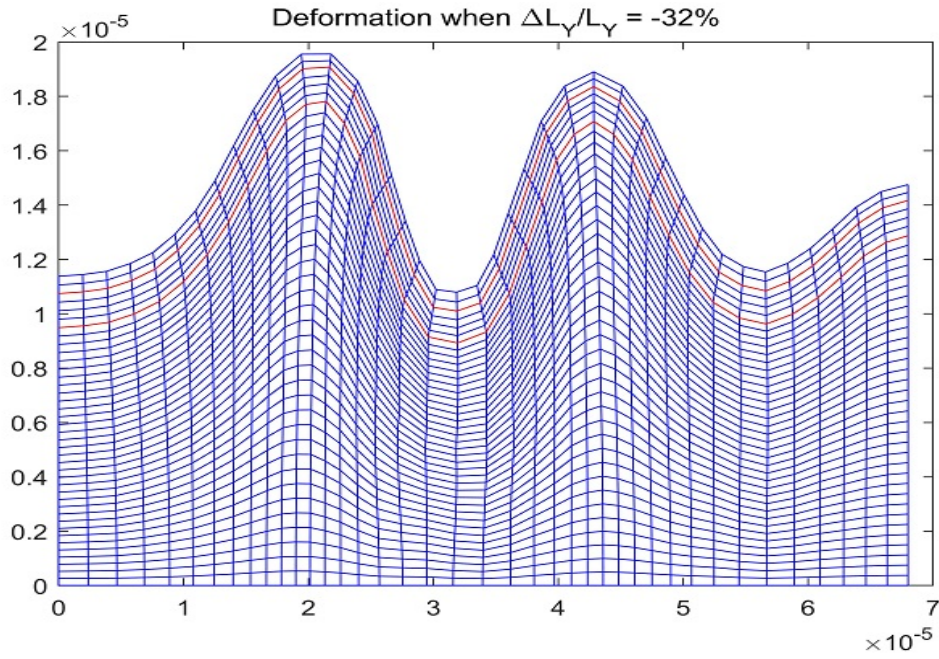


Fig. 5.25 Deformation with $E_1 = 50\text{KPa}$, $E_2 = 1\text{KPa}$, $\nu_1 = 0.3$, $\nu_2 = 0.49$, $\eta_1 = 10^3\text{Pa} \cdot \text{s}$, $\eta_2 = 10\text{Pa} \cdot \text{s}$, $L_X = 100\mu\text{m}$, $L_Y = 10\mu\text{m}$, $h_1/L_Y = 0.15$

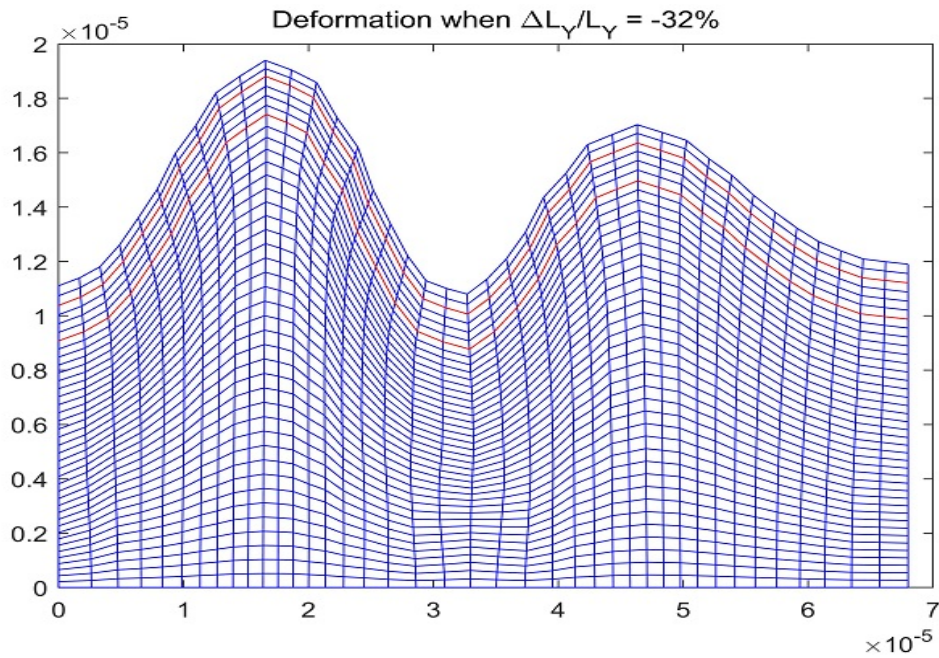


Fig. 5.26 Deformation with $E_1 = 50\text{KPa}$, $E_2 = 1\text{KPa}$, $\nu_1 = 0.3$, $\nu_2 = 0.49$, $\eta_1 = 10\text{Pa} \cdot \text{s}$, $\eta_2 = 10^{-1}\text{Pa} \cdot \text{s}$, $L_X = 100\mu\text{m}$, $L_Y = 10\mu\text{m}$, $h_1/L_Y = 0.15$

Comparing Fig.(5.24,5.25,5.26), we observe that the wave number decreases as the shear

viscosity η declines.

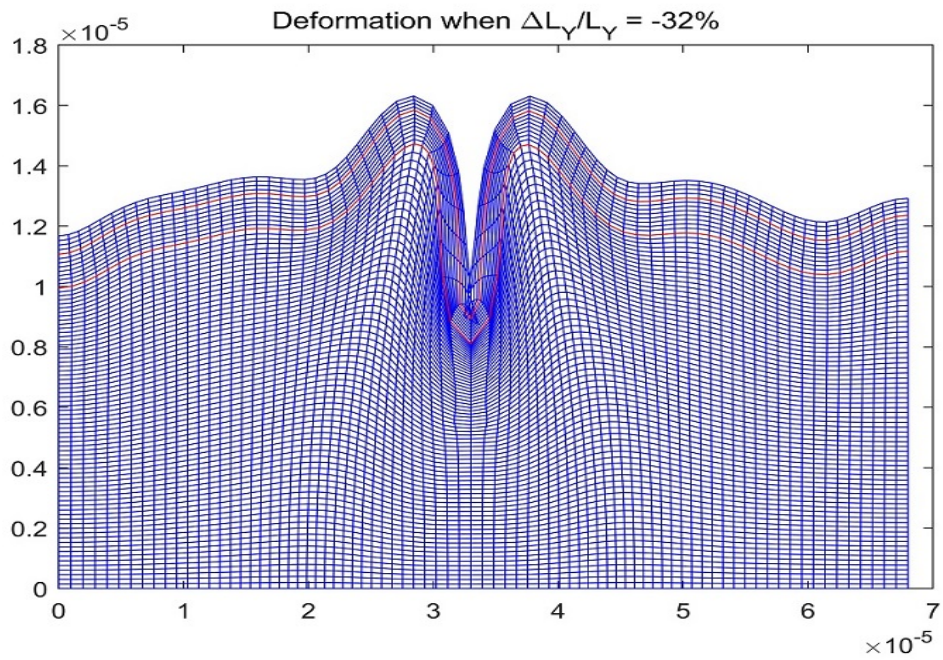


Fig. 5.27 Deformation with $E_1 = 1\text{KPa}$, $E_2 = 1\text{KPa}$, $\nu_1 = 0.3$, $\nu_2 = 0.3$, $\eta_1 = 10^5\text{Pa} \cdot \text{s}$, $\eta_2 = 10^3\text{Pa} \cdot \text{s}$, $L_X = 100\mu\text{m}$, $L_Y = 10\mu\text{m}$, $h_1/L_Y = 0.15$

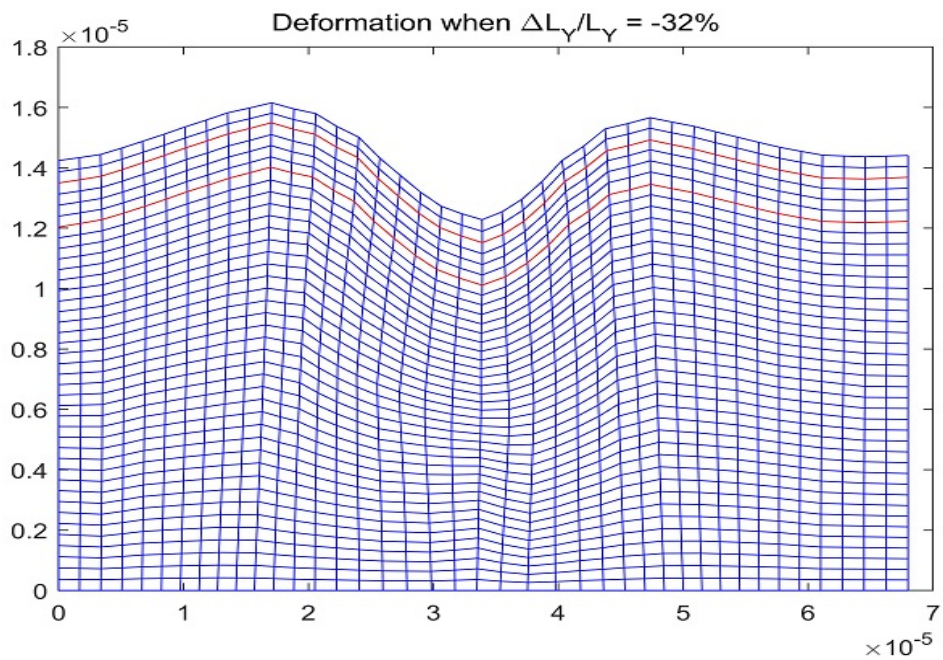


Fig. 5.28 Deformation with $E_1 = 1\text{KPa}$, $E_2 = 1\text{KPa}$, $\nu_1 = 0.3$, $\nu_2 = 0.3$, $\eta_1 = 10^{-2}\text{Pa} \cdot \text{s}$, $\eta_2 = 10^{-4}\text{Pa} \cdot \text{s}$, $L_X = 100\mu\text{m}$, $L_Y = 10\mu\text{m}$, $h_1/L_Y = 0.15$

We now adjust the stiffness. There is a ridge in Fig.(5.27) with $E_1 = E_2$. With a drop of viscosity in Fig.(5.28), the deformation tends to be flat.

c) **Clamped boundary**

We then squeeze the bilayer system assuming the left and the right side are clamped as follows

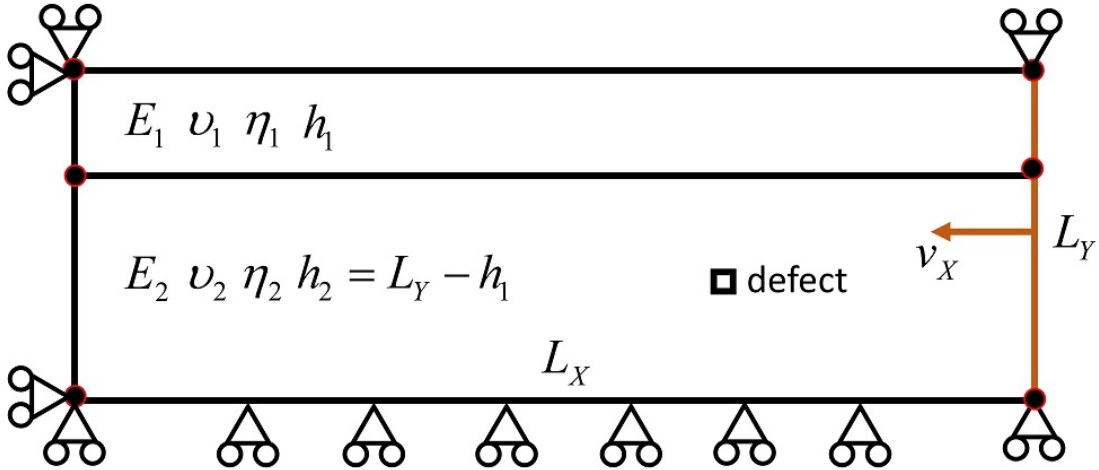


Fig. 5.29 Mechanical sketch of the simulation with fixed boundary conditions: $X = 0, v_1 = v_2 = 0$; $X = L_X, v_1 = -v_X, v_2 = 0$; $Y = 0, v_2 = 0$

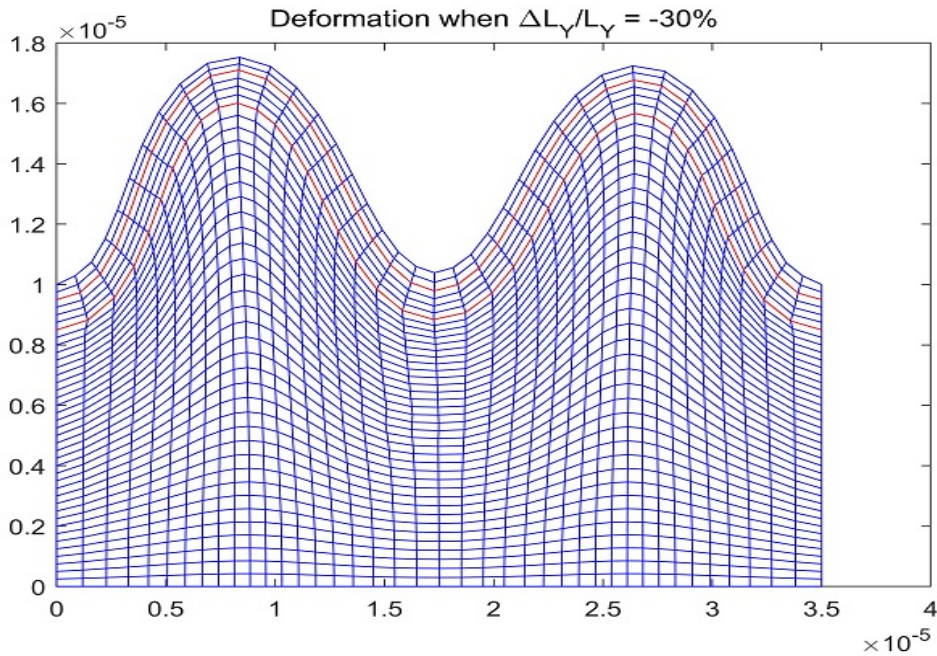


Fig. 5.30 Deformation with $E_1 = 50\text{KPa}, E_2 = 1\text{KPa}, \nu_1 = 0.3, \nu_2 = 0.49, \eta_1 = 10^5\text{Pa} \cdot \text{s}, \eta_2 = 10^3\text{Pa} \cdot \text{s}, L_X = 50\mu\text{m}, L_Y = 10\mu\text{m}, h_1/L_Y = 0.15$

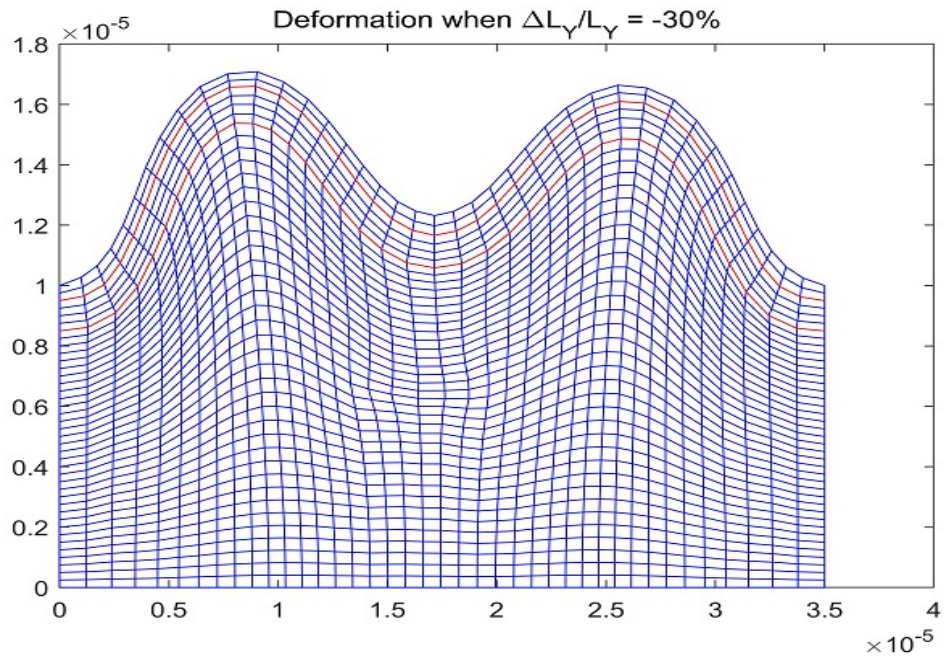


Fig. 5.31 Deformation with $E_1 = 50\text{KPa}$, $E_2 = 1\text{KPa}$, $\nu_1 = 0.3$, $\nu_2 = 0.49$, $\eta_1 = 10^3\text{Pa} \cdot \text{s}$, $\eta_2 = 10\text{Pa} \cdot \text{s}$, $L_X = 50\mu\text{m}$, $L_Y = 10\mu\text{m}$, $h_1/L_Y = 0.15$

We find two symmetric wrinkle solutions with different viscosity in Fig.(5.30) and Fig.(5.31).

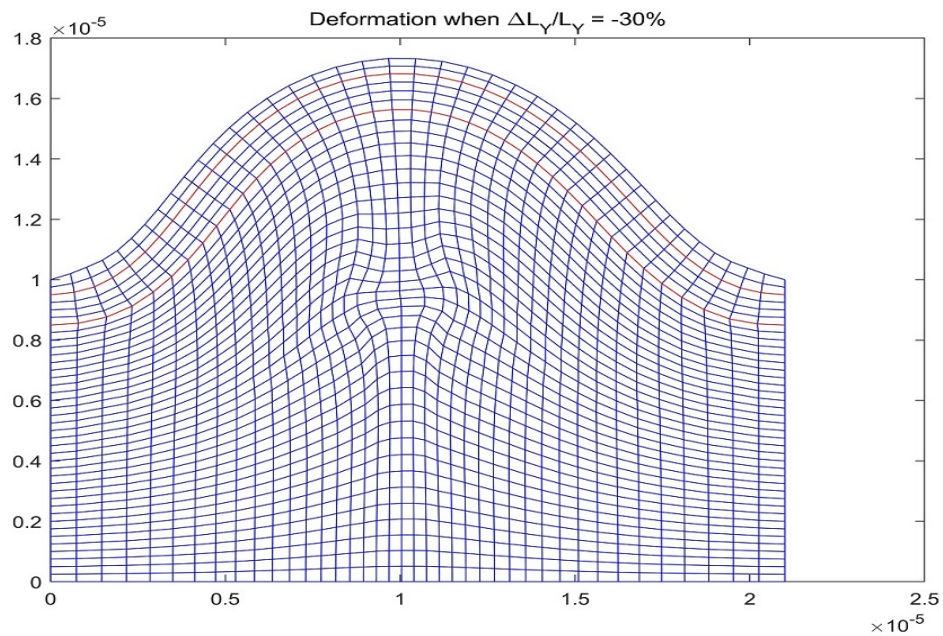


Fig. 5.32 Deformation with $E_1 = 50\text{KPa}$, $E_2 = 1\text{KPa}$, $\nu_1 = 0.3$, $\nu_2 = 0.49$, $\eta_1 = 10^5\text{Pa} \cdot \text{s}$, $\eta_2 = 10^3\text{Pa} \cdot \text{s}$, $L_X = 30\mu\text{m}$, $L_Y = 10\mu\text{m}$, $h_1/L_Y = 0.15$

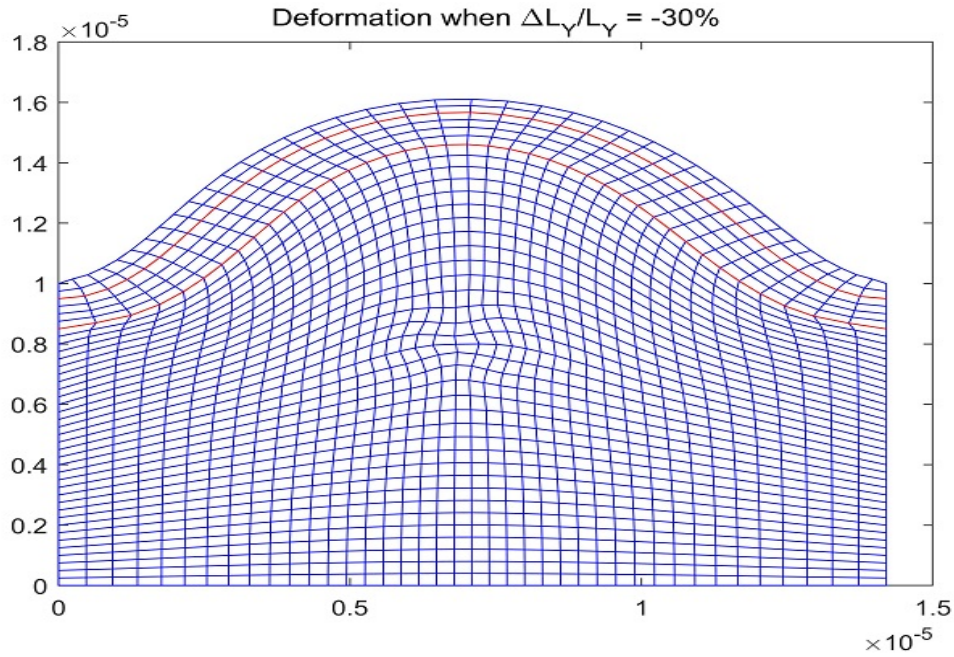


Fig. 5.33 Deformation with $E_1 = 50\text{KPa}$, $E_2 = 1\text{KPa}$, $\nu_1 = 0.3$, $\nu_2 = 0.49$, $\eta_1 = 10^5\text{Pa} \cdot \text{s}$, $\eta_2 = 10^3\text{Pa} \cdot \text{s}$, $L_X = 20\mu\text{m}$, $L_Y = 10\mu\text{m}$, $h_1/L_Y = 0.15$

Finally we reduce the length and the wave number decreases.

In this part, we have considered a bilayer system with different stiffnesses and viscosity. Geometry, material properties and boundary effects are discussed. Different buckling shapes are acquired with given parameters. In biology, growth with boundary constraints might generate amazing buckling deformation.

Results	Description
	Deformation with $E_1 = 50\text{KPa}$, $E_2 = 1\text{KPa}$, $\nu_1 = 0.3$, $\nu_2 = 0.49$, $\eta_1 = 10^5\text{Pa} \cdot \text{s}$, $\eta_2 = 10^3\text{Pa} \cdot \text{s}$, $L_X = 100\mu\text{m}$, $L_Y = 10\mu\text{m}$, $h_1/L_Y = 0.15$
	Deformation with $E_1 = 50\text{KPa}$, $E_2 = 1\text{KPa}$, $\nu_1 = 0.3$, $\nu_2 = 0.49$, $\eta_1 = 10^5\text{Pa} \cdot \text{s}$, $\eta_2 = 10^3\text{Pa} \cdot \text{s}$, $L_X = 30\mu\text{m}$, $L_Y = 10\mu\text{m}$, $h_1/L_Y = 0.15$
	Deformation with $E_1 = 50\text{KPa}$, $E_2 = 1\text{KPa}$, $\nu_1 = 0.3$, $\nu_2 = 0.49$, $\eta_1 = 10^5\text{Pa} \cdot \text{s}$, $\eta_2 = 10^3\text{Pa} \cdot \text{s}$, $L_X = 20\mu\text{m}$, $L_Y = 10\mu\text{m}$, $h_1/L_Y = 0.15$
	Deformation with $E_1 = 50\text{KPa}$, $E_2 = 1\text{KPa}$, $\nu_1 = 0.3$, $\nu_2 = 0.49$, $\eta_1 = 10^5\text{Pa} \cdot \text{s}$, $\eta_2 = 10^3\text{Pa} \cdot \text{s}$, $L_X = 100\mu\text{m}$, $L_Y = 10\mu\text{m}$, $h_1/L_Y = 0.35$
	Deformation with $E_1 = 50\text{KPa}$, $E_2 = 1\text{KPa}$, $\nu_1 = 0.3$, $\nu_2 = 0.49$, $\eta_1 = 10^5\text{Pa} \cdot \text{s}$, $\eta_2 = 10^3\text{Pa} \cdot \text{s}$, $L_X = 50\mu\text{m}$, $L_Y = 10\mu\text{m}$, $h_1/L_Y = 0.35$
	Deformation with $E_1 = 50\text{KPa}$, $E_2 = 1\text{KPa}$, $\nu_1 = 0.3$, $\nu_2 = 0.49$, $\eta_1 = 10^5\text{Pa} \cdot \text{s}$, $\eta_2 = 10^3\text{Pa} \cdot \text{s}$, $L_X = 30\mu\text{m}$, $L_Y = 10\mu\text{m}$, $h_1/L_Y = 0.35$
	Deformation with $E_1 = 50\text{KPa}$, $E_2 = 1\text{KPa}$, $\nu_1 = 0.3$, $\nu_2 = 0.49$, $\eta_1 = 10^5\text{Pa} \cdot \text{s}$, $\eta_2 = 10^3\text{Pa} \cdot \text{s}$, $L_X = 100\mu\text{m}$, $L_Y = 10\mu\text{m}$, $h_1/L_Y = 0.15$
	Deformation with $E_1 = 50\text{KPa}$, $E_2 = 1\text{KPa}$, $\nu_1 = 0.3$, $\nu_2 = 0.49$, $\eta_1 = 10^3\text{Pa} \cdot \text{s}$, $\eta_2 = 10\text{Pa} \cdot \text{s}$, $L_X = 100\mu\text{m}$, $L_Y = 10\mu\text{m}$, $h_1/L_Y = 0.15$
	Deformation with $E_1 = 50\text{KPa}$, $E_2 = 1\text{KPa}$, $\nu_1 = 0.3$, $\nu_2 = 0.49$, $\eta_1 = 10\text{Pa} \cdot \text{s}$, $\eta_2 = 10^{-1}\text{Pa} \cdot \text{s}$, $L_X = 100\mu\text{m}$, $L_Y = 10\mu\text{m}$, $h_1/L_Y = 0.15$
	Deformation with $E_1 = 1\text{KPa}$, $E_2 = 1\text{KPa}$, $\nu_1 = 0.3$, $\nu_2 = 0.3$, $\eta_1 = 10^5\text{Pa} \cdot \text{s}$, $\eta_2 = 10^3\text{Pa} \cdot \text{s}$, $L_X = 100\mu\text{m}$, $L_Y = 10\mu\text{m}$, $h_1/L_Y = 0.15$
	Deformation with $E_1 = 1\text{KPa}$, $E_2 = 1\text{KPa}$, $\nu_1 = 0.3$, $\nu_2 = 0.3$, $\eta_1 = 10^{-2}\text{Pa} \cdot \text{s}$, $\eta_2 = 10^{-4}\text{Pa} \cdot \text{s}$, $L_X = 100\mu\text{m}$, $L_Y = 10\mu\text{m}$, $h_1/L_Y = 0.15$
	Deformation with $E_1 = 50\text{KPa}$, $E_2 = 1\text{KPa}$, $\nu_1 = 0.3$, $\nu_2 = 0.49$, $\eta_1 = 10^5\text{Pa} \cdot \text{s}$, $\eta_2 = 10^3\text{Pa} \cdot \text{s}$, $L_X = 50\mu\text{m}$, $L_Y = 10\mu\text{m}$, $h_1/L_Y = 0.15$, clamped
	Deformation with $E_1 = 50\text{KPa}$, $E_2 = 1\text{KPa}$, $\nu_1 = 0.3$, $\nu_2 = 0.49$, $\eta_1 = 10^3\text{Pa} \cdot \text{s}$, $\eta_2 = 10\text{Pa} \cdot \text{s}$, $L_X = 50\mu\text{m}$, $L_Y = 10\mu\text{m}$, $h_1/L_Y = 0.15$, clamped
	Deformation with $E_1 = 50\text{KPa}$, $E_2 = 1\text{KPa}$, $\nu_1 = 0.3$, $\nu_2 = 0.49$, $\eta_1 = 10^5\text{Pa} \cdot \text{s}$, $\eta_2 = 10^3\text{Pa} \cdot \text{s}$, $L_X = 30\mu\text{m}$, $L_Y = 10\mu\text{m}$, $h_1/L_Y = 0.15$, clamped
	Deformation with $E_1 = 50\text{KPa}$, $E_2 = 1\text{KPa}$, $\nu_1 = 0.3$, $\nu_2 = 0.49$, $\eta_1 = 10^5\text{Pa} \cdot \text{s}$, $\eta_2 = 10^3\text{Pa} \cdot \text{s}$, $L_X = 20\mu\text{m}$, $L_Y = 10\mu\text{m}$, $h_1/L_Y = 0.15$, clamped

Table 5.2: Summary of computational results with 2D solids

5.3 Conclusion

In this chapter, we have built a FEM platform for geometrically nonlinear problems. The toolbox is set up in MATLAB. 3D solid elements are built in for the modeling of the growing

epithelium [7, 25]. Via structural coupling, the additional bending contribution of the ECM is achieved by appending beam elements. Growth and inner stress by beams and solids can also be considered with an updated algorithm. We employ it to the 3D strip buckling in our case. This tool box could be used as a supplementary solver for COMSOL since COMSOL lacks the Riks method for post-buckling analysis.

Then a 2D bilayer has been studied with viscosity. Different geometric and material parameters are treated with two distinct boundary conditions. In contrast to the purely elastic hypothesis, viscosity can generate more complicated buckling solutions due to growth and boundary constraints.

Chapter 6

Conclusion

The main purpose of this thesis is to study the epithelium with growth from the view point of macroscopic continuum mechanics. Two biological systems with the epithelium and ECM are concerned: *C. elegans* and *Drosophila* wing disc. We make an attempt to use classical elasticity theory as well as numerical simulations to explain the experiments. We propose a modified crack opening formula for a stress assessment on the epithelium of *C. elegans*. On the other hand, we try to use structural mechanics to mimic the *Drosophila* wing disc buckling by a homogenization method. In addition, we start to set up a FEM platform for the geometrically nonlinear problems in COMSOL and MATLAB.

6.1 Crack opening on epithelium of *C.elegans*

Finite strain theory is favored in our case of *C. elegans* elongation up to 70%. Pre-stretch with an initial opening angle of about 30° is also considered in the analysis. After simplification of the complex geometry, we succeed to provide the theoretical prediction of stress and strain. The anisotropic actin-myosin network with active stress is taken into account. In order to apply the experimental data by laser cut ablation, we amend the crack opening formula $\mathcal{F} = 2\sigma^\infty/E$ into Eq.(3.31) as $\mathcal{F}_\alpha = 2\sigma_\alpha/E_\alpha$ where σ_α is the total stress including the active part and E_α is an equivalent Young's modulus. Specially, this formula is a good estimate when the laser cut is parallel or perpendicular to the eigenvector of the stress tensor. For real size evaluation, we apply the extended finite element method (XFEM) as a numerical tool. Tilting angle and biaxial loading can be easily set during the simulation. It shows that, within the limit $\delta\beta \leq 10^\circ$ and $k_0 \leq 1$, our theoretical prediction works with an error $\leq 10\%$. The stress intensity factor (SIF) is also obtained. According to the theoretical analysis, active stress is of the same order as the passive one during *C. elegans* elongation. It explains the crack opening in both orthogonal directions even when the epithelium is under contractile deformation. Laser cut ablation technique is proved to be a practical auxiliary method for the stress distribution assessment for biological systems in vivo. But our method is not quite appropriate for large tilting angle $\delta\beta$ in the case of anisotropy. In addition, we do not consider the complex geometry in the simulations. If possible, it is necessary to take more mechanical experiments to simulate the crack opening with polymer networks.

6.2 Buckling of *Drosophila* wing disc

The Föppl-Von Kármán (FvK) model with growth is extended to a bilayer specimen including the monolayer epithelium and stiffer ECM. If the structure is relatively thin compared with other length scales, we can use the homogenization method by taking the integral over the thickness. We assume different material properties in each layer. Varying growth will lead to an inner momentum $M_{\alpha\beta}^g$, Eq.(4.7), once the neutral surface Z_n is determined. Z_n is given by minimizing the elastic energy Eq.(4.20). Hereafter we obtain the equivalent bending stiffness D in Eq.(4.7) and make the governing equations Eq.(4.6) closed with well-defined boundary conditions. Since the in-plane membrane force might affect the position of the neutral surface, we then perturbate Z_n leading to Eq.(4.30). An analytical solution is found in 1D with unsymmetrical branches shown in Fig.(4.1). An ECM defect can change the buckling shape as well as the buckling mode (see Fig.(4.2)). Then we implement this nonlinear effect as a simple quadratic term in the numerical toolbox MANLAB.

For FEM implementation, we choose two methods in chapter 4 and 5 respectively. First we use a shell module in COMSOL with an equivalent monolayer model. Growth is considered as inelastic strain with linear decomposition. Additional bending by growth and active networks is covered. We focus on the local exponential case with all kinds of parameters including the ECM defect and we utilize a self-defined weak form to consider the nonlinear effect. Different buckling shapes in 3D are obtained by appropriate input. Then we try to use beam and solid elements to simulate the buckling of bilayer structures. We employ an updated Lagrangian algorithm and simplify the biological system of the epithelium with stiffer ECM as 3D solid elements coupled with a nonlinear Euler beam network. In Fig.(5.4), we provide different buckling solutions by tuning the stiffness of the beam and growth. Furthermore, a FEM platform is under preparation in MATLAB. Finally 2D wrinkling and folding simulations are studied for a Maxwell viscoelastic bilayer. In contrast to pure elasticity, viscosity and boundary conditions can affect the final buckling shape which might explain the real situation.

However, we do not take full use of the micro structure of the biological system. We need to bridge different scales by coupling techniques and a meso-scale theory is important to understand the biophysics.

Publication

Assessing the Contribution of Active and Passive Stresses in *C. elegans* ElongationMartine Ben Amar,^{1,2,*} Paul Qiuyang-Qu,¹ Thanh Thi Kim Vuong-Brender,³ and Michel Labouesse⁴¹*Laboratoire de Physique Statistique, Ecole Normale Supérieure, PSL Research University; Sorbonne Université, UPMC Univ Paris 06; CNRS; 24 rue Lhomond, 75005 Paris, France*²*Institut Universitaire de Cancérologie, Faculté de médecine, Université Pierre et Marie Curie-Paris 6, 91 Bd de l'Hôpital, 75013 Paris, France*³*MRC Laboratory of Molecular Biology, Francis Crick Avenue, Cambridge Biomedical Campus, Cambridge CB2 0QH, United Kingdom*⁴*Laboratoire de Biologie du Développement—Institut de Biologie Paris Seine (LBD—IBPS), Sorbonne Université, UPMC Univ Paris 06, CNRS, Paris, France*

(Received 1 August 2018; revised manuscript received 17 October 2018; published 28 December 2018)

The role of the actomyosin network is investigated in the elongation of *C. elegans* during embryonic morphogenesis. We present a model of active elongating matter that combines prestress and passive stress in nonlinear elasticity. Using this model we revisit recently published data from laser ablation experiments to account for why cells under contraction can lead to an opening fracture. By taking into account the specific embryo geometry, we obtain quantitative predictions for the contractile forces exerted by the molecular motors myosin II for an elongation up to 70% of the initial length. This study demonstrates the importance of active processes in embryonic morphogenesis and the interplay between geometry and nonlinear mechanics during morphological events. In particular, it outlines the role of each connected layer of the epidermis compressed by an apical extracellular matrix that distributes the stresses during elongation.

DOI: [10.1103/PhysRevLett.121.268102](https://doi.org/10.1103/PhysRevLett.121.268102)

Mechanical stresses play a crucial role in animal embryo genesis. At the macroscopic level, differential growth generates compressive stresses creating the circumvolutions of intestine [1–3], brain cortex [4–6], and fingerprints of skin [7,8]. The folding of tissues is then directly linked to the coupling between volumetric growth, tissue properties, and geometry. At the cellular level, the interplay between mechanics and morphological events such as division, migration, and tissue organization is much more subtle. The high deformability of cells is counterbalanced by the cellular filament networks, especially by the actomyosin cortex. It comprises a network of cross-linked actin filaments located below the plasma membrane, so that the local cell contractility results from the myosin molecular motors which transform the chemical energy of ATP hydrolysis into contractile stresses. How these microscopic processes at the cell level cooperate to induce shape transition at the tissue level is central in “active matter.” At early stages in small organisms such as *Drosophila* [9] or *C. elegans* [10], the number of cells is relatively small and the structure is simple enough, giving perhaps a way to bridge scales between microscopic activity and observable tissue displacements. Both of these biological species are considered as model systems where the theoretical framework of active matter [11–15] can be applied and more importantly quantified by analyzing experimental data. Here we investigate the early stage of *C. elegans* elongation up to 70% when the embryo contains 65 epidermal cells in

the cortical position in an ovoid shell. Among available approaches, laser cuts in different locations on live embryos allow us to evaluate either the tension or the stiffness [16], quantities necessary to assess the active stresses at the origin of the elongation [17,18]. Since, in this process, there is no cytokinesis or apoptosis and no position exchange between neighboring cells, we select a continuum approach of active matter to predict the fracture opening. However, as highlighted in Refs. [19,20], the difficulty in active matter consists in evaluating the stresses: active or passive for samples with complex geometry and elastic properties. To this end, one must comprehend the nonlinearities of shape transformations in these small organisms with a limited information on mechanical quantities.

The aim of this Letter is to investigate this problematic when only some characteristics are known for *C. elegans* embryos. Our scope is to estimate the activity of the molecular motors and to compare it to the elastic resistance. For that, we establish an analytical model based on nonlinear elasticity for soft tissues and compare our predictions with measurements by laser ablation [16]. The proposed treatment can be adapted to other morphogenetic events in embryogenesis.

Laser ablation.—Fracture opening gives a way to determine the forces at the cellular level. This technique helps to experimentally deduce the tensile stress in the perpendicular direction to the fracture line when the cell stiffness is known. Conversely, when the stresses are well

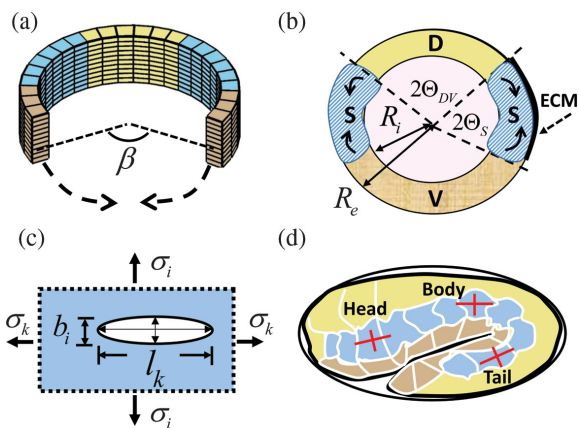


FIG. 1. The ventral enclosure of *C. elegans*. (a) Schematic representation before enclosure. (b) Horizontal section at enclosure. Different colors are chosen: yellow for the dorsal (D), blue for the seam (S), and brown for the ventral (V) cells. (c) Schema of a planar fracture under tensile stresses. (d) Position of laser fractures achieved in the embryo [16].

identified, it gives some insights on the fiber network organization. Indeed, the crack opening in linear elasticity is an ellipse [21] and the shape factor (opening b_i along x_i divided by the crack length l_k along x_k) is given by $\mathcal{F}_{ik} = b_i/l_k \sim 2\sigma_i/E$, where σ_i is the tension and E the Young modulus, see Fig. 1(c). For \mathcal{F}_{ik} , other stress components than σ_i do not play a role and for an anisotropic sample, E must be replaced by E_i the stiffness in the x_i direction [16].

In a recent work [16], Vuong-Brender *et al.* apply this technique in different parts of *C. elegans* [in Fig. 1(d)] and demonstrate that the cracks always open both in the dorso-ventral (DV) and in the anterior-posterior (AP) directions. If the crack opening is not a surprise in AP , it is more puzzling in the DV direction for various reasons, Fig. 1(d). First, cracks cannot open in compression (except in some very specific conditions [22]). Because of volume conservation, an extension in AP leads automatically to a contraction in DV . In addition, myosin II, the actin molecular motors have been observed [23–26] in the seam (S) domain [blue in Figs. 1(a), 1(b), 1(d)], and these motors are contractile. Even more intriguing, in S cells, the opening is larger in the DV than in the AP direction [16]. The theoretical interpretation of these experiments cannot be captured by the linear elasticity framework. To recover the shape factor \mathcal{F}_{ik} requires evaluating first the state of stresses or strains inside the embryo before elongation and then incorporating the active stresses due to molecular motors. By coupling them, the modeling must recover the results of the laser ablation but also the possibility to elongate the embryo up to 70%. Nonetheless, in nonlinear elasticity, and to the best of our knowledge, there is no general formula for crack opening but only local analysis of the stresses at both ends [27,28]. A simple analogy between linear and nonlinear

elasticities suggests to replace σ by the equivalent Cauchy stress σ_i and E by the local stiffness E_i . The following addresses the evaluation of these two quantities in the nonlinear elasticity framework beginning first by the geometry analysis.

Geometry and strains.—The morphogenetic events of the embryo elongation consist of cell intercalation and ventral enclosure [10]. The displacements of matter are strongly constrained by the limited space and induce significant strains [29]. In particular, the ventral enclosure, schematized by Fig. 1(a), cannot be achieved without local forces to join the two parts of the epithelial cortex, as demonstrated by myosin accumulation [23,24]. Hence, when elongation begins, the tissues have already stored prestrains and prestresses [20] and the measurements in Ref. [16] result from those cumulated stresses. Their evaluation requires a complete knowledge of the history, which is difficult to assess. A possible simplified scenario will be the enclosure of a cylindrical partial shell with a lacking angular sector β , see Fig. 1(a), by orthoradial stretching. But this shell is made of a nonhomogeneous epidermis with 3 kinds of cells called hereafter dorsal (D), seam (S), and ventral (V) cells; see Fig. 1(b). Once the suture is achieved, the embryo becomes a composite cylinder made of a row of epithelial cells and nascent intestine. Besides, it is covered by the extracellular matrix (ECM), a thin layer of secreted proteins. In the stress-free configuration, before enclosure, the D cells occupy one sector between $[-\phi_{DV}, \phi_{DV}]$, S cells are located between $[\phi_{DV}, \tilde{\beta} - \phi_{DV}]$, and V cells fill the remaining sector up to $\tilde{\beta} = \pi - \beta/2$ [Fig. 1(a) and in the Supplemental Material [30]]. From the mechanical viewpoint, we do not make a distinction between the D and V cells and now call them DV cells. As shown in the Supplemental Material [30], at full enclosure [FE, Fig. 1(b)], the position of material points are defined by R, Θ, Z and then becomes r, θ, z with elongation. At FE, the epidermis lies between the inner R_i and the outer R_e radius. It is possible to map the stress-free configuration onto the current one and then to define the elastic strains, but one must keep in mind that the experimental results refer to the beginning of elongation which is not a stress-free state. This distinction is essential in nonlinear elasticity. We call G the angular stretch defined by $\theta = G\Theta$, which varies with the axial stretch Λ_Z and the domain area. We hypothesize that at FE, all parts are stretched in the orthoradial direction so $G_0 > 1$. The two unknown parameters of the initial geometry (e.g., $\tilde{\beta}$ and Θ_{DV}) are determined in the Supplemental Material [30] by arclength measurements [16]. Looking for the simplest solution where strains and stresses remain diagonal, the deformation gradient tensor defined by $\mathbf{F} = \text{Diag}(\Lambda_R, \Lambda, \Lambda_Z)$ is then $\mathbf{F} = \text{Diag}(\partial r/\partial R, Gr/R, dz/dZ)$. Resulting from both enclosure and elongation, the elastic tensor \mathbf{F}_e defined by $\text{Diag}(\lambda_R, \lambda, \lambda_Z)$ reads $\mathbf{F}_e = \mathbf{F}\mathbf{F}_0$. \mathbf{F}_0 is the prestretch tensor defined by 2 independent eigenvalues:

$\mathbf{F}_0 = \text{Diag}((\lambda_0 \lambda_{0Z})^{-1}, \lambda_0, \lambda_{0Z})$, since the incompressibility imposes $\lambda_R = 1/(\lambda \lambda_Z)$. (See also the Supplemental Material [30]). These tensors are defined everywhere in the cylinder and are different in S or DV domains. Only the elongations Λ_Z and λ_{0Z} will remain identical in all parts for reasons of integrity. Since there is no cell division during the process, the volume conservation in the epithelium gives

$$r^2 - r_i^2 = \frac{1}{G \Lambda_Z} (R^2 - R_i^2), \quad (1)$$

which allows us to calculate G , knowing that at the border of the interior zone, $\Lambda = r_i/R_i = 1/\sqrt{\Lambda_Z}$. In the Supplemental Material [30], it is shown how the angular stretch G for S and DV cells, Fig. 2, is obtained from measurements of the circumferential lengths published in Ref. [16]. Since data are available only at $\Lambda_Z = 1.3, 1.5$, extrapolation at $\Lambda_Z = 1$ is used. Agreement between modeling and experimental data [30] validates the first steps with an epithelium thickness of order $2 \mu\text{m}$. Mechanical stresses can now be evaluated.

Equilibrium equations and boundary conditions.—The crack opening reaches its finite value after only a few seconds, which is in the same order of magnitude as the velocities of actomyosin flows (in the order of $1 \mu\text{m/s}$ [31,32]). Focusing on the equilibrium value of the slit opening, we can neglect viscoelasticity [33,34]. Then, in cylindrical geometry, the Cauchy stress σ , diagonal as the deformation gradient tensor \mathbf{F}_e , satisfies

$$\frac{\partial \sigma_r}{\partial r} + \frac{1}{r}(\sigma_r - \sigma_\theta) = 0, \quad (2)$$

where σ_r and σ_θ are the radial and orthonormal components in the current configuration. This equation is identical in

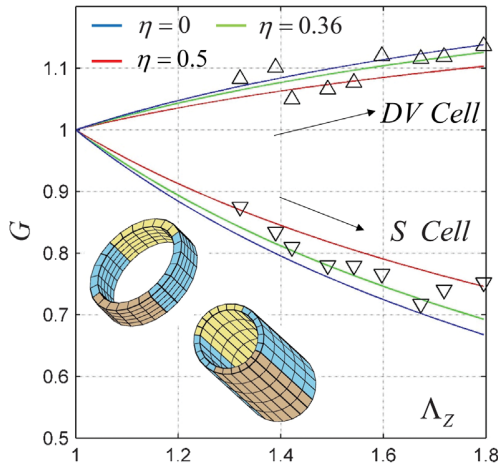


FIG. 2. Angular stretch for S and DV cells. Notice that $G_S < 1$ for S and $G_{DV} > 1$ for D cells. Theoretical curves, explained in the Supplemental Material [30], are weakly dependent of the epidermis thickness, represented by $\eta = 1 - (R_i/R_e)^2$. Comparison with experimental data from Ref. [16].

linear elasticity [35]. Equation (2) requires only one boundary condition, chosen at the apical border, just below the ECM whose thickness is about 10^{-2} the embryo radius [16,26]. So, it imposes a weak compressive surface stress, $\sigma_r \sim 0$, during elongation. Defining W_P as the passive elastic energy density, each stress component becomes $\sigma_k = \lambda_k(\partial W_P/\partial \lambda_k) + \sigma_k^a - p$ [17,18], where p is a Lagrange parameter ensuring the incompressibility and σ_k^a the active stress which only exists in the S cells. σ_k^a can be decomposed into a volumetric $\sigma^{a,v}$ and a deviatoric $\sigma^{a,d}$ part defined by: $\sigma^{a,v} = \zeta_{a,v} \mathbf{I}$ and $\sigma^{a,d} = \zeta \text{Diag}(0, 1, -1)$ [14,19]. $\zeta_{a,v}$ may be included into the Lagrange parameter p (a detailed demonstration can be found in the Supplemental Material [30]). Conversely, the deviatoric part is a traceless tensor with no specific sign. Finally, the definition of a new energy functional [36]: $\tilde{W}_P = W_P[(\lambda \lambda_Z)^{-1}, \lambda, \lambda_Z]$ enforces automatically incompressibility giving:

$$\begin{aligned} \sigma_\theta &= \sigma_\theta^p + \sigma_r + \zeta; & \sigma_z &= \sigma_z^p + \sigma_r - \zeta; \\ \sigma_\theta^p &= \lambda \frac{\partial \tilde{W}_P}{\partial \lambda}; & \sigma_z^p &= \lambda_Z \frac{\partial \tilde{W}_P}{\partial \lambda_Z}, \end{aligned} \quad (3)$$

where σ_θ^p and σ_z^p decouple from the active part ζ . Once Eq. (2) is solved, all stresses can be calculated explicitly [30]. Since fractures are made superficially on the outer surface where $\sigma_r \sim 0$, only σ_θ and σ_z are the components of interest for our study.

Evaluation of the stresses and fracture opening.—In these epithelial cells, it was found [25] that both microtubules and actin filaments are oriented mainly in the orthonormal direction in both cells. So we choose the simplest constitutive law as a superposition of a matrix and a fiber network elasticity:

$$W_P = \frac{\mu}{2} (\lambda_R^2 + \lambda^2 + \lambda_Z^2 - 3) + \frac{\tau}{4} (\lambda^2 - 1)^2, \quad (4)$$

when orientation along θ is imposed. Such superposition is currently achieved with some variants concerning the last term [37,38]. Choosing the S cell coefficient μ_S as the unit of elastic energy, we estimate that $\mu_{DV} > 1$ to represent a stiffer material and $\tau_S < \tau_{DV}$, to represent a weaker degree of fiber alignment in S cells. Since orientation is the same for actin or microtubules [16,25], a unique coefficient τ involves both filaments.

At **FE**, the state of the cylinder is characterized by 3 independent prestrain quantities which are the orthonormal stretches (λ_{0S} and λ_{0DV}) and the axial stretch λ_{0Z} ; see the Supplemental Material [30]. Within the thin epithelium approximation, $\eta = 1 - R_i^2/R^2 \ll 1$, one easily finds $G_0 \sim \lambda_0 \sqrt{\lambda_{0Z}}$, from Eq. (1). From the geometry, the lacking angle of the sector reads $\beta \sim 2(\pi - \tilde{\beta}) \sim 2\pi[1 - (\sqrt{\lambda_{0Z}} \lambda_{0S})^{-1}]$. In addition, λ_{0S} and λ_{0DV} values must be compatible with the continuity of the orthonormal stresses $\sigma_{\theta,S} = \sigma_{\theta,DV}$ at **FE**,

TABLE I. Geometric and elastic parameters of the model in different parts of the embryo.

	C_{0S} μm	C_{0DV} μm	λ_{0Z}	λ_{0S}	λ_{0DV}	α_1	α_2
Head	14.5	33.0	1.025	1.06	1.0326	2.2	1.27
Body	10.1	24.8	1.025	1.09	1.05	1.15	3.2
Tail	10.1	24.8	1.055	1.05	1.0232	1.25	2.9

Elastic coefficients: $\mu_{DV} = 1.44$, $\tau_S = 0.15$, $\tau_{DV} = 0.67$

The circumference lengths C_0 are extrapolated from Refs. [16,30]. λ_0 , values at enclosure, differ in S and DV and from head to tail. The coefficients α 's refer to active stress evolution, see Fig. 3(c). The elastic parameters of Eq. (4) do not vary along the embryo.

which fixes the ratio of stiffnesses between the S and DV cells with $\lambda_{0DV} < \lambda_{0S}$. Post enclosure, the prestrains modify the elastic strains into $\lambda = \lambda_0 \Lambda = \lambda_0 G r / R$ and $\lambda_Z = \lambda_{0Z} \Lambda_Z$ (see the Supplemental Material [30]). This explains why a tissue remains in tension even if contractile motors exert a compressive work on it. For a thin epithelium, the elastic stretch λ is transformed into $\lambda \sim \lambda_0 G / \sqrt{\Lambda_Z}$ and we have now $\sigma_{\theta,S}^p + \zeta = \sigma_{\theta,DV}^p$, which gives ζ . G_S decreases as Λ_Z increases leading to a decrease of the passive stress σ_{θ}^p . However, the active stress ζ , an increasing function of Λ_Z , compensates the opening of cracks in the DV direction. Finally, because the epithelial elasticity is both orthotropic and nonlinear, the adapted mathematical formula for the shape factor \mathcal{F}_{ik} is deduced from W_p , Eq. (4). The equivalent Young modulus in the i th direction reads

$$E_i = K_{ii} - \frac{K_{ij}^2}{K_{jj}}; \quad K_{ij} = \lambda_j \frac{\partial \sigma_i^p}{\partial \lambda_j} \quad \text{and} \quad \mathcal{F} \sim 2 \frac{\sigma_i^p + \zeta_i}{E_i}. \quad (5)$$

This evaluation presents no difficulty once the elastic energy density is known, albeit this question remains challenging for small organisms.

Results and discussion.—The incompressibility hypothesis and the cylindrical shape are tested by comparing the angular stretch G with the experimental values of each domain: seam, dorsal, and ventral (see Fig. 2 and Table I). There is a slow dependence with the thickness of the epidermis which is reassuring since this thickness in the order of $2 \mu\text{m}$ is not known with precision. By extrapolation, we derive a value of each arclength at the ‘‘supposed’’ beginning of elongation and finally an angle of order $\beta \sim 26^\circ$, indicating a significant prestretch at enclosure, associated with a prestress about 0.45 for σ_{θ} and 0.35 for σ_Z . As shown in Figs. 3(b) and 3(c) the amplitude of the active stress ζ is an increasing function of Λ_Z which saturates around the value 1.8. Above this value, a new mechanism involving muscle cells [39–41] occurs, not considered here as we focus on the role of the actomyosin network. Once the elastic energy W_p is obtained from the body results, this energy function is fixed everywhere: in the head and in the tail, only the prestretch values due to enclosure are very slightly modified as shown in Table I. After, the theoretical curves are derived from \mathcal{F} , Eq. (5) and shown in Fig. 3(a). Notice that the active stress ζ is derived from the difference between passive parts of the S and DV cells with an empirical formula of 2 parameters: $\zeta = 2\alpha_1 \pi^{-1} \tan^{-1} \alpha_2 (\Lambda_Z - 1)$. The agreement is good for the crack opening in S cells. All the results concerning this elongation step in the *C. elegans* embryonic life are gathered in Table I. The methodology to derive these parameters, which rest on the border conditions and available experimental data, is explained in detail in the Supplemental Material [30].

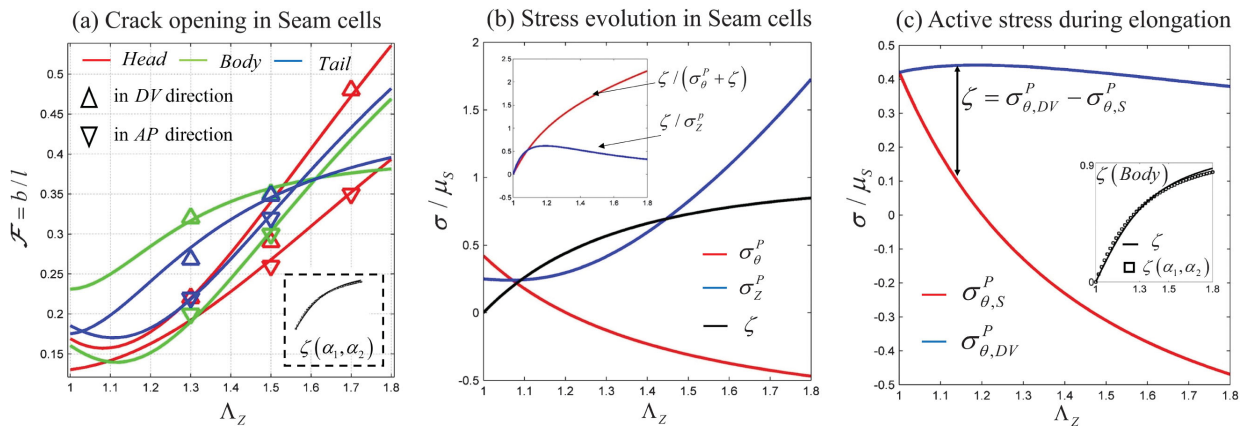


FIG. 3. (a) Crack opening in S cells for head, body and tail in the DV or AP directions, Eq. (5). Difference between curves comes from prestrain values, Table I and the Supplemental Material [30]. In the inset, the active stress ζ beginning at enclosure. (b) Comparison of passive versus active stress in S cells [Eqs. (3), (4)]. The scale for stresses is the stiffness of S cells $\mu_S = 1$. (c) Active stress evaluated as the difference of σ_{θ}^p between DV and S cells. In the inset, ζ , deduced from the model and approximated by $\zeta = 2\alpha_1 \pi^{-1} \tan^{-1} \alpha_2 (\Lambda_Z - 1)$ with 2 parameters is given in Table I.

To conclude, as emphasized in Ref. [20], it is especially delicate to extract quantitative information from nonlinear mechanical systems involving active and passive stresses and, in addition, prestretch and prestress. The complexity increases with the geometry for a multilayered inhomogeneous epidermis trapped between a central intestine and the apical ECM. *In vivo* measurements, difficult at the scale of the cell are made possible thanks to the technique of laser ablation which, combined with this analysis, gives a satisfactory picture of how molecular motors can achieve cell and embryo deformations. Even if the focus is put on *C. elegans* geometry, the theory developed here can be adapted to other systems where laser ablation is achieved to assess stresses and illustrates how prestress can be accounted for *in vivo*. The role of mechanics in embryogenesis needs not to be demonstrated anymore. However, it is crucial to develop experimental and theoretical tools to fully understand the origin of morphogenetic events in model systems.

M. B. A. would like to thank the Isaac Newton Institute of Mathematical Sciences, Cambridge, for support and hospitality during the programme “Growth, Form and Self-Organization” where work on this Letter was undertaken. M. B. A. acknowledges the partial support from the Simons Foundation, the EPSRC Grant No. EP/K032208/1 and from ANR under the Contract No. EPIMORPH (ANR-18-CE13-0008). P. Q. Q. acknowledges the support of the China Scholarship Council (CSC), file No. 201706100182. M. L. thanks the European Research Council (Grant No. 294744) for support.

*Corresponding author.
benamar@lps.ens.fr

- [1] A. J. Coulombre and J. L. Coulombre, Intestinal development: I. Morphogenesis of the villi and musculature, *Development* **6**, 403 (1958).
- [2] E. Hannezo, J. Prost, and J.-F. Joanny, Instabilities of Monolayered Epithelia: Shape and Structure of Villi and Crypts, *Phys. Rev. Lett.* **107**, 078104 (2011).
- [3] M. Ben Amar and F. Jia, Anisotropic growth shapes intestinal tissues during embryogenesis, *Proc. Natl. Acad. Sci. U.S.A.* **110**, 10525 (2013).
- [4] R. Toro and Y. Burnod, A morphogenetic model for the development of cortical convolutions, *Cereb. Cortex* **15**, 1900 (2005).
- [5] A. Goriely, M. G. Geers, G. A. Holzapfel, J. Jayamohan, A. Jérusalem, S. Sivaloganathan, W. Squier, J. A. van Dommelen, S. Waters, and E. Kuhl, Mechanics of the brain: Perspectives, challenges, and opportunities, *Biomech. Model. Mechanobiol.* **14**, 931 (2015).
- [6] M. Ben Amar and A. Bordner, Mimicking cortex convolutions through the wrinkling of growing soft bilayers, *J. Elast.* **129**, 213 (2017).
- [7] M. Kücken and A. C. Newell, Fingerprint formation, *J. Theor. Biol.* **235**, 71 (2005).
- [8] P. Ciarletta and M. Ben Amar, Papillary networks in the dermal–epidermal junction of skin: A biomechanical model, *Mech. Res. Commun.* **42**, 68 (2012).
- [9] I. Heemskerk, T. Lecuit, and L. LeGoff, Dynamic clonal analysis based on chronic *in vivo* imaging allows multiscale quantification of growth in the *Drosophila* wing disc, *Development* **141**, 2339 (2014).
- [10] A. D. Chisholm and J. Hardin, Epidermal morphogenesis, in *WormBook: The Online Review of C. elegans Biology* (2005).
- [11] P. Nardinocchi and L. Teresi, On the active response of soft living tissues, *J. Elast.* **88**, 27 (2007).
- [12] F. Jülicher, K. Kruse, J. Prost, and J.-F. Joanny, Active behavior of the cytoskeleton, *Phys. Rep.* **449**, 3 (2007).
- [13] M. C. Marchetti, J.-F. Joanny, S. Ramaswamy, T. B. Liverpool, J. Prost, M. Rao, and R. A. Simha, Hydrodynamics of soft active matter, *Rev. Mod. Phys.* **85**, 1143 (2013).
- [14] J. Prost, F. Jülicher, and J.-F. Joanny, Active gel physics, *Nat. Phys.* **11**, 111 (2015).
- [15] S. Redemann, J. Baumgart, N. Lindow, M. Shelley, E. Nazockdast, A. Kratz, S. Prohaska, J. Brugués, S. Fürthauer, and T. Müller-Reichert, *C. elegans* chromosomes connect to centrosomes by anchoring into the spindle network, *Nat. Commun.* **8**, 15288 (2017).
- [16] T. T. K. Vuong-Brender, M. Ben Amar, J. Pontabry, and M. Labouesse, The interplay of stiffness and force anisotropies drives embryo elongation, *eLife* **6**, e23866 (2017).
- [17] A. Goriely, Five ways to model active processes in elastic solids: Active forces, active stresses, active strains, active fibers, and active metrics, *Mech. Res. Commun.* **93**, 75 (2018).
- [18] F. Jülicher, S. W. Grill, and G. Salbreux, Hydrodynamic theory of active matter, *Rep. Prog. Phys.* **81**, 076601 (2018).
- [19] E. Fischer-Friedrich, Y. Toyoda, C. J. Cattin, D. J. Müller, A. A. Hyman, and F. Jülicher, Rheology of the active cell cortex in mitosis, *Biophys. J.* **111**, 589 (2016).
- [20] E. Fischer-Friedrich, Active prestress leads to an apparent stiffening of cells through geometrical effects, *Biophys. J.* **114**, 419 (2018).
- [21] P. Theocaris, D. Pazis, and B. Konstantellos, The exact shape of a deformed internal slant crack under biaxial loading, *Int. J. Fract.* **30**, 135 (1986).
- [22] A. Lucantonio, G. Noselli, X. Trepas, A. DeSimone, and M. Arroyo, Hydraulic Fracture and Toughening of a Brittle Layer Bonded to a Hydrogel, *Phys. Rev. Lett.* **115**, 188105 (2015).
- [23] C. Gally, F. Wissler, H. Zahreddine, S. Quintin, F. Landmann, and M. Labouesse, Myosin II regulation during *C. elegans* embryonic elongation: LET-502/ROCK, MRCK-1 and PAK-1, three kinases with different roles, *Development* **136**, 3109 (2009).
- [24] N. Fotopoulos, D. Wernike, Y. Chen, N. Makil, A. Marte, and A. Piekny, *Caenorhabditis elegans* anillin (ani-1) regulates neuroblast cytokinesis and epidermal morphogenesis during embryonic development, *Dev. Biol.* **383**, 61 (2013).
- [25] S. Quintin, S. Wang, J. Pontabry, A. Bender, F. Robin, V. Hyenne, F. Landmann, C. Gally, K. Oegema, and M. Labouesse, Non-centrosomal epidermal microtubules act in parallel to LET-502/ROCK to promote *C. elegans* elongation, *Development* **143**, 160 (2016).

- [26] T. T. K. Vuong-Brender, S. K. Suman, and M. Labouesse, The apical ECM preserves embryonic integrity and distributes mechanical stress during morphogenesis, *Development* **144**, 4336 (2017).
- [27] Z. Suo, Singularities, interfaces and cracks in dissimilar anisotropic media, *Proc. R. Soc. A* **427**, 331 (1990).
- [28] M. Ben Amar, Creases and cracks in finite elasticity, *Mech. Res. Commun.* **93**, 23 (2018).
- [29] P. Ciarletta, M. Ben Amar, and M. Labouesse, Continuum model of epithelial morphogenesis during *Caenorhabditis elegans* embryonic elongation, *Phil. Trans. R. Soc. A* **367**, 3379 (2009).
- [30] See Supplemental Material at <http://link.aps.org/supplemental/10.1103/PhysRevLett.121.268102> for full description of the geometry, elasticity, fracture modeling and data analysis.
- [31] A.-C. Reymann, F. Staniscia, A. Erzberger, G. Salbreux, and S. W. Grill, Cortical flow aligns actin filaments to form a furrow, *eLife* **5**, e17807 (2016).
- [32] A. Saha, M. Nishikawa, M. Behrmdt, C.-P. Heisenberg, F. Jülicher, and S. W. Grill, Determining physical properties of the cell cortex, *Biophys. J.* **110**, 1421 (2016).
- [33] I. Bonnet, P. Marcq, F. Bosveld, L. Fetler, Y. Bellache, and F. Graner, Mechanical state, material properties and continuous description of an epithelial tissue, *J. R. Soc. Interface* **9**, 2614 (2012).
- [34] S. Tlili, E. Gauquelin, B. Li, O. Cardoso, B. Ladoux, H. Delano-Ayari, and F. Graner, Collective cell migration without proliferation: Density determines cell velocity and wave velocity *R. Soc. Open Sci.*, **5**, 172421 (2018).
- [35] L. D. Landau and E. M. Lifshitz, *Theory of Elasticity* (Elsevier, New York, 1986), Vol. 7.
- [36] R. W. Ogden, *Non-Linear Elastic Deformations* (Dover Publications, Mineola, 1997).
- [37] T. C. Gasser, R. W. Ogden, and G. A. Holzapfel, Hyperelastic modelling of arterial layers with distributed collagen fibre orientations, *J. R. Soc. Interface* **3**, 15 (2006).
- [38] G. A. Holzapfel, J. A. Niestrawska, R. W. Ogden, A. J. Reinisch, and A. J. Schriefl, Modelling non-symmetric collagen fibre dispersion in arterial walls, *J. R. Soc. Interface* **12**, 20150188 (2015).
- [39] B. D. Williams and R. H. Waterston, Genes critical for muscle development and function in *Caenorhabditis elegans* identified through lethal mutations, *J. Cell Biol.* **124**, 475 (1994).
- [40] H. Zhang, F. Landmann, H. Zahreddine, D. Rodriguez, M. Koch, and M. Labouesse, A tension-induced mechanotransduction pathway promotes epithelial morphogenesis, *Nature (London)* **471**, 99 (2011).
- [41] R. De Vita, R. Grange, P. Nardinocchi, and L. Teresi, Mathematical model for isometric and isotonic muscle contractions, *J. Theor. Biol.* **425**, 1 (2017).

Modeling the mechanics of growing epithelia with a bilayer plate theory

Joseph Ackermann¹, Paul-Qiuyang Qu¹, Loïc LeGoff^{3,*} and Martine Ben Amar^{1,2}

¹ Laboratoire de Physique de l'Ecole normale supérieure, ENS, Université PSL, CNRS, Sorbonne Université, Université de Paris, F-75005 Paris, France

² Institut Universitaire de Cancérologie, Faculté de médecine, Sorbonne Université, 91 Bd de l'Hôpital, 75013 Paris, France

³ Aix Marseille Univ, CNRS, Centrale Marseille, Institut Fresnel, Turing Center for Living Systems, Marseille, France

* Corresponding author: Loïc LeGoff, email: loic.le-goff@univ-amu.fr

Received: date / Revised version: date

Abstract. Epithelia, which consists of cell sheets lying on a substrate, are prevalent structures of multi-cellular organisms. The physical basis of epithelial morphogenesis has been intensely investigated in recent years. However, as 2D mechanics focused most attention, we still lack a rigorous description of how the mechanical interactions between the cell layer and its substrate can lead to 3D distortions. This work provides a complete description of epithelial mechanics using the most straightforward model of an epithelium: a thin elastic bilayer. We first provide experimental evidence in *Drosophila* tissues that localized alterations of the cell-substrate (the extracellular matrix) can lead to profound 3D shape changes in epithelia. We then develop an analytical model modifying the Föppl-von Kármán equation with growth for bilayers. We provide a complete description of all contributions from biophysical characteristics of epithelia. We show how any localized inhomogeneity of stiffness or thickness drastically changes the bending process when the two layers grow differently. Comparison with finite-element simulations and experiments performed on *Drosophila* wing imaginal discs validate this approach for thin epithelia.

PACS. ERC Keywords : PE3-11,PE3-15,PE3-16,LS3-11

Contents

1	Introduction	1
2	Experimental motivation: biomechanics of <i>Drosophila</i> wing imaginal discs	2
3	Modeling	4
4	FvK equations for the bilayer case	6
5	Position of the neutral surface Z_n for uniaxial loading	8
6	Results for uni-axial folding	10
7	Numerical Simulations with Finite-Element Method	15
8	Discussion and conclusion	19
9	Author Contributions	19
10	Acknowledgements	19

1 Introduction

Biological cell assemblies are often organized in laminar structures called epithelia. Epithelia cover most of our hollow organs, such as the esophagus [1], intestine [2,3] and stomach. The skin is also an epithelium constituted of several cell layers. The structure of epithelia is of one or several attached cell layers, which rest on a more disorganized polymeric substrate, called the extra-cellular matrix (ECM). Even the simplest epithelium, constituted of a single cell layer, must rest on an abutting ECM layer.

In the past decade, a lot of emphasis has been put on the role of the cytoskeletal cortex on the apical side of the cells (the side away from the ECM layer) in setting mechanical properties of epithelia [4]. However, recent investigations have established that the mechanical properties of the ECM may be as important in setting the shape of a tissue [5]. Both the cell layer and the ECM must be taken into account in the mechanical description of epithelia.

From the biomechanical viewpoint, an epithelium may be viewed as a bilayer made of two different soft materials with different stiffnesses and different ways to grow: the cell layer grows by mass increase and proliferation, while the ECM grows by addition of polymer-chains and swelling. A bilayer can also serve as a suitable approximation for more complex geometries, such as the multilayered skin, sub-divided into the dermis and the epidermis. In between layers of cells or in between cells and connective tissues, the ECM may develop into a stiff membrane enriched in collagen filaments called the basal membrane [6]. Epithelial cells may also have a reinforced cortex at their basal side, increasing the interfacial stiffness [7,8]. A more realistic mechanical view of epithelia would thus be that of a bilayer with the addition of stiff interfaces originating from the ECM or the cytoskeleton.

When one layer is a very soft substrate, several studies have attempted to deal with such bilayered systems [9–14] by treating the soft layer as an elastic foundation or as an ad-hoc resistance potential [10,11]. These models become essentially single-layered and cannot account for the diversity of behavior of two-layered systems where the two layers play similar roles and have similar properties. We aim here to present a simple mechanical model of thin bilayers using the Föppl-von Kármán equations (FvK) with growth. In the context of a thin plate hypothesis, the FvK equations allow a 3D to 2D dimensional reduction which considerably simplifies the analytical treatment of plate mechanics. The FvK equations are thus well adapted to incorporate many different biological features of layered tissues which are difficult to handle analytically in a fully three-dimensional formalism. It has recently been shown that FvK equations with growth allow to explain the buckling of thin objects such as flowers and algae in a rather simple way [15,16], when compared to the full treatment of finite elasticity with growth [17]. In addition, a slight modification of these equations allows to treat initially weakly curved membrane. This prompted us to use the same approach for a bilayer with growth. When modeling a single-layered epithelium, the two layers of the model are the ECM and the cells, while the interfacial stiffness represents the basal cytoskeletal cortex of cells (left inset in fig. (1)). When modeling a more complex system, such as the skin, one layer of the model represents the cell layers of the epidermis, the second layer is the dermis (a connective tissue) and the interfacial stiffness represents the extra-cellular basal lamina (right inset in fig. (1)), see reference ([6]). Our model can account for local variations in the stiffness or in the thickness of the layers as well as interfacial stiffnesses. Such variations are often present in biological tissues, and are thought to be shape generators in morphogenetic processes. These local variations in mechanical properties can also be induced in the context of perturbative experiments.

As much as elasto-mechanical processes may drive the shape of epithelia, this shape builds upon a long and intricate history of growth, stress distribution, and changes in mechanical properties. On the other hand, our formalism, which uses linear elasticity with moderate non-linear elastic strains, can only account for slight shape variations, spanning time intervals typically smaller than the doubling time of cells within the tissue. To mitigate this problem, we encapsulate all the previous history of development and morphogenesis in an initial shape and a pre-stress. This allows confrontation with experiments where the tissue, at the onset of observation, is rarely in a flat and stressless configuration and where the full history of development is also inaccessible. We show that the model can treat many aspects of biological tissues, which are not so common in material sciences. Although the formalism was initially developed to treat biological growth, it could also serve for the opposite case of resorption, which could be of interest both in a biological and material science context.

In this paper, we first demonstrate experimentally how alteration of the ECM can substantially impact the shape of an epithelium. For this, we genetically degrade the ECM in a band of cells in the *Drosophila* wing imaginal disc -the precursor of the adult wing. Subsequent sections are devoted to developing an analytical and numerical treatment of a bilayer model. We aim to account for the experimentally observed distortion of the tissue and provide a general framework to address the mechanics of growing bilayered tissues at large. Section (3), is devoted to the geometry of the sample under study and a reminder of the necessary approximations to incorporate the formalism of finite elasticity with growth into the FvK approach. In sect.(4), we give the main equations for a bilayer and an approach of the treatment of the interface. In sect.(5), we derive the Euler-Lagrange equations for the elastic bilayer equivalent to the FvK equations and we demonstrate the peculiar role of the neutral surface for the bending of the plate. Its position is derived for arbitrary stiffness and thickness, not necessarily constant, of the two layers. Section (6) focuses on uniaxial deformations, which simplify the FvK modified equations for a bilayer with additive terms at the origin of buckling. In this section, numerical results illustrate the various cases for pre-stressed plates but also for slightly curved membranes, and the theory is confronted to experimental data. In sect.(7), results obtained with finite element simulations achieved in the same context of growth, thickness, stiffness and defects are presented. Finally, we conclude in sect.(8) by giving some perspectives.

The model can be adapted to many other biological systems, as epithelia are ubiquitous in most living species. It could also be used for other thin objects such as leaves or algae.

2 Experimental motivation: biomechanics of *Drosophila* wing imaginal discs

The *Drosophila* wing imaginal discs (the precursors of the adult wing) are epithelial tissues that became, over the years, one of the most studied and best characterized system to study growth [18]. The growing wing imaginal disc displays a highly patterned field of mechanical stresses[19–21]. Cells at the periphery of the epithelium sustain a strong mechanical stretch. This pre-stress builds up as the tissue grows. In addition, the tissue becomes curved as development proceeds, gradually changing from a simple flat surface to a more complex curved surface.

Please give a shorter version with: \authorrunning and \titlerunning prior to \maketitle

3

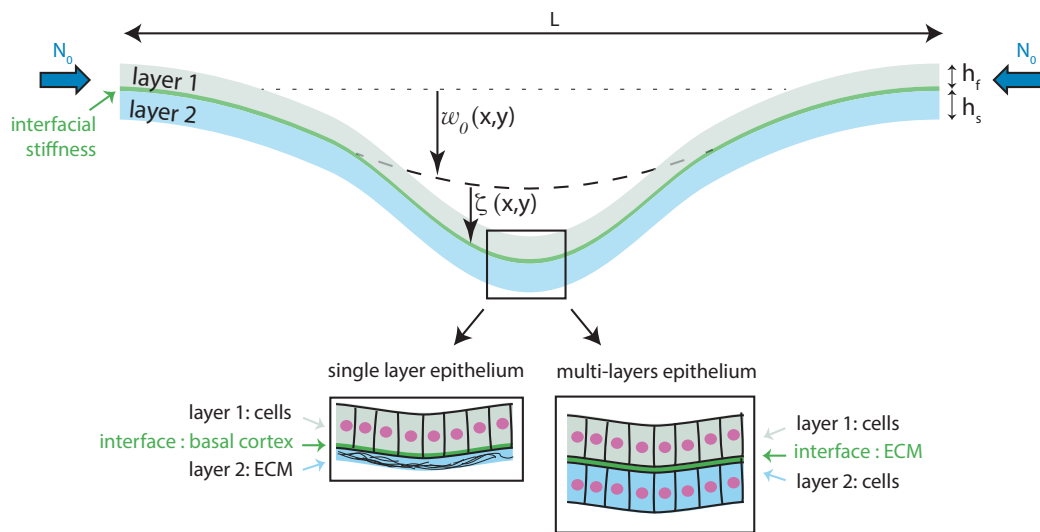


Fig. 1. Geometry of the bilayer model. $w_0(x, y)$ is the deviation of the initial configuration from a flat surface; $\zeta(x, y)$ is the displacement from this initial configuration as a result of elastic energy minimization under the action of growth and pre-stress (N_0). The schema at bottom represent biological context that can be modeled by the theory: the two layers can either be cell or ECM layers of different height, Young modulus and growth rate; the stiff interface can be a cytoskeletal cortex or a thin ECM.

Until recently, most attention was brought upon the role of the apical surface of the epithelium in setting its mechanical properties. It was however recently demonstrated that the extracellular matrix upon which the epithelium sits plays a major role in shaping the tissue. Alterations in the basement membrane composition, which includes collagen IV, laminin, nidogen, and heparan-sulfate proteoglycans, have profound effects on the shape of the wing imaginal disc [22]. Alterations of the basement membrane have also been shown to play an active part in setting the 3D shape of the wing disc by promoting the formation of the folds that gradually arise in the tissue [23,24]. From these experiments, it now stands that wing imaginal discs, and most epithelia in general, are two layered composite structures. Both the cell layer and the ECM layer take an active part in shaping the tissue [25].

To assess the role of basement membranes in setting mechanical properties of the imaginal discs, we used *Drosophila* genetics to express the matrix-cleaving metallo-protease Mmp2 in a band of cells, located at the center of the wing imaginal disc along the Dpp-Gal4 genetic pattern (fig.(2a)). The genotype of the observed tissues is *ubi-cad:GFP UAS-GFP tub-Gal80_{ts/+}; Dpp-Gal4/UAS-Mmp2*. It combines the necessary transgenes to express the metallo-protease locally and to visualize cells with a cadherin: GFP fusion. The biochemical action of Mmp2 is to degrade structural components of the ECM [26], which in mechanical terms implies a possible change of ECM stiffness as well as the thickness. We cannot rule out also an indirect effect on the the basal cytoskeletal cortex of cells, as an altered ECM in the vicinity of the cell layer implies a reduced activation of integrin receptors. Our elastic model will need to take into account these different contributions. The metallo-protease expression is controlled in time via the thermo-sensitive mutant of Gal80, by switching *Drosophila* from 18°C to 29°C 24h before observations (fig.(2b)). Such a timing corresponds to approximately 18 hours of Mmp2 expression since 6 hours are required to reach full Gal4 expression after the temperature switch [27]. To image the imaginal discs, we performed *ex-vivo* cultures of wing imaginal discs as in [19]. The living tissues were then imaged with a spinning disc confocal microscope.

Figure (2c) shows the cross-section of an imaginal disc 18 hours after metalloprotease expression. The region of perturbation, identified by RFP expression, is shaded in red on the figure. Figure (2d) shows the profile of the apical surface of the epithelium, which has a region of inflection near the protease expression. This profile (fig.(2c,d)) corresponds to a wing imaginal disc that was initially flat. Alternatively, fig.(2d,e). shows the same perturbation outcome on a wing imaginal disc that was initially curved - curvature normally builds up at late stages of wing disc development (around 80 hours after egg laying). The resulting tissue is very different from the previous case. This time, the profile shows a more complex configuration: the naturally occurring curvature is prevalent on the borders of the wing disc; at the same time, the metalloprotease action in the region of perturbation induces an inversion of the curvature there.

To conclude, we observed that upon ECM degradation (which may impact the stiffness, the thickness, and the interfacial mechanics), the epithelium curves in the perturbation region (fig.(2h)). We observed two archetypal outcomes depending on whether the tissue was initially flat or curved, which can lead to the inversion of the naturally occurring curvature in the perturbation region. These experimental observations will be subsequently confronted to our FvK bilayer model and our finite-element simulations (see fig.(8) and fig.(10)).

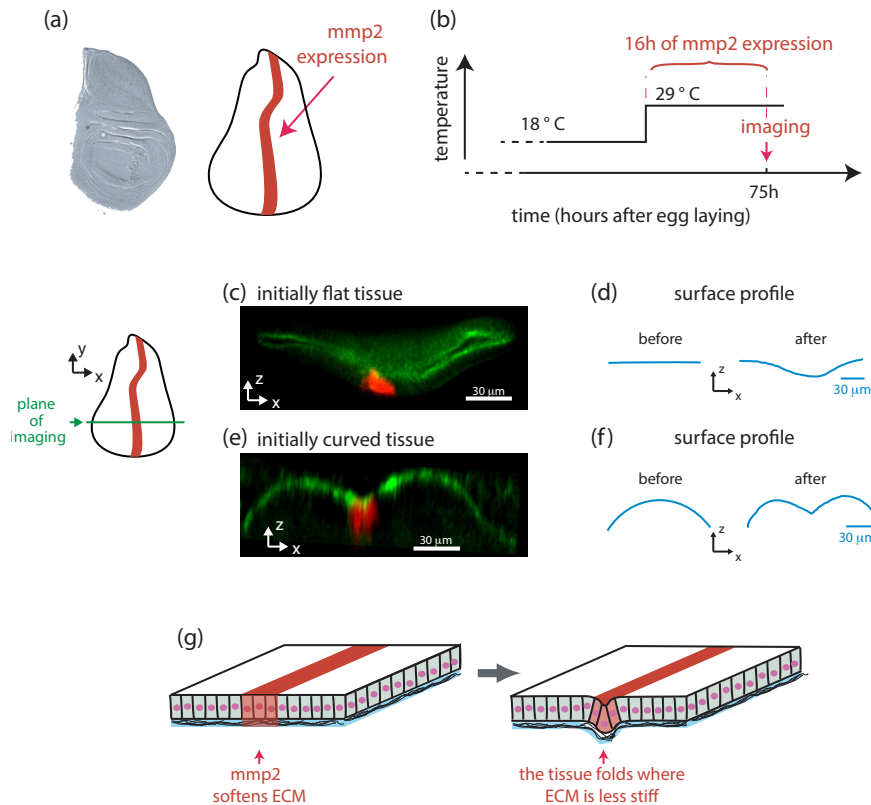


Fig. 2. Folding an epithelium by local ECM degradation. (A) Transmission light imaging of a *Drosophila* wing imaginal disc (left) and corresponding sketch with the region of localised expression of the protease Mmp2 shaded in red (right). (B) To control expression of the metalloprotease, the sample is switched from 18°C to 29°C several hours before observation. (C-F) Experimental demonstration. (C) An xz cross section demonstrates the shape of an initially flat wing imaginal disc under the effect of a localized metalloprotease expression (in the red colored region). The schema in (D) demonstrates the change in shape of the tissue. (E,F) Same as (C,D) but with an initially curved wing imaginal disc. (G) A schematic representation of the shape changes observed in the wing imaginal disc.

3 Modeling

The geometry of the model is represented in fig.(1): two layers of different thickness (h_f and h_s), stiffness and growth rate are organized in a bilayer, with an interface which may also bear a stiffness. The shape of the initial configuration (see explanations in fig.(1)) is given by $w_0(x, y)$, the deviation from the horizontal line; the vertical deflection arising from the elastic minimization is denoted $\zeta(x, y)$. There are no explicit rules about the difference in stiffness or thickness of the two layers, but they have the same order of magnitude most of the time for living species. While there is also no rules regarding the thin interface layer, it will only play a role if it is much stiffer. Contrary to inert materials, changes in the shape of the structure arises from inner processes such as volumetric growth rather than through external loading, although this latter is not eliminated *a priori* from the model. The bilayer can model, with different degrees of accuracy, a single or a multi-layered epithelium.

A decade ago, Dervaux *et al.* established the formalism of a growing plate using the theory of finite elasticity with growth [15, 16]. Here, we extend their analysis of a single layer to a thin bilayer, both layers having different growth rates and different elastic properties but remaining thin. Indeed, the FvK equations rest on some limitations: the order of magnitude of the vertical deflection ζ due to the buckling and the initial deviation from the horizontal line w_0 must remain small compared to the horizontal length L (they may be larger than the thickness h of the plate).

In the following, we first present the model for the general 2D case with arbitrary buckling deformations, and subsequently treat the simpler uni-axial folding.

3.1 The geometric and elastic strain

We consider two different layers with thickness h_f (top) and h_s (bottom). When volumetric growth or degrowth occurs in an elastic sample, each point is displaced and the gradient of this displacement is a geometric tensor called the deformation tensor:

F. According to the famous *Kroner-Lee* decomposition [28], \mathbf{F} results from both the elastic tensor \mathbf{A} and the growth tensor \mathbf{G} in a simple way :

$$\mathbf{F} = \mathbf{A}\mathbf{G} \quad (1)$$

Here, plasticity is neglected. The amount of growth per unit volume is given by $\text{Det } \mathbf{G} - 1$, which is negative for mass resorption and positive for growth. When it is small, the growth tensor \mathbf{G} can be decomposed into : $G_{ij} = \delta_{ij} + \delta g_{ij}$ with $|\delta g_{ij}| \ll 1$. The deformation tensor is then also small leading to the following displacement of the points originally located at $\mathbf{r} = (x, y, Z)$:

$$\begin{aligned} \mathbf{u}(\mathbf{r}) &= \mathbf{u}^0(x, y) + (Z - Z_n)\mathbf{u}^1(x, y) + \mathbf{w}_0(x, y) \\ &= (U_1^0(x, y) + (Z - Z_n)U_1^1(x, y)) \mathbf{e}_1 + (U_2^0(x, y) + (Z - Z_n)U_2^1(x, y)) \mathbf{e}_2 + (\zeta(x, y) + w_0(x, y)) \mathbf{e}_3 \end{aligned} \quad (2)$$

where $w_0(x, y)$ represents the initial position of the interface bilayer, and $\zeta(x, y)$ the deflection due to the buckling event. Each \mathbf{e}_i represents a cartesian unit vector and the superscripts "0" or "1" stand for the order of perturbation. Indeed, the ratio between the thickness of the bilayer and the horizontal size L is one small parameter $\epsilon_1 = h/L$ but the magnitude of the displacement in the Z direction compared to L is a second independent small parameter $\epsilon_2 = \zeta/L$. We assume that both layers have comparable thickness and h means either h_f or h_s . In the classical FvK approach, $\epsilon_2 \simeq \sqrt{\epsilon_1}$ a scaling which is justified below and which will constrain \tilde{g}_{ij} and w_0 . Since we examine here a composite material, the choice of the origin of the Z axis is free at this stage. We define this origin at the physical interface between both layers. We also introduce Z_n , a possible shift in the expansion of order h , whose role is to minimize the elastic strains. This surface defines the surface of separation between parallel surfaces in extension compared to the ones in compression due only to the buckling process. In the single plate geometry, Z_n corresponds to the position of the neutral surface and is located at $h/2$. We can then define the geometric deformation gradient :

$$F_{ij} = \delta_{ij} + \frac{\partial u_i}{\partial x_j} \quad (3)$$

where, as in Landau's book of elasticity [29], the index i indicates an index varying between 1 and 3 while greek letters restrict to 1 or 2. The elastic strain that we deduce from eq.(1) when A and G are close to unity reads :

$$A_{ij} = \delta_{ik} G_{kj}^{-1} + \frac{\partial u_i}{\partial x_k} G_{kj}^{-1} \quad (4)$$

Defining $\mathbf{G}^{-1} = \mathbf{I} - \tilde{\mathbf{g}}$, each component of $\tilde{\mathbf{g}}$ must remain a small quantity to validate the FvK approach. In addition, we assume no change of the thickness of the sample which means $\tilde{g}_{33} = 0$, this hypothesis simplifies the equations and can be easily revisited. A spatially constant value of \tilde{g}_{33} over the sample simply enters in the definition of h . We also assume that $\tilde{g}_{\alpha\beta}$ scales as ϵ_2^2 while $\tilde{g}_{\alpha 3}$ and $\tilde{g}_{3\alpha}$ scale as ϵ_2 . To order 2 in ϵ_2 , the elastic strain ϵ reads:

$$\epsilon_{\alpha\beta} \approx \frac{1}{2} \left(\frac{\partial u_\alpha}{\partial x_\beta} + \frac{\partial u_\beta}{\partial x_\alpha} - g_{\alpha\beta} - \tilde{g}_{3\alpha} \frac{\partial \zeta}{\partial x_\beta} - \tilde{g}_{3\beta} \frac{\partial \zeta}{\partial x_\alpha} + \frac{\partial \zeta}{\partial x_\alpha} \frac{\partial \zeta}{\partial x_\beta} + \frac{\zeta}{R_\alpha} \delta_{\alpha\beta} \right) \quad (5)$$

where we only keep the quadratic term in ζ for the deformation tensor, all the other contributions being neglected. In addition, to simplify the notations, we define $g_{\alpha 3} = \tilde{g}_{3\alpha} + \tilde{g}_{\alpha 3}$ and $g_{\alpha\beta} = \tilde{g}_{\alpha\beta} + \tilde{g}_{\beta\alpha} - \tilde{g}_{3\alpha}\tilde{g}_{3\beta}$. The last term in eq.(5) represents the geometric stretch of the deformation due to the eventual curvature of the initial shell formulated with R_x and R_y , the local radii of curvature, in the direction x and y [10]. A more precise mathematical formulation can be found in [30] in function of the curvature tensor of the shell. To simplify, we have assumed that R_x and R_y are the principal radii of curvatures of the initial shell, positive for a concave membrane. So $R_x^{-1} = -\partial_{xx} w_0(x, y)$ and $R_y^{-1} = -\partial_{yy} w_0(x, y)$ for a slightly curved membrane.

For a consistent expansion, all terms in this relation must have the same order of magnitude. This implies several scaling relations. We get for the horizontal deformation: $u \simeq \zeta^2/L$, for the growth element $g_{\alpha\beta} \simeq \zeta^2/L^2$ and for the two radii of curvature R_i or R_j : $R \simeq L^2/\zeta \simeq L\epsilon_2^{-1}$.

3.2 Dimensional reduction of the Hooke's Law for one layer

We aim here to establish the equilibrium equations of a growing bilayer under initial pre-stress (represented by N_0 in fig.(1) when it is initially planar or weakly curved. For that, as in Landau *et al.* book [29] and in [11, 15, 16], our strategy consists in calculating the elastic energy and deriving the Euler-Lagrange equations through variations. Most importantly, we write the stress and strain tensors as a function of x and y only. First, we consider each layer independently since each of them has its own elastic coefficients and its own growth characteristics. The coupling will be realized via the boundary conditions. Due to the weakness of the deformation for slender objects, we can apply the Hooke's Law which is the constitutive equation of linear elasticity, but we maintain the nonlinearities of the strains according to the strategy of the FvK equations. We also consider the usual membrane

hypothesis: $\sigma_{i3} = 0$ which is equivalent to the plane stress approach. Then, it reads for the Cauchy stress components $\sigma_{\alpha\beta}$ where α and β are restricted to x, y :

$$\sigma_{\alpha\beta} = \frac{E}{1-\nu^2} ((1-\nu)\epsilon_{\alpha\beta} + \nu\epsilon_{\gamma\gamma}\delta_{\alpha\beta}) \quad (6)$$

with $\nu \simeq 1/2$ for the incompressible case, an assumption commonly used for living tissues. In order to determine the elastic energy \mathcal{Y} , we then write the elastic strain tensor (also a function of x and y), which we decompose in orders of $(Z - Z_n)$ with the help of the expansion 2), so that

$$\epsilon_{\alpha\beta} = \epsilon_{\alpha\beta}^0 + (Z - Z_n)\epsilon_{\alpha\beta}^1$$

First the zero order:

$$\epsilon_{\alpha\beta}^0 = \frac{1}{2} \left(\partial_\alpha U_\beta^0 + \partial_\beta U_\alpha^0 + \partial_\alpha \zeta \partial_\beta \zeta - g_{\alpha\beta} - \tilde{g}_{3\alpha} \frac{\partial \zeta}{\partial x_\beta} - \tilde{g}_{3\beta} \frac{\partial \zeta}{\partial x_\alpha} + \frac{\zeta}{R_\alpha} \delta_{\alpha\beta} \right) \quad (7)$$

The first order results from the cancellation of the stresses of the third dimension : $\sigma_{33} = \sigma_{13} = \sigma_{23} = 0$, so $\epsilon_{13} = \epsilon_{23} = 0$ (see [29]) and using the definition eq.((5)), we derive:

$$U_1^1(x, y) \approx -\frac{\partial}{\partial x} \zeta + g_{13}; \quad U_2^1(x, y) \approx -\frac{\partial}{\partial y} \zeta + g_{23} \quad (8)$$

Thus the strains at first order become :

$$\epsilon_{\alpha\beta}^1 = -\partial_{\alpha\beta}^2 \zeta + \frac{1}{2} (\partial_\alpha g_{\beta 3} + \partial_\beta g_{\alpha 3}) \quad (9)$$

One recovers the bending contribution $\partial_{\alpha,\beta}^2 \zeta$, multiplied by $Z - Z_n$. Following the equilibrium equation eq.(6) and the decomposition of the elastic strain (eq.((7))) and eq.((9))), we can also decompose $\sigma_{\alpha\beta}$ as $\sigma_{\alpha\beta} = \sigma_{\alpha\beta}^0 + (Z - Z_n)\sigma_{\alpha\beta}^1$.

4 FvK equations for the bilayer case

As in Landau's book of linear elasticity [29], we average the elastic energy in the thickness of the bilayer.

4.1 Averaging the FvK equation

An important problem in the construction of the model is to establish the position of the neutral surface when the layer is not perfectly homogeneous or for multiple layers. According to [29], the neutral surface defines the separation between layers in compression from layers in tension when the structure is weakly bent. For an homogeneous sample, the neutral surface is naturally the middle surface of the sample. But for a bilayer, the position of the neutral surface is unknown. The interface between both layers seems to be the natural choice for the definition of the origin of the Z coordinate but it is not the neutral surface. So, we put the neutral surface at a position Z_n that we ignore and this position will also contribute to the minimization of the elastic energy \mathcal{Y} .

$$\mathcal{Y} = \int_{-h_s}^{h_f} dZ \iint_{S_0} dS \left(\frac{1}{2} \sigma_{\alpha\beta} \epsilon_{\alpha\beta} \right) \quad (10)$$

The Euler-Lagrange equations result from variations of \mathcal{Y} with respect to ζ and u_α , the linearity between σ and ϵ leading to $\delta\mathcal{Y} = \sigma_{\alpha\beta} \delta\epsilon_{\alpha\beta}$. These variations, taken one after the other must vanish at linear order. Special attention must be given if the growth tensor or the Young modulus E are dependent on Z as it is obviously the

Case 1 for the bilayer, and sometimes of the other coordinates x and y . The variation of \mathcal{Y} with respect to the horizontal deformation u_α is easily derived and gives:

$$\delta\mathcal{Y}(u_\alpha, \zeta, Z_n; u_\alpha) = - \iint_{S_0} dS \delta u_\alpha \left\{ \frac{\partial}{\partial x_\beta} \left(\int_{-h_s}^{h_f} \sigma_{\alpha\beta} dZ \right) \right\} = 0 \quad (11)$$

This corresponds to the second equation in the FvK formalism [29], sometimes re-written with the Airy potential, which is very useful for analytical or numerical solutions of a 2D problem. Variation of \mathcal{Y} with respect to ζ gives:

$$\delta\mathcal{Y}(u_\alpha, \zeta, Z_n; \zeta) = \iint_{S_0} dS \delta \zeta \left\{ \int_{-h_s}^{h_f} dZ \left(-(Z - Z_n) \partial_{\alpha\beta}^2 \sigma_{\alpha\beta} - \partial_\alpha (\partial_\beta \zeta \cdot \sigma_{\alpha\beta}) + \frac{\sigma_{\alpha\alpha}}{R_\alpha} + \frac{\sigma_{\beta\beta}}{R_\beta} \right) \right\} = 0 \quad (12)$$

In eq.(11,12), the two bracketed terms mush vanish. We do not mention explicitly the contributions coming from integration by part which fixes the boundary conditions for free boundaries. In the following, we consider only clamped boundary conditions. Finally, there remains one free parameter, Z_n , that we will use to minimize the bending energy. Indeed at a low level of stress, the bending contribution given by eq.(12) ([29]) is the dominant one. As mentioned above, the neutral surface Z_n is a characteristic of the bilayer structure and geometry and does not depend on any loading and/or any growth process. Considering \mathcal{Y} in the limit of a tiny buckling mode ζ in eq.(10) and separating σ as $\sigma_{\alpha\beta} = \sigma_{\alpha\beta}^0 + (Z - Z_n)\sigma_{\alpha\beta}^1$, we have:

$$\delta\mathcal{Y}(u_\alpha, \zeta, Z_n; Z_n) = - \iint_{S_0} dS \delta Z_n \int_{-h_s}^{h_f} dZ (\sigma_{\alpha\beta}^0 \epsilon_{\alpha\beta}^1 + 2(Z - Z_n) \sigma_{\alpha\beta}^1 \epsilon_{\alpha\beta}^1) = 0 \quad (13)$$

where we have separated in $\sigma_{\alpha\beta}$ the contribution of zero and first order in $(Z - Z_n)$ as for $\epsilon_{\alpha\beta}$, both terms satisfying the Hooke's law independently. In the limit of negligible in-plane stresses and tiny bending deformations, with $\zeta \ll h$, the scaling evaluations estimated before indicate that the first term will behave as $E(Z)\zeta^3/L^4$ while the second term behaves as $E(Z)h\zeta^2/L^4$ and so the second term dominates, giving an implicit equation for the neutral surface position:

$$\int_{-h_s}^{h_f} E(Z, x, y)(Z - Z_n) dZ = 0 \quad (14)$$

since $\epsilon_{\alpha\beta}^1$ does not depend on Z . Notice that if E is also a function of (x, y) , Z_n becomes also a function of (x, y) . It is now possible to transform eq.(12) once we define the new bending coefficient and the new spontaneous curvature due to growth:

$$D = \frac{1}{1 - \nu^2} \int_{-h_s}^{h_f} E(Z, x, y)(Z - Z_n)^2 dZ; \quad C_{\alpha\beta} = \frac{1}{2} \int_{-h_s}^{h_f} \frac{E(Z, x, y)}{1 - \nu^2} (Z - Z_n)^2 \left(\frac{\partial g_{\alpha 3}}{\partial x_\beta} + \frac{\partial g_{\beta 3}}{\partial x_\alpha} \right) dZ \quad (15)$$

Doing again the separation of σ into σ^0 and σ^1 , an intermediate step consists in integrating $\sigma_{\alpha\beta}$ over the Z variable, which gives first:

$$\Sigma_{\alpha\beta} = - \int_{-h_s}^{h_f} (Z - Z_n) \sigma_{\alpha\beta} dZ = (1 - \nu)(D \partial_{\alpha\beta}^2 \zeta - C_{\alpha\beta}) + \nu(D \Delta \zeta - C_{\gamma\gamma}) \delta_{\alpha\beta} + M_{\alpha\beta} \quad (16)$$

where we have dropped the dependence of D and $C_{\alpha\beta}$ in x, y to simplify notations, introduced the 2D Laplacian $\Delta = \partial_{\alpha\alpha}$, and a new tensor $M_{\alpha\beta}$:

$$M_{\alpha\beta} = \int_{-h_s}^{h_f} \frac{E(Z, x, y)}{1 - \nu^2} (Z - Z_n) \{ (1 - \nu)g_{\alpha\beta} + \nu g_{\mu\mu} \delta_{\alpha\beta} \} dZ \quad (17)$$

The simplification of M is due to the definition of the neutral surface and the fact that only the growth component $g_{\alpha\beta}$ may depend on Z . If it is not the case, $M_{\alpha\beta}$ vanishes. At last, eq.(12) gives the equivalent of the first FvK equation:

$$\partial_{\alpha\beta}^2 \Sigma_{\alpha\beta} - \partial_\alpha \left\{ \int_{-h_s}^{h_f} \sigma_{\alpha\beta} \partial_\beta \zeta dZ \right\} + \left(\frac{\int_{-h_s}^{h_f} \sigma_{xx} dZ}{R_x} + \frac{\int_{-h_s}^{h_f} \sigma_{yy} dZ}{R_y} \right) = P \quad (18)$$

where P is a vertical pressure, possibly applied to the bilayer.

This last equation, eq.(18), governs mostly the bending deformation. In the nonlinear regime of the FvK formalism, it is coupled to the horizontal stresses $\sigma_{\alpha\beta}$ whose equilibrium is given by eq.(11). When not stated otherwise, $\sigma_{\alpha\beta}$ is the total stress. D appears to be an effective bending coefficient of the composite structure and $C_{\alpha\alpha}$ as a spontaneous curvature associated with growth. For a homogeneous layer with no growth $Z_n = h/2$, $M_{\alpha\beta}$ vanishes and one recovers the traditional FvK equations without growth, see [29]. Notice that in eq.(18), we also recover the spontaneous curvature $\kappa = \partial_\alpha g_{\alpha 3}$ found in [16]. Let us focus now on the uniaxial folding where all the equations simplify.

4.2 New FvK equations governing uniaxial folding

For uniaxial folding, the only dependence is along the x axis and all the tensors are reduced to one element, which simplifies a lot the analysis but reduces the diversity of observed buckling patterns, as explored in previous works [12, 14]. The elastic plane stress equilibrium equation, eq.(11) gives :

$$N = \int \sigma_{11} dZ = -N_0 \quad (19)$$

where N_0 is a constant that we choose positive. N_0 indicates a lateral compression, a situation easily realized in material sciences but in embryo it results from accumulated pre-stress [31, 20] (see fig.(1)). The bending equilibrium equation now reads:

$$\underbrace{\frac{d^2}{dx^2} \left(D \frac{d^2 \zeta}{dx^2} \right)}_{\text{Elastic term}} + \underbrace{N_0 \frac{d^2(\zeta + w_0)}{dx^2}}_{\text{Pre-stress}} = \underbrace{\frac{d^2}{dx^2} (C_{11} - M_{11})}_{\text{Growth contribution}} + \underbrace{P(x)}_{\text{External stress}} \quad (20)$$

where we detail M_{11} in the simplified case of growth occurring only in a single layer.

$$\begin{cases} M_{11} = \int_{-h_s}^{h_f} \frac{E(Z-Z_n)}{1-\nu^2} g_{11} dZ = \int_0^{h_f} \frac{E(Z-Z_n)}{1-\nu^2} g_{11}^f dZ + \int_{-h_s}^0 \frac{E(Z-Z_n)}{1-\nu^2} g_{11}^s dZ \\ C_{11} = \int_{-h_s}^{h_f} \frac{E(Z-Z_n)^2}{1-\nu^2} \frac{dg_{13}}{dx} dZ = \int_0^{h_f} \frac{E(Z-Z_n)^2}{1-\nu^2} \frac{dg_{13}^f}{dx} dZ + \int_{-h_s}^0 \frac{E(Z-Z_n)^2}{1-\nu^2} \frac{dg_{13}^s}{dx} dZ \end{cases} \quad (21)$$

We have derived an effective equation for the bilayer, which takes into account that the growth may differ from the top to the bottom layer via C_{11} and M_{11} . Contrary to C_{11} , M_{11} appears only if the growth tensor component g_{11} is different in both layers. If in addition, the second derivative of these two quantities does not vanish, they appear equivalent to a vertical loading acting on the bilayer giving it a curvature in absence of an initial one ($w_0 = 0$). This will destroy the perfect symmetry up and down, once averaged over the thickness of the bilayer and explain the bending in the case of growth. We now examine in more detail how the structure of the bilayer and eventually how defects affect the bending one-dimensional equation.

4.3 Boundary conditions for the bilayer.

Boundary conditions concern the top and the bottom interfaces between the surrounding fluid and the two layers, as well as the interface between the two layers ($Z = 0$). In solid mechanics, the interface between layers is often considered as a line of discontinuity. More realistically, it is a thin zone of sharp variations for physical constants - in our case for growth coefficients or stiffness. Moreover, it may happen that the elasticity of the interface is not simply the mean-value of both elastic coefficients. As discussed above, this happens when the interface of a cell layer and the ECM is enriched in intracellular cytoskeletal filaments, or when a thin basal lamina separates two cell layers, both circumstances leading to a stiffer interface. If the interface is really smaller than each layer, we can consider it as a transition zone around $Z = 0$, then avoiding the application of boundary conditions to a system of 3 layers. A way to avoid writing boundary conditions is to represent the sample as a unique layer where the elastic parameters such as the Young modulus vary continuously. If the interface is very thin, one needs only to know its thickness relative to the thickness of the bilayer, the detail of the description is not really important. The fact that we use the so-called membrane hypothesis with cancellation of the stresses $\sigma_{13} = \sigma_{23} = \sigma_{33} = 0$ ensure automatically the continuity of the normal and shear stress at the upper and lower boundaries and at the interface of the two layers ($Z = 0$). So only the continuity of the displacements is required at the interface. Choosing a "continuous approach" and aiming to transform the bilayer into a unique layer whose entire thickness will be $h_f + h_s$, we assume that the Young modulus E and any growth number $g_{\alpha\beta}$ can be written as:

$$E(Z) = \frac{E_f + E_s}{2} + \frac{(E_f - E_s)}{2} \tanh(Z/l_0) \quad \text{with } l_0 \lll h_f \quad \text{and } l_0 \lll h_s \quad (22)$$

and

$$g_{ij}(Z) = \frac{g_{ij}^f + g_{ij}^s}{2} + \frac{(g_{ij}^f - g_{ij}^s)}{2} \tanh(Z/l_0) \quad \text{with } l_0 \lll h_f \quad \text{and } l_0 \lll h_s \quad (23)$$

When a thin stiff membrane superposes to the two main layers of the sample at a position Z_m which can be on top $Z_m = h_f$, or at the bottom $Z_m = -h_s$, or at the surface of separation: $Z_m = 0$, as justified above, then we can slightly modify eq.(22) into

$$E(Z) = \frac{E_f + E_s}{2} + \frac{(E_f - E_s)}{2} \tanh(Z/l_0) + E_m e^{-\alpha_m^2 (Z-Z_m)^2 / l_0^2} \quad \text{with } l_0 \lll h_f \quad \text{and } l_0 \lll h_s \quad (24)$$

the Young modulus of the membrane, E_m , can be much larger than both E_f and E_s . α_m is a numerical coefficient characterizing the thickness of the membrane. Another boundary layer may exist on top or bottom of the bilayer, in addition to the interfacial one. The formulation of the Young modulus, $E(Z)$, must then also include this new contribution. Such definition of $E(Z)$ can be implemented into eq.(15) very easily to deliver the new FvK equations. We focus now on the the neutral surface position and on the bending coefficients when either the elastic coefficients or the thicknesses present a sharp but small in size variation along the sample.

5 Position of the neutral surface Z_n for uniaxial loading

We can guess from the definition of the coefficients (eq.(21)) of the bending FvK equation (eq.(20)), that the position of the neutral surface is crucial for the shape of the sample when growing and buckling. We consider first the position of the neutral surface for layers of constant thickness and constant Young modulus and we introduce a linear perturbation dependent on the x variable. If the linear approximation is not valid, a numerical solution is always possible as in sect.(7).

5.1 Position of the neutral surface for a bilayer without structural defects

In the case of an ideal bilayer with no structural defects, $Z_n^{(0)}$ is determined implicitly via eq.(14) with a Young modulus $E(Z)$ defined by: $E(Z) = E_f$ if $0 \leq Z \leq h_f$ and $E(Z) = E_s$ if $-h_s \leq Z \leq 0$. D is deduced from eq.(15) and it reads:

$$Z_n^{(0)} = \frac{E_f h_f^2 - E_s h_s^2}{2(E_f h_f + E_s h_s)} \quad D^{(0)} = \frac{E_f^2 h_f^4 + 4E_f E_s h_f^3 h_s + 6E_f E_s h_f^2 h_s^2 + 4E_f E_s h_f h_s^3 + E_s^2 h_s^4}{12(1 - \nu^2)(E_f h_f + E_s h_s)} \quad (25)$$

where the superscript “ (0) ” for Z_n and D reminds us that these formula are restricted to ideal cases. One can notice that if the two layers have the same elastic coefficient, one recovers the standard bending stiffness: $D = E(h_s + h_f)^3 / (12(1 - \nu^2))$ and the neutral surface is located at the middle of the layer of thickness $(h_f + h_s)/2$. We can convince ourselves that the neutral layer is located inside the bilayer since $-h_s < Z_n^{(0)} < h_f$, which is a necessary condition. These two quantities $Z_n^{(0)}$ and $D^{(0)}$ play a deep role in the bending equation, first equation of the FvK set of equation eq.(18) and for the definition given by eq.(15). It is why we consider now the departure from the ideal situation:

$$Z_n = Z_n^{(0)} + \delta Z_n; \quad \text{and} \quad D = D^{(0)} + \delta D \quad (26)$$

Hereafter, several causes are investigated at linear order in the perturbation amplitude.

5.2 Position of the neutral surface for diffuse or stiff interfaces

We allow a diffuse interface according to the representation given by eq.(22). The thickness of the interface l_0 is small compared to h_f or h_s . Although an exact calculation of Z_n is doable, it involves unusual analytical functions so we give here only an asymptotic formula for the result up to a correction of order e^{-h/l_0} :

$$Z_n = Z_n^{(0)} + b_l; \quad b_l \simeq -\frac{\pi^2 l_0^2 (E_f - E_s)}{24(E_f h_f + E_s h_s)} \quad (27)$$

This is a tiny effect being of order l_0^2/h^2 . In the presence of a stiff interface with E_I larger than E_f or E_s , the correction to Z_n is more important:

$$Z_n \simeq \frac{(E_f h_f^2 - E_s h_s^2) - \pi^2 l_0^2 (E_f - E_s)/12}{2(E_f h_f + E_s h_s) + \sqrt{\pi} E_I l_0 / \alpha_I} \quad (28)$$

where the symbol \simeq indicates also a correction of order e^{-h/l_0} , h being either h_f or h_s . In the presence of an additional stiff layer, on top or on the bottom, with a different stiffness E_b , we derive in the limit of vanishing e^{-h/l_0} , the following value for the neutral surface position:

$$Z_n \simeq \frac{(E_f h_f^2 - E_s h_s^2) + \tau_b E_b l_0 (h_s / \alpha_b - l_0 / \alpha_b^2) - \pi^2 l_0^2 (E_f - E_s)/12}{2(E_f h_f + E_s h_s) + \sqrt{\pi} l_0 (E_b / (2\alpha_b) + E_I / \alpha_I)} \quad (29)$$

with $\tau_b = 1$ when the stiff layer is on top, and $\tau_b = -1$ when the stiff layer is at the bottom. Knowing that the interface stiffness E_I or E_b may be an order of magnitude larger than E_f or E_s , this correction may modify significantly the values of the D coefficient in the FvK equations. The addition of thin layers, as described here, to the initial bilayered system will change the position of the neutral surface and the resulting D coefficient, but it will not change the structure of the FvK equations.

5.3 Localized defects of the thickness

Let us consider now a weak and localized variation of the thickness of one of the two layers. The neutral surface will then be distorted. We derive its new position by a simple linear expansion of Z_n . This induces an equivalent expansion on the parameter D which multiplies the bending term in the equation eq.(20). Assuming that the thickness varies as

$$h = h_i(1 + \beta_i(x)) \quad \text{then} \quad Z_n \simeq Z_n^{(0)} + \frac{\partial Z_n^{(0)}}{\partial h_i} h_i \beta_i(x) \quad \text{and} \quad D \simeq D^{(0)} + \frac{\partial D^{(0)}}{\partial h_i} h_i \beta_i(x). \quad (30)$$

where $D^{(0)}$ and $Z_n^{(0)}$ are given by eq.(25). and \simeq means an expansion restricted to first order. It reads

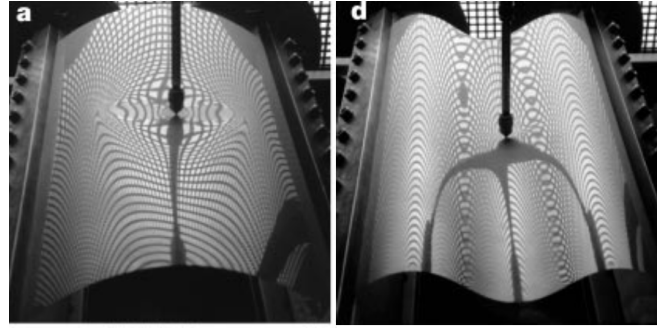


Fig. 3. Cylindrical mylar shell under a localized forcing. Originally the plate has a length of $\lambda = 35$ cm and a width $L = 17.5$ cm. The Young modulus of the mylar plate is 3.810^9 Pa.s and the Poisson ratio is $\nu = 0.4$. The initial bending is realized by imposing the boundary conditions. On left, one notices that for a low value of the imposed deviation $Z = 4$ mm, the pattern of sinking is quite elliptical while it becomes cylindrical for $Z = 15$ mm representing a folding in the opposite direction of the initial one. Image extracted from [32]

– On the top layer, we get:

$$Z_n \simeq Z_n^{(0)} + \frac{E_f (h_f - Z_n^{(0)})}{(E_f h_f + E_s h_s)} h_f \beta_f(x); \quad \text{and} \quad D \simeq D^{(0)} + \frac{E_f}{(1 - \nu^2)} (h_f - Z_n^{(0)})^2 h_f \beta_f(x) \quad (31)$$

– On the lower layer:

$$Z_n \simeq Z_n^{(0)} - \frac{E_s (h_s + Z_n^{(0)})}{(E_f h_f + E_s h_s)} h_s \beta_s(x); \quad \text{and} \quad D \simeq D^{(0)} + \frac{E_s}{(1 - \nu^2)} (h_s + Z_n^{(0)})^2 h_s \beta_s(x) \quad (32)$$

It is to be noted that a dip in either the upper or the lower layer means a negative value for the coefficients $\beta_i(x)$ so, as expected, a local decrease of the stiffness of the sample.

5.4 Localized inhomogeneity of the Young modulus

We now consider a localized variation of the Young modulus, which we treat through the expansion:

$$E \simeq E_i(1 + \delta_i(x)) \quad \text{and} \quad Z_n \simeq Z_n^{(0)} + \frac{\partial Z_n}{\partial E_i} E_i \delta_i(x) \quad \text{and} \quad D \simeq D^{(0)} + \frac{\partial D}{\partial E_i} E_i \delta_i(x) \quad (33)$$

Leading to:

– Inhomogeneity in the top layer:

$$Z_n \simeq Z_n^{(0)} + \frac{E_f E_s h_f h_s (h_f + h_s)}{(E_f h_f + E_s h_s)^2} \delta_f(x); \quad \text{and} \quad D \simeq D^{(0)} + \frac{E_f}{3(1 - \nu^2)} (h_f^3 - 3h_f^2 Z_n^{(0)} + 3h_f (Z_n^{(0)})^2) \delta_f(x) \quad (34)$$

– Inhomogeneity in the bottom layer:

$$Z_n \simeq Z_n^{(0)} - \frac{E_f E_s h_f h_s (h_f + h_s)}{(E_f h_f + E_s h_s)^2} \delta_s(x); \quad \text{and} \quad D \simeq D^{(0)} + \frac{E_f}{3(1 - \nu^2)} (h_s^3 + 3h_s^2 Z_n^{(0)} + 3h_s (Z_n^{(0)})^2) \delta_s(x) \quad (35)$$

6 Results for uni-axial folding

As mentioned above, the uniaxial case simplifies a lot the analytical analysis but reduces the diversity of buckling patterns that can be accounted for compared to the $2D$ case. Nevertheless, the $1D$ approximation is still of great experimental relevance for some experimental systems. In the case of the experiments of fig.(2), for example, the tissue and the genetic perturbation can be assumed to be spatially invariant along the y -coordinate, making it essentially a $1D$ problem. In this context, the present section provides an in-depth analysis of bending contributions of the bilayer in the uniaxial case, with and without structural defects. We first analyze the bending equation of the uni-axial folding analytically. We then address the problem numerically by selected possible $1D$ examples using the software of resolution Mathematica. Finally, simulations from the FEM (Finite-element method) software COMSOL Multi-Physics are presented.

6.1 Source of bending in bilayers

We will demonstrate in the following that the source of bending for growing bilayers are numerous and diverse and may have different biological origins. We analyze here some cases as examples. First, we define dimensionless parameters which will govern our FvK equations for a bilayer made of two layers with constant elastic coefficients.

6.1.1 Dimensionless bending equation

Using as length unit the length L of the sample, eq.(20) reads:

$$\underbrace{\frac{d^2}{dX^2} \left\{ (1 + \delta D) \frac{d^2 \zeta}{dX^2} \right\}}_{\text{Elastic term}} + \underbrace{\mathcal{N}_0 \frac{d^2(\zeta + W_0)}{dX^2}}_{\text{Pre-stress}} = \underbrace{\frac{d^2}{dX^2} (C - M)}_{\text{Growth contribution}} \quad (36)$$

where we keep the same notation for $\zeta(X)$ which becomes $\zeta(x)/L$, $X = x/L$, $\mathcal{N}_0 = N_0 L^2 / D^{(0)}$, $\delta D = (D - D^{(0)}) / D^{(0)}$, $M = M_{11} L / D^{(0)}$, $C = C_{11} / (D^{(0)} L)$ are dimensionless quantities and $W_0(X) = w_0(x) / L$ represents the initial position of the curved sample. External vertical loading is discarded. It is worth noting however that the equivalent of a loading can arise from the growth contribution (right-hand term of eq.(36)) owing to the fact that it involves spatial second derivatives, like the pre-stress term. For such a growth-induced loading to arise, growth of the two layers must differ to get a non-vanishing M value, and at least one of the terms (C or M) must vary spatially. This growth induced loading accords with previous investigations that demonstrated the need for differential growth of apposed layers to induce buckling of brain cortical folds for example [33–36]. Even with homogeneous growth, the right hand term can lead to a non-vanishing contribution, for example in the case of a structural defect that will change Z_n , and induce high spatial frequency components in C or M . Nevertheless, it is difficult to discuss a priori the ζ profile which is added to W_0 as a result of the growth term, since it depends also on the boundary conditions. We can intuitively predict that inhomogeneous growth is responsible to a "fictitious pressure" or on the contrary to a tension added to the sample. The simplest case may be the one of a homogeneous bilayer that we consider first.

6.1.2 Bilayer without structural defects

This case corresponds to sect.(5.1). For simplification, we do not consider the case of a sharp interface and the bilayer is made of two perfect layers of constant thickness and Young modulus. The growth process occurs mostly in one layer. Assuming first $g_{11}^f(X)$ in the upper layer and $g_{11}^s(X) = 0$ in the lower layer, we have for M_0^f and C_0^f according to eq.(21):

$$M_0^f = g_{11}^f(X) \left(\frac{E_f h_f (h_f - 2Z_n^{(0)})}{2D^{(0)}(1 - \nu^2)} \right); \quad C_0^f = \frac{dg_{13}^f}{dX} \left(\frac{E_f h_f (h_f^2 - 3Z_n^{(0)}(h_f - Z_n^{(0)}))}{3D^{(0)}(1 - \nu^2)} \right) \quad (37)$$

where $Z^{(0)}$ and $D^{(0)}$ are given by eq.(25). It is easy to check that both parameters M_0 and C_0 have the same sign as the growth elements g_{11}^f and $\partial_X g_{13}^f$. If growth occurs in the lower layer and not in the upper layer, it reads

$$M_0^s = -g_{11}^s(X) \left(\frac{E_s h_s (h_s + 2Z_n^{(0)})}{2D^{(0)}(1 - \nu^2)} \right) \quad C_0^s = \frac{dg_{13}^s(X)}{dX} \left(E_s h_s \left\{ \frac{h_s^2 + 3Z_n^{(0)}(h_s + 3Z_n^{(0)})}{3D^{(0)}(1 - \nu^2)} \right\} \right) \quad (38)$$

Here again, $h_s + 2Z_n^{(0)}$ is a positive quantity and the sign of M_0^s is opposite to the sign of g_{11}^s while the sign of C_0^s is automatically given by the growth coefficient derivative. Without pre-stress it is possible to observe a buckling of an initially flat plate because of a differential and inhomogeneous growth process. It exists a competition of the origin of this buckling between g_{11} or g_{13} , or between M_0 and C_0 . Differences in growth of the two layers induces a symmetry breaking between up and down. It is non trivial to compute the sign of the growth term -whether it contributes to a vertical pressure or tension-owing to the fact that it stems from the competition of two terms (M_0 and C_0) through their second derivatives. Notice however, if the growth is not x dependent, these terms will disappear from the buckling equation, on the contrary they will become more efficient if they strongly depend on x . Localized defects will increase the efficiency of the buckling as shown hereafter.

6.1.3 Analysis of structural defect in growing bilayers

a) Localized stiffness variation in one layer

We first consider that the stiffness can be locally modified as discussed in fig.(2), inducing a small change in the position of the neutral surface. We focus on the linear variation of M^f or M^s , and C^f or C^s , simply deduced from eq.(37,38). The

modification of these quantities are simply deduced taking into account the variation of δZ_n reported by eq.(34,35) in sect.(5.4), which reads:

$$\delta M^f = \frac{\partial M_0^f}{\partial Z_n^{(0)}} \frac{\partial Z_n^{(0)}}{\partial E_i} \delta E_i; \quad \delta C^f = \frac{\partial C_0^f}{\partial Z_n^{(0)}} \frac{\partial Z_n^{(0)}}{\partial E_i} \delta E_i \quad (39)$$

where E_i is the Young modulus of the layer affected by the defect: E_f or E_s and δE_i is represented by $E_i \delta_i(X)$, in a similar way to eq.(34,35). Similar results apply for δM^s which corresponds to growth in the lower layer and for δC^s . We give here only the results but we define first the following positive quantities:

$$m^f = \frac{E_f^2 E_s h_f^2 h_s (h_s + h_f)}{2D^{(0)}(1 - \nu^2)(E_f h_f + E_s h_s)^2} \quad c^f = \frac{(E_f E_s h_f h_s (h_f + h_s))^2}{2D^{(0)}(1 - \nu^2)(E_f h_f + E_s h_s)^3} \quad (40)$$

– When the growth occurs in the upper layer, which also exhibits a stiffness defect, then

$$\begin{cases} \delta M^f = -g_{11}^f(X) m^f \delta_f(X); & \delta C^f = -\frac{dg_{13}^f}{dx} c^f \delta_f(X) & \text{defect on top} \\ \delta M^f = g_{11}^f(X) m^f \delta_s(X); & \delta C^f = \frac{dg_{13}^f}{dx} c^f \delta_s(X) & \text{defect on the bottom} \end{cases} \quad (41)$$

– When the growth occurs in the substrate, perturbation occurs now on M_0^s and C_0^s and one needs to consider again a defect of the stiffness either on top or on the lower layer.

$$\begin{cases} \delta M^s = -g_{11}^s(X) m^f \frac{E_s h_s}{E_h h_f} \delta_f(X); & \delta C^s = \frac{dg_{13}^s}{dx} c^f \delta_f(X) & \text{defect on top} \\ \delta M^s = g_{11}^s(X) m^f \frac{E_s h_s}{E_h h_f} \delta_s(X); & \delta C^s = -\frac{dg_{13}^s}{dx} c^f \delta_s(X) & \text{defect on the bottom} \end{cases} \quad (42)$$

b) *Localized variation of the thickness of one layer.*

A defect in the thickness affects the position of the neutral surface but also, when the thickness defect occurs in the same layer as the growth, the averaged value of the coefficients of eq.(21) related to the first bending FvK equation, eq.(20). We give here only the schema when a dip appears in the lower layer, the growth occurring either on the top or the lower layer. A similar analysis gives

$$\delta M^f = \frac{dM_0^f}{dZ_n^{(0)}} \delta Z_n = g_{11}(X) \mathcal{M}^f \beta_s(X); \quad \delta C^f = \frac{dC_0^f}{dZ_n^{(0)}} \delta Z_n = \frac{dg_{13}^f}{dX} C^f \beta_s(X) \quad (43)$$

where as in sect.(5.3), $\beta_s(X)$ describes the shape of a notch and \mathcal{M}^f and C^f are dimensionless positive quantity.

$$\mathcal{M}^f = E_f E_s h_f h_s \frac{E_s h_s^2 + E_f h_f (2h_s + h_f)}{2D^{(0)}(1 - \nu^2)(E_f h_f + E_s h_s)^2}; \quad C^f = \frac{E_s h_s (h_f + h_s)}{E_h h_f + E_s h_s} \mathcal{M}^f \quad (44)$$

We examine now the case where growth occurs in the bottom layer where also the defect is localized: .

$$\delta M^s = -g_{11}^s(X) \mathcal{M}^f \beta_s(X); \quad \delta C^s = \frac{d^s g_{13}}{dx} C^s \beta_s(X) \quad (45)$$

with

$$C^s = \frac{E_s^2 h_s^3 + E_f E_s h_f h_s (-h_f + h_s) + E_f^2 h_f^2 (h_f + 2h_s)}{2E_f h_f (E_f h_f + E_s h_s)} \mathcal{M}^f \quad (46)$$

c) *Shape of defects*

Localized defects can be positioned in any place of the sample. From eq.(36), we have noticed that they may induce an equivalent forcing on the sample if they contribute to strong variation of the second derivatives of the coefficients δM and/or δC . Choosing a sharp defect in the center of the sample, a good representation may be $\delta = e_Y e^{-X^2/\ell^2}$ where e_Y is the relative amplitude of the stiffness defect which can be positive or negative, 2ℓ depicts qualitatively its width. The second derivative is $\partial_{XX} \delta$ is of order $-2e_Y/\ell^2$ which for a defect of width 0.05 corresponds to an amplitude of $200e_Y$ at the center. It is to be noted that the sign is opposite to e_Y . So the sign of the second derivative of δM or δC can be easily found from paragraph (a). The convention for thickness defect is the following: $h_i \beta_i(X)$ where $\beta_i(X)$ is negative for a notch and positive for a protusion. Here again, $\partial_{xx} \beta$ will be opposite to β . In any case, it remains that the prediction of the global sign of the second member of eq.(36). is hard to predict due to the competition between g_{11} and g_{13} . Let us remember that a positive sign of a localized contribution will be equivalent to a localized forcing which will mimic the experiment [32] shown in fig.(3).

Please give a shorter version with: \authorrunning and \titlerunning prior to \maketitle

13

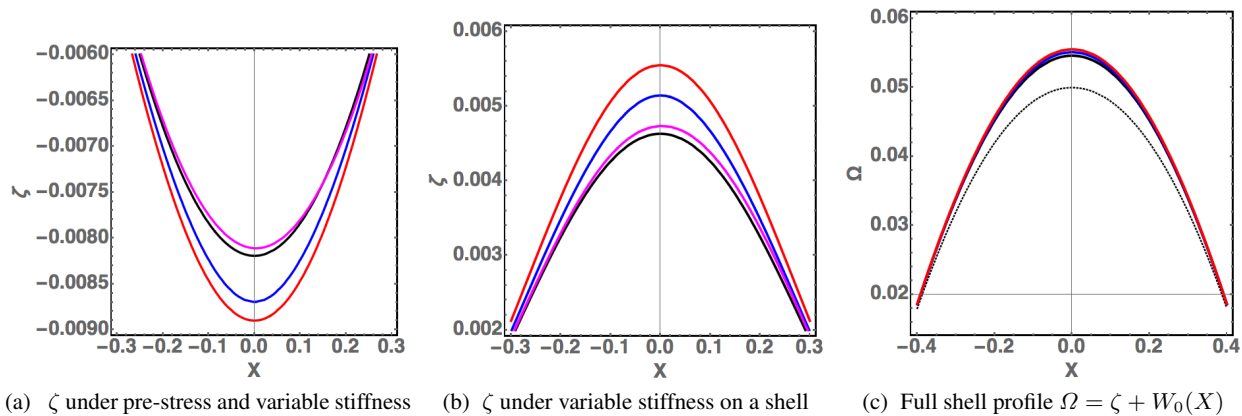


Fig. 4. Buckling deviation due to a variable stiffness coefficient $D(X)$, in a *pre-stressed non-growing* plate or shell. In (a), the profile ζ of an initial elastic plate under pre-stress $N_0 = 4$ is plotted as a function of the X coordinate. The X -domain is reduced to the interval $\{-0.3, 0.3\}$ for clarity. At both ends, $X \pm 0.5$, $\zeta = 0$ and $X = \pm 0.5$, $\partial_X \zeta \pm 0.03$. $\delta D = -D_0 e^{-(X-X_d)^2/l_d^2}$ with $D_0 = 0$ for the black line and $D_0 = 0.3$ for the blue, red, magenta colored lines. Except for the magenta line, the dip is centered on $X = 0$, otherwise, it is located at $X_d = 0.3$. The blue and magenta curves correspond to a narrow dip with $l_d = 0.1$, the red curve to a larger one with $l_d = 0.3$. Notice that a dip located far from the center has no effect and the deflection remains weak in any case (scale of the vertical line). In (b), ζ for a pre-stressed shell of equation $W_0(X) = (1/4 - x^2)/5$ of negative curvature and clamped boundary conditions: $X \pm 1/2, \zeta = \partial_X \zeta = 0$. In (c) the full profile $\Omega = \zeta + W_0(X)$ with dotted black line for W_0 . The same code of colors is applied in the three panels (a, b, c).

6.2 Numerical investigations of the FvK bilayer for a plate or a shell.

In this section, we aim to demonstrate the role of defects on plates and slightly curved shell portion under pre-stress. To simplify we focus first on a homogeneous growth process: it means a process independent of X and identical in both layers or equivalently a non growing sample. Then we will give numerical examples to illustrate the analytical results of the previous section when differential growth occurs contingently to defects.

6.2.1 Decrease of thickness on a non-growing pre-stressed plate or shell

In this section, we will evaluate the role of a sharp variation on the D coefficient of a pre-stressed sample initially flat or curved. For numerical purpose the defect has the shape of a penetrating peak and is represented by a Gaussian so $\delta D = -D_0 e^{-(X-X_d)^2/l_d^2}$. D_0 is a positive coefficient which can be evaluated with either eq.(31) or eq.(32), l_d is an estimation of the scale of the defect compared to the scale of the sample L and X_d is its relative position in the sample. For a plate, a curvature is initially induced by the pre-stress and applying a slope at both ends. In fig.(4a) the imposed slope is $\partial_X \zeta \pm 0.03$ at $X \pm 0.5$ giving a deflection below the horizontal (black line). This deviation increases with the defect since it weakens the stiffness more and more with the amplitude $D_0 = 0.2$ (blue curve), $D_0 = 0.3$ amplitude (red curve). Even for a sharp-pointed defect, with $l_d = 1/10$, the deviation ζ remains small and not very selective. In addition, a displacement on the position of the defect does not affect ζ too much (magenta curve). For a shell which is initially curved in the positive Z direction with clamped conditions at both ends, as shown in fig.(4b,c), the deviation ζ is amplified by the initial curvature and the pre-stress. Here again, any deviation on the right of the defect weakens its role on ζ since we cannot distinguish the deviation with lateral defect (magenta line) from the black line. When the whole profile $\Omega = \zeta + w_0(X)$ is considered, we clearly observe on increase of the total curvature when the defect is centered at the maximum of deflection.

6.2.2 Thickness defects on growing plates and shells

The thickness variation on δD gives a very intuitive result. A much less intuitive result concerns the sign of $\partial_{X^2} \delta M$ and $\partial_{X^2} \delta C$ of eq.(36) since the results are dependent of the second derivative of these growth coefficients. These quantities have been studied in details in sect.(6.1.3). We must notice that they have an opposite sign a priori and in practical situations, we will have little information except by comparison with genetically modified tissues. So we will join these two contributions into a unique term $\delta \mathcal{S}_G = -(\delta M - \delta C) = s_g e^{-(X-X_d)^2/l_d^2}$ in the right-hand-side of eq.(36). Intuitively, as soon as this term is differentiated 2 times, it behaves as either a pressure if it is positive or a tension in the opposite case while the initial curvature of the concave shell behaves like a pressure and a convex one like a tension. Knowing that a groove in the substrate is represented by a negative profile, the second derivative is then positive for $X = X_d$ being given by $\partial_{X^2} \delta \mathcal{S}_R \sim -2/l_d^2 s_g e^{-(X-X_d)^2/l_d^2}$. Illustration is

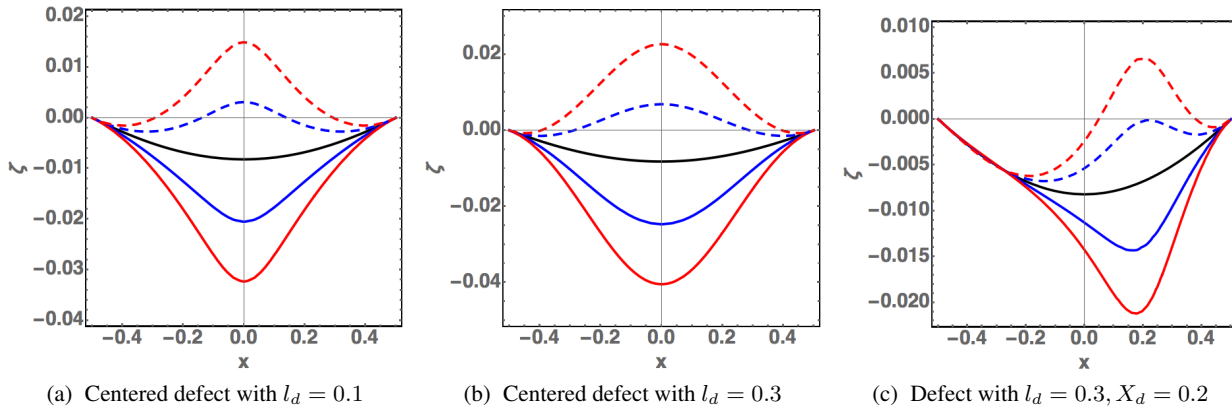


Fig. 5. Buckling deviation ζ in a pre-stressed *growing* plate. The prescribed boundary conditions are: $\zeta = 0$ and $\partial_X \zeta = \pm 0.03$ at $X \pm 0.5$, $N_0 = 4$ and the black line is the initial shape of the plate under pre-stress. The defect is as follows: for $D, \delta D^{(0)} = -0.3e^{-(X-X_d)^2/l_d^2}$, $\delta S_G = s_g e^{-(X-X_d)^2/l_d^2}$ with $s_g = 0.5$ (resp. -0.5) represented by a continuous blue line (resp. a dot-dashed blue line) and $s_g = 1$ (resp. $s_g = -1$) represented by a continuous red line (resp. dotted-dashed red line) for the 3 panels. In (a), $X_d = 0$ and $l_d = 0.1$. In (b), $X_d = 0$ and $l_d = 0.3$. In (c) the same as in (a) for an eccentric defect positioned at $X_d = 0.2$. Notice the strong asymmetry of all curves in panel (c).

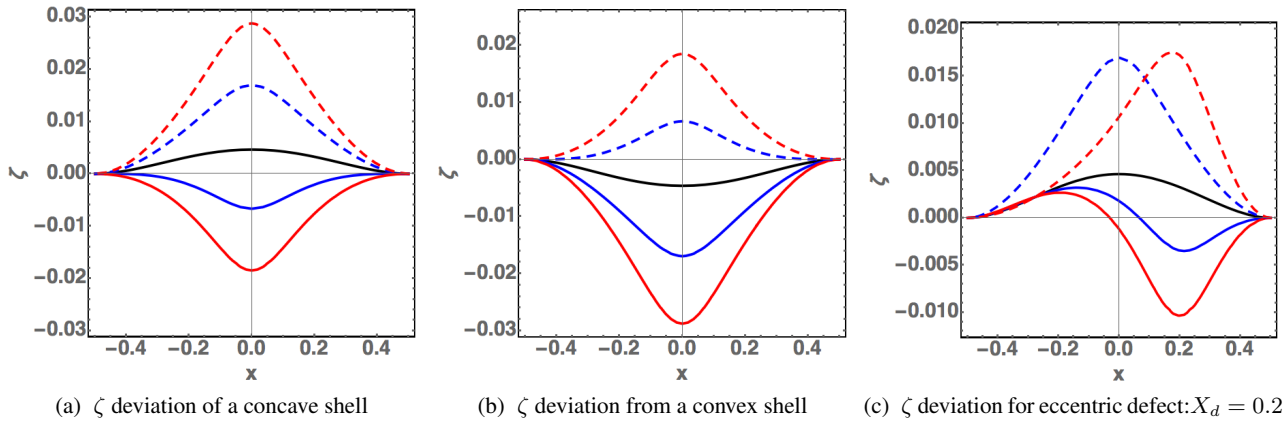


Fig. 6. Buckling deviation ζ for a pre-stressed ($N_0 = 4$) shell. The same definition and color codes apply as in fig.(5): black no defect, blue continuous $s_g = 0.5$, blue discontinuous $s_g = -0.5$, red continuous curve $s_g = 1$ and $l_d = 0.1$, red discontinuous $s_g = 1$ for the 3 panels. Clamped boundary conditions are applied. In (a), the shell is initially concave and $l_d = 0.1$. In (b) the shell is initially convex. In (c), the defect is localized on right $x_d = 0.2$ and the shell is concave. $W_0(X) = (1/4 - X^2)/5$, for concave shape and $W_0(X) = (X^2 - 1/4)/5$ for convex shape

given in fig.(5) for a pre-stress plate with defect localized at $X = 0$ with two different length-scales: $l_d = 0.1$ and $l_d = 0.3$ and different amplitudes for $s_g = \pm 0.5$ and ± 1 . A defect put on the right is also shown with a noticeable distortion in panel (c) of fig.(5). In fig.(6), the same set of perturbations act on a shell either concave (panel(a)) or convex (panel(b)) and the deviation ζ is plotted with boundary conditions $\zeta = \partial_X \zeta = 0$ for $X \pm 0.5$. For the concave case (a), the deviation due to the defect is decreased for $s_g > 0$ and increased otherwise. The opposite result is obtained for in the convex case panel (b). The distortion is shown in panel (c) only for the concave case. Once the deviation is superposed on the initial shell, depending on the respective sign of the deviation versus the shell geometry, it is possible to observe an inversion of the curvature. This is demonstrated in the three panels of fig.(7).

6.3 Confrontation of the uniaxial FvK bilayer model with experiments

In section (2), we presented experimental evidences that a local change in the mechanical properties of the ECM can induce major morphological changes in the wing imaginal disc epithelium. Here, we confront our bilayer FvK formalism in the uniaxial geometry to experimental profiles extracted from the images of fig.(2c,e).

We first focus on the tissue presented in fig.(2c), that we rescale in unit of the lateral size of the imaginal disc (fig.(8a)). The

Please give a shorter version with: \authorrunning and \titlerunning prior to \maketitle

15

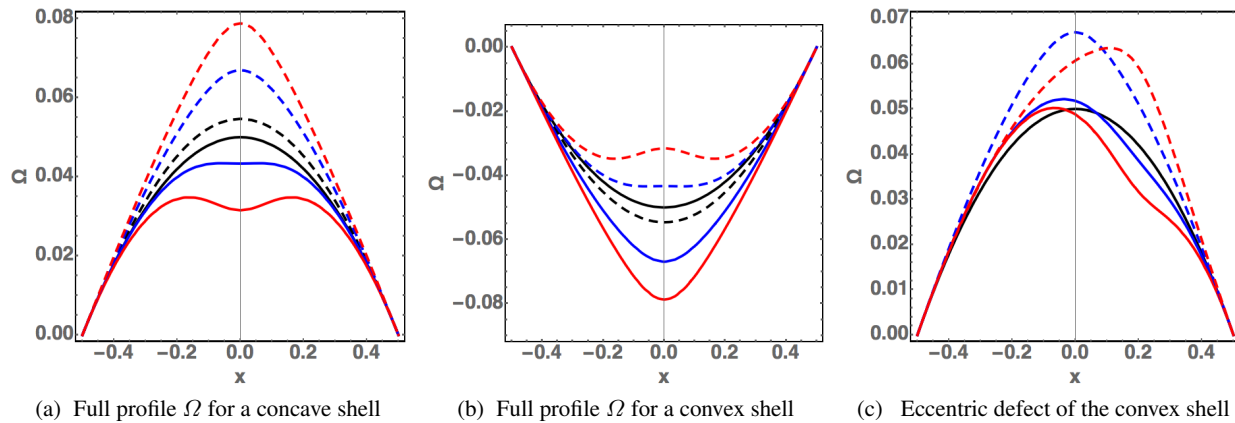


Fig. 7. In (a,b,c) The shell profile $\Omega(X) = W_0(X) + \zeta(X)$. The colored lines correspond to the buckling conditions of fig.(6). Notice the possibility to observe an inversion of curvature in panel (a) and (b) for a suitable size of s_g with respect to the curvature of the shell.

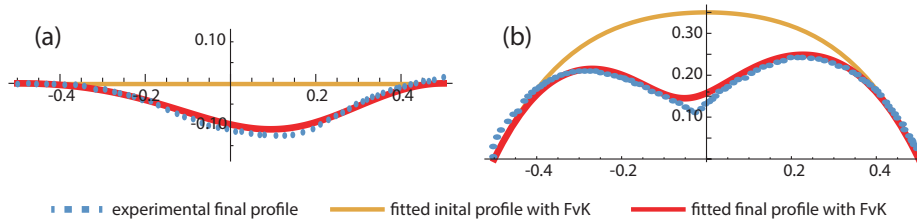


Fig. 8. Fitting experimental wing disc profiles with the uniaxial FvK bilayer theory. (a): Theoretical fit of an early wing imaginal disc, for which the initial profile before perturbation was flat (same as fig.(2c)). (b): Theoretical fit of an older wing imaginal disc, for which the initial profile before perturbation was curved (same as fig.(2e)).

perturbation of the ECM was induced before the naturally occurring curvature could develop in the tissue. We therefore assume no initial curvature: a horizontal plate only under pre-stress. We fix the slope conditions at the border, making the hypothesis that the tissue periphery is not affected by the perturbation. This hypothesis is justified by the fact that the defect is well localized at the center of the tissue. The fit of parameters is achieved by a limited number of trials. Fitted parameters converge to the following values: a pre-stress of order 9 in unit of D and a parameter $D_0 = 0.3$; a defect characterized by an amplitude $s_g = 4$, position $x_d = 0.1$ and width $l_d = 0.25$, when the defect is modeled by the relation $s_g e^{-(X-X_d)^2/l_d^2}$, see sect.(6.2.2). Finally in fig.(8b), the shape of the disc at the boundaries and the developmental timing of the perturbation, suggest that the tissue was already curved at the onset of the perturbation. We then used the shell treatment with a best guess for the unperturbed shape $w_0(X) = 0.7(1/4 - X^2 + 4(1/16 - X^4))$, N_0 has little effect and is put to zero, which suggests that in old epithelia, the outer stresses have relaxed which is not the case for young epithelia. The amplitude of the defect have increased: it is now $s_G = 10$; localization is $X_d = -0.05$, and width $l_d = 0.1$. Thus, the bilayered FvK theory can account for the mechanics at play in the growing wing imaginal disc in the presence of a localized defect in the ECM, both when the tissue is initially flat and curved.

7 Numerical Simulations with Finite-Element Method

We now consider the problem of the bilayer bending in the linear Hookean elasticity approach using Comsol Multiphysics which computes the deformations in the real geometry of the bilayer, two different connected layers, without averaging the elastic properties. The bilayer we study in the following is made of a thin ($h_f = 10\mu\text{m}$) and relatively soft ($E_f = 50\text{ kPa}$) upper layer and a thicker ($h_s = 12\mu\text{m}$) and stiffer ($E_s = 75\text{ kPa}$) bottom layer. The length of the bilayer is $L = 500\mu\text{m}$. The layers are submitted to growth and pre-stress, and the boundaries are either free or constrained. We investigate a defect, as a local removal of the basal layer in the middle of the bilayer with an extension of $10\mu\text{m}$ and a thickness $h_d \leq h_s$, and as a local change of stiffness and growth in the bilayer. The growth is anisotropic and is introduced in a tensorial form: $G_{ij} = 1 + g \delta_{1i} \delta_{1j}$, with $g \sim 0 - 0.1$. The growth may be introduced in the top layer only as in sect.(7.2), the bottom layer only in sect.(7.4), or in both layers as in sect.(7.3). The pre-stress consists in an anisotropic compression or tension, so that $\sigma_{ij}^{PS} = -\sigma^{PS} \delta_{1i} \delta_{1j}$ where $\sigma^{PS} \sim 0 - 500\text{ Pa}$.

We also study the case of the shell on the further deviation of the sample. We set an initial curvature to the shell: $W_0 = H \times (L/2)^{-2}((L/2)^2 - X^2)$ where H is the displacement at $X = 0$. In order to compare the different results, we plot the profile of the interface between the upper and lower layer (the red line in fig.(9e)).

Finally, we fit FEM simulations to the experiment described in sect.(2). The result is compared to the one obtain from the FvK calculation sect.(6.3).

7.1 Pre-stress on an initially curved bilayer

In fig.(9a) we investigate different initial shell shapes with different curvatures characterized by $H = -20 \mu\text{m}, 0 \mu\text{m}, 20 \mu\text{m}$ with the same pre-stress $\sigma^{PS} = 200 \text{ Pa}$ in the bilayer. For a plate, with no initial curvature, a bending toward the stiffer and thicker basal side is obtained while for a convex or a concave shell, the initial curvature of the shell is reinforced in absolute value. This is consistent with the previous FvK model for shells. In fact the bending deviation follows the initial shape of the shell.

7.2 Thickness and growth defect on growing plates and shells

In biological systems, the two layers in epithelia are not independent. For instance, the basal membrane regulates the proliferation and the differentiation in the epithelium. In general, the basal layer structures the upper layer of the epithelium, and a defect in the lower layer can have consequences on the proliferation and metabolism of the upper layer. Therefore, we now investigate the shape change at the level of a defect which alters the thickness of the basal layer and consequently the growth of the upper growing layer. Figure (9b) displays the results when the basal layer is removed in proportion of 85% (dotted lines) in thickness and the upper layer is not growing at the defect level, as well as the case with no defect (continuous lines). We observe a buckling towards the basal membrane, in the neighborhood of the defect.

7.3 Place of a defect

Defects can appear anywhere along a bilayer. In fig.(9c) we impose defects on a planar bilayer, located at $X = 0, 0.08, 0.16$ for the blue, green and red lines respectively. Both layers grow to the same extent $g = 0.1$. The defect consists in removing a part of the bottom layer. Interestingly, with the same size of the defect, the amplitude of the deformation is different, and the shift of the defect is not only a shift in the deformation.

7.4 Dependence on boundary conditions

The comparison between confined and free geometries is a recurrent topic in cellular growth studies [37,38] from multiple perspectives, such as the folding of epithelial sheets [39]. The boundary conditions of bilayer plates or shells are also necessary for the analytical and numerical study of the system. But unfortunately, they are not always perfectly known. When the set-up is symmetric, one can use those symmetries to constrain the problem, and the system has free-boundary conditions. Sometimes the experiment is such that the system is clamped, or loses its symmetry. Confined systems are strongly dependent on boundary conditions.

In fig.(9d) we compare the buckling in a constrained and free geometry. The buckling is very different, and its direction (up or down) even changes when starting with a concave geometry. It may lead to strong inaccuracies in FEM simulations of rectangular geometry and semi-analytical treatments become necessary, see reference [40]. Notice that in the previous sections, sect.(6.2.1,6.2.2), boundary conditions are always fixed symmetrically for plates and clamped boundary conditions for shell deviations. This point is important for comparing our numerical results to the experiments as shown in the next section. There can be a few types of constrained geometry. In fig.(9d), it is obtained by imposing a zero displacement at two points on the lateral boundaries. In fig.(9f), the whole lateral boundaries are imposed a zero displacement. In the second case, the Z-displacement is close to have a zero derivative as boundary conditions.

7.5 Confrontation of the finite-element simulations with experiments

We use the finite element method to reproduce qualitatively the side to which the imaginal wing curves. We assume that the stress inside the cell layer is induced by growth, and is relaxed when a defect is introduced. Since in classical mechanics only the stress-free configuration and the configuration obtained after the process are to be taken into account, we make a multi-layer growth with and without defect. In our simulations, we observed that a 2-layer model could not reproduce the experimentally observed change of curvature upon ECM degradation. Only when an apical membrane is introduced in the model, can we reproduce the behavior - making it essentially a 3 layers model. Indeed, contrary to the resolution of the FvK equation where boundary

Please give a shorter version with: \authorrunning and \titlerunning prior to \maketitle

17

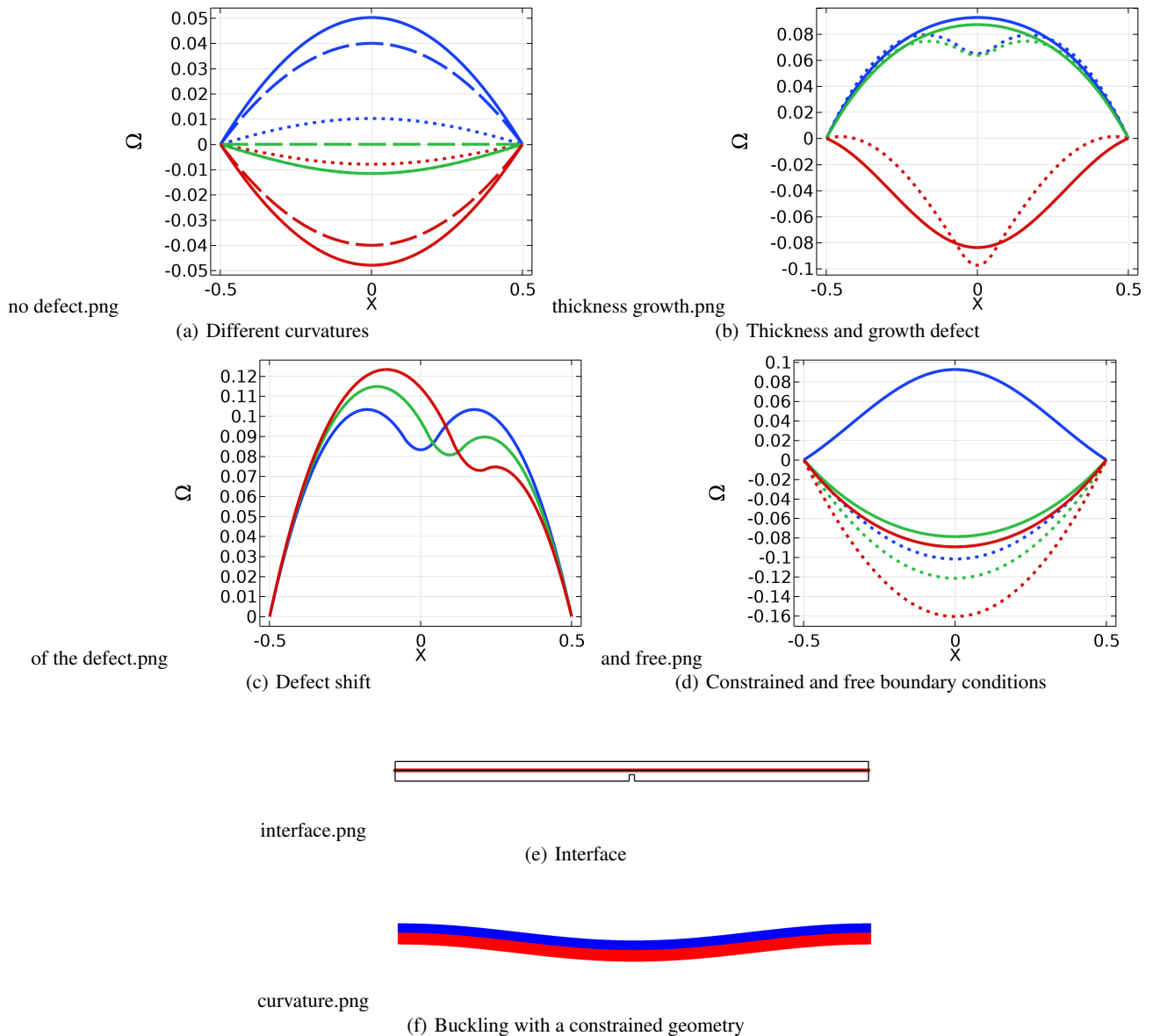


Fig. 9. (a): Profile of the interface between the two layers for different curvatures and a pre-stress $\sigma^{PS} = 200$ Pa, with no defect in the lower layer. The continuous, dashed, and dotted lines correspond respectively to $W_0 + \zeta$, W_0 and ζ . The red, green and blue lines correspond respectively to $H = \{-20, 0, 20\}$ μm . (b): Profile of the interface between the two layers for a case with a defect of relative thickness $h_d/h_s = 0.85$ with h_d the defect thickness and h_s the bottom layer thickness. The growth parameter is $g = 0.05$. The green, blue, and red curves correspond respectively to cases with an initial zero, concave and convex curvatures $H = 0, 20, -20$. (c): Different shifts for the defect, which is at $X = 0, 0.08, 0.16$ respectively for the blue, green, and red line. The amplitude of the deformation depends on the localization of the defect. The growth parameter takes the value $g = 0.1$. (d): Comparison between constrained (dashed lines) and free (continuous lines) boundary conditions for zero, convex and concave initial curvatures ($H = 0, -20, 20$ for the green, red and blue lines) and a growing bottom layer ($g = 0.03$). (e): Interface between the lower and upper layer in red. (f): Buckling for a constrained bilayer with a growing bottom layer and an initial concave curvature.

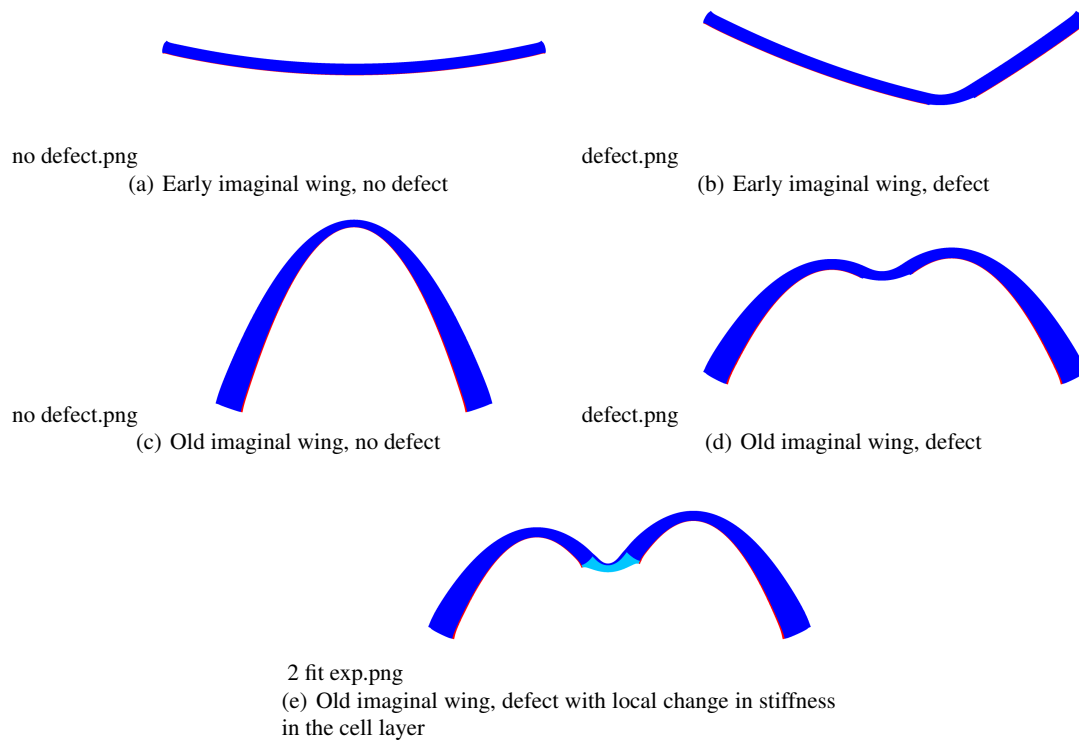


Fig. 10. Cuts of the imaginal wing for the different FEM simulations with and without defect. The colors reflect the stiffness: red for the basal ECM, blue for the upper membrane and the cell layer, and cyan for the zone of the cell layer around the defect that softens in the refined model.

conditions are imposed, we use free boundary conditions with the Finite Element Method. Therefore a third layer has to be added in order to constrain the system to bend towards the correct side.

More precisely, we simulated a thick ($15\ \mu\text{m}$) cell layer of length $L = 500\ \mu\text{m}$, growing between two non growing thin layers. This process creates a compressive stress in the two non growing layers. The top layer has a thickness of $5\ \mu\text{m}$ and the lower layer has a thickness of $2\ \mu\text{m}$. The apical membrane may represent the apical cortex, and the apical adherens layer that dominates apical mechanics in epithelia [4], whereas the basal membrane represents the ECM. The growth deformation gradient is written as: $G_{ij} = 1 + \delta_{1i}\delta_{1j}g_{11}$. The boundary conditions are free.

We fit the experiment (fig.(11a,11b)) and we find a basal ECM stiffer ($E_b = 100\ \text{kPa}$ or $E_b = 30\ \text{kPa}$) than the upper membrane and that the cell layer ($E = 10\ \text{kPa}$). In the case of the early imaginal wing, $g_{11} = 0.2$ and $E_b = 30\ \text{kPa}$, and for the old imaginal wing $g_{11} = 0.25$ and $E_b = 100\ \text{kPa}$. We also introduce an asymmetry for the place of the defect at $X = -0.025$ for the old epithelium and $X = 0.15$ for the early epithelium. The apparent growth is thus higher and the ECM stiffer for the old imaginal wing when compared to the early imaginal wing. This set-up results in a bending toward the upper layer in the case with no defect for the old imaginal wing and a slight bending towards the basal side for the early imaginal wing (fig.(10a,10c)). However, when a defect of length $l_d = 100\ \mu\text{m}$ is introduced in the form of a removal of the basal ECM, the curvature undergoes an inversion toward the basal side in in both cases (fig.(10b,10d)).

It seems that for the early imaginal disc this model is sufficient to properly reproduce the experimental profile (fig.(11a)). However, the agreement was not as good for the older initially curved imaginal disc (fig.(11b)). We then modified the FEM model with the same strategy as for the FvK model, by changing the stiffness at the level of the defect, making the cell layer softer. This refined model provided a better fit to the experiments (fig.(10e,11c)). The new values of the fit for the old imaginal wing are: $g_{11} = 0.43$ and $E = 1.7\ \text{kPa}$ in the cell layer at the defect level. The other parameters remain unchanged. Contrarily, changing the growth rate at the level of the defect does not improve the fit. We deduce that the contribution s_g of the defect in sect.(6.3) is mostly due to a change of the stiffness in the growing cell layer at the level of the defect, rather than a change of growth. This is consistent with the duration of Mmp2 expression during the experiment (18-24 h), see sect.(2). No pre-stress was introduced in the FEM simulations, since this pre-stress is assumed to be caused by growth, and the growth can be introduced explicitly with an order of magnitude larger than with FvK. For the same reason, growth generates the curvature, which is not introduced explicitly. To conclude, FEM simulations validate the FvK calculations.

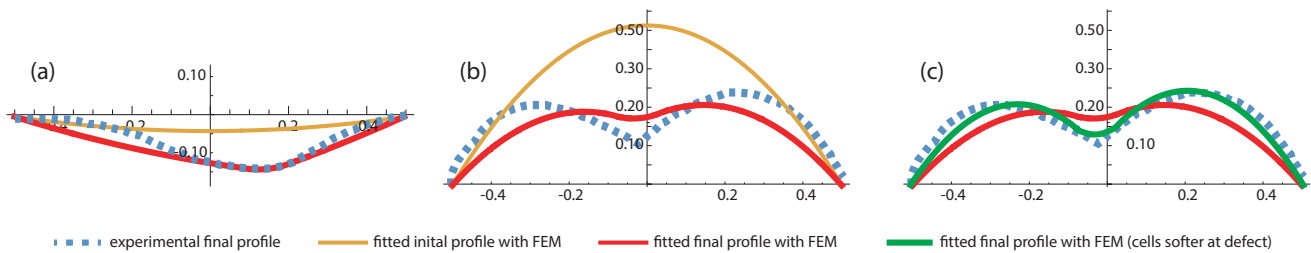


Fig. 11. Fitting experimental wing disc profiles with the FEM model. **(a):** Theoretical fit of an early wing imaginal disc, for which the initial profile before perturbation was flat (same as fig.(2c)). **(b):** Theoretical fit of an older wing imaginal disc, for which the initial profile before perturbation was curved (same as fig.(2e)). The stiffness of the cell layer is not altered by the defect. **(c):** Comparison between the refined fit when the stiffness of the cell layer is altered by the defect (in green) and the case when it is not (red).

8 Discussion and conclusion

Motivated by experimental evidence that the ECM plays an important role in shaping epithelia in 3D, as shown in fig.(2), this work provides a mechanical description of growing epithelia in the Föppl-von Kármán framework. In the context of embryogenesis and organo-genesis, previous theoretical studies have modeled epithelia using the vertex model [41–43] inspired from the physics of foams [44]. Indeed, epithelia are cellular pavings where the main unit has a polygonal shape in 2D or a shape of polyhedrons in 3D. Vertex models approximate cells as polygons, make hypothesis about the mechanics of individual cells (*e.g.* their growth, surface or line tension and stiffness) and simulate the behavior of cell assemblies from these elementary rules. These simulations are based on energy minimisation, as in the present work. One limitation of cell-based models is the fact that simulating cell assemblies may become difficult at very large cell number, notably when the parameter-space must be explored. In addition, it is rather hard to extract macroscopic physical quantities such as Young modulus or surface tension from microscopic parameters describing the cells.

Most of the aforementioned theoretical works focused on the 2D mechanics of the apical surface of epithelia, with only few studies addressing the 3D aspects of tissues [45,46]. Epithelia are usually thin layers and the elasticity of slender elastic objects such as plates, tubes or membranes can be good candidates to describe their mechanical properties especially in the presence of bending. However, a single plate may be too simple a model when it comes to explain the behavior of epithelia, which are intrinsically multilayered systems. In the present paper we have considered the multi-component structure of epithelia from the view point of elasticity. Local changes in elastic coefficients and differential growth are at the origin of stresses able to buckle the sample. Not only could our bilayered elastic model predict a broad range of morphogenetic behavior, it also yielded surface profiles that were in very good agreement with experimentally observed ones. Notably, it could account for the localized degradation of the ECM on two experimental observations that were limit cases: one initially flat and one initially curved wing imaginal discs (figs. (2,8)). The morphogenetic processes that we observed and modeled -fold formation upon ECM degradation- were artificially induced *via* an ectopic genetic expression of the metalloprotease Mmp2. These experiments, as such, fall in the realm of "synthetic morphogenesis". Nevertheless, similar processes are naturally occurring in tissues. For example, deep folds that develop at late stage of the wing imaginal disc are thought to arise through such a local degradation of the ECM [23,24]. In this paper, we performed experimental observations of tissues exclusively after the action of the genetic perturbation. Ideally, one would need to image the tissues before and after the onset of the perturbation to completely disentangle the origin of the buckling. This is experimentally possible in *Drosophila* with chronic imaging [47].

In the uniaxial geometry (with only one dimension for the sample), defects generates buckling distortions of the shape due to variation of thickness, stiffness but also of growth process. For a 1D bending process, the in-plane elastic equation is trivially solved and only the bending equation exhibits interesting degrees of distortions. It is not the case for 2D modes of deformations where spatial patterns happen on the outer periphery of the samples ([15, 16]). One can then expect interesting patterns in these geometries.

9 Author Contributions

The two first authors contribute equally. Both LL and MBA conceive the project and wrote the manuscript.

10 Acknowledgements

The authors acknowledge the support of ANR (Agence Nationale de la Recherche) under the contracts MecaTiss (ANR-17-CE30-0007) and GuideFusion (ANR-18-CE13-028); Excellence Initiative of Aix-Marseille University - A*Midex (capostromex), a

French Investissements d’Avenir programme. PQQ acknowledges the support of the China Scholarship Council (CSC), file N^o 201706100182.

References

1. B. Li, Y.-P. Cao, and X.-Q. Feng, “Growth and surface folding of esophageal mucosa: a biomechanical model,” *Journal of biomechanics*, vol. 44, no. 1, pp. 182–188, 2011.
2. M. Ben Amar and F. Jia, “Anisotropic growth shapes intestinal tissues during embryogenesis,” *Proceedings of the National Academy of Sciences*, vol. 110, no. 26, pp. 10525–10530, 2013.
3. E. Hannezo, J. Prost, and J.-F. Joanny, “Instabilities of monolayered epithelia: shape and structure of villi and crypts,” *Physical Review Letters*, vol. 107, no. 7, p. 078104, 2011.
4. D. Pinheiro and Y. Bellaïche, “Mechanical force-driven adherens junction remodeling and epithelial dynamics,” *Developmental cell*, vol. 47, no. 1, pp. 3–19, 2018.
5. N. Khalilgharibi and Y. Mao, “To form and function: on the role of basement membrane mechanics in tissue development, homeostasis and disease,” *Open Biology*, vol. 11, no. 2, p. 200360, 2021.
6. P. Ciarletta and M. Ben Amar, “Papillary networks in the dermal–epidermal junction of skin: a biomechanical model,” *Mechanics Research Communications*, vol. 42, pp. 68–76, 2012.
7. J. Bateman, R. S. Reddy, H. Saito, and D. Van Vactor, “The receptor tyrosine phosphatase dlar and integrins organize actin filaments in the drosophila follicular epithelium,” *Current Biology*, vol. 11, no. 17, pp. 1317–1327, 2001.
8. I. Delon and N. H. Brown, “The integrin adhesion complex changes its composition and function during morphogenesis of an epithelium,” *Journal of cell science*, vol. 122, no. 23, pp. 4363–4374, 2009.
9. M. A. Biot, “Folding of a layered viscoelastic medium derived from an exact stability theory of a continuum under initial stress,” *Quarterly of Applied Mathematics*, vol. 17, no. 2, pp. 185–204, 1959.
10. M. Kücken and A. C. Newell, “A model for fingerprint formation,” *EPL (Europhysics Letters)*, vol. 68, no. 1, p. 141, 2004.
11. M. Kücken and A. C. Newell, “Fingerprint formation,” *Journal of theoretical biology*, vol. 235, no. 1, pp. 71–83, 2005.
12. B. Audoly and A. Boudaoud, “Buckling of a stiff film bound to a compliant substrate—part iii:: Herringbone solutions at large buckling parameter,” *Journal of the Mechanics and Physics of Solids*, vol. 56, no. 7, pp. 2444–2458, 2008.
13. P. M. Reis, F. Corson, A. Boudaoud, and B. Roman, “Localization through surface folding in solid foams under compression,” *Physical review letters*, vol. 103, no. 4, p. 045501, 2009.
14. J. Yin, J. L. Yagüe, D. Eggenspieler, K. K. Gleason, and M. C. Boyce, “Deterministic order in surface micro-topologies through sequential wrinkling,” *Advanced materials*, vol. 24, no. 40, pp. 5441–5446, 2012.
15. J. Dervaux and M. Ben Amar, “Morphogenesis of growing soft tissues,” *Physical review letters*, vol. 101, no. 6, p. 068101, 2008.
16. J. Dervaux, P. Ciarletta, and M. Ben Amar, “Morphogenesis of thin hyperelastic plates: a constitutive theory of biological growth in the Föppl–von Kármán limit,” *Journal of the Mechanics and Physics of Solids*, vol. 57, no. 3, pp. 458–471, 2009.
17. E. K. Rodriguez, A. Hoger, and A. D. McCulloch, “Stress-dependent finite growth in soft elastic tissues,” *Journal of biomechanics*, vol. 27, no. 4, pp. 455–467, 1994.
18. J. V. Beira and R. Paro, “The legacy of drosophila imaginal discs,” *Chromosoma*, vol. 125, no. 4, pp. 573–592, 2016.
19. L. LeGoff, H. Rouault, and T. Lecuit, “A global pattern of mechanical stress polarizes cell divisions and cell shape in the growing drosophila wing disc,” *Development*, vol. 140, no. 19, pp. 4051–4059, 2013.
20. Y. Mao, A. L. Tournier, A. Hoppe, L. Kester, B. J. Thompson, and N. Tapon, “Differential proliferation rates generate patterns of mechanical tension that orient tissue growth,” *The EMBO journal*, vol. 32, no. 21, pp. 2790–2803, 2013.
21. C. Rauskolb, S. Sun, G. Sun, Y. Pan, and K. D. Irvine, “Cytoskeletal tension inhibits hippo signaling through an ajuba-warts complex,” *Cell*, vol. 158, no. 1, pp. 143–156, 2014.
22. J. C. Pastor-Pareja and T. Xu, “Shaping cells and organs in drosophila by opposing roles of fat body-secreted collagen iv and perlecan,” *Developmental cell*, vol. 21, no. 2, pp. 245–256, 2011.
23. L. Sui, G. O. Pflugfelder, and J. Shen, “The dorsocross t-box transcription factors promote tissue morphogenesis in the drosophila wing imaginal disc,” *Development*, vol. 139, no. 15, pp. 2773–2782, 2012.
24. L. Sui, S. Alt, M. Weigert, N. Dye, S. Eaton, F. Jug, E. W. Myers, F. Jülicher, G. Salbreux, and C. Dahmann, “Differential lateral and basal tension drive folding of drosophila wing discs through two distinct mechanisms,” *Nature communications*, vol. 9, no. 1, pp. 1–13, 2018.
25. W. Ramos-Lewis and A. Page-McCaw, “Basement membrane mechanics shape development: Lessons from the fly,” *Matrix Biology*, vol. 75, pp. 72–81, 2019.
26. A. Page-McCaw, A. J. Ewald, and Z. Werb, “Matrix metalloproteinases and the regulation of tissue remodelling,” *Nature reviews Molecular cell biology*, vol. 8, no. 3, pp. 221–233, 2007.
27. C. Bergantiños, M. Corominas, and F. Serras, “Cell death-induced regeneration in wing imaginal discs requires jnk signalling,” *Development*, vol. 137, no. 7, pp. 1169–1179, 2010.
28. A. Goriely, *The mathematics and mechanics of biological growth*, vol. 45. Springer, 2017.
29. L. D. Landau, A. Kosevich, L. P. Pitaevskii, and E. M. Lifshitz, *Theory of elasticity*. Butterworth, 1986.
30. I. Bock and J. Jarušek, “Dynamic contact problem for a von kármán–donnell shell,” *ZAMM-Journal of Applied Mathematics and Mechanics/Zeitschrift für Angewandte Mathematik und Mechanik*, vol. 93, no. 10-11, pp. 733–744, 2013.
31. L. LeGoff, H. Rouault, and T. Lecuit, “A global pattern of mechanical stress polarizes cell divisions and cell shape in the growing drosophila wing disc,” *Development*, vol. 140, no. 19, pp. 4051–4059, 2013.

32. A. Boudaoud, P. Patrício, Y. Couder, and M. Ben Amar, “Dynamics of singularities in a constrained elastic plate,” *Nature*, vol. 407, no. 6805, pp. 718–720, 2000.
33. P. Bayly, R. Okamoto, G. Xu, Y. Shi, and L. Taber, “A cortical folding model incorporating stress-dependent growth explains gyral wavelengths and stress patterns in the developing brain,” *Physical biology*, vol. 10, no. 1, p. 016005, 2013.
34. M. B. Amar and A. Bordner, “Mimicking cortex convolutions through the wrinkling of growing soft bilayers,” *Journal of Elasticity*, vol. 129, no. 1, pp. 213–238, 2017.
35. D. Ambrosi, M. Ben Amar, C. J. Cyron, A. DeSimone, A. Goriely, J. D. Humphrey, and E. Kuhl, “Growth and remodelling of living tissues: perspectives, challenges and opportunities,” *Journal of the Royal Society Interface*, vol. 16, no. 157, p. 20190233, 2019.
36. J. Weickenmeier, C. Fischer, D. Carter, E. Kuhl, and A. Goriely, “Dimensional, geometrical, and physical constraints in skull growth,” *Physical review letters*, vol. 118, no. 24, p. 248101, 2017.
37. K. Alessandri, B. R. Sarangi, V. V. Gurchenkov, B. Sinha, T. R. Kießling, L. Fetler, F. Rico, S. Scheuring, C. Lamaze, A. Simon, *et al.*, “Cellular capsules as a tool for multicellular spheroid production and for investigating the mechanics of tumor progression in vitro,” *Proceedings of the National Academy of Sciences*, vol. 110, no. 37, pp. 14843–14848, 2013.
38. A. Kiran, N. Kumar, and V. Mehandia, “Distinct modes of tissue expansion in free versus earlier-confined boundaries for more physiological modeling of wound healing, cancer metastasis, and tissue formation,” *ACS omega*, vol. 6, no. 17, pp. 11209–11222, 2021.
39. Y. Inoue, I. Tateo, and T. Adachi, “Epithelial tissue folding pattern in confined geometry,” *Biomechanics and modeling in mechanobiology*, pp. 1–8, 2019.
40. E. Ruocco and M. Fraldi, “An analytical model for the buckling of plates under mixed boundary conditions,” *Engineering structures*, vol. 38, pp. 78–88, 2012.
41. R. Farhadifar, J.-C. Röper, B. Aigouy, S. Eaton, and F. Jülicher, “The influence of cell mechanics, cell-cell interactions, and proliferation on epithelial packing,” *Current Biology*, vol. 17, no. 24, pp. 2095–2104, 2007.
42. D. B. Staple, R. Farhadifar, J.-C. Röper, B. Aigouy, S. Eaton, and F. Jülicher, “Mechanics and remodelling of cell packings in epithelia,” *The European Physical Journal E*, vol. 33, no. 2, pp. 117–127, 2010.
43. F. Graner and J. A. Glazier, “Simulation of biological cell sorting using a two-dimensional extended potts model,” *Physical review letters*, vol. 69, no. 13, p. 2013, 1992.
44. D. L. Weaire and S. Hutzler, *The physics of foams*. Oxford University Press, 2001.
45. C. Bielmeier, S. Alt, V. Weichselberger, M. La Fortezza, H. Harz, F. Jülicher, G. Salbreux, and A.-K. Classen, “Interface contractility between differently fated cells drives cell elimination and cyst formation,” *Current Biology*, vol. 26, no. 5, pp. 563–574, 2016.
46. E. Hannezo, J. Prost, and J.-F. Joanny, “Theory of epithelial sheet morphology in three dimensions,” *Proceedings of the National Academy of Sciences*, vol. 111, no. 1, pp. 27–32, 2014.
47. I. Heemskerk, T. Lecuit, and L. LeGoff, “Dynamic clonal analysis based on chronic in vivo imaging allows multiscale quantification of growth in the drosophila wing disc,” *Development*, vol. 141, no. 11, pp. 2339–2348, 2014.

List of figures

List of Figures

0.1	Simple classification of epithelium tissue	v
0.2	Stratified classification of epithelium tissue	v
0.3	<i>C. elegans</i> embryonic elongation: ventral cells are shown in pink, seam cells in yellow, and dorsal cells in teal. Contractile forces are produced predominantly by seam epidermal cells (arrows pointing toward one another), and transmitted to dorsal and ventral cells via adherens junctions (black ovals), which anchor circumferential actin filament bundles (CFBs) in dorsal and ventral cells (black lines and arrows within dorsal and ventral cells). CFBs are thought to transmit and distribute the forces of contraction evenly throughout the epidermis. Scale bar = $5\mu m$ (from [4]).	vi
0.4	Actin filament organization during <i>C. elegans</i> embryonic elongation when $\Delta L/L_0 = 30\%, 50\%, 70\%$ (from [8]).	vi
0.5	Cross-section of the outer layers of the <i>C. elegans</i> tissue showing muscle cells below the epidermis and cuticle viewed by transmission electron microscopy (from [9]).	vii
0.6	Images of a stretched disc for increasing force-displacement (F-d) values (from [7]).	viii
0.7	Classical apical constriction. In a monolayer where cells keep constant volumes, accumulated actomyosin meshwork at the apical end of the cells constricts, giving rise to wedge-shaped cells. This forces the epithelium into a concave apical surface with an enlarged basal area. Red, actomyosin (note enrichment on the apical side of the cells); blue, basal lamina; purple, nucleus (from [15]).	viii
1.1	Illustration of the deformation map	2
1.2	Illustration of geometry	7
1.3	Illustration of the surface coordinates	10
2.1	Deformation map from left to right columns are: Before closure (BE) and also the reference stress-free configuration B_r , initial state B_0 with cylindrical coordinates R, Θ, Z and the current elongated configuration B_t with coordinates r, θ, z . The pictures of the third row are taken from the experiments: we observe an opening angle (red dotted line) in the left slice. The opening angle is closed in the region of cells (brown area of the first row) with residual circumferential tensile stress (see middle slice). The picture on the right shows the position of the laser cuts during elongation.	18

2.2	Geometry of a simplified cylindrical tube for the strain calculation: The first picture (a) is the reference configuration B_r with an opening angle for pre-stress and C_r represents the arc-length of the outer surface for each part respectively. The second and the third sketch (b) show the initial complete tube B_0 after closure which is the domain for the following stress computation. D means dorsal section, V is the ventral part and S denotes the seam cell. Here we assume stress-free condition on the exterior boundary for the thin membrane tube. R is the radius varying from R_i to R_e and G_i is the angular change which shall be defined later. Θ_i is the absolute angle for each part $\{D, V, S\}$ and we take the double value because of the symmetry of the geometry. The exterior surface is covered by the extracellular matrix (ECM), a thin layer of secreted proteins.	19
2.3	(a) Experimental circumferential length of the seam cellular domain. In blue the best fitting curve corresponding to $C = C_0\Lambda$ and the ortho-radial stretch in the top inset. Red squares are experimental data [8]. (b) Analytical Results for the DV cells using Eq.(2.6) and Eq.(2.7). Experimental points [8] are included for comparison. (c) Theoretical G_S value as a function of Λ_Z according to Eq.(2.7) when the epithelium thickness is varied.	21
2.4	Depiction of \tilde{W} in Eq.(2.11) with dimensionless parameter $\tau/\mu = 0.15$	22
2.5	Mechanism of the actin-myosin network with motors: (a) (From [87]) One representative volume element where there are numerous actin filaments with motors. Energy transmission happens through actin monomers resulting in polymer (filament) reorganization. (b) Visualization of the interaction between filaments. Contractility is produced through the concerted movement of myosin heads (green) along actin thin filaments, which are made up of f-actin (blue) and tropomyosin (red)	24
2.6	Distribution of the planar fiber/filament direction in seam cells: Points in red are experimental data [8] when elongation Λ_Z equals 1.3 in comparison of points in green as Λ_Z equals 1.5. The curves in black are fitting results of the Von Mises distribution function [42]. φ is the angle along the average alignment and $\varphi = 0$ means that fibers align completely along the circumferential direction e_θ in our case and $\varphi = \pm\pi/2$ is the vertical direction e_z . The dispersion value κ characterizes the disorder of fiber anisotropy. Because of symmetry, we can calculate all the quantities as a function of $\varphi = [0, \pi/2]$ in practice.	24
2.7	Sketch of the two mechanisms in the epithelium during elongation. In D cells (yellow area), the arrangement of the filaments will change with external loading. In S cells (blue rectangular), positive active stress from the active network shortens the material with an contribution to the stretch of the D cell as $u(t)$. Here k_{DV} represents the stiffness of the D cell. Both cells are in a tension state.	27
2.8	Angle distribution $\varphi(x, y)$ with color bar after deformation: $\mu = 33356\text{Pa}$, $K = 1.67 \times 10^7\text{Pa}$, $b_n = 1\text{Pa} \cdot \text{s}$, $K_n = 10^{-4}\text{Pa} \cdot \text{m}^2$, $\gamma_n = 0.8$, $u(t) = 0.01 * t$	28
2.9	Contour of $\sigma_x[\text{Pa}]$ with given material parameters in Fig.(2.8)	28
2.10	Angle distribution $\varphi(x, y)$ with color bar after deformation: $\mu = 33356\text{Pa}$, $K = 1.67 \times 10^7\text{Pa}$, $b_n = 1\text{Pa} \cdot \text{s}$, $K_n = 10^{-4}\text{Pa} \cdot \text{m}^2$, $\gamma_n = 0.8$, $u(t) = 0.01 * t$	29
2.11	Contour of $\sigma_x[\text{Pa}]$ with given material parameters in Fig.(2.10)	29

3.1	Geometry of the Mode I open crack: $2a$ is the initial crack length and σ_0 is boundary stress in the y direction.	35
3.2	Schematic diagram of the different modes (from [110]).	36
3.3	Geometry of the inclined crack with boundary loading (from [74]): $2a$ is the initial crack length and k could be negative.	37
3.4	Geometry of an open crack with initial length l_β and opening length b_α in the biaxial loading state.	39
3.5	Flow chart of fracture factor \mathcal{F} with stress in finite elasticity.	40
3.6	Elongation by active stress with $Z/Z_0 = 1.3, 1.5, 1.7$	40
3.7	List of parameters and available data from [8] concerning three positions in the embryo: head, body and tail and two different kinds of cells: S and DV. Number of unknowns: 18, measurements: 17 and continuity equations: 10.	41
3.8	Calculation map with equivalent Young's modulus defined by Eq.(3.31).	42
3.9	Estimate of active stress: (a) Fitting curve for crack factor $\mathcal{F} = b/l \sim 2\sigma_\alpha/E_\alpha$ with experimental data; (b) Dimensionless passive stress versus elongation; (c) Estimate of active stress calculated by the connection equation $\sigma_\theta^S = \sigma_\theta^{DV}$	42
3.10	Demonstration of enriched nodes and elements	46
3.11	Level Set functions ψ^n and ψ^t	46
3.12	Sketch of mode I opening with the geometric effect in full size	47
3.13	$E = 10^5 \text{Pa}, \nu = 0.3, \sigma_Y^\infty = 10^4 \text{Pa}, K_I^g \approx 9.84 \times 10^3 \text{Pa}\sqrt{\text{m}}$ (a) Open Crack (Half size) under uniaxial stretch with $\mathcal{F} \approx 0.22, K_I^{comp} = 9.72 \times 10^3 \text{Pa}\sqrt{\text{m}}$; (b) Open Crack (Full size) under uniaxial stretch with $\mathcal{F} \approx 0.236, K_I^{comp} = 9.83 \times 10^3 \text{Pa}\sqrt{\text{m}}$	48
3.14	Stress contour of components σ_{xx} and σ_{xy}	49
3.15	Stress contour of components σ_{yy} and Von Mises value σ_{vm}	49
3.16	Sketch of mixed mode crack opening with tilting angle $\delta\beta = \pi/2 - \beta$ and biaxial loading parameter k_0	50
3.17	$E = 10^5 \text{Pa}, \nu = 0.3, \sigma_Y^\infty = 10^4 \text{Pa}, \beta = 88^\circ, k_0 = 0, K_I^g \approx 9.83 \times 10^3 \text{Pa}\sqrt{\text{m}}, K_{II}^\beta \approx 0.34 \times 10^3 \text{Pa}\sqrt{\text{m}}$. Calculation results are $\mathcal{F} \approx 0.215, K_I^{comp} = 9.80 \times 10^3 \text{Pa}\sqrt{\text{m}}, K_{II}^{comp} = 0.32 \times 10^3 \text{Pa}\sqrt{\text{m}}$	51
3.18	Stress contour of components σ_{yy} and Von Mises value σ_{vm} with $\beta = 88^\circ, k_0 = 0$	52
3.19	$E = 10^5 \text{Pa}, \nu = 0.3, \sigma_Y^\infty = 10^4 \text{Pa}, \beta = 85^\circ, k_0 = 0, K_I^g \approx 9.77 \times 10^3 \text{Pa}\sqrt{\text{m}}, K_{II}^\beta \approx 0.85 \times 10^3 \text{Pa}\sqrt{\text{m}}$. Calculation results are $\mathcal{F} \approx 0.214, K_I^{comp} = 9.74 \times 10^3 \text{Pa}\sqrt{\text{m}}, K_{II}^{comp} = 0.85 \times 10^3 \text{Pa}\sqrt{\text{m}}$	52
3.20	Stress contour of components σ_{yy} and Von Mises value σ_{vm} with $\beta = 85^\circ, k_0 = 0$	53
3.21	$E = 10^5 \text{Pa}, \nu = 0.3, \sigma_Y^\infty = 10^4 \text{Pa}, \beta = 80^\circ, k_0 = 0, K_I^g \approx 9.55 \times 10^3 \text{Pa}\sqrt{\text{m}}, K_{II}^\beta \approx 1.68 \times 10^3 \text{Pa}\sqrt{\text{m}}$. Calculation results are $\mathcal{F} \approx 0.207, K_I^{comp} = 9.58 \times 10^3 \text{Pa}\sqrt{\text{m}}, K_{II}^{comp} = 1.69 \times 10^3 \text{Pa}\sqrt{\text{m}}$	53
3.22	Stress contour of components σ_{yy} and Von Mises value σ_{vm} with $\beta = 80^\circ, k_0 = 0$	54
3.23	$E = 10^5 \text{Pa}, \nu = 0.3, \sigma_Y^\infty = 10^4 \text{Pa}, \beta = 85^\circ, k_0 = 0.2, K_I^g \approx 9.78 \times 10^3 \text{Pa}\sqrt{\text{m}}, K_{II}^\beta \approx 0.68 \times 10^3 \text{Pa}\sqrt{\text{m}}$. Calculation results are $\mathcal{F} \approx 0.205, K_I^{comp} = 9.76 \times 10^3 \text{Pa}\sqrt{\text{m}}, K_{II}^{comp} = 0.68 \times 10^3 \text{Pa}\sqrt{\text{m}}$	55
3.24	Stress contour of components σ_{yy} and Von Mises value σ_{vm} with $\beta = 85^\circ, k_0 = 0.2$	55

3.25	$E = 10^5 \text{Pa}, \nu = 0.3, \sigma_Y^\infty = 10^4 \text{Pa}, \beta = 85^0, k_0 = 0.5, K_I^g \approx 9.81 \times 10^3 \text{Pa}\sqrt{\text{m}}, K_{II}^\beta \approx 0.43 \times 10^3 \text{Pa}\sqrt{\text{m}}$. Calculation results are $\mathcal{F} \approx 0.201, K_I^{comp} = 9.78 \times 10^3 \text{Pa}\sqrt{\text{m}}, K_{II}^{comp} = 0.42 \times 10^3 \text{Pa}\sqrt{\text{m}}$	56
3.26	Stress contour of components σ_{yy} and Von Mises value σ_{vm} with $\beta = 85^0, k_0 = 0.5$	56
3.27	$E = 10^5 \text{Pa}, \nu = 0.3, \sigma_Y^\infty = 10^4 \text{Pa}, \beta = 85^0, k_0 = 1.0, K_I^g \approx 9.85 \times 10^3 \text{Pa}\sqrt{\text{m}}, K_{II}^\beta \approx 0 \text{Pa}\sqrt{\text{m}}$. Calculation results are $\mathcal{F} \approx 0.186, K_I^{comp} = 9.82 \times 10^3 \text{Pa}\sqrt{\text{m}}, K_{II}^{comp} = -7 \times 10^{-3} \text{Pa}\sqrt{\text{m}}$	57
3.28	Stress contour of components σ_{yy} and Von Mises value σ_{vm} with $\beta = 85^0, k_0 = 1.0$	57
3.29	$E = 10^5 \text{Pa}, \nu = 0.3, \sigma_Y^\infty = 10^4 \text{Pa}, \beta = 80^0, k_0 = 0.2, K_I^g \approx 9.61 \times 10^3 \text{Pa}\sqrt{\text{m}}, K_{II}^\beta \approx 1.35 \times 10^3 \text{Pa}\sqrt{\text{m}}$. Calculation results are $\mathcal{F} \approx 0.204, K_I^{comp} = 9.64 \times 10^3 \text{Pa}\sqrt{\text{m}}, K_{II}^{comp} = 1.34 \times 10^3 \text{Pa}\sqrt{\text{m}}$	58
3.30	Stress contour of components σ_{yy} and Von Mises value σ_{vm} with $\beta = 80^0, k_0 = 0.2$	59
3.31	$E = 10^5 \text{Pa}, \nu = 0.3, \sigma_Y^\infty = 10^4 \text{Pa}, \beta = 80^0, k_0 = 0.5, K_I^g \approx 9.70 \times 10^3 \text{Pa}\sqrt{\text{m}}, K_{II}^\beta \approx 0.84 \times 10^3 \text{Pa}\sqrt{\text{m}}$. Calculation results are $\mathcal{F} \approx 0.202, K_I^{comp} = 9.73 \times 10^3 \text{Pa}\sqrt{\text{m}}, K_{II}^{comp} = 0.82 \times 10^3 \text{Pa}\sqrt{\text{m}}$	59
3.32	Stress contour of components σ_{yy} and Von Mises value σ_{vm} with $\beta = 80^0, k_0 = 0.5$	60
3.33	$E = 10^5 \text{Pa}, \nu = 0.3, \sigma_Y^\infty = 10^4 \text{Pa}, \beta = 80^0, k_0 = 1.0, K_I^g \approx 9.85 \times 10^3 \text{Pa}\sqrt{\text{m}}, K_{II}^\beta \approx 0 \text{Pa}\sqrt{\text{m}}$. Calculation results are $\mathcal{F} \approx 0.189, K_I^{comp} = 9.88 \times 10^3 \text{Pa}\sqrt{\text{m}}, K_{II}^{comp} = 7.8 \times 10^{-3} \text{Pa}\sqrt{\text{m}}$	60
3.34	Stress contour of components σ_{yy} and Von Mises value σ_{vm} with $\beta = 80^0, k_0 = 1.0$	61
4.1	Analytical solution with $\nu = 0.5, \alpha = 50, \eta_f = 0.0005, \eta_S = 0.01, \epsilon_b = 1, b^*/D^* \approx O(10)$: (a) bifurcation map (b) deflection shape of two branches with increasing N	71
4.2	Defects with $D(x)$. (a) Different buckling shapes between analytical solutions (left) and results in consideration of bending stiffness distribution (right); (b) buckling shapes and the bifurcation diagram with given parameters. Arrows point out the rise of the membrane force N induced by constant growth in Eq.(4.23)	72
4.3	Results with $D_0 = 1, D_d = 0.5, x_m = 0.5, dw = 0.2, k_1 = 0, k_2 = 10000, p(x) = 0$. (a) Buckling shape with ECM defect; (b) diagram with given parameters	73
4.4	Results with $D_0 = 1, D_d = 0.5, x_m = 0.5, dw = 0.1, k_1 = 0, k_2 = 10000, p(x) = 100\delta(0.5) - 100\delta(0.3) - 100\delta(0.7)$. (a) Buckling shape with ECM defect; (b) diagram with given parameters	74
4.5	Results with $D_0 = 1, D_d = 0.5, x_m = 0.5, dw = 0.2, k_1 = 0, k_2 = 10000, p(x) = 100\delta(0.5) - 100\delta(0.3) - 100\delta(0.7)$. (a) Buckling shape with ECM defect; (b) diagram with given parameters	74
4.6	Results with $D_0 = 1, D_d = 0.5, x_m = 0.5, dw = 0.2, k_1 = 0, k_2 = 100, p(x) = 100\delta(0.5) - 100\delta(0.3) - 100\delta(0.7)$. (a) Buckling shape with ECM defect; (b) diagram with given parameters	75

4.7 Results with $D_0 = 1, D_d = 0.5, x_m = 0.5, dw = 0.2, k_1 = 0, k_2 = 10000, p(x) = -100\delta(0.5) + 100\delta(0.3) + 100\delta(0.7)$. (a) Buckling shape with ECM defect; (b) diagram with given parameters 75

4.8 Results with $D_0 = 1, D_d = 0.5, x_m = 0.5, dw = 0.2, k_1 = 0, k_2 = 100, p(x) = -100\delta(0.5) + 100\delta(0.3) + 100\delta(0.7)$. (a) Buckling shape with ECM defect; (b) diagram with given parameters 76

4.9 Sketch of bilayer: $L_x = 1, L_y = 0.5, h_S = 0.01, h_f = h_S/20, E_S = 1\text{Kpa}, E_f = 50\text{Kpa}, \nu = 0.3, Z_n = -0.00125, D = 3 * 10^{-4}\text{Pa} \cdot \text{m}^3, \bar{E} = 2.9\text{Kpa}$ 77

4.10 Deformation by active bending in clamped-clamped boundary condition: (a) deflection curve: vertical displacement w versus x with $L_x = 1, L_y = 0.5$ in Fig.(4.9); (b) Von Mises stress contour 78

4.11 Deformation by differential growth along the x axis in clamped-clamped boundary condition: $\delta = 0.1, \gamma = 1000, x_m = 0.5$ (a) deflection curve: vertical displacement w versus x with $L_x = 1, L_y = 0.5$ in Fig.(4.9); (b) Von Mises stress contour 78

4.12 Sketch of geometry in COMSOL: Ellipsoid surface $(\frac{x}{R_x})^2 + (\frac{y}{R_y})^2 + (\frac{z}{R_z})^2 = 1, -R_x \leq x \leq R_x, -R_y \leq y \leq R_y, z(x, y) \geq 0$ with $R_x = 0.5, R_y = 0.2, R_z = 0.05$ and thickness $d = 0.001$; $E = 1\text{Kpa}, \nu = 0.33$. Initially all boundaries are fixed. 79

4.13 Buckling shape with $x_m = 0, \alpha^{th} = 0.03, \beta^{th} = 1, \gamma^{th} = 1000, d = 0.001$ 80

4.14 Deflection shape $w + Z$ in Fig.(4.13) for $\lambda^{th} = 0, 0.2, 0.4, 0.6, 0.8, 1.0$ with given parameters: (a) along path AOA' ; (b) along path BOB' 80

4.15 Buckling shape with $x_m = 0, \alpha^{th} = 0.03, \beta^{th} = 1, \gamma^{th} = 10, d = 0.001$ 81

4.16 Deflection shape $w + Z$ in Fig.(4.15) for $\lambda^{th} = 0, 0.2, 0.4, 0.6, 0.8, 1.0$ with given parameters: (a) along path AOA' ; (b) along path BOB' 81

4.17 Buckling shape with $x_m = 0, \alpha^{th} = 0.03, \beta^{th} = -1, \gamma^{th} = 10, d = 0.001$ 82

4.18 Deflection shape $w + Z$ in Fig.(4.17) for $\lambda^{th} = 0, 0.2, 0.4, 0.6, 0.8, 1.0$ with given parameters: (a) along path AOA' ; (b) along path BOB' 82

4.19 Buckling shape with $x_m = 0, \alpha^{th} = 0.03, \beta^{th} = -1, \gamma^{th} = 1000, d = 0.001$. . . 83

4.20 Deflection shape $w + Z$ in Fig.(4.19) for $\lambda^{th} = 0, 0.2, 0.4, 0.6, 0.8, 1.0$ with given parameters: (a) along path AOA' ; (b) along path BOB' 83

4.21 Buckling shape with $x_m = 0, \alpha^{th} = 0.03, \beta^{th} = 1, \gamma^{th} = 1000, d = 0.001, Z_n = 0$ 84

4.22 Deflection shape $w + Z$ in Fig.(4.21) for $\lambda^{th} = 0, 0.2, 0.4, 0.6, 0.8, 1.0$ with given parameters: (a) along path AOA' ; (b) along path BOB' 85

4.23 Buckling shape with $x_m = 0, \alpha^{th} = 0.03, \beta^{th} = -1, \gamma^{th} = 1000, d = 0.001, Z_n = 0$ 85

4.24 Deflection shape $w + Z$ in Fig.(4.23) for $\lambda^{th} = 0, 0.2, 0.4, 0.6, 0.8, 1.0$ with given parameters: (a) along path AOA' ; (b) along path BOB' 86

4.25 Buckling shape with $x_m = 0, \alpha^{th} = 0.03, \beta^{th} = 1, \gamma^{th} = 1000, d = 0.001, Z_n = 0, \beta_d = 0.1, x_d = 0, w_d = 0.1$ 87

4.26 Deflection shape $w + Z$ in Fig.(4.25) for $\lambda^{th} = 0, 0.2, 0.4, 0.6, 0.8, 1.0$ with given parameters: (a) along path AOA' ; (b) along path BOB' 87

4.27 Buckling shape with $x_m = 0, \alpha^{th} = 0.03, \beta^{th} = 1, \gamma^{th} = 1000, d = 0.001, Z_n = 0, \beta_d = 0.5, x_d = 0, w_d = 0.1$ 88

4.28	Deflection shape $w + Z$ in Fig.(4.27) for $\lambda^{th} = 0, 0.2, 0.4, 0.6, 0.8, 1.0$ with given parameters: (a) along path AOA' ; (b) along path BOB'	88
4.29	Buckling shape with $x_m = 0, \alpha^{th} = 0.03, \beta^{th} = 1, \gamma^{th} = 1000, d = 0.001, Z_n = 0, \lambda_b^{II} = 0.001$	89
4.30	Deflection shape $w + Z$ in Fig.(4.29) for $\lambda^{th} = 0, 0.2, 0.4, 0.6, 0.8, 1.0$ with given parameters: (a) along path AOA' ; (b) along path BOB'	90
4.31	Buckling shape with $x_m = 0, \alpha^{th} = 0.03, \beta^{th} = 1, \gamma^{th} = 1000, d = 0.001, Z_n = 0, \lambda_b^{II} = -0.001$	90
4.32	Deflection shape $w + Z$ in Fig.(4.31) for $\lambda^{th} = 0, 0.2, 0.4, 0.6, 0.8$ with given parameters: (a) along path AOA' ; (b) along path BOB'	91
5.1	Flow chart of calculation	96
5.2	Deflection shapes for $\lambda_g = 0.002, 0.04, 0.15, 0.5$ with $\Delta T = 1, u_0 = 0.5$	97
5.3	Buckling shape of the structure	98
5.4	Geometry of 3D stripe	99
5.5	Mesh diagram of the system: The region in green is the normal part without growth and the piece in red has isotropic growth with a loading parameter λ_g . Blue circles represent stiffer beam elements which have additional bending energy	99
5.6	$L_X = 1, L_Y = 0.2, L_Z = 0.05, \Omega_2 : 0.5 \leq X \leq 0.7, AB \approx \delta \sin(2\pi X), E_1 = E_3 = 10^3 \text{Pa}, E_2 = 0.5 \times 10^3 \text{Pa}, E_{beam} = 50 * E_1, \nu_1 = \nu_2 = \nu_3 = 0.3, \Delta T = 1, N_{step} = 5, \lambda_g = 0.2$	100
5.7	$L_X = 1, L_Y = 0.2, L_Z = 0.05, \Omega_2 : 0.5 \leq X \leq 0.7, AB \approx \delta \sin(2\pi X), E_1 = E_3 = 10^5 \text{Pa}, E_2 = 0.5 \times 10^5 \text{Pa}, E_{beam} = 50 * E_1, \nu_1 = \nu_2 = \nu_3 = 0.3, \Delta T = 1, N_{step} = 8, \lambda_g = 0.5$	101
5.8	$L_X = 1, L_Y = 0.2, L_Z = 0.05, \Omega_2 : 0.5 \leq X \leq 0.7, AB \approx \delta \sin(2\pi X), E_1 = E_3 = 10^5 \text{Pa}, E_2 = 0.5 \times 10^5 \text{Pa}, E_{beam} = 50 * E_1, \nu_1 = \nu_2 = \nu_3 = 0.3, \Delta T = 1, N_{step} = 10, \lambda_g = 0.8$	101
5.9	$L_X = 1, L_Y = 0.2, L_Z = 0.05, \Omega_2 : 0.5 \leq X \leq 0.7, AB \approx \delta \sin(3\pi X), E_1 = E_3 = 10^3 \text{Pa}, E_2 = 0.5 \times 10^3 \text{Pa}, E_{beam} = 50 * E_1, \nu_1 = \nu_2 = \nu_3 = 0.3, \Delta T = 1, N_{step} = 3, \lambda_g = 0.02$	102
5.10	$L_X = 1, L_Y = 0.2, L_Z = 0.05, \Omega_2 : 0.5 \leq X \leq 0.7, AB \approx \delta \sin(3\pi X), E_1 = E_3 = 10^3 \text{Pa}, E_2 = 0.5 \times 10^3 \text{Pa}, E_{beam} = 50 * E_1, \nu_1 = \nu_2 = \nu_3 = 0.3, \Delta T = 1, N_{step} = 5, \lambda_g = 0.1$	103
5.11	$L_X = 1, L_Y = 0.2, L_Z = 0.05, \Omega_2 : 0.5 \leq X \leq 0.7, AB \approx \delta \sin(3\pi X), E_1 = E_3 = 10^3 \text{Pa}, E_2 = 0.5 \times 10^3 \text{Pa}, E_{beam} = 50 * E_1, \nu_1 = \nu_2 = \nu_3 = 0.3, \Delta T = 1, N_{step} = 7, \lambda_g = 0.3$	103
5.12	$L_X = 2, L_Y = 0.2, L_Z = 0.05, \Omega_2 : 0.5 \leq X \leq 1.5, AB \approx \delta \sin(6\pi X), E_1 = E_3 = 10^3 \text{Pa}, E_2 = 0.5 \times 10^3 \text{Pa}, E_{beam} = 50 * E_1, \nu_1 = \nu_2 = \nu_3 = 0.3, \Delta T = 1, N_{step} = 5, \lambda_g = 0.01$	104
5.13	$L_X = 2, L_Y = 0.2, L_Z = 0.05, \Omega_2 : 0.5 \leq X \leq 1.5, AB \approx \delta \sin(6\pi X), E_1 = E_3 = 10^3 \text{Pa}, E_2 = 0.5 \times 10^3 \text{Pa}, E_{beam} = 50 * E_1, \nu_1 = \nu_2 = \nu_3 = 0.3, \Delta T = 1, N_{step} = 10, \lambda_g = 0.06$	105
5.14	$L_X = 2, L_Y = 0.2, L_Z = 0.05, \Omega_2 : 0.5 \leq X \leq 1.5, AB \approx \delta \sin(6\pi X), E_1 = E_3 = 10^3 \text{Pa}, E_2 = 0.5 \times 10^3 \text{Pa}, E_{beam} = 50 * E_1, \nu_1 = \nu_2 = \nu_3 = 0.3, \Delta T = 1, N_{step} = 15, \lambda_g = 0.16$	105

5.15	Mechanical sketch of the simulation with boundary conditions: $X = 0, v_1 = 0$; $X = L_X, v_1 = -v_X$; $Y = 0, v_2 = 0$	107
5.16	Wrinkling deformation with $E_1 = 50\text{KPa}, E_2 = 1\text{KPa}, \nu_1 = 0.3, \nu_2 = 0.49, \eta_1 = 10^5\text{Pa} \cdot s, \eta_2 = 10^3\text{Pa} \cdot s, L_X = 100\mu\text{m}, L_Y = 10\mu\text{m}, h_1/L_Y = 0.25$	108
5.17	Folding deformation with $E_1 = 1\text{KPa}, E_2 = 50\text{KPa}, \nu_1 = 0.3, \nu_2 = 0.3, \eta_1 = 10^3\text{Pa} \cdot s, \eta_2 = 10\text{Pa} \cdot s, L_X = 100\mu\text{m}, L_Y = 10\mu\text{m}, h_1/L_Y = 0.15$	108
5.18	Deformation with $E_1 = 50\text{KPa}, E_2 = 1\text{KPa}, \nu_1 = 0.3, \nu_2 = 0.49, \eta_1 = 10^5\text{Pa} \cdot s, \eta_2 = 10^3\text{Pa} \cdot s, L_X = 100\mu\text{m}, L_Y = 10\mu\text{m}, h_1/L_Y = 0.15$	109
5.19	Deformation with $E_1 = 50\text{KPa}, E_2 = 1\text{KPa}, \nu_1 = 0.3, \nu_2 = 0.49, \eta_1 = 10^5\text{Pa} \cdot s, \eta_2 = 10^3\text{Pa} \cdot s, L_X = 30\mu\text{m}, L_Y = 10\mu\text{m}, h_1/L_Y = 0.15$	110
5.20	Deformation with $E_1 = 50\text{KPa}, E_2 = 1\text{KPa}, \nu_1 = 0.3, \nu_2 = 0.49, \eta_1 = 10^5\text{Pa} \cdot s, \eta_2 = 10^3\text{Pa} \cdot s, L_X = 20\mu\text{m}, L_Y = 10\mu\text{m}, h_1/L_Y = 0.15$	110
5.21	Deformation with $E_1 = 50\text{KPa}, E_2 = 1\text{KPa}, \nu_1 = 0.3, \nu_2 = 0.49, \eta_1 = 10^5\text{Pa} \cdot s, \eta_2 = 10^3\text{Pa} \cdot s, L_X = 100\mu\text{m}, L_Y = 10\mu\text{m}, h_1/L_Y = 0.35$	111
5.22	Deformation with $E_1 = 50\text{KPa}, E_2 = 1\text{KPa}, \nu_1 = 0.3, \nu_2 = 0.49, \eta_1 = 10^5\text{Pa} \cdot s, \eta_2 = 10^3\text{Pa} \cdot s, L_X = 50\mu\text{m}, L_Y = 10\mu\text{m}, h_1/L_Y = 0.35$	112
5.23	Deformation with $E_1 = 50\text{KPa}, E_2 = 1\text{KPa}, \nu_1 = 0.3, \nu_2 = 0.49, \eta_1 = 10^5\text{Pa} \cdot s, \eta_2 = 10^3\text{Pa} \cdot s, L_X = 30\mu\text{m}, L_Y = 10\mu\text{m}, h_1/L_Y = 0.35$	112
5.24	Deformation with $E_1 = 50\text{KPa}, E_2 = 1\text{KPa}, \nu_1 = 0.3, \nu_2 = 0.49, \eta_1 = 10^5\text{Pa} \cdot s, \eta_2 = 10^3\text{Pa} \cdot s, L_X = 100\mu\text{m}, L_Y = 10\mu\text{m}, h_1/L_Y = 0.15$	113
5.25	Deformation with $E_1 = 50\text{KPa}, E_2 = 1\text{KPa}, \nu_1 = 0.3, \nu_2 = 0.49, \eta_1 = 10^3\text{Pa} \cdot s, \eta_2 = 10\text{Pa} \cdot s, L_X = 100\mu\text{m}, L_Y = 10\mu\text{m}, h_1/L_Y = 0.15$	114
5.26	Deformation with $E_1 = 50\text{KPa}, E_2 = 1\text{KPa}, \nu_1 = 0.3, \nu_2 = 0.49, \eta_1 = 10\text{Pa} \cdot s, \eta_2 = 10^{-1}\text{Pa} \cdot s, L_X = 100\mu\text{m}, L_Y = 10\mu\text{m}, h_1/L_Y = 0.15$	114
5.27	Deformation with $E_1 = 1\text{KPa}, E_2 = 1\text{KPa}, \nu_1 = 0.3, \nu_2 = 0.3, \eta_1 = 10^5\text{Pa} \cdot s, \eta_2 = 10^3\text{Pa} \cdot s, L_X = 100\mu\text{m}, L_Y = 10\mu\text{m}, h_1/L_Y = 0.15$	115
5.28	Deformation with $E_1 = 1\text{KPa}, E_2 = 1\text{KPa}, \nu_1 = 0.3, \nu_2 = 0.3, \eta_1 = 10^{-2}\text{Pa} \cdot s, \eta_2 = 10^{-4}\text{Pa} \cdot s, L_X = 100\mu\text{m}, L_Y = 10\mu\text{m}, h_1/L_Y = 0.15$	115
5.29	Mechanical sketch of the simulation with fixed boundary conditions: $X = 0, v_1 = v_2 = 0$; $X = L_X, v_1 = -v_X, v_2 = 0$; $Y = 0, v_2 = 0$	116
5.30	Deformation with $E_1 = 50\text{KPa}, E_2 = 1\text{KPa}, \nu_1 = 0.3, \nu_2 = 0.49, \eta_1 = 10^5\text{Pa} \cdot s, \eta_2 = 10^3\text{Pa} \cdot s, L_X = 50\mu\text{m}, L_Y = 10\mu\text{m}, h_1/L_Y = 0.15$	116
5.31	Deformation with $E_1 = 50\text{KPa}, E_2 = 1\text{KPa}, \nu_1 = 0.3, \nu_2 = 0.49, \eta_1 = 10^3\text{Pa} \cdot s, \eta_2 = 10\text{Pa} \cdot s, L_X = 50\mu\text{m}, L_Y = 10\mu\text{m}, h_1/L_Y = 0.15$	117
5.32	Deformation with $E_1 = 50\text{KPa}, E_2 = 1\text{KPa}, \nu_1 = 0.3, \nu_2 = 0.49, \eta_1 = 10^5\text{Pa} \cdot s, \eta_2 = 10^3\text{Pa} \cdot s, L_X = 30\mu\text{m}, L_Y = 10\mu\text{m}, h_1/L_Y = 0.15$	117
5.33	Deformation with $E_1 = 50\text{KPa}, E_2 = 1\text{KPa}, \nu_1 = 0.3, \nu_2 = 0.49, \eta_1 = 10^5\text{Pa} \cdot s, \eta_2 = 10^3\text{Pa} \cdot s, L_X = 20\mu\text{m}, L_Y = 10\mu\text{m}, h_1/L_Y = 0.15$	118

List of tables

List of Tables

3.1	Summary of analytical solutions using the linear hypothesis (from lecture notes by Prof. VE Saouma)	32
3.2	Geometry and material parameters	41
4.1	Summary of computational results with COMSOL shell	91
5.1	Summary of computational results with beams and solids	106
5.2	Summary of computational results with 2D solids	119

Bibliography

- [1] A. Skirycz & D. Inzé; *More from less: plant growth under limited water*; *Current Opinion in Biotechnology* **21**, pp. 197–203 (2010). [v](#)
- [2] M. Uyttewaal, A. Burian, K. Alim, B. Landrein, D. Borowska-Wykret, A. Dedieu, A. Peaucelle, M. Ludynia, J. Traas, A. Boudaoud, D. Kwiatkowska & O. Hamant; *Mechanical Stress Acts via Katanin to Amplify Differences in Growth Rate between Adjacent Cells in Arabidopsis*; *Cell* **149**, pp. 439–451 (2012). [v](#)
- [3] L. LeGoff & T. Lecuit; *Mechanical forces and growth in animal tissues*; *Cold Spring Harbor perspectives in biology* **8**, p. a019232 (2016). [v](#)
- [4] A. D. Chisholm & J. Hardin; *Epidermal morphogenesis*; *WormBook: The Online Review of C. elegans Biology* [Internet] (2005). [vi](#), [153](#)
- [5] T. Bittig, O. Wartlick, M. González-Gaitán & F. Jülicher; *Quantification of growth asymmetries in developing epithelia*; *The European Physical Journal E* **30**, pp. 93–99 (2009). [vi](#)
- [6] L. LeGoff, H. Rouault & T. Lecuit; *A global pattern of mechanical stress polarizes cell divisions and cell shape in the growing Drosophila wing disc*; *Development* **140**, pp. 4051–4059 (2013). [vi](#)
- [7] F. Atzeni, F. Lanfranconi & C. M. Aegerter; *Disentangling geometrical, viscoelastic and hyperelastic effects in force-displacement relationships of folded biological tissues*; *The European Physical Journal E* **42**, p. 47 (2019). [vi](#), [viii](#), [120](#), [153](#)
- [8] T. T. K. Vuong-Brender, M. Ben Amar, J. Pontabry & M. Labouesse; *The interplay of stiffness and force anisotropies drives embryo elongation*; *Elife* **6**, p. e23866 (2017). [vi](#), [vii](#), [ix](#), [15](#), [18](#), [21](#), [24](#), [31](#), [38](#), [41](#), [50](#), [54](#), [153](#), [154](#), [155](#)
- [9] A. K. Corsi, B. Wightman & M. Chalfie; *A transparent window into biology: a primer on Caenorhabditis elegans*; *Genetics* **200**, pp. 387–407 (2015). [vii](#), [153](#)
- [10] N. Gjorevski & C. M. Nelson; *The mechanics of development: Models and methods for tissue morphogenesis*; *Birth Defects Research Part C: Embryo Today: Reviews* **90**, pp. 193–202 (2010). [vii](#), [43](#)
- [11] K. Sugimura, P.-F. Lenne & F. Graner; *Measuring forces and stresses in situ in living tissues*; *Development* **143**, pp. 186–196 (2016). [vii](#), [43](#)

- [12] O. Campas; *A toolbox to explore the mechanics of living embryonic tissues*; in *Seminars in cell & developmental biology*, volume 55pp. 119–130 (Elsevier) (2016). [vii](#), [43](#)
- [13] C. J. Chan, C.-P. Heisenberg & T. Hiiragi; *Coordination of morphogenesis and cell-fate specification in development*; *Current Biology* **27**, pp. R1024–R1035 (2017). [vii](#), [43](#)
- [14] P. Roca-Cusachs, V. Conte & X. Trepat; *Quantifying forces in cell biology*; *Nature cell biology* **19**, pp. 742–751 (2017). [vii](#), [43](#)
- [15] E. J. Pearl, J. Li & J. B. Green; *Cellular systems for epithelial invagination*; *Philosophical Transactions of the Royal Society B: Biological Sciences* **372**, p. 20150526 (2017). [viii](#), [153](#)
- [16] A. Trushko, I. Di Meglio, A. Merzouki, C. Blanch-Mercader, S. Abuhattum, J. Guck, K. Alessandri, P. Nassoy, K. Kruse, B. Chopard *et al.*; *Buckling of an epithelium growing under spherical confinement*; *Developmental cell* **54**, pp. 655–668 (2020). [viii](#)
- [17] T. Savin, N. A. Kurpios, A. E. Shyer, P. Florescu, H. Liang, L. Mahadevan & C. J. Tabin; *On the growth and form of the gut*; *Nature* **476**, pp. 57–62 (2011). [viii](#)
- [18] S. Oldham, R. Böhni, H. Stocker, W. Brogiolo & E. Hafen; *Genetic control of size in Drosophila*; *Philosophical Transactions of the Royal Society of London. Series B: Biological Sciences* **355**, pp. 945–952 (2000). [ix](#)
- [19] Z. G. Qu, X. C. He, M. Lin, B. Y. Sha, X. H. Shi, T. J. Lu & F. Xu; *Advances in the understanding of nanomaterial–biomembrane interactions and their mathematical and numerical modeling*; *Nanomedicine* **8**, pp. 995–1011 (2013). [ix](#)
- [20] R. Farhadifar, J.-C. Röper, B. Aigouy, S. Eaton & F. Jülicher; *The Influence of Cell Mechanics, Cell-Cell Interactions, and Proliferation on Epithelial Packing*; *Current Biology* **17**, pp. 2095–2104 (2007). [ix](#)
- [21] F. Graner, B. Dollet, C. Raufaste & P. Marmottant; *Statistical tools to characterize discrete rearranging patterns, in two or three dimensions: cellular materials, assemblies of particles*; preprint (2007). [ix](#)
- [22] G. Brodland & R. Gordon; *Intermediate filaments may prevent buckling of compressively loaded microtubules*; (1990). [ix](#)
- [23] G. Brodland & D. Clausi; *Embryonic tissue morphogenesis modeled by FEM*; (1994). [ix](#)
- [24] D. A. Clausi & G. W. Brodland; *Mechanical evaluation of theories of neurulation using computer simulations*; *Development* **118**, pp. 1013–1023 (1993). [ix](#)
- [25] M. Tozluoglu, M. Duda, N. J. Kirkland, R. Barrientos, J. J. Burden, J. J. Muñoz & Y. Mao; *Planar differential growth rates initiate precise fold positions in complex epithelia*; *Developmental cell* **51**, pp. 299–312 (2019). [ix](#), [120](#)
- [26] M. Ben Amar, P. Qiuyang-Qu, T. T. K. Vuong-Brender & M. Labouesse; *Assessing the contribution of active and passive stresses in C. elegans elongation*; *Physical Review Letters* **121**, p. 268102 (2018). [ix](#), [18](#), [31](#)

- [27] J. E. Marsden & T. J. Hughes; *Mathematical foundations of elasticity* (Courier Corporation) (1994). 1, 2, 3, 4
- [28] R. W. Ogden; *Non-linear elastic deformations* (Courier Corporation) (1997). 1, 2, 3, 4, 21
- [29] G. Holzapfel; *Nonlinear solid mechanics: a continuum approach for engineering*; second print edition (John Wiley & Sons) (2001). 1, 2, 3, 4
- [30] K.-J. Bathe; *Finite element procedures* (Klaus-Jurgen Bathe) (2006). 2, 4, 93
- [31] R. De Borst, M. A. Crisfield, J. J. Remmers & C. V. Verhoosel; *Nonlinear finite element analysis of solids and structures* (John Wiley & Sons) (2012). 2, 4, 93, 96
- [32] A. C. Eringen; *Microcontinuum field theories: I. Foundations and solids* (Springer Science & Business Media) (2012). 3
- [33] S. Forest; *Mechanics of generalized continua: construction by homogenization*; *Le Journal de Physique IV* **8**, pp. Pr4–39 (1998). 3
- [34] G. A. Maugin & A. V. Metrikine; *Mechanics of generalized continua*; (2010). 3
- [35] M. M. Attard; *Finite strain—*isotropic hyperelasticity**; *International Journal of Solids and Structures* **40**, pp. 4353–4378 (2003). 4
- [36] J. Schröder & P. Neff; *Invariant formulation of hyperelastic transverse isotropy based on polyconvex free energy functions*; *International journal of solids and structures* **40**, pp. 401–445 (2003). 4
- [37] A. F. Bower; *Applied mechanics of solids* (CRC press) (2009). 4, 32
- [38] T. Belytschko, W. K. Liu, B. Moran & K. Elkhodary; *Nonlinear finite elements for continua and structures* (John Wiley & Sons) (2013). 4, 12, 43, 44, 93
- [39] P. Wriggers; *Nonlinear finite element methods* (Springer Science & Business Media) (2008). 4
- [40] J. Bonet & R. D. Wood; *Nonlinear continuum mechanics for finite element analysis* (Cambridge university press) (1997). 4
- [41] A. M. Sonnet & E. G. Virga; *Dissipative ordered fluids: theories for liquid crystals* (Springer Science & Business Media) (2012). 4, 5
- [42] G. A. Holzapfel & R. W. Ogden; *On the tension–compression switch in soft fibrous solids*; *European Journal of Mechanics-A/Solids* **49**, pp. 561–569 (2015). 6, 24, 25, 154
- [43] P. G. Ciarlet; *A justification of the von Kármán equations*; *Archive for Rational Mechanics and Analysis* **73**, pp. 349–389 (1980). 6
- [44] P. L. Gould; *Analysis of shells and plates* (Springer Science & Business Media) (2012). 6, 11
- [45] J. N. Reddy; *Mechanics of laminated composite plates and shells: theory and analysis* (CRC press) (2003). 6, 12

- [46] D. Chapelle & K.-J. Bathe; *The finite element analysis of shells-fundamentals* (Springer Science & Business Media) (2010). 6, 13, 76
- [47] P. G. Ciarlet & C. Mardare; *An introduction to shell theory*; Differential geometry: theory and applications **9**, pp. 94–184 (2008). 6
- [48] W. T. Koiter; *On the nonlinear theory of thin elastic shells*; Proc. Koninkl. Ned. Akad. van Wetenschappen, Series B **69**, pp. 1–54 (1966). 6, 10
- [49] A. K. Noor; *Bibliography of monographs and surveys on shells*; (1990). 6
- [50] L. D. Landau, A. Kosevich, L. P. Pitaevskii & E. M. Lifshitz; *Theory of elasticity* (Butterworth) (1986). 9
- [51] J. L. Sanders Jr; *Nonlinear theories for thin shells*; Quarterly of Applied Mathematics **21**, pp. 21–36 (1963). 9, 10, 11
- [52] E. Abbena, S. Salamon & A. Gray; *Modern differential geometry of curves and surfaces with Mathematica* (CRC press) (2017). 9
- [53] B. Audoly & Y. Pomeau; *Elasticity and Geometry* (Oxford University Press) (2010). 9
- [54] W. T. Koiter & A. Van Der Heijden; *WT Koiter's elastic stability of solids and structures* (Cambridge University Press Cambridge, UK; New York, NY, USA) (2009). 10, 13
- [55] B. Budiansky; *On the 'best' first-order linear shell theory*; The Prager Anniversary Volume-Progress in Applied Mechanics (1963). 10
- [56] B. Budiansky; *Notes on nonlinear shell theory*; (1968). 10
- [57] M. Amabili; *Nonlinear mechanics of shells and plates in composite, soft and biological materials* (Cambridge University Press) (2018). 11
- [58] J. S. Hale, M. Brunetti, S. P. Bordas & C. Maurini; *Simple and extensible plate and shell finite element models through automatic code generation tools*; Computers & Structures **209**, pp. 163–181 (2018). 11, 12
- [59] S. Idelsohn; *On the use of deep, shallow or flat shell finite elements for the analysis of thin shell structures*; Computer Methods in Applied Mechanics and Engineering **26**, pp. 321–330 (1981). 11
- [60] A. J. Ferreira & N. Fantuzzi; *MATLAB Codes for Finite Element Analysis: Solids and Structures*; volume 157 (Springer Nature) (2020). 12
- [61] E. Oñate; *Structural analysis with the finite element method. Linear statics: volume 2: beams, plates and shells* (Springer Science & Business Media) (2013). 12, 97
- [62] M. Ben Amar & Y. Pomeau; *Crumpled paper*; Proceedings of the Royal Society of London. Series A: Mathematical, Physical and Engineering Sciences **453**, pp. 729–755 (1997). 12
- [63] O. C. Zienkiewicz, R. L. Taylor, P. Nithiarasu & J. Zhu; *The finite element method*; volume 3 (McGraw-hill London) (1977). 12, 44

- [64] P. Patrício da Silva & W. Krauth; *Numerical solutions of the von Karman equations for a thin plate*; International Journal of Modern Physics C **8**, pp. 427–434 (1997). [13](#)
- [65] G. Sander & S. Idelsohn; *A family of conforming finite elements for deep shell analysis*; International Journal for Numerical Methods in Engineering **18**, pp. 363–380 (1982). [13](#)
- [66] D. G. Robinson; *Nonlinear Plate Models for the Numerical Simulation of Thin Elastic Sheets*; Ph.D. thesis (2019). [13](#)
- [67] H. Tian, M. Potier-Ferry & F. Abed-Meraim; *A numerical method based on Taylor series for bifurcation analyses within Föppl–von Karman plate theory*; Mechanics Research Communications **93**, pp. 154–158 (2018). [13](#)
- [68] E. Barbieri, L. Ventura, D. Grignoli & E. Bilotti; *A meshless method for the nonlinear von Kármán plate with multiple folds of complex shape*; Computational Mechanics **64**, pp. 769–787 (2019). [13](#)
- [69] S. Tlili, C. Gay, F. Graner, P. Marcq, F. Molino & P. Saramito; *Colloquium: Mechanical formalisms for tissue dynamics*; The European Physical Journal E **38**, pp. 1–31 (2015). [13](#)
- [70] M. Misra, B. Audoly, I. G. Kevrekidis & S. Y. Shvartsman; *Shape transformations of epithelial shells*; Biophysical journal **110**, pp. 1670–1678 (2016). [13](#)
- [71] C. T. Nguyen & S. Oterkus; *Peridynamics for the thermomechanical behavior of shell structures*; Engineering Fracture Mechanics **219**, p. 106623 (2019). [13](#)
- [72] A. Morshedifard, M. Ruiz-García, M. J. A. Qomi & A. Košmrlj; *Buckling of thermalized elastic sheets*; Journal of the Mechanics and Physics of Solids **149**, p. 104296 (2021). [13](#)
- [73] P. Theocaris & J. Michopoulos; *A closed-form solution of a slant crack under biaxial loading*; Engineering Fracture Mechanics **17**, pp. 97–123 (1983). [15](#), [31](#), [36](#), [38](#)
- [74] P. Theocaris, D. Pazis & B. Konstantellos; *The exact shape of a deformed internal slant crack under biaxial loading*; International Journal of Fracture **30**, pp. 135–153 (1986). [15](#), [31](#), [36](#), [37](#), [38](#), [155](#)
- [75] A. M. Turing; *The chemical basis of morphogenesis*; Bulletin of mathematical biology **52**, pp. 153–197 (1990). [17](#)
- [76] A. J. Coulombre & J. L. Coulombre; *Intestinal development: I. Morphogenesis of the villi and musculature*; Development **6**, pp. 403–411 (1958). [17](#)
- [77] E. Hannezo, J. Prost & J.-F. Joanny; *Instabilities of monolayered epithelia: shape and structure of villi and crypts*; Physical Review Letters **107**, p. 078104 (2011). [17](#)
- [78] M. Ben Amar & F. Jia; *Anisotropic growth shapes intestinal tissues during embryogenesis*; Proceedings of the National Academy of Sciences **110**, pp. 10525–10530 (2013). [17](#)
- [79] R. Toro & Y. Burnod; *A morphogenetic model for the development of cortical convolutions*; Cerebral cortex **15**, pp. 1900–1913 (2005). [17](#)

- [80] A. Goriely, M. G. Geers, G. A. Holzapfel, J. Jayamohan, A. Jérusalem, S. Sivaloganathan, W. Squier, J. A. van Dommelen, S. Waters & E. Kuhl; *Mechanics of the brain: perspectives, challenges, and opportunities*; Biomechanics and modeling in mechanobiology **14**, pp. 931–965 (2015). 17
- [81] M. Ben Amar & A. Bordner; *Mimicking cortex convolutions through the wrinkling of growing soft bilayers*; Journal of Elasticity **129**, pp. 213–238 (2017). 17
- [82] M. Kücken & A. C. Newell; *Fingerprint formation*; Journal of theoretical biology **235**, pp. 71–83 (2005). 17
- [83] P. Ciarletta & M. Ben Amar; *Papillary networks in the dermal–epidermal junction of skin: a biomechanical model*; Mechanics Research Communications **42**, pp. 68–76 (2012). 17
- [84] T. T. K. Vuong-Brender, S. K. Suman & M. Labouesse; *The apical ECM preserves embryonic integrity and distributes mechanical stress during morphogenesis*; Development **144**, pp. 4336–4349 (2017). 18, 23, 31, 38, 50
- [85] S. Quintin, S. Wang, J. Pontabry, A. Bender, F. Robin, V. Hyenne, F. Landmann, C. Gally, K. Oegema & M. Labouesse; *Non-centrosomal epidermal microtubules act in parallel to LET-502/ROCK to promote C. elegans elongation*; Development **143**, pp. 160–173 (2016). 23
- [86] A. Goriely; *Five ways to model active processes in elastic solids: Active forces, active stresses, active strains, active fibers, and active metrics*; Mechanics Research Communications **93** (2017). 23, 25
- [87] J. Prost, F. Jülicher & J.-F. Joanny; *Active gel physics*; Nature physics **11**, pp. 111–117 (2015). 24, 154
- [88] M. Kojic & K.-J. Bathe; *Inelastic analysis of solids and structures*; volume 2 (Springer) (2005). 25, 79
- [89] A. Goriely, M. Destrade & M. Ben Amar; *Instabilities in elastomers and in soft tissues*; The Quarterly Journal of Mechanics & Applied Mathematics **59**, pp. 615–630 (2006). 25
- [90] C. E. Inglis; *Stresses in a plate due to the presence of cracks and sharp corners*; Trans Inst Naval Archit **55**, pp. 219–241 (1913). 31
- [91] H. M. Westergaard; *Bearing pressures and cracks*; Trans AIME, J. Appl. Mech. **6**, pp. 49–53 (1939). 31, 32, 33
- [92] N. I. Muskhelishvili; *Some Basic Problems of the Mathematical Theory of Elasticity* (Springer Netherlands) (1977). 31, 33, 36
- [93] C. Kirsch; *Die theorie der elastizität und die bedürfnisse der festigkeitslehre*; Zeitschrift des Vereines Deutscher Ingenieure **42**, pp. 797–807 (1898). 32
- [94] G. Kolossoff & C. Inglis; *Solution of plate with an elliptical hole*; Transactions of the Royal Institute of Naval Arch (1913). 32, 33

- [95] M. Williams; *Stress singularities resulting from various boundary conditions in angular corners of plates in extension*; Journal of applied mechanics **19**, pp. 526–528 (1952). [32](#)
- [96] M. Williams; *The stresses around a fault or crack in dissimilar media*; Bulletin of the seismological society of America **49**, pp. 199–204 (1959). [32](#)
- [97] G. C. Sih, P. Paris & G. Irwin; *On cracks in rectilinearly anisotropic bodies*; International Journal of Fracture Mechanics **1**, pp. 189–203 (1965). [32](#), [34](#), [35](#)
- [98] V. E. Saouma, M. L. Ayari & D. A. Leavell; *Mixed mode crack propagation in homogeneous anisotropic solids*; Engineering Fracture Mechanics **27**, pp. 171–184 (1987). [32](#)
- [99] Z. Suo; *Singularities, interfaces and cracks in dissimilar anisotropic media*; Proceedings of the Royal Society of London. A. Mathematical and Physical Sciences **427**, pp. 331–358 (1990). [32](#)
- [100] J. W. Hutchinson & Z. Suo; *Mixed mode cracking in layered materials*; Advances in applied mechanics **29**, pp. 63–191 (1991). [32](#)
- [101] C. MacGregor; *The potential function method for the solution of two-dimensional stress problems*; Transactions of the American Mathematical Society **38**, pp. 177–186 (1935). [33](#)
- [102] O. D. Kellogg; *Foundations of potential theory*; volume 31 (Courier Corporation) (1953). [33](#)
- [103] G. Sih; *On the Westergaard method of crack analysis*; International Journal of Fracture Mechanics **2**, pp. 628–631 (1966). [33](#), [34](#)
- [104] G. C. Sih; *Methods of analysis and solutions of crack problems*; volume 1 (Springer Science & Business Media) (2013). [33](#), [34](#), [35](#), [36](#), [44](#)
- [105] P. C. Paris & G. C. Sih; *Stress analysis of cracks*; in *Fracture toughness testing and its applications*, (ASTM International) (1965). [34](#), [36](#), [44](#)
- [106] H. Tada, P. C. Paris & G. R. Irwin; *The Stress Analysis of Cracks Handbook, Third Edition* (ASME Press) (2000). [34](#), [35](#), [36](#), [44](#), [47](#)
- [107] T. L. Anderson; *Fracture mechanics: fundamentals and applications* (CRC press) (2017). [34](#), [36](#), [47](#)
- [108] A. T. Zehnder; *Lecture notes on fracture mechanics*; (2007). [35](#), [36](#)
- [109] S. Lekhnitskii; *Theory of Elasticity of an Anisotropic Body* (Moscow: MIR); (1981). [35](#)
- [110] E. Preiß; *Fracture toughness of freestanding metallic thin films studied by bulge testing*; (2018). [36](#), [155](#)
- [111] J. RICE; *A Path independent integral and approximate analysis of strain concentration by notches and cracks*; Journal of Applied Mechanics **35**, pp. 379–386 (1968). [43](#)

- [112] A. O. Ayhan & H. Nied; *Stress intensity factors for three-dimensional surface cracks using enriched finite elements*; International Journal for Numerical Methods in Engineering **54**, pp. 899–921 (2002). 43, 44
- [113] A. O. Ayhan; *Stress intensity factors for three-dimensional cracks in functionally graded materials using enriched finite elements*; International Journal of Solids and Structures **44**, pp. 8579–8599 (2007). 43
- [114] A. Asadpoure, S. Mohammadi & A. Vafai; *Crack analysis in orthotropic media using the extended finite element method*; Thin-Walled Structures **44**, pp. 1031–1038 (2006). 43, 44
- [115] A. Asadpoure & S. Mohammadi; *A new approach to simulate the crack with the extended finite element method in orthotropic media*; International Journal for Numerical Methods in Engineering **69**, pp. 2150–2172 (2007). 43, 44
- [116] S. Bordas, P. V. Nguyen, C. Dunant, A. Guidoum & H. Nguyen-Dang; *An extended finite element library*; International Journal for Numerical Methods in Engineering **71**, pp. 703–732 (2007). 43
- [117] P. Sollero & M. Aliabadi; *Fracture mechanics analysis of anisotropic plates by the boundary element method*; International Journal of Fracture **64**, pp. 269–284 (1993). 43
- [118] S. Zhou, X. Zhuang & T. Rabczuk; *A phase-field modeling approach of fracture propagation in poroelastic media*; Engineering Geology **240**, pp. 189–203 (2018). 43
- [119] T. Tang, S. Kim, J. Jordon, M. Horstemeyer & P. T. Wang; *Atomistic simulations of fatigue crack growth and the associated fatigue crack tip stress evolution in magnesium single crystals*; Computational materials science **50**, pp. 2977–2986 (2011). 43
- [120] M. Pais; *2D MATLAB XFEM Codes*; (2010). 43, 45
- [121] P. G. Ciarlet & J.-L. Lions; *Handbook of Numerical Analysis: VOL II: Finite Element Methods.(Part I)*. (North-Holland) (1991). 44
- [122] M. J. Gander & G. Wanner; *From Euler, Ritz, and Galerkin to modern computing*; Siam Review **54**, pp. 627–666 (2012). 44
- [123] S. Natarajan; *Enriched finite element methods: advances & applications*; Ph.D. thesis; Cardiff University (2011). 44
- [124] N. Moës, A. Gravouil & T. Belytschko; *Non-planar 3D crack growth by the extended finite element and level sets—Part I: Mechanical model*; International journal for numerical methods in engineering **53**, pp. 2549–2568 (2002). 44
- [125] J. Dervaux, P. Ciarletta & M. Ben Amar; *Morphogenesis of thin hyperelastic plates: a constitutive theory of biological growth in the Föppl–von Kármán limit*; Journal of the Mechanics and Physics of Solids **57**, pp. 458–471 (2009). 65
- [126] W. M. van Rees, E. Vouga & L. Mahadevan; *Growth patterns for shape-shifting elastic bilayers*; Proceedings of the National Academy of Sciences **114**, pp. 11597–11602 (2017). 65

- [127] J. Ackermann, P.-Q. Qu, L. LeGoff & M. Ben Amar; *Modeling the mechanics of growing epithelia with a bilayer plate theory*; (2021). 65
- [128] E. K. Rodriguez, A. Hoger & A. D. McCulloch; *Stress-dependent finite growth in soft elastic tissues*; *Journal of biomechanics* **27**, pp. 455–467 (1994). 65
- [129] A. G. Evans, M. Rühle, B. J. Dalgleish & P. G. Charalambides; *The fracture energy of bimaterial interfaces*; *Metallurgical Transactions A* **21**, pp. 2419–2429 (1990). 67
- [130] S. P. Timoshenko & S. Woinowsky-Krieger; *Theory of plates and shells* (McGraw-hill) (1959). 67
- [131] S. Karkar, B. Cochelin, C. Vergez, O. Thomas & A. Lazarus; *User guide manlab 2.0*; Technical report; Laboratoire de Mécanique et d’Acoustique (LMA), CNRS UPR 7051 (2012). 69, 72
- [132] R. W. Pryor; *Multiphysics modeling using COMSOL®: a first principles approach* (Jones & Bartlett Publishers) (2009). 70
- [133] D. A. Dillard, B. Mukherjee, P. Karnal, R. C. Batra & J. Frechette; *A review of Winkler’s foundation and its profound influence on adhesion and soft matter applications*; *Soft matter* **14**, pp. 3669–3683 (2018). 72
- [134] T. Sussman & K.-J. Bathe; *3D-shell elements for structures in large strains*; *Computers & Structures* **122**, pp. 2–12 (2013). 76
- [135] Y. Ko, P.-S. Lee & K.-J. Bathe; *The MITC4+ shell element and its performance*; *Computers & Structures* **169**, pp. 57–68 (2016). 76
- [136] Y.-B. Yang & S.-R. Kuo; *Theory and analysis of nonlinear framed structures* (Prentice Hall PTR) (1994). 97
- [137] L. Andersen & S. Nielsen; *Elastic beams in three dimensions*; Aalborg University (2008). 97
- [138] A. E. H. Love; *A treatise on the mathematical theory of elasticity* (Cambridge university press) (2013). 97
- [139] A. A. Almet, H. M. Byrne, P. K. Maini & D. E. Moulton; *Post-buckling behaviour of a growing elastic rod*; *Journal of mathematical biology* **78**, pp. 777–814 (2019). 97
- [140] J. Dervaux & M. Ben Amar; *Mechanical instabilities of gels*; *Annu. Rev. Condens. Matter Phys.* **3**, pp. 311–332 (2012). 106
- [141] H. Alawiye, E. Kuhl & A. Goriely; *Revisiting the wrinkling of elastic bilayers I: linear analysis*; *Philosophical Transactions of the Royal Society A* **377**, p. 20180076 (2019). 106
- [142] I. Valizadeh & O. Weeger; *Nonlinear multiscale simulation of instabilities due to growth of an elastic film on a microstructured substrate*; *Archive of Applied Mechanics* **90**, pp. 2397–2412 (2020). 106
- [143] F. Irgens; *Continuum mechanics* (Springer Science & Business Media) (2008). 107

RÉSUMÉ

Les formes dans la nature, du chou-fleur au cerveau, proviennent de la croissance des tissus. Pour comprendre l'émergence des formes, en particulier dans les tissus biologiques, il faut saisir les caractéristiques mécaniques inhérentes au matériau vivant. De plus, de nombreux objets vivants minces sont composés de plusieurs couches qui ont des propriétés élastiques différentes et suivent également des règles de croissance différentes. Dans cette thèse, nous essayons d'utiliser l'élasticité non linéaire pour modéliser la croissance de l'épithélium de *C.elegans* et de la drosophile. Nous étudions d'abord le mécanisme de l'élongation embryonnaire de *C.elegans*. Nous étudions l'effet de l'application de la technique d'ablation laser pour l'évaluation des contraintes sur l'épiderme externe. L'hyperélasticité avec renforcement par fibres est considérée dans la relation constitutive. La contrainte interne induite par le réseau actif est examinée dans le calcul. En outre, une formule modifiée est proposée pour la fissure ouverte sur la surface de l'animal. Les résultats avec les données expérimentales prouvent la validité de notre approche. Ensuite, nous essayons de simuler le flambage du tissu épithélial du disque alaire de la drosophile. Un modèle de Föppl-Von Kármán bicouche avec croissance est obtenu pour une fine lamelle avec une matrice extracellulaire (ECM). La contribution à la flexion par le réseau actif est incluse dans le modèle. Nous obtenons une solution analytique des équations non linéaires. Le défaut de l'ECM est pris en compte pour l'expérience. Nous utilisons le logiciel commercial COMSOL pour la simulation numérique en 3D. Une plateforme d'éléments finis est également préparée dans MATLAB pour les besoins de cette recherche.

MOTS CLÉS

croissance, épithélium, élasticité non linéaire, réseau actif, bicouche

ABSTRACT

Shapes in nature, from the cauliflower to the brain, arise from growth of tissues. Understanding ultimately the emergence of shapes, in particular in biological tissues, requires to capture the mechanical features that are inherent to the living material. Besides, many thin living objects are composed of several layers which have varying elastic properties and also follow different rules of growth. In this thesis, we try to employ nonlinear elasticity to model the growing epithelium of *C.elegans* and *Drosophila*.

We first study on the mechanism of *C.elegans* embryonic elongation. We investigate the effect of the application of laser ablation technique for the stress assessment on the external epidermis. Hyper-elasticity with fiber reinforcement is considered in the constitutive relation. Inner stress induced by active networks is examined in the calculation. In addition, a modified formula is proposed for the crack opening on the animal surface. Results with experimental data prove the validity of our approach. Then we try to simulate the buckling of the epithelial tissue of the *Drosophila* wing disc. A bilayer Föppl-Von Kármán model with growth is obtained for a thin lamina with an extracellular matrix (ECM). Bending contribution by active networks is included in the model. We acquire an analytical solution of the nonlinear governing equations. Defects of ECM are taken into account for the experiment. We employ commercial software COMSOL for numerical simulations in 3D. A finite element platform is also prepared in MATLAB for research purpose.

KEYWORDS

growth, epithelium, nonlinear elasticity, active network, bilayer